Wrinkling behaviour of biaxial non-crimp fabrics during preforming

Johan Verner Viisainen

Department of Engineering
University of Cambridge

This thesis is submitted for the degree of
Doctor of Philosophy

Declaration

This thesis is the result of my own work and includes nothing which is the outcome of work done in collaboration except as declared in the Preface and specified in the text. I further state that no substantial part of my thesis has already been submitted, or, is being concurrently submitted for any such degree, diploma or other qualification at the University of Cambridge or any other University or similar institution except as declared in the Preface and specified in the text. It does not exceed the prescribed word limit for the relevant Degree Committee.

<div align="right">

Johan Verner Viisainen

September 2021

</div>

Wrinkling behaviour of biaxial non-crimp fabrics during preforming

Johan Verner Viisainen

The necessary lightweighting of the transport sector to meet emission reduction targets can be helped through the expanded use of composites. However, for the high volume production of composites to be cost-effective, it is needed that they can be manufactured through automated liquid composite moulding (LCM). Furthermore, the defects that occur during the initial preforming stage of LCM, notably wrinkles, are a key obstacle preventing automation and adoption of LCM, because wrinkles significantly compromise the component performance, and because there is currently no reliable method for mitigating them. To pave the way towards wrinkling mitigation during preforming, this thesis aims to characterise the wrinkling behaviour of non-crimp fabrics (NCFs) as well as to investigate how the wrinkling severity is affected by the tool geometry.

These aims are achieved through both experimental and numerical approaches. Firstly, experimental forming tests are conducted to characterise the mechanisms, severity and variability of wrinkling for a $\pm45°$ biaxial NCF during preforming, considering four contrasting benchmark geometries. Secondly, a large dataset of forming simulations for various tool geometries is generated and used to investigate the effect of geometry on wrinkling severity, and to develop a deep learning based surrogate model for rapidly predicting the fabric wrinkling over a given tool geometry.

The results demonstrate that two macroscale wrinkling mechanisms exist for this NCF and that the most severe wrinkles occur consistently via lateral fabric compression during material draw-in rather than tow compression at shear-lockup. Furthermore, they show that the wrinkling variability is significant and is especially apparent for multi-layer forming. Additionally, the tool geometry is shown to have a substantial effect on wrinkling with more tapered geometries leading to less severe wrinkling. Lastly, the surrogate model is demonstrated to achieve similar predictions to the finite element simulations but at a much lower computational cost, thus enabling the optimisation of component geometry for minimal wrinkling.

To Kirsi, Lena and Cui Er, three bold women who have all inspired me greatly.

Acknowledgements

This thesis would not have been possible without financial support from the Engineering and Physical Sciences Research Council, as well as the contributions and support of the following people, to whom I owe a debt of gratitude.

First of all, I would like to thank my supervisor Professor Michael Sutcliffe for helping guide this research from the beginning, always providing positive yet decisive feedback, and being supportive and approachable during the difficult moments. My thanks are also extended to my advisor Dr Graham McShane, who offered useful comments during the first and second year assessments in particular.

Furthermore, I want to acknowledge both Dr Jin Zhou and Dr Andrea Codolini, with whom I had the pleasure of working on this research. They were both able to offer crucial insights at critical points of this PhD journey, with Andrea also offering his time to run key simulations for Chapter 5. Dr Burigede Liu is also acknowledged for helping me with developing the post-processing method for Chapter 3. In addition, Dr Abbas Hosseini's previous work into wrinkling mechanisms contributed to the findings in Chapter 3. The previous work of MEng students at Cambridge on developing the forming rig that I inherited is also acknowledged and appreciated. I would also like to thank Dr Graham Treece for his advice in contributing towards the variability calculation method in Chapter 4. Additionally, Chapter 5 would not have been possible without the modelling expertise of Dr Fei Yu, Dr Shuai Chen and their supervisor Dr Lee Harper from the University of Nottingham, who kindly allowed me to use their finite element model. Furthermore, thank you to Dr Reza Sourki for making transatlantic collaboration an enjoyable process.

The unsung heroes of any experimental work are the technicians who make it possible and in this case, the experiments in Chapter 3 and Chapter 4 were only feasible due to the amazing technicians in Division C, from whom I learnt so much. In particular, I would like to thank Mr Simon Marshall and Mr Graham Smith, with Simon being instrumental in building the forming rig and getting me familiar with DIC, and Graham being instrumental in keeping me sane during those long days of testing. The assistance of Mr Stefan Savage, Mr Tony Dennis, Mr Len Howlett, Mr Gary Bailey and Mr David Sayles is also acknowledged.

Table of contents

List of figures

List of tables

Chapter 1

Introduction

1.1 Motivation for thesis

As shown by the UK Climate Change Act and the 2015 Paris Agreement respectively, there are both national legal requirements and a global agreement on the rapid need to decarbonise every aspect of society and to reach net-zero carbon dioxide (CO_2) emissions by 2050, if we are to avoid the worst effects of climate change. This requirement applies equally to the transport sector, which contributes around 20% of global CO_2 emissions due mainly to the use of fossil fuels for propulsion [1]. Thus there is an urgent need for the automotive and aerospace industries to electrify their vehicles, where this is feasible, and significantly improve their energy efficiency otherwise. With fully electric commercial plane travel not being projected to be feasible within the next 30 years, improving energy efficiency will be critical for continued operation at lower emissions [2], particularly as there are significant environmental concerns associated with the adoption of bio-fuels [3].

With respect to the automotive sector, the shift towards ground-based electric vehicles is well underway and projected to grow rapidly in the coming years [4] but these more efficient, low emission vehicles are currently limited by their travel range, which can only be counteracted by adding more heavy batteries [5]. These have a negative effect on efficiency as the maximum energy efficiency of a vehicle is limited by its overall mass and thus those batteries must be counterbalanced by weight reductions elsewhere. As a result, for both industries, there is increasing attention to a previously secondary objective: to reduce the mass of structural components through 'lightweighting': redesigning components using alternative materials that provide the same mechanical properties at a lower density or improved specific strength and stiffness.

Advanced composite materials such as carbon fibre reinforced plastic (CFRP), are an attractive class of materials that have similar strength and stiffness but much lower density compared to the more conventional structural materials used in the transport sector: steel and aluminium alloys [6]. Given these properties, CFRP is an attractive option for the lightweighting of the transport sector and has already seen significant use in the structural components of high-budget, low volume vehicles such as sports cars, Formula 1 cars and the Boeing 787 Dreamliner aircraft. In the latter case, composites make up 50% of the structure by weight, leading to 20% overall weight savings [7]. However, the wider adoption of CFRP within the automotive sector for mass-produced vehicles is held back by the high material cost of the 'prepreg' material and the traditionally low volume and high-cost method of autoclave moulding [8, 9]. Thus to address this barrier, alternative approaches for the manufacturing of CFRP need to be adopted that allow for low cost and high volume production.

Preforming of the fabric layup   Resin injection into the preform   Final composite component
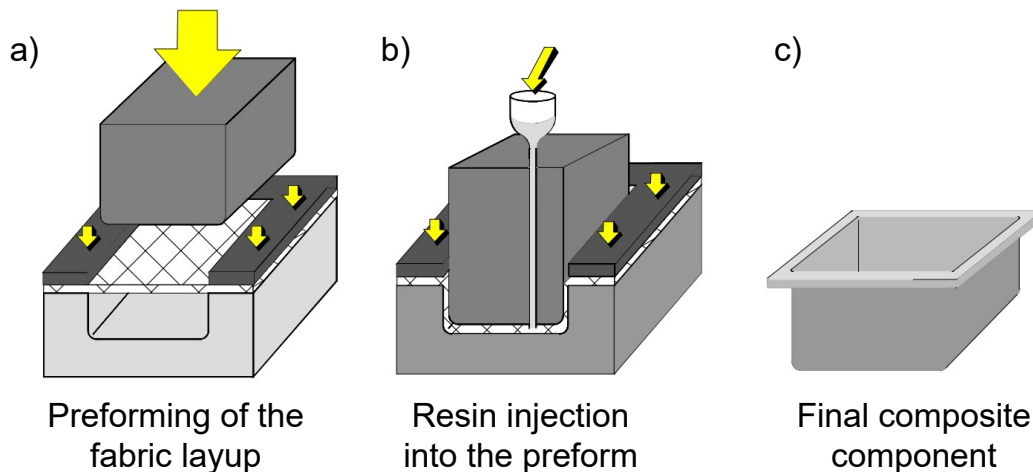
Fig. 1.1 Overview of a liquid composite moulding (LCM) manufacturing process. In this case, the resin transfer moulding (RTM) process is depicted, consisting of two key stages: a) preforming of the fabric layup and b) resin injection into the preform, which then result in c) the final composite component. Adapted from [10].

Using dry textile reinforcements that are manufactured into 'textile composites' through liquid composite moulding (LCM) presents a feasible way to make CFRP at high volumes and relatively low cost. There are various LCM approaches including resin transfer moulding (RTM), the steps of which are shown in Figure 1.1. A key example of a vehicle manufactured in this way is the BMW i3, which was the first mass-market vehicle with a structure made fully from CFRP [11] and has inspired further incorporation of composites within the automotive industry [12]. LCM approaches minimise the cost of the raw material by avoiding prepreg and thus keeping the fibres and resin separate until the infusion/curing phase. Furthermore, the

manufacturing rate and cost are improved as LCM processes can be automated with short cycle times and implemented into a continuous production, thus significantly reducing labour costs and improving processing times compared to manual layup and autoclave moulding.

However, while using dry textile reinforcements (also called fabrics) instead of unidirectional (UD) prepreg tapes is attractive from a manufacturing point of view due to their improved handleability, the inherent crimp in woven carbon fibre fabrics is associated with significant reductions in mechanical properties (both strength and stiffness) of the final component compared to components made from UD [13]. Thus, it makes woven fabric composites less suitable for lightweighting as thicker layups are required for the same performance.

Non-crimp fabrics (NCFs) are a relatively recent class of textile reinforcement, made up of layers of straight fibre tows that are stitched together. Thus they avoid the tow undulations of woven fabrics that cause a drop in mechanical properties while maintaining their handleability, making them highly suited for automated manufacturing. By combining the best features of UD and woven, they are thus an ideal material for use with LCM that can achieve high-performance parts at lower cost and higher volume. However, due to the customisability of NCFs in terms of layers, tow orientations and stitch types, they are generally much less well understood than woven fabrics in terms of their behaviour. Therefore, further work is needed to better understand how these promising fabrics can be most optimally manufactured via LCM.

The key impediments that hinder the automated production of textile composites through LCM are the significant defects that arise during production, particularly at the initial preforming stage of LCM, where the fabric layup is draped over the tool geometry (Figure 1.1a). These defects mean that any advantages of automated production are offset by an increase in scrapped parts and poorer overall part quality, which then result in added costs and production time. Thus the preforming step currently represents over 39% of the total cost of an RTM manufactured component [14], a similar proportion to the cost of the expensive raw material (42%). Numerous studies have highlighted the additional challenges with forming of biaxial NCFs compared to woven fabrics, namely the addition of relative ply sliding [15] and the asymmetric shear behaviour [16]. These defects during preforming need to be eliminated or mitigated so that textile composite components can meet the industrial safety and performance requirements, and enable the lightweighting of the automotive and aerospace sectors.

While the defects and their severity can vary significantly, a critical defect that is common to most forming processes is fabric wrinkling. This defect, consisting of either fibres buckling along their length or the fabric folding out-of-plane can have detrimental effects on the mechanical performance of the final component and thus has seen significant attention within industry and academia over the last few decades. However, progress has been hindered by a

lack of fundamental understanding of the underlying wrinkling mechanisms and the inherent variability of wrinkling [17], which makes them more challenging to predict. Therefore, the mitigation of wrinkling during preforming remains an unresolved problem that prevents the higher volume production of CFRP.

The wrinkling of fabrics is particularly severe during the preforming of complex, doubly curved geometries. The high level of wrinkling can be partly explained by the fact that some wrinkles are an inevitable result of mapping continuous fibre tows over a curved geometry [18] but it is not clear whether any particular wrinkle is a design-induced feature or a manufacturing defect caused by poor selection of process parameters. Thus it is critical to better understand how the tool geometry contributes towards wrinkling during preforming and whether these defects can be eliminated through design optimisation.

1.2   Thesis aims and objectives

As outlined, a key challenge in the necessary lightweighting of the automotive sector through the wider use of textile composites remains developing a better understanding of NCF wrinkling behaviour and how this wrinkling can be mitigated during the preforming of complex geometries. This thesis contributes towards addressing this challenge by considering the wrinkling of biaxial NCFs during the preforming process. The two central aims of this thesis are:

1. To characterise the wrinkling mechanisms and variability of a biaxial NCF during preforming (Aim #1).

2. To investigate the effect of the tool geometry on NCF wrinkling severity during preforming (Aim #2).

In order to address these aims, the following six objectives are investigated through a mixture of experimental and numerical approaches:

1. To characterise the wrinkling behaviour and mechanisms of a pillar-stitched $\pm45°$ biaxial NCF formed over a hemisphere (as part of Aim #1).

2. To investigate how the wrinkling behaviour changes when the NCF is formed over three other benchmark geometries: a double dome, a tetrahedron and a triangular prism (as part of Aim #2).

3. To develop a novel variability calculation method that can decouple the wrinkling variability of fabrics in terms of wrinkle amplitude and wrinkle location (as part of Aim #1).

4. To apply this variability calculation method to characterise the experimental variability in the wrinkling defects of a preformed biaxial NCF compared against other materials, and with contrasting preforming conditions and layups (as part of Aim #1).

5. To develop a deep learning surrogate model to rapidly predict the wrinkling severity for a given convex tool geometry during double diaphragm preforming for a biaxial NCF (as part of Aim #2).

6. Based on the simulated data used to develop the surrogate model, to investigate the relationship between geometrical characteristics of the tool geometry and the severity of wrinkling (as part of Aim #2).

The motivation for these specific objectives will be further elaborated on through the literature review presented in Chapter 2.

1.3 Thesis outline

This thesis is divided up into six chapters that attempt to address these objectives, with three key investigations presented that consider in turn: wrinkling characterisation, the variability of wrinkling and the prediction of wrinkling. The full outline of the subsequent chapters in this thesis is thus as follows:

- Chapter 2 presents a detailed literature review into the wrinkling of textile reinforcements, providing background to NCFs and preforming, as well as highlighting the gaps in the literature that motivate the thesis objectives.

- Chapter 3 addresses the first two objectives by experimentally analysing the wrinkling behaviour for a biaxial non-crimp fabric for a range of tool geometries, to highlight the varying mechanisms by which wrinkles form in textile reinforcements and how these are affected by tool geometry.

- Chapter 4 focuses on the third and fourth thesis objectives by characterising the variability in wrinkling behaviour between 'identical' samples formed under the same conditions using a novel image-based method. The investigation also extends to consider the effect of different process conditions on the overall variability of forming and the wrinkling defects produced.

- Chapter 5 targets the fifth and sixth thesis objectives through a numerical study to evaluate the links between geometry and wrinkling severity, while also using this numerical data

to train a deep learning surrogate model for rapidly predicting the wrinkling behaviour for a given tool geometry.

- Chapter 6 concludes the thesis by summarising the key contributions made, listing the specific conclusions from Chapters 3-5 and presenting possible avenues for future work.

To summarise the structure of the thesis, a graphical thesis outline is presented in Figure 1.2.
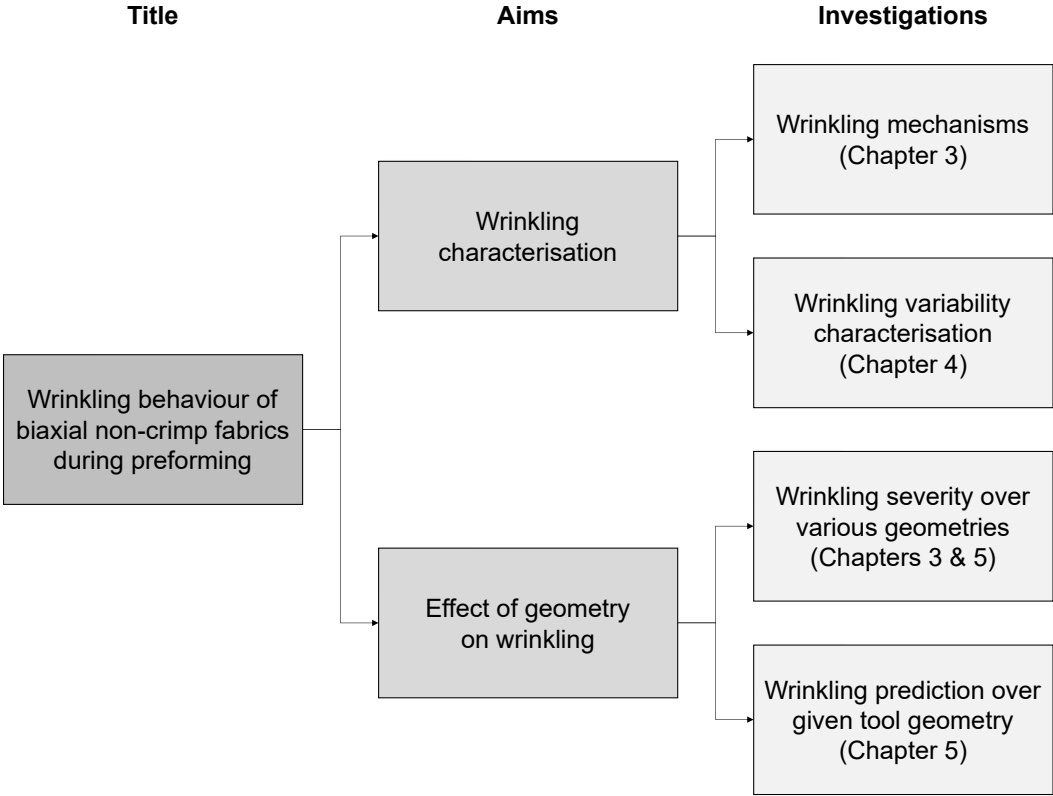
Fig. 1.2 Graphical thesis outline showing the thesis title, the two aims and how these aims were investigated through four distinct investigations that are spread across Chapters 3-5.

Chapter 2

Literature review

2.1 Introduction

This chapter presents an overview of the available literature related to the preforming of fabrics and their wrinkling behaviour, with particular emphasis placed on biaxial non-crimp fabrics (NCFs). The chapter will cover an overview of NCFs, key preforming processes and their defects before elaborating further on research related to the wrinkling defects, and attempts made to characterise and simulate the preforming and wrinkling behaviour of fabrics.

Spurred on by industrial interest into wider adoption of textile composites and the automated manufacturing of composites, understanding into the forming of textile reinforcement and particularly their wrinkling behaviour has grown significantly over the last 25 years within academia. There have been major breakthroughs being made in developing experimental methods for characterising and understanding the fabric behaviour [19], and in developing more advanced models for simulating the forming behaviour [20], that are now capable of capturing their complex wrinkling behaviour [21]. The large majority of this work has been focused on conventional woven fabrics but, since the early 2000s, increasing attention in academia and industry has been directed towards NCFs.

2.2 Background to NCFs and preforming

2.2.1 Non-crimp fabrics

NCFs, also known as multiaxial reinforcements, are a type of textile reinforcement made up of oriented layers of aligned unidirectional (UD) fibre tows with the layers held together through stitching. They are attractive because of their improved mechanical properties (stiffness and

strength) over woven textile reinforcements while also providing superior handleability over unidirectional (UD) tapes [8]. These properties are a result of the stitching, which ensures that the fibre tows in the NCF are kept straight (rather than inter-woven) to achieve mechanical properties comparable to UD [22], and holds the straight fibre tows together as a fabric making NCFs handleable and suitable for lower cost manufacturing through LCM [8]. Thus NCFs represent are an ideal hybrid material system between UD and woven in terms of properties and ease of manufacturing.

The mechanical properties of the consolidated NCF composite for a given architecture are largely determined by the choice of fibre material used in the NCF: either carbon fibre, glass fibre or aramid, with carbon fibre resulting in the highest stiffness and strength [22]. However, for the purposes of preforming and wrinkling, all the fibre systems behave similarly [23] and thus different fibre materials are not considered in this thesis. The NCFs used in this thesis are made of carbon fibre but the observations apply equally to other fibres as long as the NCF fibre architecture is comparable.

An overview of the many different types of fabrics that are considered NCFs is shown in Figure 2.1. The most common type, and the one that will be referred to as an 'NCF' for the rest of this thesis, is the warp-knitted NCF. This is distinguished from weft-knitted NCFs by the stitch loop formation being parallel with the production direction of the fabric [24], thus making it more suited for automated machine production as multiple threads can be laid down in parallel along the width of the fabric.

There are numerous types of warp-knitted NCFs and their fabric architecture can be primarily categorised by the number of tows layers, the layer directions and the type of stitching used. The number of layers in a NCF is typically either one (unidirectional-NCF), two (biaxial NCF), three (triaxial NCF) or four (quadaxial NCF), with each layer adding an increased level of complexity and causing differing fabric behaviour [25]. This thesis will primarily focus on biaxial NCFs, which most closely resemble woven fabrics in their architecture.

The inherent customisability of NCFs means that the potential choice of layer directions are only limited the by capability of the production machine but typically only certain combinations are used in industry. These orientations are always balanced about the stitching direction and for biaxial NCFs they are typically orthogonal to each other to mimic woven fabrics. As a result, the biaxial orientations that are most commonly used in industry are either $\pm 45°$ [16, 26, 27] (also called a bidiagonal NCF) or $0°/90°$ [28, 26, 29], with the less conventional $\pm 30°$ [30] and $\pm 60°$ [25] also offered by manufacturers.
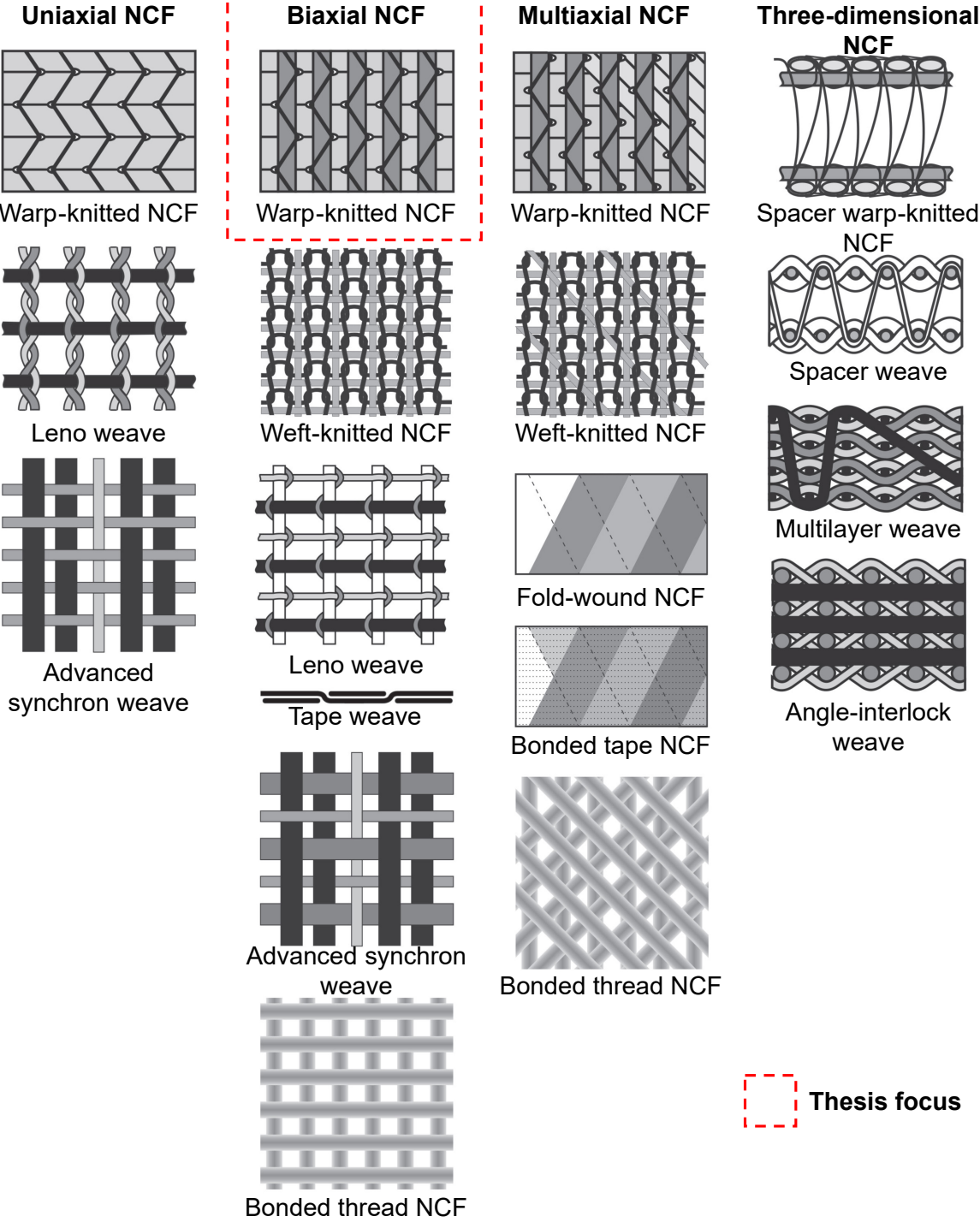
Fig. 2.1 Overview of the different types of non-crimp fabrics (NCFs) with the NCFs focused on in this study highlighted. The figure is adapted from [24].

Decreasing bending stiffness

Increasing formability

| Pillar | Tricot | Plain | Satin |

Thesis Focus   Most Common
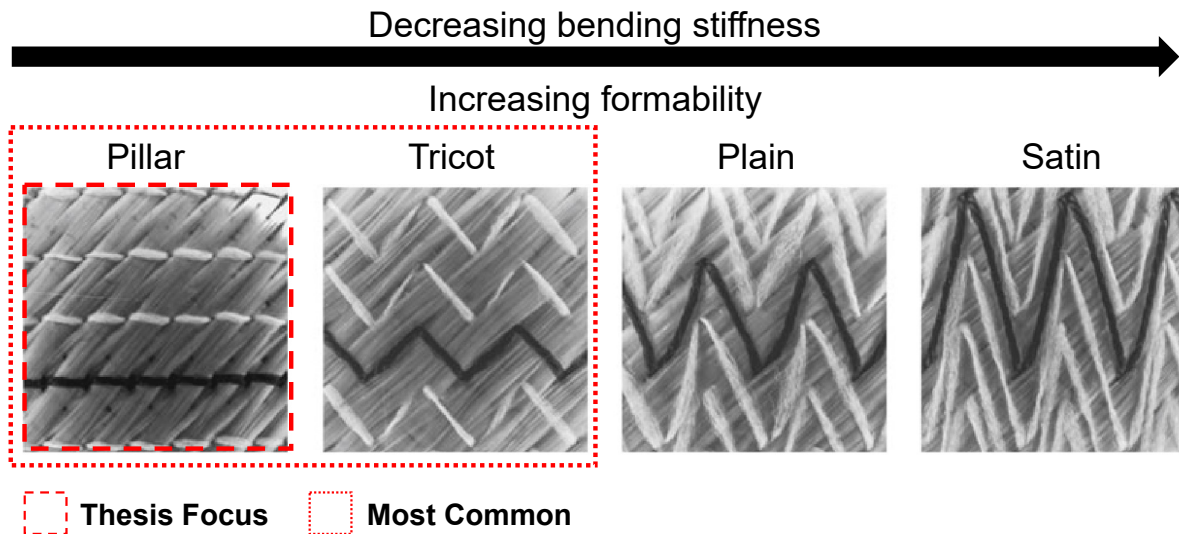
Fig. 2.2 Four different stitch types for non-crimp fabrics (NCFs), ordered in ascending order of NCF formability from left to right: pillar, tricot, plain and satin. Note that hybrid stitch types that combine two or more stitch types are also possible (e.g. pillar-tricot stitch). The figure is adapted from [31].

The stitch types that are used to bond NCFs are characterised by the transverse displacement of the knitting needle during the stitching process, with the most basic 'pillar' (also called 'chain' or 'warp') stitch (Figure 2.2a) consisting of no transverse movement and each parallel stitch being independent of the other. As the transverse displacement of the needle is increased (measured in increments of the needle gauge, which equals the distance between neighbouring needles) is increased to one, two and three, the corresponding stitch types are referred to as 'tricot', 'plain' and 'satin' stitch respectively (Figure 2.2b-d) [31]. For the production of NCFs, two most types common stitch types used are the pillar stitch [16, 27, 32] and the tricot stitch [33, 34], with occasionally a hybrid version of the two - the tricot-pillar stitch - being used [35, 36]. For the 0°/90° NCF, the tricot or the tricot-pillar stitch are almost exclusively used, with the transverse overlapping of the tricot stitch pattern allowing for the tows along the 0° to be held in place, which would not be possible with a pillar stitch. In contrast, ±45° NCFs are not limited by the choice of stitch type and both tricot [33] and pillar [16] stitch variations are used. As a result of the overlap of adjacent stitches, tricot-stitched NCFs are more formable compared to pillar-stitched NCFs (Figure 2.2) but at the expense of lower shear and bending stiffness [23]. Given that high fabric stiffness is a necessary condition for robot handling during automated production [23], pillar-stitched NCFs hold more promise for low cost manufacturing. In addition, NCFs can be further customized by changing their stitch gauge

length, the stitch length, stitch tension and yarn count but these have a less significant effect on forming behaviour compared to the stitch type [23, 37].

The above discussion highlights how the ±45° NCFs investigated in this thesis are attractive from an automated manufacturing point of view, in comparison to an equivalent 0/90° NCF. This is because they can be made with simpler pillar stitches and are suitable for automated production due to their higher bending stiffness. However, previous studies have shown that the formability of 0/90° NCFs is typically superior [26] and thus if ±45° NCFs are to be used more extensively, their forming behaviour must be better understood such that they can be used to produce components with minimal defects.

2.2.2   Types of preforming and defects

The preforming of dry textile reinforcements can be achieved through various methods that can be generally divided into press tool forming and diaphragm forming approaches, with each of these shown in Figure 2.3.
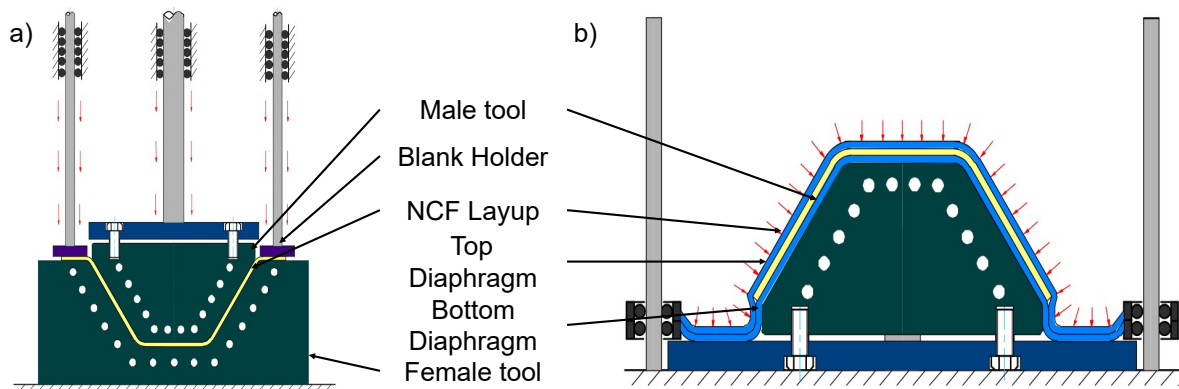
Fig. 2.3 Comparison of the press tool forming (a) and the double diaphragm forming (b) processes. The figures are adapted from [12].

Press tool forming

Press tool forming consists of one or two fixed tools and a fabric layup held in place under tension (typically under a blank holder), while the male tool is gradually moved at a constant speed through the tensioned layup for a predetermined distance or until it reaches the female tool. With a single tool, it is most commonly conducted with a male rather than a female tool [25] and the tool is often referred to as the 'punch'. However, to better constrain the deformation of the fabrics, a male-female tool configuration is most typically used in industry [12] and is referred to as 'matched tool forming'. However, the manufacturing of fixed tooling,

particularly for matched tool forming, is costly, making it only really suitable for very high volume manufacturing (>100,000 parts/annum) where no changes in tooling is expected [12]. Nonetheless, given the relatively simple experimental arrangement that can often be fitted within existing mechanical testing machines, it is the most common preforming process considered in academia and is used to characterise material preforming behaviour. This characterisation is most commonly done over a hemispherical geometry, given its axial symmetry and lack of distinct features [16, 26]. Hemispherical forming is employed in Chapter 3 and Chapter 4 for wrinkling characterisation. While the matched-tool forming arrangement is unfeasible for the study of the geometrical effect due to tooling costs, press tool forming using one male tool is also suited to study the effects of different tool geometries (Chapter 3).

Diaphragm forming

Diaphragm forming consists of replacing one of the rigid tools from press tool forming with a flexible diaphragm that is held under a vacuum against the layup in order to apply a hydrostatic pressure that forces the fabric to form into the required shape. Diaphragm forming can be done with either a male or a female tool. There are two versions of diaphragm forming: single diaphragm forming (SDF) and double diaphragm forming (DDF). In the SDF configuration, there is only a top diaphragm and a vacuum is created between it and the layup, while in DDF, there is an additional bottom diaphragm that creates a vacuum between the tool and the layup. SDF is more flexible than DDF as it allows for layer-wise forming but it is less effective in reducing variability and defects for more complex geometries due to the lack of the bottom diaphragm that constrains the plies relative to the tool [38].

The key advantages of DDF over press tool forming are the lower tooling costs meaning it is economically viable for use with less high volume production (around 30,000 parts/annum) [12] and there is much less material wastage as no excess material is required to tension the material under the blank holder, meaning preforms can be produced at near net-shape [39]. Finally, given the flexible diaphragms, it is particularly suited for comparative studies of different tool geometries and thus will be the focus of the simulated work in Chapter 5.

Defect types

The common defects that can occur during these preforming processes for NCFs are macroscale wrinkling (fabric folding), mesoscale wrinkling (tow buckling or fibre waviness), stitch bending, stitch rupture, laddering (gapping between tows) and bridging [16, 26, 40, 38]. Although most of the defects occur in both press tool forming and diaphragm forming, bridging is exclusive to

diaphragm forming and occurs when the fabric is unable to fully form over a sharp radius of the tool [38]. While the other defects should also be avoided where possible, the most critical defect is macroscale wrinkling as it has the most potential for causing detrimental losses in mechanical performance (Subsection 2.3.2). Thus it is the main focus of this thesis while the mechanisms for mesoscale wrinkling are also considered in Chapter 3.

2.2.3 Geometries of interest
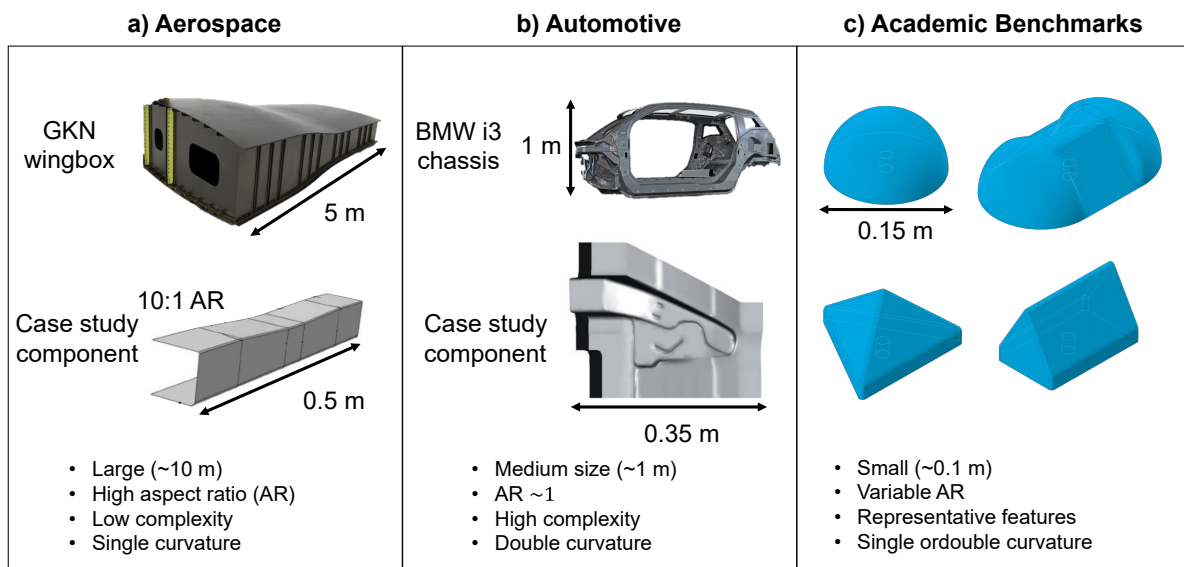
Fig. 2.4 Geometries of interest for composites manufacturing via liquid composite moulding within: a) the aerospace industry, b) the automotive industry and c) academia (academic benchmark geometries). Smaller case study components are shown in a) and b) alongside larger, more industrially relevant components. The images in a) and b) are adapted from [41] (GKN wingbox), [42] (aerospace case study component), [43] (BMW i3 chassis) and [34] (automotive case study component).

This thesis is concerned with trying to better understand the relationship between forming defects and geometries over which these defects form. However, the types of geometries that are of interest for composites manufacturing and thus preforming, are highly dependent on the particular industry and context. While composites are also used in a wide variety of applications in e.g. the sports, space and maritime industries, the two most prominent industries for advanced structural composite components are the aerospace and automotive industries. Both industries have distinct requirements of the types of geometries that are of interest in terms of composites manufacturing via LCM.

Aerospace structural components are relatively simple geometries, long (of the order of 10 m) with typically large aspect ratios, single curvatures and spread out geometrical features. Typical examples of such geometries are shown in (Figure 2.4a) with the wing box representing the true large scale of such components while the spar geometry shown has been scaled down to be suitable for use as a case study in academia. The large sizes of these components means that any defects are many orders of magnitude smaller than the component, making both experimental [44] and computational study [45] of their forming defects more challenging and costly.

In contrast, structural automotive components (such as the BMW i3 chassis in Figure 2.4b) are smaller (of the order of 1 m), with significant levels of complexity, multiple geometric features in close proximity and often including double curvatures. The smaller length scales make defects easier to investigate but the proximity of multiple interacting features means that defect-free forming is challenging to achieve and isolating how particular geometrical features hinder or mitigate those defects is not feasible. However, like for aerospace components, they are still often scaled down to smaller size for use in academia (see case study component in Figure 2.4b).

While the scaled-down, case study components are shown in Figure 2.4a & b are useful to some extent for proof of concept [42, 34], it is challenging to derive any fundamental or generalised understanding from them about fabric deformations, and they make comparisons across research groups more challenging due to their size and complexity. As a result, it is neither practical or desirable to use directly industrially relevant geometries for the study of fabric forming and associated defects within an academic context. Instead there is an inclination to utilise particular benchmark geometries (Figure 2.4c) that allow comparisons to be made across research groups and enable the characterisation of different fabrics to be done comprehensively [46]. These benchmark geometries are typically smaller in scale and do not correspond exactly to the desired industrial components, but rather they incorporate certain representative geometrical features, and thus also allow for more general insights to be made about fabric formability for industrial purposes. In particular, geometries incorporating double curvatures are often used as these have been identified as particularly difficult to form without defects [47]. In this thesis, experimental preforming tests are conducted on four common benchmark geometries: a hemisphere, a double dome, a triangular prism and a tetrahedron (Chapter 3), and finite element simulations are used to extend this investigation to a larger class of geometries that contains various geometrical features relevant to both the aerospace and the automotive industries (Chapter 5).

2.3   Wrinkling defect

In both of the two preforming processes considered, wrinkling is a critical defect. There has been significant attention to fabric wrinkling in industry and academia in the last 25 years since the foundational work of Prodromou and Chen [48] that analytically showed that excess in-plane shearing leads to fabric wrinkling. Since then, although there has been a multitude of studies attempting to characterise [25, 49] and to simulate [50, 21, 51] the occurrence and development of fabric wrinkling during preforming, mitigating them remains an unresolved issue.

2.3.1   Definition and descriptors of wrinkling
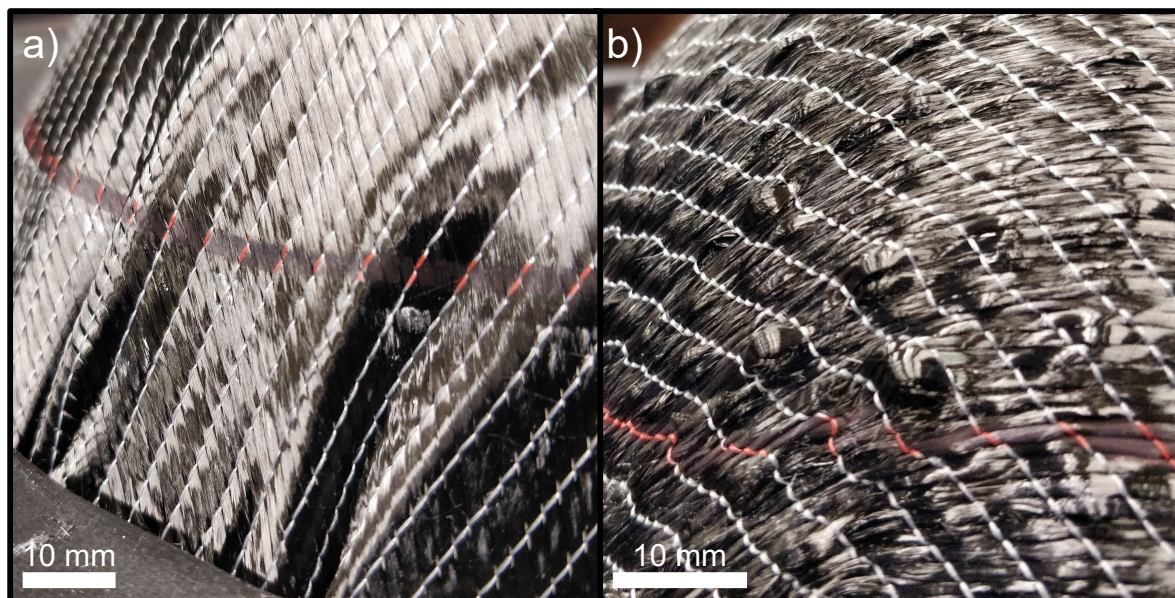
Fig. 2.5 a) Macroscale wrinkling and b) mesoscale wrinkling

There is no consistent definition for wrinkling within the composites manufacturing community due to ambiguities with respect to the scale at which these wrinkles occur and the primary mechanism causing them. Thus it is important to clearly define wrinkling for the purposes of this thesis. Generally, a wrinkle can be described as any in-plane or out-of-plane surface deviation from an ideally smooth surface. In this thesis, a distinction is made between macroscale and mesoscale wrinkling whereby macroscale wrinkling (Figure 2.5a) refers to the out-of-plane folding of the fabric perpendicular to the tool perimeter while mesoscale wrinkling (also called tow waviness [52], or tow buckling [26]) (Figure 2.5b) refers to either the out of plane or

in-plane folding of the fibre tow along its length. These naming conventions are consistent with those used by Chen [12]. Where the term 'wrinkling' is used without a descriptor in this thesis, this is to be taken to refer to macroscale wrinkling.

Macroscale wrinkles have been characterised using various different descriptors, depending on the context in which they occur and on what data can be reasonably obtained. In its simplest one dimensional form, a wrinkle can be characterised as a sinusoidal wave with a wavelength (λ) and an amplitude (δ) with severity or maximum waviness angle (θ) given by [53]:

$$\theta = \arctan\frac{\pi\delta}{\lambda} \tag{2.1}$$

While such a description of wrinkling is useful in certain scenarios such as modelling the consolidation of a layup over a single curvature geometry [54] or for investigating the effect of an embedded wrinkle within a layup stack [53], it is limited for describing the wrinkles observed during preforming of complex doubly curved components where the macroscale wrinkles are also 3D in nature and no waviness angle can be easily defined.

As the most popular predictor of wrinkling in more than one dimension, the shear locking angle (γ_l) is used to quantify the limiting shear angle beyond which shear wrinkling initiates, and has often been used to identify the locations on a preform where wrinkling is likely to have occurred [47]. However, γ_l is limited to predicting wrinkles in regions of significant shear, is not a sufficient predictor of wrinkling [21, 55, 47] under all conditions and cannot describe wrinkling severity. Another predictor that has been more recently used to identify wrinkle locations is the local Gauss curvatures (K) of the fabric preform, with K also indirectly indicating the severity of particular wrinkles [56, 57]. Using K has been shown to be a useful descriptor for validating the wrinkling predictions of a forming model relative to the experimental ground truth by allowing for point-wise quantitative comparison [58]. Despite this, the local curvature of the fabric is not an entirely reliable measure as its calculation is often subject to spurious outliers [56] and does not provide any intuitive sense of wrinkling size. Thus more explicit descriptors of the wrinkling severity are preferred if these can be obtained.

The most obvious measure of wrinkling severity, which has recently gained popularity, is the wrinkle amplitude (a_w) which is defined as the normal distance from the wrinkled fabric surface to either a reference smooth fabric surface [25] or the tool surface [36]. In this thesis, the wrinkle amplitude is used as the primary descriptor of wrinkling and the former definition is used by determining a smooth reference surface for each wrinkled surface. The wrinkle amplitude is a useful measure of wrinkling because it directly quantifies the local severity of wrinkling while also allowing us to identify where these wrinkles are occurring. As such it

has been used significantly in recent years, both in experimental [25, 49] and simulation [57] contexts. Given that from a structural performance point of view, it does not matter whether these wrinkles point outwardly or inwardly, it is useful to take the absolute value of the wrinkle amplitude distribution across the fabric surface ($|a_w|$). From this distribution, a maximum value ($|a_w|_{max}$) can be derived to describe the most severe level of wrinkling observed. In addition, another useful measure, the 'wrinkle area' (A_w), can be derived from $|a_w|$, which attempts to quantify how widespread the wrinkling is on the fabric preform. This measure was initially proposed as the 'wrinkle ratio' by Shen et al. [49] and refers to the percentage of fabric surface where a_w has exceeded a certain threshold level ($|a_w|_t$). Shen et al. [49] used a range of $|a_w|_t$ (1 mm, 2 mm and 4 mm) to compare the distribution of different sized wrinkles on tufted preforms. In this thesis, $|a_w|_t$ is set to 1 mm throughout.

2.3.2 Effect of wrinkles on component

Wrinkles developing during the preforming stage can have significant effect for the rest of the manufacturing process and on the mechanical performance of the final component. Thus they must be treated as a critical defect to be mitigated or eliminated. Wrinkles can cause in-plane fibre misalignment up to 50° [17] and they also disrupt the resin infusion process, leading to resin-rich zones and dry spots in the component [17]. Furthermore, this fibre misalignment has been shown to cause large degradation of composite strength due to the misalignment of fibre tows, with strength losses of up to $40-70\%$ in tension and 50% in compression for severe wrinkles having been reported by Potter et al. [17]. Furthermore, Hamidi and Altan [59] used a variety of previous studies to show that the wrinkle severity (defined by $\frac{\delta}{\gamma}$) correlates strongly with the reduction in component stiffness, which can be as much as 80% with the most severe wrinkles. However, smaller wrinkles can be tolerated within the safety factors of the component and thus it becomes critical to be able to accurately quantify the extent of the wrinkling in order to evaluate whether a component is safe or not. While the severity is simple enough to characterise in 1D, historically the focus for 2D wrinkles has largely been focused on solely predicting or evaluating whether wrinkling has or has not occurred in a binary manner [16, 60]. To address this gap, the focus of this thesis is on measuring this wrinkling severity when fabrics are formed over complex geometries.

2.3.3   Characteristics of biaxial NCFs related to wrinkling

Shear behaviour

Due to the inextensibility of the fibre tows, the in-plane deformation behaviour of NCFs is dominated by its in-plane shear behaviour and this is used as the basis for assessing the formability of a particular material. The stitching has been shown to have a significant influence on the shearing, leading to an asymmetric shear behaviour for $\pm45°$ biaxial NCFs [61] (see Figure 2.6a). These NCFs exhibit differing behaviour depending on whether the stitch is parallel or perpendicular relative to the shear loading direction [26]. This is explained by Chen et al. [16] in Figure 2.6b, which shows how the stitching becomes taut in positive but not negative shear, thus restricting further shearing. This asymmetric shear behaviour is in contrast to woven fabrics and $0°/90°$ NCFs that display symmetric shearing behaviour [16, 26]. Thus their in-plane deformation is more consistent and easier to predict using the shear locking angle (γ_l). With regards to wrinkling, Mei et al. [26] qualitatively showed that under the same forming conditions, a $\pm45°$ biaxial NCF leads to macroscale wrinkles, unlike the $0°/90°$ NCF. This observation cannot be accounted for by the shear locking angle theory [27] and suggests there could be an alternative wrinkling mechanism for these NCFs, as discussed in Subsection 2.3.4 and further explored in Chapter 3.
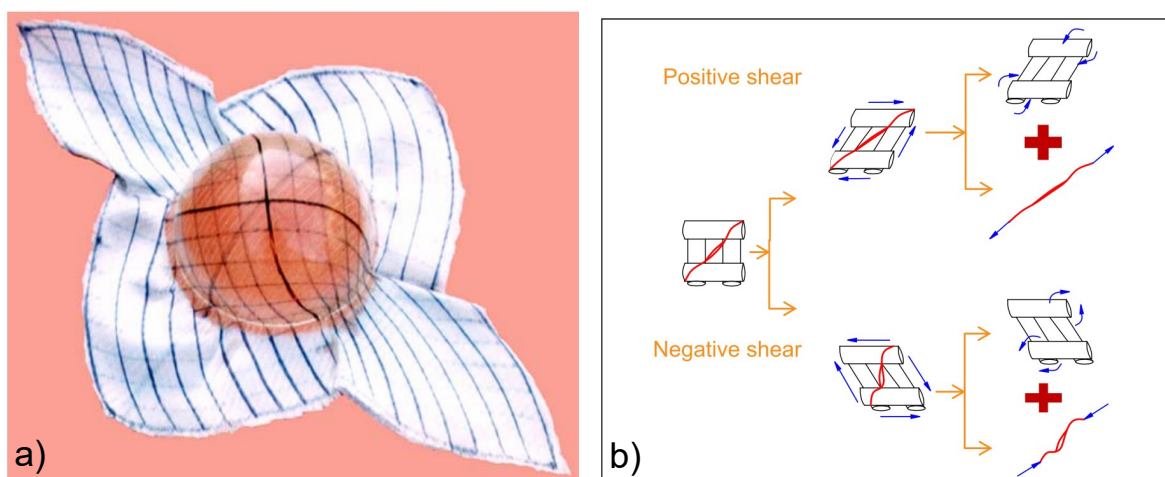
Fig. 2.6 a) Asymmetric shear behaviour of a $\pm45°$ non-crimp fabric (adapted from [62]) and b) the explanation for the asymmetric shear behaviour, caused by the stitching being in tension when in positive shear (adapted from [16]).

Bending behaviour

Beyond the shearing behaviour which relates to the occurrence of wrinkles, a key characteristic of NCFs that determines the shape and severity of the wrinkles in the final preform is their bending stiffness [21]. The bending stiffness of fabrics is significantly lower than their axial stiffness and has been shown to be non-linear, as a function of the local curvature [63]. Despite this, for simplicity, the bending stiffness is typically characterised as linear using a standardised cantilever test for fabrics [64]. There are significant differences in bending stiffness for biaxial NCFs of different stitch types, with the pillar stitch NCF resulting in a stiffer fabric compared to the same NCF with tricot stitch (Figure 2.7). The bending stiffness of a pillar-stitched $\pm45°$ NCF has also been shown to be an order of magnitude larger than those of woven fabrics [57]. As a result of this larger bending stiffness, it is thus likely to result in larger wrinkles of reduced quantity [65], making it an ideal material for the study of wrinkling in this thesis as any wrinkling observed will be magnified.
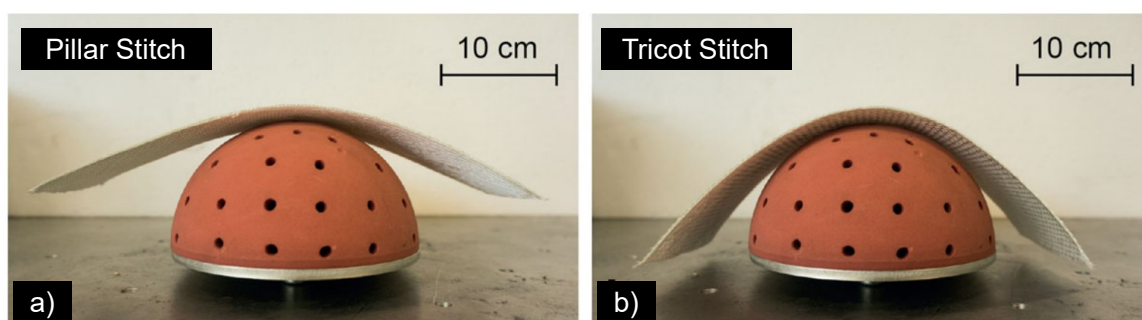
Fig. 2.7 Comparison of the bending behaviour over a hemisphere of two biaxial non-crimp fabrics with a (a) pillar stitch and (b) tricot stitch pattern respectively. The figure is adapted from [23].

Stitching

The stitching is the most distinctive feature of NCFs and the effect of the stitching parameters on NCF performance is an area of ongoing study [66] with efforts being made to understand the most important parameters when it becomes to improving the formability of the fabric.

The stitch type and tow orientations relative to it have been shown to dictate the formability and stability of the fabric, influencing both their shear and bending behaviour [23]. Furthermore, as described previously, there are significant differences in the deformation behaviour between a $\pm45°$ and $0°/90°$ NCF, with the $\pm45°$ NCF being notable for exhibiting asymmetric shear behaviour [62, 16] (as shown in Figure 2.6). These observations about the effect of stitching

led Krieger et al. [23] to develop tailored NCF stitching patterns where the stitch angles are optimised such as to reduce this asymmetry.

With regards to other stitch parameters, Bardl et al. [37] showed that changing the stitch length, stitch length and yarn count of a $\pm 45°$ NCF introduced some changes in the asymmetry of the preform but the effects were negligible in comparison to changing the process parameters such as the blank holder force (Subsection 2.3.5). This demonstrates the crucial effect of the initial tow orientations within each NCF for determining its forming and wrinkling behaviour. Thus the global shear behaviour for one biaxial NCF can be considered similar to another as long as they share the same tow orientation, despite certain differences in stitching. In contrast, the bending behaviour is significantly influenced by the stitch type [23] and thus wrinkling severity is affected.

2.3.4   Mechanisms of NCF wrinkling

The wrinkling of textile reinforcements, especially NCFs, can occur via differing mechanisms and lead to either macroscale or mesoscale wrinkles. Conventionally, fabrics have been shown to wrinkle on a macroscale owing to compression under shear lockup but recent work suggests that this can also occur in certain fabrics via an alternative mechanism [27] when fabric shearing is limited. Furthermore, biaxial NCFs are particularly susceptible to mesoscale wrinkling due to tow compression [16]. These three aforementioned mechanisms of biaxial NCF wrinkling are expanded upon below.

Macroscale shear wrinkling

The most commonly discussed wrinkles for fabrics are macroscale shear wrinkles that occur when a critical local shear angle is reached, leading to adjacent tows to lock up and buckle out-of-plane. While this type of wrinkling will be referred to as shear wrinkling in this thesis, it is important to note that these wrinkles do not occur due to the shear itself but instead are initiated by a compressive force at the point at which no further shear can take place. This wrinkling mechanism and the locking angle principle was originally developed in 1996 by Prodromou and Chen [48] for woven fabrics and similar shear wrinkling has been noted for biaxial NCFs [27, 16]. Given that textile reinforcements typically deform via an in-plane shear mechanism, this wrinkling type is the most common and thus the shear angle distribution is often directly used as a predictor of wrinkling in forming finite element simulations [67]. However, this approach over-simplifies fabric wrinkling: it has been shown experimentally that exceeding the critical shear angle does not always lead to the onset of wrinkling [68], and

simulations have shown that fabric bending stiffness and in-plane tension also play a significant part in wrinkle formation [21, 63, 69, 70].

Macroscale non-shear wrinkling

In addition to shear macroscale wrinkling, there is another less frequently discussed macroscale wrinkling mechanism that can occur during forming. Similar macroscale wrinkles can also occur via lateral compression when the shearing of the fabric is restricted significantly. This is the wrinkling commonly seen in isotropic sheet metals [71], whereby the fabric compresses along the surface of the forming geometry leading to fabric folds. These wrinkles are similar in appearance to their shear counterparts but occur under different circumstances and via a different mechanism due to the absence of shear [72]. This wrinkling mechanism has received little attention for textile reinforcements, which are assumed to wrinkle exclusively at large shear angles due to their typically low shear resistance. However, Skordos et al. [73] were able to show this is the primary wrinkling mechanism observed during the forming of woven prepregs, which are more restricted in shear than dry woven fabrics due to the resin. It is possible that this wrinkling mechanism can be induced in dry woven fabrics with high shear resistance. For example, Lee et al. [27] showed that for a biaxial $\pm 45°$ NCF with a pillar stitch, some wrinkles occurred in regions of low shear, suggesting that these are occurring not due to the established typical shear mechanism. In Chapter 3, using a similar NCF, this observation is expanded upon and investigated further to better understand this alternative mechanism and how exactly it occurs.

Mesoscale wrinkling

The third possible wrinkling mechanism relates to the aforementioned mesoscale wrinkles, whereby the fibre tows of the fabric buckle along their length as a result of fibre tow compression. During open mould forming, the fibre tows buckles out-of-plane and during closed mould forming (where out of plane movement is restricted), tows buckle in-plane resulting in apparent fibre waviness, as was observed by Chen et al. [16] for a biaxial NCF. A similarly named defect called 'tow buckling' has been shown to occur for certain woven fabrics [74]. However, curiously, this defect is not buckling due to tow compression as the name would suggest but rather it has been shown to occur due to the in-plane bending of the tows [75], and the defect has a visibly different nature to those seen for biaxial NCFs in [16]. As such, tow buckling is likely a separate defect to the mesoscale wrinkling described. It is as of yet unclear what conditions are necessary for this tow compression and subsequent wrinkling to occur in NCFs.

In Chapter 3, we use the same biaxial fabric as Chen et al. [16], to further investigate the development of these mesoscale wrinkles.

2.3.5 Factors affecting wrinkling

There are numerous controllable factors that affect the occurrence and severity of wrinkles during preforming. These include the fabric architecture, the process conditions, the frictional conditions, the layup and the tool geometry.

Fabric architecture

The fabric architecture of the NCF significantly affects the resultant wrinkling behaviour with the number of ply layers in the NCF, the orientation of those plies relative to the stitch direction and the type of stitching used contributing significantly to wrinkling. Arnold et al. [25] performed the most comprehensive comparison between different NCFs in terms of wrinkling and found that UD-NCFs exhibit the least wrinkling while triaxial NCFs are prone to the largest wrinkles with biaxial NCFs somewhere in between the two. It was also found that a triaxial $45°/0°/-45°$ NCF with pillar stitch results in larger wrinkles than the equivalent (albeit lighter) NCF with a tricot stitch, highlighting the effect of the stiffer pillar stitch on wrinkling. Equally not all biaxial NCFs wrinkle to a similar extent, with the tow orientations appearing to have significant effect, as a $\pm60°$ tricot NCF wrinkles with much greater severity than the equivalent $0°/90°$ tricot NCF [25]. This was further confirmed by Mei et al. [26] who showed that a $\pm45°$ NCF results in large macroscale wrinkles while the $0°/90°$ NCF does not, under the same hemispherical forming conditions. In this thesis, the investigation will be primarily based on a carbon fibre biaxial $\pm45°$ NCF with pillar stitch that has previously been characterised by Chen et al. [16] but comparisons are made to a $45°/0°/-45°$ triaxial NCF in Chapter 4 in terms of wrinkling variability and severity.

Process conditions

The process conditions of the forming process can significantly affect the wrinkling in the final preform. In particular, the effect of increasing the global blank holder force (BHF) during press forming has been shown to reduce the asymmetry of shear behaviour as well as reduce the severity of resulting wrinkles [27, 76, 25]. This is because the BHF converts to in-plane tension along the fibre directions, meaning compressive forces are counteracted and thus wrinkling is delayed or avoided altogether. There is also significant evidence for shear-tension coupling in woven fabrics and thus this additional tension increases the critical shear angle at which

wrinkling initiates [77, 78]. As a result, during industrial matched-tool forming processes, the global blank holder force is typically set at a high level (on the order of kNs) to get more predictable forming behaviour [79]. However, it has been shown that increasing BHF cannot completely mitigate wrinkles with fibre tow tearing or slippage possible at high BHFs [80]. Thus more novel, less brute force approaches for wrinkling mitigation are needed, as will be outlined in Subsection 2.3.6. For the investigation of wrinkling behaviour and severity on a lab-scale, it is preferable to use a lower BHF as this is more representative of the fabric's true deformation behaviour. As a result, in this study the BHF is limited to a maximum of 0.2 kN. In Chapter 4, the effects of the modifying blank holder force and the forming diameter are investigated with regards to their effect on the variability of wrinkling.

Friction and layup

The effect of friction on fabric wrinkling is significant, particularly when considering multilayer forming and given the anisotropic nature of this interply friction [81], this frictional effect is closely linked to the fabric layup [82]. While typically fabric forming studies have been limited to single fabric forming, the more industrially relevant multi-ply forming and its associated frictional effects have recently gained increased attention in the literature [83, 84, 82, 51], focusing on woven fabrics. In particular, Guzman-Maldonado et al. [84] showed through simulation that increasing the frictional coefficient between plies corresponds to a greater number of wrinkles of larger amplitude. Within the same study, Guzman-Maldonado et al. [84] also showed experimentally that a quasi-isotropic layup ($[0°/90°, -45°/45°]_2$) wrinkles over a hemisphere in contrast to no wrinkling for two equivalent layups with no relative differences in fabric orientation. This occurs because, as shown by previously by Allaoui et al. [85], the relative ply sliding between non-aligned tows generates high tangential forces that initiate the development of wrinkles through the creation of compression zones [84]. This is in agreement with the findings of Vanclooster et al. [86] who showed that increasing the relative orientation of two woven fabrics from 0° to 45° significantly reduces the formability and increases the amount of wrinkling. Thus this highlights the important contributions that inter-ply friction and the particular layup can have on wrinkling severity for woven fabrics. While similar multi-ply forming studies have not been conducted for NCFs, it is suggested that this frictional effect could be exacerbated for NCFs due to the additional *inter-NCF* sliding between stitched tows [15]. Considering this, the effect of layup orientation on wrinkling variability is investigated in Chapter 4.

Tool geometry

The influence of geometry on the forming behaviour of textile reinforcements has received limited attention in the literature, although the forming geometry evidently has a significant effect on how the material behaves. For example, in research conducted by Zhu et al. [87], it has been demonstrated that shear angle distribution of the draped woven fabrics is closely related to the geometry of the punch and the initial orientation of the blank. They stated that shear distribution of the draped fabric can be estimated through two decoupled terms, namely the geometry of the punch and the orientation of the blank. Such an analytical investigation to describe the shear behaviour over a geometry has previously not been extended to NCFs. In terms of typical geometries studied, there are a few double curvature benchmark geometries that are typically used in these forming tests, which are the hemisphere [25, 88, 89, 79, 15, 90], double dome [91–94], tetrahedron [88, 29, 95] and triangular prism [96, 85]. However, there are rarely comparisons between these benchmark shapes, except in the work of Allaoui et al. [88] where a square box, prism and a tetrahedron are compared as they all consist of a case corner and the study by Pazmino et al. [97] where a tetrahedron and a double are compared. Comparisons are necessary to identify general trends for optimal geometries that minimise wrinkling at the design stage. Other studies have focused on employing specific complex 'case study' geometries from industrial partners for forming studies [34, 98] but such studies offer isolated insight for a specific case and make it difficult to identify any useful guidelines for geometry selection to minimise wrinkling defects. In Chapter 3, the effect on wrinkling between four different benchmark geometries will be compared.

However, the high cost of manufacturing large numbers of fixed tooling and the near infinite possible variations in tool geometry make exhaustively analysing the effect of geometry experimentally unfeasible, although this was previously attempted by Wang and Cao [99] for metal forming. Using validated simulations, a more exhaustive and cost-effective study could be conducted to understand more generally how the tool geometry affects wrinkling severity and develop guidelines for designing components for improved manufacturing and minimal wrinkling. By characterising and classifying geometries based on their geometric features [100] and simulating the forming of a large number of geometries using the state of the art models [45, 39], a more thorough understanding of the geometrical effect can be achieved. However, no such comprehensive study looking into fabric preforming behaviour has previously been carried out and will thus be investigated in Chapter 5 for the double diaphragm forming process.

2.3.6   Approaches for mitigating wrinkling

The mitigation or elimination of wrinkling during preforming represents the end goal of all the investigations into understanding fabric forming and wrinkling behaviour. Thus it is important to examine what methods have been developed in this regard and how successful they have been. Methods for mitigating wrinkling during the preforming process can be divided up into global and local process approaches, as well as design approaches.

Global approaches

Global methods for wrinkle mitigation apply a uniform condition onto the entire preform that is hoped to reduce or eliminate the amount of wrinkling observed. This approach is exemplified by the use of an increased BHF around the preform, as discussed previously. In addition, numerous alternatives to blank holders have also been proposed that achieve a similar effect such as through the use of tensioning elements [92] or flexible tracking devices [101]. As a more elaborate global strategy, Nosrat Nezami et al. [102] developed an active blank holder system to reduce the inter-ply friction through the introduction of metal sheets in between the plies and actively vibrating these plies to further reduce friction. However, applying excessive in-plane forces can lead to the fabric tows or stitches being destroyed, and thus BHF optimisation is required [87, 92]. Furthermore, while it reduces macroscale wrinkles, it can also introduce other unwanted defects such mesoscale wrinkles [103]. Thus while global process approaches are the simplest, they have been found to not be sufficient for wrinkle mitigation.

Local process approaches

In an attempt to improve upon the deficiencies of global mitigation strategies, local mitigation solutions are more targeted and attempt to change the fabric behaviour in particular regions of interest. For this, many different approaches have been suggested. For example, Chen et al. [92] showed that by locally optimising spring tensions around the preform, the maximum shear angle in the preform could be reduced significantly. As a proposed improvement over the spring tensioning approach, Jagpal et al. [36] outlined a promising strategy for using locally placed magnets to apply variable clamping forces while not restricting interply slip. Additionally, Chen et al. [104] have shown that placing rigid blocks in optimised locations around the preform can reduce the presence of wrinkles through modifying local shear angle distributions. Similarly, Rashidi and Milani [105] designed a geometrically modified blank holder that introduces localised variations in applied tension and thus can reduce wrinkles to a greater extent than a conventional blank holder under the same loading. Finally, Turk et al. [106] developed a

method applying local resin patches to locally stiffen the fabric behaviour in regions where wrinkles are likely to occur. Whilst many promising methods have been proposed, it is not clear how successfully these work across the range of material systems and forming processes, and thus further work is needed.

Design approaches

Beyond modifications to the forming process that attempt to mitigate defects at the manufacturing stage, design approaches to mitigation are focused on identifying how the component design, including layup and geometry, can be optimised for minimal defects. This is critical because not all defects originate at the manufacturing stage but are the result of choices made at the design stage [18] that then result in geometry-induced defects. As an example of design-based mitigation, Krieger et al. [23] addressed the formability of biaxial NCFs by locally alternating the stitching types used in the formed fabric between tricot and pillar stitching depending on the local forming requirements, with the less stiff tricot stitch used in locations of high curvature. Such an approach has promise for creating complex geometry parts without defects.

The other part of the design equation is the component geometry, which could be optimised so as to minimise defects and offer a root-cause approach for wrinkling mitigation. However, due to the historical separation between design and manufacture stages of production and a lack of understanding about the effect of geometry, such a strategy has been largely overlooked until recently. Notably, Zimmerling et al. [107] showed that a machine learning based method could be used to optimise the design of composite components for improved formability. Taking a similar approach, the investigation in Chapter 5 will attempt to develop a method through which wrinkling mitigation could be achieved by modifications to the component geometry.

2.4 Variability in wrinkling and preforming

All of the above discussion points to the complexities involved in predicting and mitigating wrinkling but the wrinkling defect is additionally prone to significant variability, as noted by Giorgio et al. [108]. They observed a wide variety of wrinkling morphologies during bias extension tests of the same woven fabric under the same process conditions. Furthermore, the more loose and complex architecture of NCFs makes them particularly prone to variability, with Endruweit et al. [109] observing that biaxial NCFs have much higher variability in fibre tow angles than equivalent woven fabrics. Such variability impacts all experimental studies into fabric wrinkling behaviour and hinders attempts to validate models that try to capture

wrinkling behaviour [39, 84]. Thus, as a precursor to mitigating wrinkling during preforming, the variability of wrinkling must be characterised and understood so that more representative wrinkling models can be developed. To address this, a recent study by Harrison and Gonzalez Camacho [110] briefly examined the variability of wrinkling for two woven fabrics during forming, noting that the variability was largest in the case with no blank holder. However, no previous study has thoroughly investigated the variability of biaxial NCF wrinkling, which Chapter 4 aims to do.

2.4.1 Definition

Variability is defined here as the unexpected difference(s) from the nominal result under identically designed production protocols. This variability causes changes in the final component that cannot be easily accounted for, thus making any resultant defects more difficult to eliminate as they cannot be predicted. This variability is particularly significant when manufacturing with fabrics such as NCFs because their inherent tow architecture is subject to changes in orientation and thickness during production, leading to potential localised, irregular effects. As noted by Mesogitis et al. [111], variability is introduced at every stage of textile composite production and, on an industrial scale, such variability can cause scrapped parts during automated production due to unexpectedly severe defects. Additionally in academia, it hinders the experimental study of the material behaviour and makes it challenging to create suitable preforming simulations that are able to accurate capture production defects. It is therefore essential, as argued by Potter et al. [17], that the variability in the material and the process are both accounted for.

2.4.2 Wrinkling variability due to material production

The two primary sources of fabric wrinkling variability are the material production process and the preforming process. In terms of composites fabrics, the 'material variability' results from the production of the fabric roll from individual fibres. This defines the minimum variability in the final component [18] when assuming that no variability is introduced during the composite manufacturing process. It can either take the form of local variability in a given fabric roll or global variability between production batches.

Local material variability in the produced fabric rolls refers to local variations from the nominal across the produced roll such as fibre tow misalignment, tow waviness, tow size/shape variations, gaps between tows etc. [111]. These variations need to be identified at the point of production and could cause certain rolls to be scrapped if they do not meet quality thresholds.

However, it is unavoidable that some level of local variability exists in the as-produced roll, particularly when taking into account handling and transport. It has been demonstrated that the variability in the manufactured fibre tow directions (initial fibre misalignment) can be highly significant. For example, Yu et al. [76] showed that for a $\pm 45°$ glass fibre NCF, the mean measured orientation differed from the expected fibre orientation by 2.3° and the measured distribution had a standard deviation of 5.6°. Similar observations were made by Skordos and Sutcliffe [112] for a woven prepreg fabric. While the distributions will vary depending on the exact fabric and its production quality, some local variability in alignment cannot be avoided and should be expected for all produced fabrics. In addition, it is possible to find local variability in the global properties of the material such as areal weight and thickness: e.g. Potter [18] showed that for a given unidirectional prepreg roll, samples from the edges consistently exhibited different areal mass compared to those in the middle of the roll. Such local variability is thought to play a critical role in non-linear phenomena, such as wrinkling [111].

Global material variability refers to the differences in the global properties of the fabric such as areal weight, thickness and roll width between different production batches. These are accounted for by measurement and ensuring that differences are within the acceptable tolerance for fabric production machinery. For example, the areal weight of the two fabrics used in Chapter 4 has an uncertainty of 5% on the mass of the fabric as produced, leading to potential variability between separate production batches. To minimise global variability in this study, material from the same production batch is used. However, these global variations can become significant in continuous industrial production where multiple batches are used.

While previous studies have analysed and compared the as-produced material variability between a number of textile reinforcements: e.g. [113], this study extends this to characterise experimentally the wrinkling variability after the preforming step, considering the combined effect of the material and the preforming process.

2.4.3 Wrinkling variability due to preforming process

Along with material variability, the preforming stage of manufacturing textile composites has been shown to be a significant source of variability in the final composite [102, 114], with the stochastic simulations by Yu et al. [76] supporting the same conclusion. This is because any draping of fabric causes local distortions in the fibre orientations as the fabric attempts to conform to the tool surface while deforming within the limits of its architecture. This then amplifies any existing local variations in the material and inconsistencies in the initial conditions of the process [18]. Examples of initial conditions that are subject to variability

include the initial orientations of the layup relative to the tool [18] and the variations in the applied blank holder pressure [73], with these likely to be more pronounced when the process is conducted manually [111]. However, for any automated process, it is even more critical that these potential sources and effects of variability are thoroughly understood as these cannot be manually corrected in this case.

Fabrics are particularly prone to wrinkling when formed over doubly-curved geometries [47], where the geometry has a significant influence on local deformation and draping paths. In addition, Nosrat Nezami et al. [102] reported high wrinkling variability when woven fabrics were formed into a hemisphere and more complex geometries using identical test configurations.

In order to investigate this wrinkling variability due to the preforming process, Chapter 4 evaluates the effect of prescribed changes to the preforming conditions (material, layup and process conditions) on the wrinkling variability in the preformed fabric. It is expected that the quantified variability is specific to a particular forming setup but that trends related to changes in variability can be extrapolated to other preforming processes if using similar materials.

2.5   Experimental methods for characterising wrinkling

Beginning in the late 90s, significant advancements in the experimental characterisation of the fabrics have been made. Notable highlights have been the development of the picture frame test in 1997 and bias extension test in 1998 by McGuinness and Ó Brádaigh [115], and Wang et al. [116] respectively. These tests crucially allowed the characterisation of the fabrics' in-plane shear behaviour, which was seen as the most critical deformation mode during forming as it allows the fabric to drape over the desired 3D geometry and is indirectly correlated with wrinkling. However, in recent years, with a greater understanding of the wrinkling phenomenon and the availability of new experimental tools, there has been a focus on experimentally characterising the wrinkling behaviour of fabrics during preforming.

2.5.1   Test types for wrinkling investigations

Experimental investigations into the wrinkling behaviour of fabrics can be conducted using two types of tests: forming tests or shear characterisation tests, but forming tests are the only approach that allows for the effect of geometry to be considered. Shear characterisation tests such as the bias extension [50] or the picture frame test [117], offer a controlled loading and testing environment for observing macroscale wrinkles in fabrics, with any observed out-of-plane displacement of the fabric corresponding to wrinkling [63]. While the bias extension test

does not replicate the boundary conditions of the forming processes, the boundary conditions of the picture frame test are to some extent similar to those of the forming processes [118]. Having said that, they both do not take into account the effect of geometry.

Forming tests, that attempt to represent the industrial preforming process on a laboratory scale, can be further broken down into benchmark forming tests and case study component forming tests, but both will vary based on the exact preforming process they are trying to replicate (e.g. double diaphragm forming [38]). Case study component forming tests investigate the formability of a fabric over a mould for a representative component that could be used in industry [34]. This makes these tests more industrially relevant but their specificity and complexity make them less useful for further understanding of the underlying mechanisms of defect generation or generalising for the effects of geometry. Benchmark forming tests are conducted using particular, double curvature geometries that have been agreed upon across research groups for the study of textile reinforcements [46], allowing results to be easily compared. In Chapter 3, a benchmark forming test approach with four different benchmark geometries will be used to investigate the effect of geometry on wrinkling.

2.5.2 Wrinkling characterisation

Recent advances in imaging technology and new post-processing methods have made accurate characterisation of wrinkling possible. For example, Arnold et al. [25] employed a single digital camera and a 'shape-from-focus' method to measure the wrinkle amplitude across the surface at discrete intervals during forming for a variety of NCFs. With similar outcomes, Shen et al. [49] employed a 'structure-from-motion' approach to characterise the final wrinkling patterns for tufted 3D composite preforms. Alternative methods including structured white light scanning [63] and photogrammetry [110, 36] are all relatively cheap and well adapted for capturing the static shape of the final preform, from which the wrinkle patterns can be obtained. However, none of these approaches are able to also determine the strains in the fabric. On the other hand, the 3D digital image correlation (3D-DIC) method allows for the full field tracking of a speckle surface from which both displacements and surface strains can be obtained [119]. This method has previously been employed to measure the wrinkle amplitude for bias extension tests [63, 50] as well as being used to measure the local shear angle during forming tests [97, 28]. To date, experimental investigations into forming have either quantified the wrinkling of the fabric or the fabric strains but not both simultaneously, meaning no correlations could be made between them and there is thus a lack of understanding about how the strains in the fabric relate to the wrinkling severity. To address this, the study in Chapter 3 is the first to employ a

3D-DIC approach to obtain wrinkle amplitudes directly during a forming test and relate these to measured strains.

2.5.3   Wrinkling variability characterisation

Measuring variability during composite manufacturing processes such as preforming has historically been limited due to a lack of suitably accurate measurement techniques. However, recent advances in image-based approaches have allowed for the characterisation of key material and preforming process variables such as initial fibre misalignment [112, 120], final fibre orientations [34], local shear angles [16] and wrinkle amplitudes in the final preform [25, 49], thus allowing for the variability to be explored. In addition, the final geometrical variability of the produced composite can be evaluated using similar techniques, capturing the cumulative variability introduced throughout the whole manufacturing process [121].

In order to characterise the variability in fabric wrinkling, the shape of the deformed fabric at the end of forming needs to be captured. For this, there are now multiple proven methods including photogrammetry and structured white light scanning (Subsection 2.5.2). While 3D-DIC [119] is best suited for capturing the dynamic wrinkling behaviour throughout the process, it can also be used to capture the end state of the preform, albeit with some loss of data. Due to the availability of the DIC equipment and the necessity of using it for the dynamic wrinkling analysis in Chapter 3, the 3D-DIC method is also used Chapter 4 in order to capture the preform shape while being aware of its limitations. The focus of the variability characterisation investigation is developing a method for characterising variability and this can be equally applied to data from any of the aforementioned cheaper wrinkle characterisation methods.

2.6   Modelling methods for preforming and wrinkling

Modelling the behaviour of fabrics such as NCFs is an inherently challenging task due to their customisability, non-orthogonality, multiple length scales and distinct deformation modes. The accurate modelling of wrinkling requires being able to characterise the tensile, shear and, in particular, the bending behaviour of the fabric successfully, meaning simple kinematic models are not sufficient [21]. Despite this complexity, significant advances have been made in the development of various modelling approaches, particularly using finite element (FE) methods, with the most recent state of art models being able to accurately capture the wrinkling of woven fabrics and NCFs. While these developments are encouraging and are widely used in academia,

the adoption of FE models within industry has so far been limited due to the higher level of user expertise required to use these models [122], them requiring expensive material characterisation tests [122], and being prohibitively slow to run in an industrial setting where rapid results are desired.

2.6.1   Modelling approaches

A review of the modelling approaches for the preforming process was conducted by Gereke et al. [19] in 2013 with an update provided by the review of Bussetta and Correia [20] in 2018. The various forming modelling approaches for fabrics and their ability to model wrinkles are shown in Figure 2.8. On a global level, the modelling approaches can be classified into kinematic models based on a mapping-based approach and mechanistic models using finite element methods [20].

The initial models of fabric behaviour were based upon the pin-jointed net or 'trellis' model that was first developed for homogeneous materials by Weissenberg [123] and were first extended to the forming of composite woven cloths in 1981 by Robertson et al. [124]. The initial models were developed for woven fabrics with symmetric shear behaviour but an energy-based kinematic model was developed for bidiagonal NCFs that takes into account the asymmetric shear behaviour [61]. These models are now referred to as 'kinematic' models as they do not consider the forces involved in the process, relying solely on a geometric mapping. This simplistic assumption provides the main limitation of this approach as kinematic models do not capture the mechanical behaviour of the fabrics or the loading conditions of the forming process and thus remain limited in their accuracy, particularly for changing process conditions. Despite this, they still remain the industry standard for fabric forming because their inherent simplicity allows for a rapid computation speed and because they are able to give a reasonable prediction of the ideal in-plane shear deformation [122].

With the development of new imaging and image analysis technologies in the late 90s, it became possible to accurately examine and measure the fabric geometry, leading to the development of more representative models such as the unit cell geometry model developed by McBride and Chen [125]. It was also around this time that the first FE models for textile reinforcements were developed [126], and this has since become the dominant method for modelling fabrics in academia because of its robustness in being able to consider the mechanics of the process and its adaptability to various modelling approaches at different length scales.

The three main modelling approaches for mechanistic modelling of the preforming process are, in terms of length scales, a 'macroscale' approach [76, 16], a 'semi-discrete' approach

[127, 55] and a 'mesoscale' approach [89]. Macroscale models are on the scale of fabric with the fabric homogenised as a continuum, while mesoscale models are at the scale of fibre yarns with repeatable unit cells developed to build up the entire fabric. Semi-discrete approaches are a combination of the macroscale and mesoscale approaches that use unit cells at the mesoscale but are defined in such a way that the unit cell properties can be characterised at the macroscale (tension, shear and bending) [128]. While even smaller 'microscale' models have been developed [129] that model each fibre tow individually, no feasible way has so far been found to model a full scale fabric at the microscale and thus cannot be used for wrinkling modelling. Additionally, while mesoscale models of NCFs have been shown to be capable of successfully modelling laboratory scale experiments, such as the bias extension test and hemispherical forming [89], due to the computational cost, their use is limited in practice. As a result, for the optimisation of wrinkling or for industrial purposes, the feasible modelling options are either using a semi-discrete or a macroscale approach.
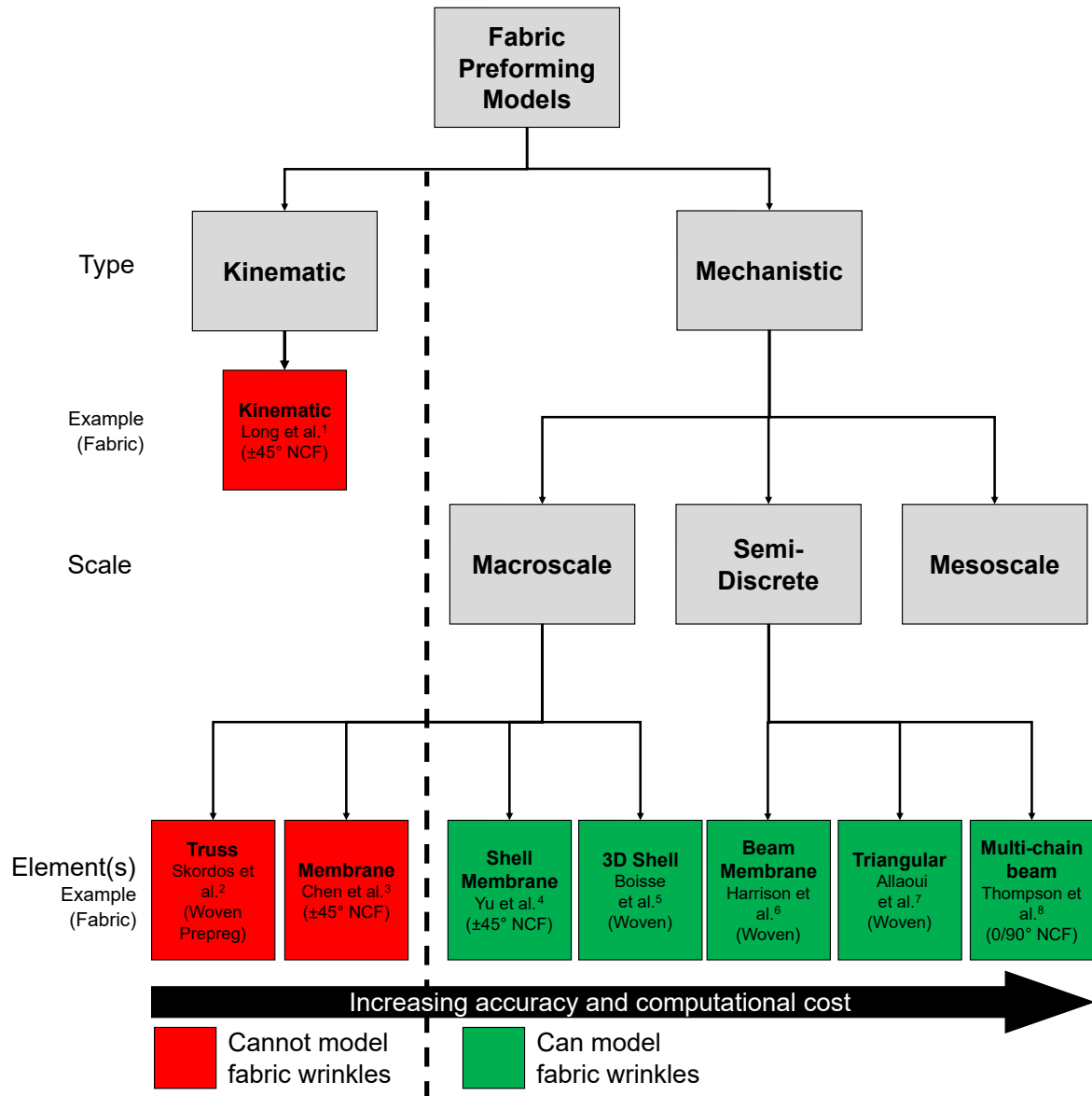
Fig. 2.8 Flowchart showing the various approaches that have been used to model the preforming of fabrics, with these divided up by type, scale and the element types used. For each specific modelling approach, an example from the literature is given. If the particular approach has been applied to biaxial non-crimp fabrics (NCFs), then such a work is given, otherwise, a study based on an alternative fabric (e.g. woven) is given. The corresponding references for the examples provided are the following: [1]:[130], [2]:[73],[3]:[16],[4]:[63], [5]:[51], [6]:[127], [7]:[55] and [8]:[29].

2.6.2   Semi-discrete forming models

Combining the advantages of macroscale and mesoscale models, semi-discrete models are currently the most accurate model for capturing the forming and wrinkling behaviour of fabrics that can be feasibly simulated for industrial-scale components. The three most prominent approaches to developing semi-discrete models are the custom triangular element mesh developed by Allaoui et al. [55], the mutually constrained membrane-beam mesh proposed by Harrison [127] and the multi-chain beam element mesh proposed by Thompson et al. [29] for 0°/90° NCFs (Figure 2.8). The triangular element model was extended to capture forming of a biaxial 0°/90° NCF by combining two triangular elements connected by a bar element to represent the stitching [81], which was successfully able to capture the ply sliding that is characteristic of NCFs. Furthermore, an alternative semi-discrete model for tricot stitch ±45° NCFs was recently analytically presented but with no simulation results shown, it is currently unclear how accurate this model is in reality [131]. These hybrid models have promise but further work is needed to identify the most promising strategy that could be viable for industrial use with further increases in computing power [39]. At present, they are only viable with highly specialised computing systems: Harrison and Gonzalez Camacho [110] reporting a run time of 12-15h using 48 CPU cores and a mesh size of 4 mm. Furthermore, currently, no semi-discrete modelling approach has been presented for pillar stitch ±45° NCFs that are of interest in this thesis, with these having been modelled exclusively using macroscale forming models.

2.6.3   Macroscale forming models

Macroscale forming models are the most commonly used fabric constitutive model, in which fabric components are homogenised as a single continuum and the key fabric properties are characterised through experimental testing. Macroscale material fabric models typically consist of a hypoelastic non-orthogonal constitutive model, which was first proposed for NCFs by Yu et al. [76], although hyperelastic models have also been proposed [93]. The key types of macroscale models that have successfully been employed for fabric modelling are, in ascending order of computational cost, the membrane [16], the shell-membrane [57, 39] and the 3D shell model [51] (Figure 2.8), with the latter only been used for woven fabrics. Membrane models have been shown to not be suitable for modelling the wrinkling of fabrics as they cannot describe the out-of-plane bending behaviour, with any 'wrinkles' being only a function of the mesh size [51].

On the other hand, using superimposed and decoupled shell-membrane elements has been identified as a promising approach that allows for the modelling of fabric wrinkling.

This approach has become popular recently due to its balancing of suitable accuracy and computational cost, with multiple research groups converging towards a similar model [63, 39]. The approach has been shown to be equally applicable to woven and biaxial NCFs, and relatively inexpensive, with Yu et al. [57] reporting a run time of 12 h using 4 cores and a 2 mm mesh. Boisse et al. [51] argues that this decoupling of membrane and shell elements is 'not founded on the physics of textile reinforcement[s]', and that 3D shell elements should be used instead. However, the shell-membrane models have been thoroughly validated against experimental results, including for multi-ply forming, in being capable of being able to capture both the severity and location of wrinkles during press forming [57] and double diaphragm forming [57, 39]. Furthermore, Yu et al. [57] showed that the accuracy of wrinkling prediction can be further improved by implementing a non-linear bending model, albeit with a 33% increase in computing time. However, as is the case with all macroscale NCF models, the stitching is only implicitly modelled through the experimental shear curve and thus they are unable to accurately capture the stitch-tow or tow-tow interactions that can lead to stitch failure or tow sliding [81]. Despite this, for the purposes of modelling macroscale wrinkling, they are sufficient.

2.6.4   Key elements of a macroscale wrinkling model

Based on the available literature, the key features of a macroscopic FE model for simulating the wrinkling behaviour of fabrics during preforming, and how they might be implemented, can be summarised as follows:

- Non-orthogonality: the fibre tows of the fabric, that are initially orthogonal, rotate relative to each other as they deform meaning that the local coordinate systems must be defined as non-orthogonal allowing for the stresses and strains to be correctly updated along the fibre tow directions. This can be achieved using established Abaqus subroutines such as '*FABRIC' [132], 'VFABRIC' [16] or 'VUMAT' [39].

- In-plane shear: the in-plane shear behaviour of the material must be accurately characterised using a picture frame or bias extension test to obtain shear force vs shear angle curve [16, 83]. The shearing can then be modelled using membrane elements [16]. If the model only needs to predict the strains during forming or predict the onset of shear wrinkles, then it has been shown that a simplified model using membrane elements is sufficient [133].

- Tension: the tensile stiffness of fabrics along the fibre direction is large (of the order of GPa [16, 127]) and can be assumed to be linear in NCFs [16] but not necessarily for

woven fabrics [127]. This is because studies have shown coupling between the tension in the warp and weft tows in woven fabrics due to them being inter-woven together [134].

- Shear-tension coupling: the shear and tensile behaviour are typically modelled as decoupled for NCFs, but for woven fabrics, Komeili and Milani [135] showed that incorporating the shear-tension coupling enables a more accurate prediction of the wrinkles and residual stresses.

- Bending stiffness: the bending stiffness of fabrics is low in comparison to the tensile stiffness but is a critical component for accurately capturing the wrinkle shape [136]. The bending stiffness can be included by using shell or 3D elements and is typically characterised as linear. However, a non-linear bending characterisation, implemented via a user subroutine, has been shown to produce more realistic wrinkle patterns, albeit at a higher computational cost [57, 45].

- In-plane/out-of-plane decoupling: Boisse et al. [137] showed that standard continuum mechanics models cannot suitably capture the bending behaviour of fabrics due to the out-of-plane bending being coupled with the in-plane behaviour. Standard continuum mechanics models do not work because the tensile and shear stiffness are orders of magnitude higher than the bending stiffness of any fabric and thus these must be decoupled from each other to accurately model the fabric deformation and wrinkling shape. This decoupling can be achieved through the superimposition of shell elements and membrane elements that are fitted onto the same nodes [39, 63].

- Friction: the tool-ply and ply-ply frictional behaviour have been extensively studied [138–140] and shown to be anisotropic over the duration of the forming process [103]. Furthermore, increasing the interply frictional coefficient has been shown to lead to larger wrinkles [84]. Despite this, detailed frictional modelling is typically neglected in favour of a simplified Coulomb friction model, that is characterised using a friction sled test [38]. Further work is needed to understand whether an anisotropic frictional model significantly impacts wrinkling predictions.

2.6.5   Virtual process optimisation

While preforming models have become reasonably mature and the accuracy of these models is now sufficient to predict wrinkling defects, the development of methods for virtual process optimisation of preforming with respect to minimising defects and increasing formability

remains largely unexplored in the literature [141]. Virtual process optimisation is necessary to avoid the large costs associated with the current trial and error methods used to try eliminate preforming defects, and thus it should remain the ultimate goal of all forming simulations.

The existing work into fabric forming optimisation has relied upon either kinematic or membrane based FE models due to their computational efficiency. For example, Skordos et al. [142] used a kinematic model to optimise woven fabric forming using a genetic algorithm while Chen et al. [92] employed a similar algorithm with a membrane-element FE model to optimise the material draw-in of a biaxial NCF during forming. However, using a genetic algorithm is currently incompatible for use with any higher accuracy models due to the computational requirements, yet higher accuracy models are required to capture the wrinkling behaviour. Thus, developing alternative approaches that allow the use of higher accuracy models is critical for the optimisation and mitigation of wrinkling.

A promising optimisation approach that allows the use of higher accuracy models with a much lower overall computational cost is surrogate-based (or meta-model-based) optimisation [143]. In a surrogate model, a cheap-to-evaluate phenomenological relationship between the input process parameters and the model output is developed on the basis of a parent model and then used to generate rapid predictive results that are highly suited for optimisation. A more detailed review of surrogate models is presented in Chapter 5, with a particular focus on deep learning surrogate models. In order to expand the possibilities for wrinkling optimisation and develop a wrinkling model that is suitable for industrial deployment, Chapter 5 also develops such a surrogate model for the prediction of wrinkling patterns for any given tool geometry.

2.6.6   Modelling preforming variability

The characterisation of the material variability has given rise to numerous modelling approaches that are able to simulate the impact of this variability on the final preform or composite component, as reviewed thoroughly by Mesogitis et al. [111]. The most common approach for including material variability is through stochastic simulation: e.g. Skordos and Sutcliffe [112] developed an image-based approach, based on Fourier Transform and correlation analysis, to characterise the fibre tow misalignment in a woven fabric, and using the developed stochastic model they showed that this misalignment caused significant variations in wrinkling strain (coefficients of variation in the range of 10–20%). However, if the tow fabric directions in the stochastic model are randomly assigned, it can cause spurious tensile stresses and thus Abdiwi et al. [113] developed an alternative meshing method for incorporating the full field variability in tow orientation that is based on pin-jointed nets. Such approaches have the potential to be

implemented within existing wrinkling models in order to better capture the uncertainty in fabric wrinkling, but so far this not been done.

2.7   Gaps in the literature

The objectives of this thesis, which were previously outlined in Section 1.2, are motivated by the gaps identified in the literature in this chapter. These gaps can be summarised as follows:

1. The asymmetric shear behaviour of $\pm 45°$ biaxial NCFs has been well established but it is not clear how this contributes to its unique wrinkling behaviour.

2. The effect of tool geometry on wrinkling severity during preforming is not well understood, with investigations limited by the cost of tooling and the large variety in possible geometries.

3. The variability in wrinkling behaviour of fabrics during preforming has been widely acknowledged but the extent of this variability has not been systematically quantified.

4. It is not clear how the wrinkling variability is affected by changes in preforming conditions.

5. Mitigation techniques for wrinkling are focused on modifying the preforming process conditions but mitigation through tool geometry optimisation has generally not been considered.

6. Finite element models for accurately predicting wrinkling are too computationally expensive to be feasible for virtual preforming optimisation or for industrial use.

Chapter 3

Wrinkling behaviour and mechanisms of a biaxial NCF

3.1 Introduction

As reviewed in Chapter 2, it is evident that further work is required to develop a more generalised understanding of the wrinkling behaviour of NCFs. To develop an improved understanding, the possible wrinkling mechanisms and the impact of tool geometry on the resultant wrinkles should be investigated. In particular, biaxial ±45° NCFs with a pillar stitch have been shown to wrinkle during forming in ways that are not well understood [27, 16]. In contrast to previous similar studies on wrinkle characterisation [25, 49], this work measures the severity of wrinkling and local strains *during* preforming over four benchmark geometries, allowing the wrinkling mechanisms to be investigated by relating the growth of fabric strains with the development in wrinkle amplitude. Furthermore, Chapter 2 showed that differing tool geometries are rarely compared within the same study with the same material and thus, in this case, four different benchmark geometries are experimentally tested allowing the effect of tool geometry on wrinkling to be studied. Thus the specific objectives of this chapter are the following:

- To characterise the wrinkling behaviour and mechanisms of a pillar-stitched ±45° biaxial NCF formed over a hemisphere.

- To investigate how the wrinkling behaviour changes when the NCF is formed over three other benchmark geometries: a double dome, a tetrahedron and a triangular prism.

3.2   Method

3.2.1   Experimental forming setup

Material and geometry selection

The material used for this study is a biaxial NCF with carbon fibre tows at $\pm 45°$ to the stitch direction and a polyester 'pillar' stitch (see Figure 3.1a), manufactured by Hexcel with under the name 'HiMax™ CGL4790 - FCIM359 NCF.' Detailed material parameters for this fabric are shown in Table 3.1. The shear behaviour of this fabric has previously been characterised via a picture frame test, which showed its asymmetric shear behaviour, with large normalised shear stiffness in positive shear (where the fabric is shear loaded such that the angle between initially perpendicular fibre tows reduces) of approximately 1000 N m^{-1} due to the stitching [16]. The fabric is cut into circular samples of 380 mm diameter (see the sample geometry in Figure 3.1b) using a rotary cutter and a Perspex template, similarly to [25].

The four particular punch geometries were selected based on their previous use as benchmark geometries and because they display a range of similar and contrasting features, allowing for the effect of geometry to be suitably investigated. These geometries are the hemisphere, the double dome, the tetrahedron and the triangular prism (see Figure 3.1c), with the round features of the hemisphere and double dome being in stark contrast to the sharp corners of the tetrahedron and the triangular prism. The punches were manufactured out of modelling board, with each punch having a forming height (h), of 75 mm. For each geometry, an associated blank holder was also manufactured out of 10 mm thick Perspex, such that the gap between each punch and the inner perimeter of the blank holder is constant at 15 mm (see Figure 3.2 and Appendix A).
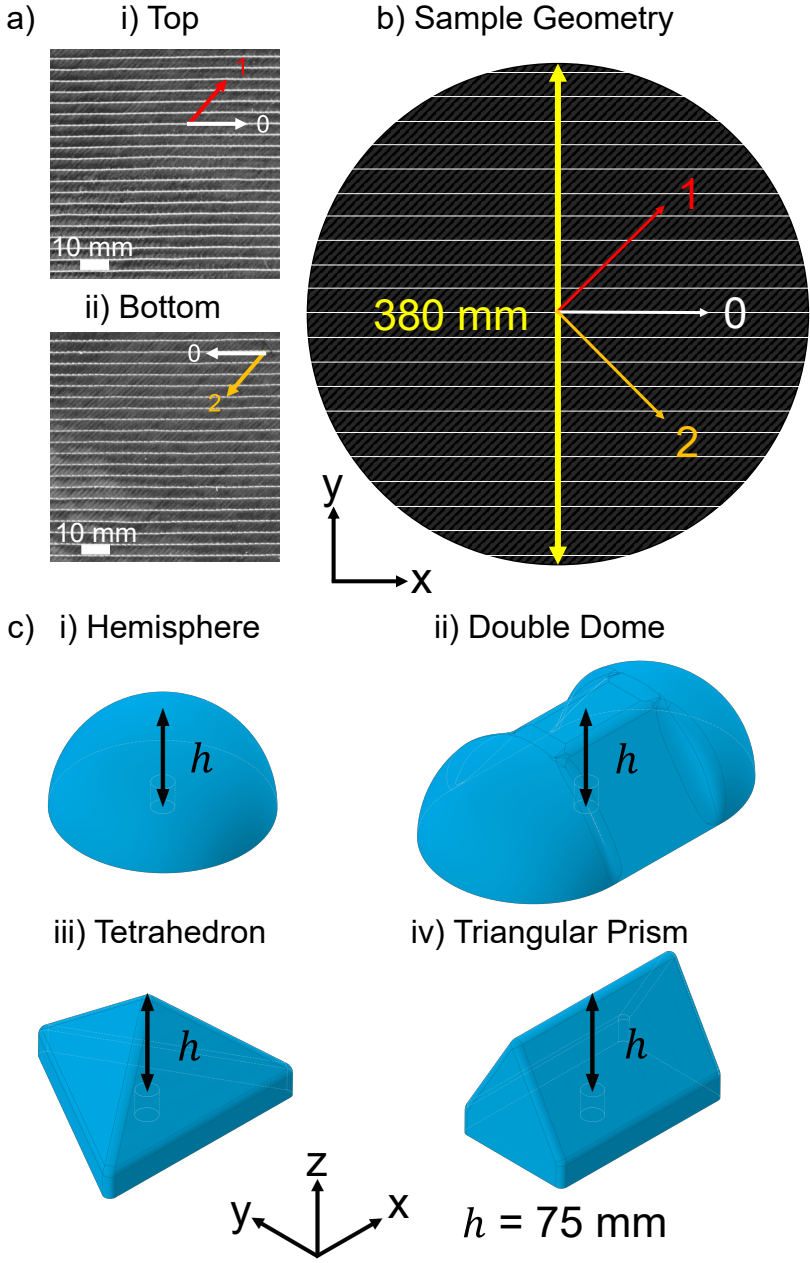
Fig. 3.1 a) The top and bottom surfaces of the biaxial ±45° non-crimp fabric with pillar stitch used in this chapter (Hexcel 'FCIM359'), b) The sample geometry and orientation used for each forming test, showing the initial fibre tow directions ('1' - top layer, '2' - bottom layer) and the initial stitching direction ('0'), and c) generated images of the four punch geometries tested, each with a forming height (h) of 75 mm.

Table 3.1 The parameters of the biaxial non-crimp fabric (NCF) used in this study, as obtained from the manufacturer (Hexcel).

Fabric		Fibre		Stitching	
Type	Biaxial NCF	Material	Standard modulus carbon	Type	Pillar
Areal weight/ g m^{-2}	441	Filaments per tow	24K	Material	Texturised polyester
Tow orientations/°	-45/45	Tex/g km^{-1}	1850	Thread thickness/ g per 10 km	78
Stitch orientation/°	0	Gauge/stitches per 25.4 mm	2.1	Gauge/stitches per 25.4 mm	6
		Areal weight/ g m^{-2}	216	Length/mm	2.12
				Areal weight/ g m^{-2}	9

Speckle pattern application

The surface of the carbon fabric samples was sprayed with a speckle pattern to allow DIC tracking. However, the typical choice of spray paint cannot be used on fabrics because it makes them exceptionally stiff, resulting in unrealistic fabric deformations [50]. Instead, a minimal amount of graphite powder spray was applied as the base layer to remove the reflections of the carbon fibre, similar to [50]. To ensure consistency between samples, the spray pressure was kept constant by the use of a modified spray can gun. To minimise any effect from the graphite, the spraying distance was optimised (to 500 mm - see Appendix C) such that the increase in bending stiffness of a sprayed rectangular fabric sample was negligible relative to a non-sprayed sample, based on the ASTM standard cantilever test [64]. White speckles were evenly applied with an alcohol-based powder spray, typically used as a flaw detector developer. This low density, dry powder sits on top of the fabric surface, without affecting its deformation. For each sample, only the area visible to the DIC cameras (see Figure 3.2) was sprayed to further minimise the effect of the speckle pattern.

Preforming test setup
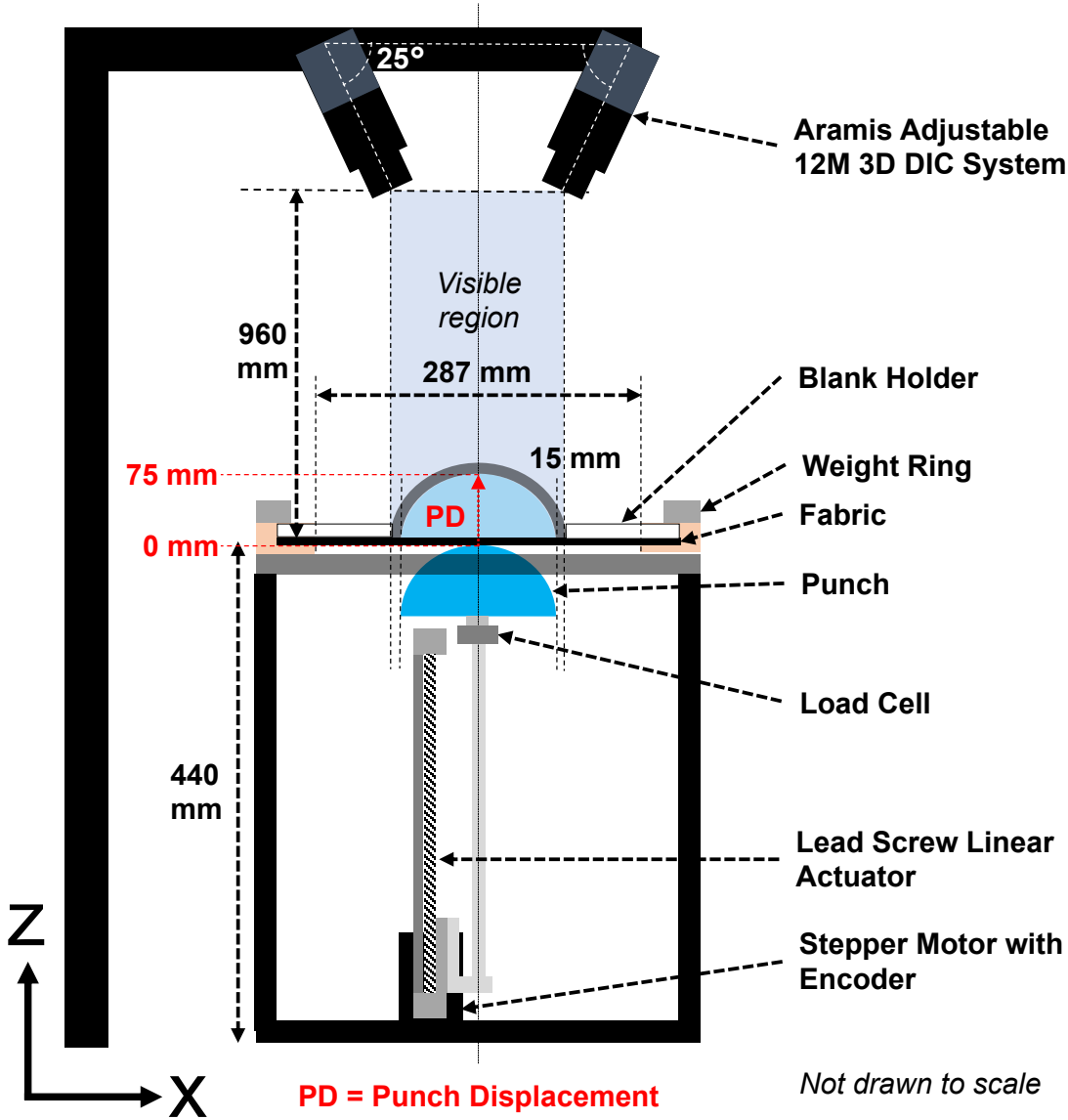
Fig. 3.2 The experimental forming setup, showing the open mould forming rig used to deform the fabric and the 3D-DIC system used to track the deformation of the fabric.

The forming tests are conducted using the experimental rig shown in Figure 3.2, which is based on the rig used in [25], with the addition of the Aramis 3D-DIC system and an improved actuation system. The development of the preforming rig is documented in Appendix A. The key details of the 3D-DIC system are shown in Table 3.2. For each test, the speckled NCF

sample is placed onto the rig and held down with a blank holder and a weight ring, onto which weights are hung to generate a blank holder force (BHF), applying a uniform pressure on the fabric regions that are under the blank holder. The BHF applied varies slightly (99-101 N) for each punch geometry due to variations in the mass of their respective blank holders. For each test, the punch moves up at a constant speed of 1 mm s^{-1} until it reaches a punch displacement (PD) of 75 mm. Images are captured at a rate of 1 Hz by the DIC cameras. The facet size for DIC tracking is set to 26 pixels, while the facet separation is set to 20 pixels, with a pixel side length of 0.1 mm. The complete experimental forming test procedure is detailed in Appendix B.

Table 3.2 The key parameters relating to the 3D digital image correlation system used in the forming experiments.

System specifications		Experiment parameters	
System name	GOM ARAMIS 12M	Lens length/mm	50
Camera resolution/ px x px	4000 × 3000	Measuring volume/ mm × mm	400 × 300
Camera chip	CMOS	Slider distance/mm	396
Max frame rate/Hz	58	Camera angle/°	25
Strain measuring range/%	0.02 - 100	Calibration object	CP20 350 ×280
Strain accuracy/%	up to 0.01	Depth of field /mm	8
Lens coating	Titanar	Pixel side length/mm	0.1

3.2.2   Post-processing of experimental data

Wrinkle calculation
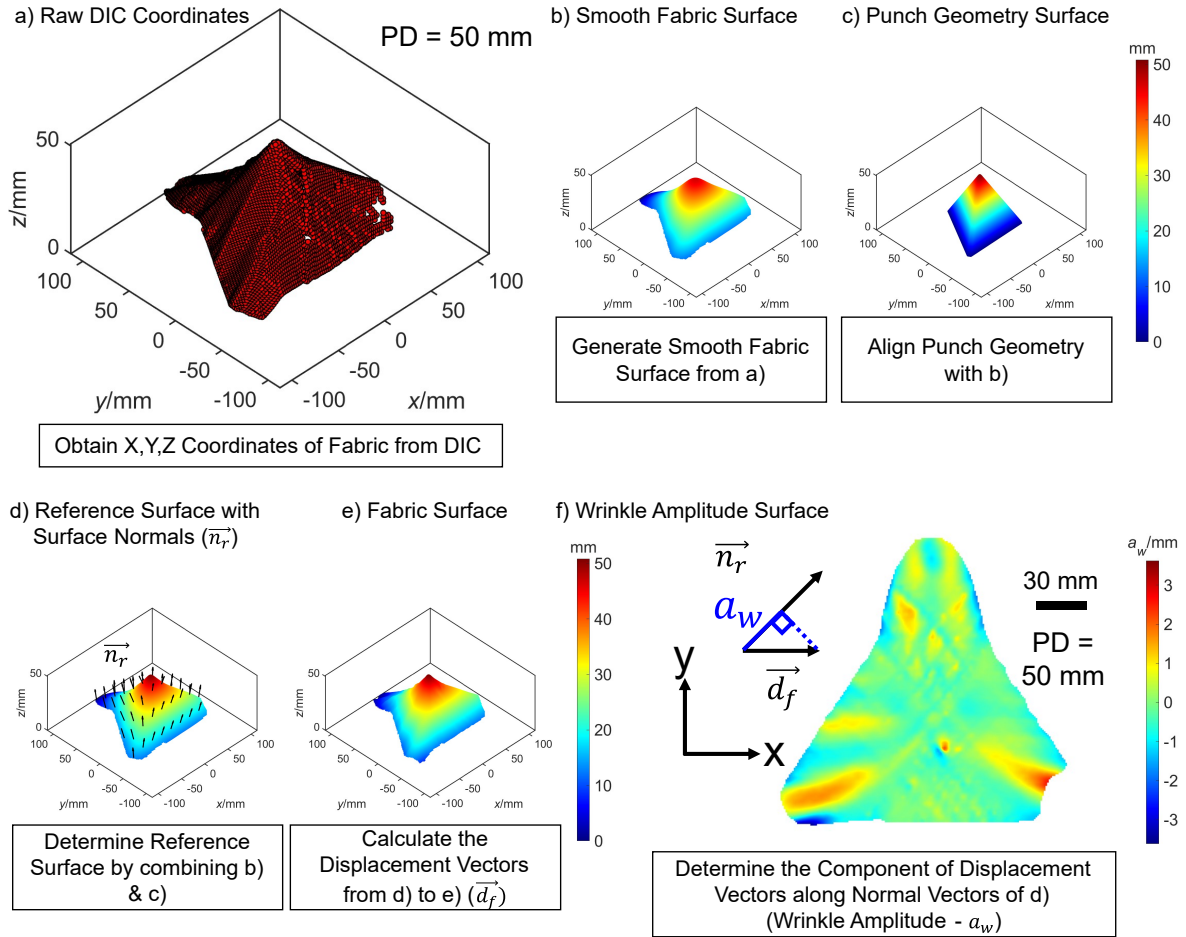
Fig. 3.3 An outline of the method for calculating the wrinkle amplitude on the visible fabric surface (shown here for a tetrahedron at a punch displacement (PD) of 50 mm): a) the raw DIC coordinates of the facet points, b) the smooth fabric surface, c) the punch geometry surface, d) the reference surface with a selection of surface normal vectors drawn, e) the fabric surface based on the raw DIC coordinates, and f) the wrinkle amplitude surface obtained.

The wrinkle amplitude (a_w), defined as the height of the out-of-plane deviations across the fabric surface, is calculated with respect to a reference surface, as shown in Figure 3.3. The reference surface represents an ideally formed fabric surface with no visible defects (Figure 3.3d). The wrinkle amplitude corresponds to the local surface normal ($\overrightarrow{n_r}$) component of the displacement vector ($\overrightarrow{d_f}$) from the reference surface to the actual fabric surface. The reference surface is

obtained by combining a bi-directionally smoothed fabric surface (Figure 3.3b) with the CAD geometry of the punch (Figure 3.3c). At any local grid position (x, y) on the fabric surface, the wrinkle amplitude (a_w) is calculated by the inner product of $\vec{d_f}$ and $\vec{n_r}$ as follows:

$$a_w[mm] = \frac{\vec{d_f} \cdot \vec{n_r}}{|\vec{n_r}|} \tag{3.1}$$

where $\vec{d_f}$ is the outward displacement vector at a particular grid position (x, y) from the reference surface to the corresponding point on the fabric surface, $\vec{n_r}$ is the outwardly normal vector to the reference surface at the particular grid position (x, y) (see schematic in Figure 3.3f).

To consider the spread of wrinkling, the 'wrinkle area' (A_w) (similar to the 'wrinkle ratio' from [49]) is calculated by taking the ratio of the area where $|a_w|$ exceeds an arbitrary absolute wrinkling limit of 1 mm ($A_{|a_w|>1mm}$), divided by the total visible area (A) at that stage of forming:

$$A_w[\%] = \frac{A_{|a_w|>1mm}}{A} \tag{3.2}$$

Local shear angle and strain calculation

As shown in Figure 3.4, the local shear angle across the surface of the NCF is calculated by interpolating the changes in local fibre tow orientations from the known deformation of the fabric, which also allows the surface fibre and stitch strains to be obtained. Firstly, the local changes in fibre tow position and direction are obtained by defining a series of parallel lines along the 45°, 0°, −45° directions to define the '1' fibre tow, '0' stitch and '2' fibre tow directions, respectively (defined in Figure 3.4a). These are then mapped on to the initial fabric surface coordinates using linear interpolation (Figure 3.4a). Each virtual tow line (m = total lines) is divided into short segments of 5 mm (n = total segments) and the initial fibre tow directions are obtained by taking the difference in coordinates between the start and end position vectors of each segment:

$$\vec{D}_{n,m} = \vec{x}_{n+1,m} - \vec{x}_{n,m} \tag{3.3}$$

where $\vec{x}_{n+1,m}$ is the end position vector of the nth fibre tow segment, $\vec{x}_{n,m}$ is the start position vector of the nth fibre tow segment, $\vec{D}_{n,m}$ is the local direction vector of the nth virtual fibre tow segment of the mth virtual tow line.
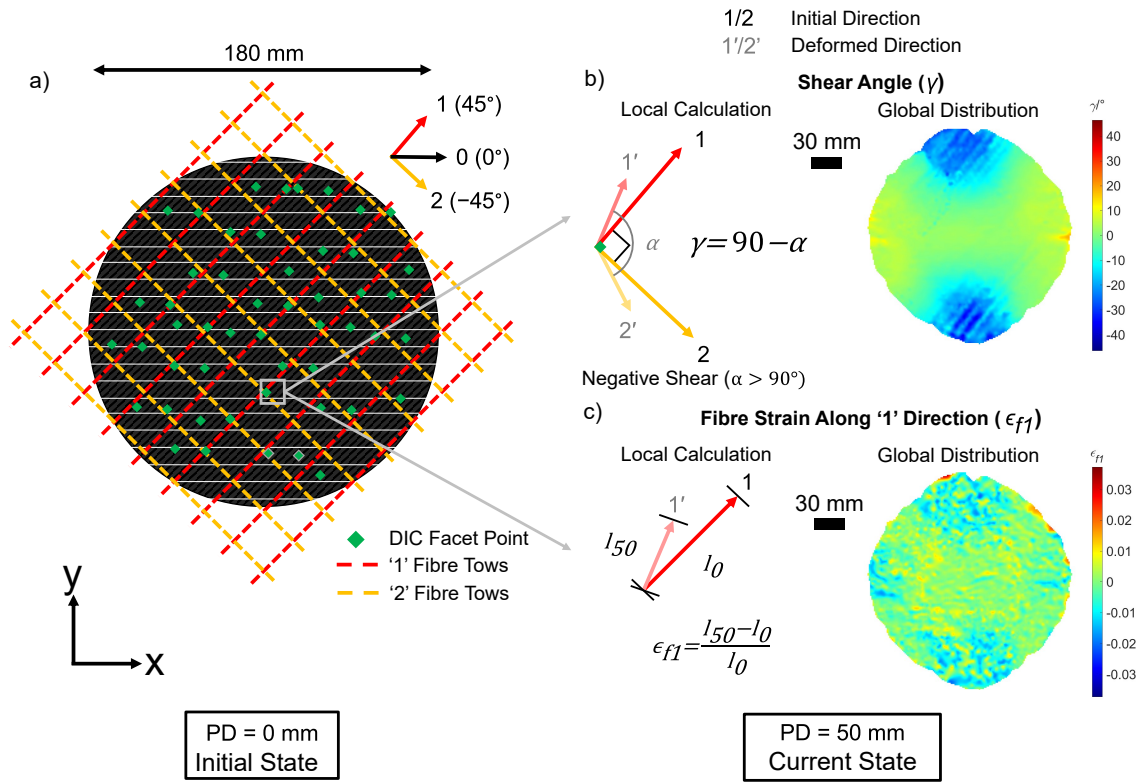
Fig. 3.4 An outline of the method for calculating the local shear angles and local fibre strains (shown here for a hemisphere at a punch displacement (PD) of 50 mm): a) the visible (to the DIC cameras) fabric surface at the start of hemispherical forming, with virtual fibre tows mapped onto it, corresponding to the known initial fibre tow directions, b) the local calculation for the shear angle (γ) at each facet point and the resultant global γ distribution over the visible fabric surface, and c) the local calculation of the of the strain along the fibre tow on the top NCF layer (ε_{f1}) during the forming process and the resultant global ε_{f1} distribution over the visible fabric surface.

For each successive forming step (Figure 3.4b & c), a linear interpolation function between the reference facet positions and the current positions is used to obtain the new fibre/stitch segment coordinates. From these segment coordinates, the current fibre directions at each facet are obtained and the angle between the two tow directions (α) can be found as follows, assuming that $\overrightarrow{f_1}$ and $\overrightarrow{f_2}$ are unit vectors:

$$\alpha[°] = \arctan\left(\frac{|\overrightarrow{f_1} \times \overrightarrow{f_2}|}{\overrightarrow{f_1} \cdot \overrightarrow{f_2}}\right) \tag{3.4}$$

where $\overrightarrow{f_1}$ is the normalised unit local fibre tow direction vector on the top surface of the NCF at each facet point, $\overrightarrow{f_2}$ is the normalised unit local fibre tow direction vector on the bottom

surface of the NCF at each facet point and $-180° \leq \alpha \leq 180°$ (the unambiguous value of α is obtained by considering the signs of the numerator and the denominator, using the *atan*2 function).

Knowing α, the local shear angle (γ) is found by subtracting from the initial angle between them (90°) (Figure 3.4b):

$$\gamma[°] = 90 - \alpha \tag{3.5}$$

where $\alpha < 90°$ represents the case of 'positive shear', corresponding to the fibre directions getting closer to each other after shearing, and $\alpha > 90°$ corresponds to 'negative shear' where the deformed fibre tows point further away from each other than in the initial configuration (as depicted in Figure 3.4b).

Equation 3.5 allows for the shear angle to be determined without requiring any additional tracking of the NCF's bottom tow layer, which is not visible to the DIC cameras. This method assumes that the $-45°$ virtual fibres evolve along the same path as those on the bottom layer and that the bottom fibres are at approximately the same amplitude as those on the (visible) top layer. It was previously shown by Chen et al. [16] that the variation in grid position between top and bottom layers at the end of forming is negligible, justifying that the bottom layer positions can be determined via the top layer. To validate the accuracy of this method, calculated shear angles are compared against direct measurement in two distinct regions of the NCF formed over a hemisphere (Table 3.3), with the absolute difference between calculated and measured angles being less than the uncertainty in the measurement.

Table 3.3 Validation of the calculated stitch strain and shear angle values by comparison with directly measured values at two particular locations in the positive and negative shear regions for the biaxial NCF formed over a hemisphere. Stitch strain measured using a Vernier caliper and shear angle using a protractor. Note that PS refers 'positive shear' and NS refers to 'negative shear'.

Region	Position rel. to fabric centre (x,y)/mm	Variable	Calculated (C) value (interpolation)	Measured (M) value ($\pm$)	Absolute difference ($|C-M|$)
PS	(50,0)	Stitch strain (ε_{s0})	0.038	0.037 ± 0.02	0.001
		Shear angle (γ)/°	4.1	1.6 ± 4	2.6
NS	(0,-50)	Stitch strain (ε_{s0})	-0.15	-0.17 ± 0.02	0.012
		Shear angle (γ)/°	-24.2	-27 ± 4	2.7

Additionally, the local strains along the top fibre tow and stitching directions are determined by considering the local changes in length of virtual fibre tow segments. The term 'strain' is used here, as per convention, to refer to the change in length along a given path, even though when in compression, the meaning of this for the tow/stitch can become ambiguous due to local path waviness or rigid body movements. The local fibre strains along the '1' fibre direction (ε_{f1}) and the '0' stitch direction, (ε_{s0}) are found as follows (see Figure 3.4c):

$$\varepsilon = \frac{l_x - l_0}{l_0} \tag{3.6}$$

where l_x is the local virtual segment length at punch displacement (PD) = x mm, l_0 is the local virtual segment length at the initial stage (PD = 0 mm) = 5 mm, and $\varepsilon = \varepsilon_{f1}$ or ε_{s0}.

The calculated stitch strains are likewise validated in Table 3.3 by comparing against direct measurement in the positive and negative shear regions of the fabric. Due to the low magnitude of the calculated fibre strains, it is not possible to directly measure these and thus they are validated via corollary from the stitch strain.

As only compressive fibre tow strain is likely to have an effect on wrinkling, only the compressive fibre tow 'strain' ($\varepsilon_{f1c} = \varepsilon_{f1} < 0$) is considered in Section 3.3. To account for possible dispersion in calculated strains and wrinkle amplitudes, five identical samples are tested and the mean values at each stage of deformation are used in Section 3.3.

Representative 'maximum' and 'minimum' values

To account for noise in the DIC data, all summative plots in Section 3.3 that look at the development of a particular variable over the course of forming, representative 'maximum' or 'minimum' values at each stage of forming are used, which correlate to the general growth of that variable. The 'representative maximum' (e.g. x_{max}) is defined as the mean of all the surface values above the 97th percentile. The 'representative minimum' (e.g. x_{min}) is defined as the mean of all the surface values below the 3rd percentile. Thus for a surface variable, x, at a particular stage during forming, these can be calculated as follows:

$$x_{max} = \frac{1}{n - n_{97}} \sum_{i=n_{97}}^{n} x_i, \quad n_{97} = 0.97 N_x \tag{3.7}$$

$$x_{min} = \frac{1}{n_3} \sum_{i=1}^{n_3} x_i, \quad n_3 = 0.03 N_x \tag{3.8}$$

where x is a surface variable (e.g. $|a_w|$) that contains all recorded values for that variable at that time step, N_x is an ordered list of all values of x, n is the total number of values in x

(ordinal rank corresponding to 100th percentile), n_{97} is the ordinal rank corresponding to the 97th percentile, n_3 is the ordinal rank corresponding to the 3rd percentile. The 97th and 3rd percentiles are chosen based on a comparison of wrinkle amplitude development based on a range of potential percentiles, and identifying the highest possible percentile (for maximum) or smallest possible percentile (for minimum) that eliminates erroneous local effects.

3.3 Results

The appearance of the fabric at the end of forming is qualitatively analysed in Subsection 3.3.1 in order to demonstrate the wrinkling types observed and the deformation behaviour of the fabric over the four geometries. Quantitative analysis of the wrinkling and strain behaviour follows in Subsections 3.3.2-3.3.7.

3.3.1 Observations at the end of forming

Wrinkle types

There are two different types of wrinkles that develop consistently for this NCF and they occur in three distinct locations of the fabric during hemispherical forming, as seen in Figure 3.5. Macroscale wrinkles are observed on the left and right edges of the hemisphere, and extending across the blank holder boundary (Figure 3.5a & b). In addition, similar macroscale wrinkles are observed at the end of forming underneath the blank holder in the top and bottom regions of the hemisphere (Figure 3.5a & c). These latter macroscale wrinkles appear somewhat different in orientation and size to those on the hemisphere surface, but as these occur outside the 'visible region' of the DIC cameras (Figure 3.2), they cannot be measured via the proposed DIC method. The other wrinkles observed are mesoscale wrinkles, as shown in Figure 3.5d. These wrinkles occur in the critical curved region of the hemisphere, only in the top and bottom parts of the visible region (Figure 3.5a).
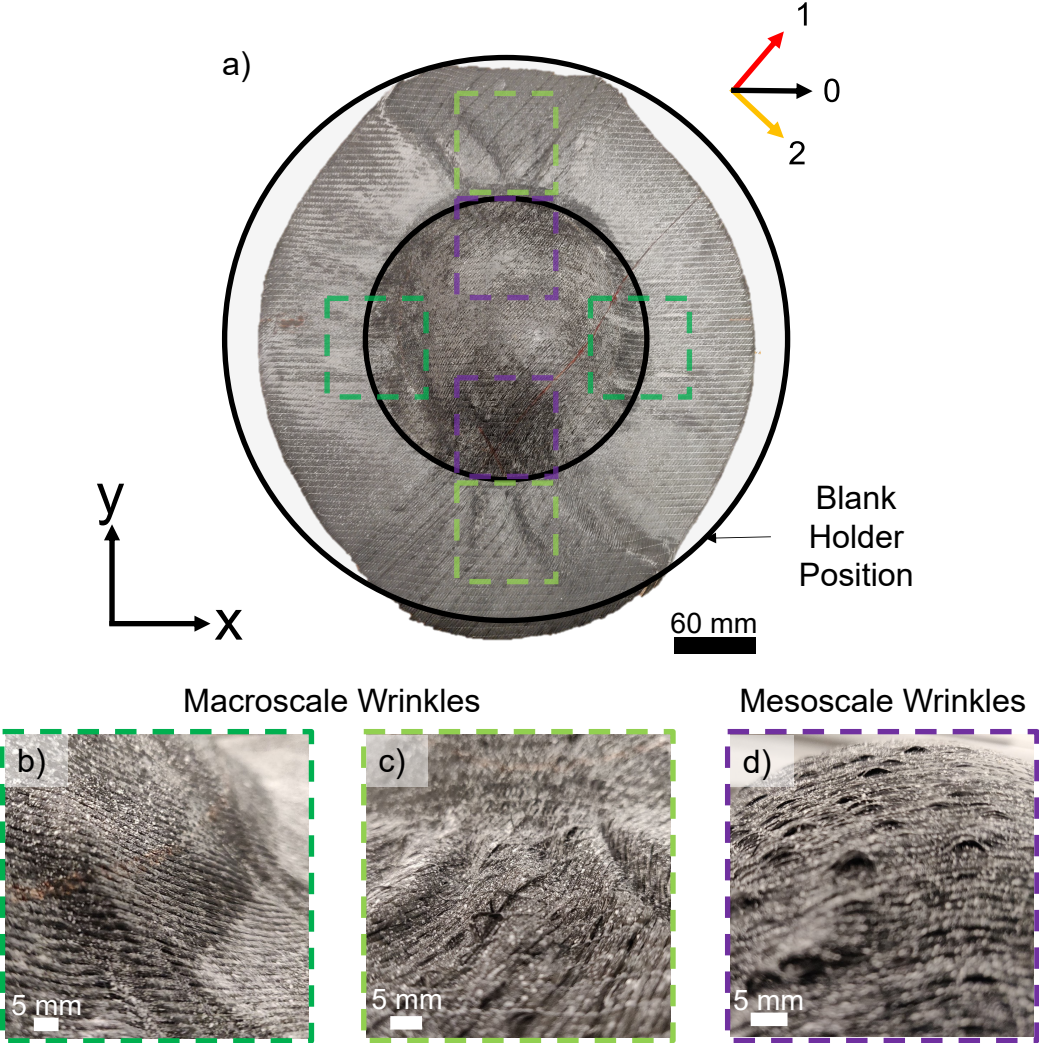
Fig. 3.5 A representative fabric sample (single biaxial NCF) after being formed over a hemisphere, showing the resultant wrinkling defects and their locations: a) the formed fabric sample with the relative position of the top blank holder shown, b) macroscale wrinkles extending across the blank holder boundary on the left and right sides of the hemisphere, along the stitching direction ('0'), c) macroscale wrinkles under the blank holder on the top and bottom sides of the hemisphere, perpendicular to the stitching direction ('0'), and d) mesoscale wrinkles within the visible region of the fabric on the top and bottom sides of the hemisphere.

Material draw-in and shearing of NCF

As evidenced by observing the fabric before and after hemispherical forming in Figure 3.6, this NCF appears to only deform via in-plane shear in the top and bottom regions, while the amount of shear in the left and right regions is not significant. The final outline of the fabric at the end of hemispherical forming is oval in shape (Figure 3.6a), in contrast to the initial circular sample geometry (Figure 3.1), highlighting that the material draw-in of the fabric around a uniform hemisphere is not uniform but still maintains symmetry about the stitching direction ('0'). More specifically, observing the local fibre tow paths on the non-speckled bottom ply (Figure 3.6b), there is minimal shearing in the regions of largest material draw-in (left and right) while there is significant shearing in the regions of least material draw in (top and bottom). In addition, it can be noted from comparing Figure 3.6a & 6b, that the wrinkles observed on the top ply correlate directly with those on the bottom ply, confirming that the bottom fibre tow amplitudes can be assumed from the top ply measurement.
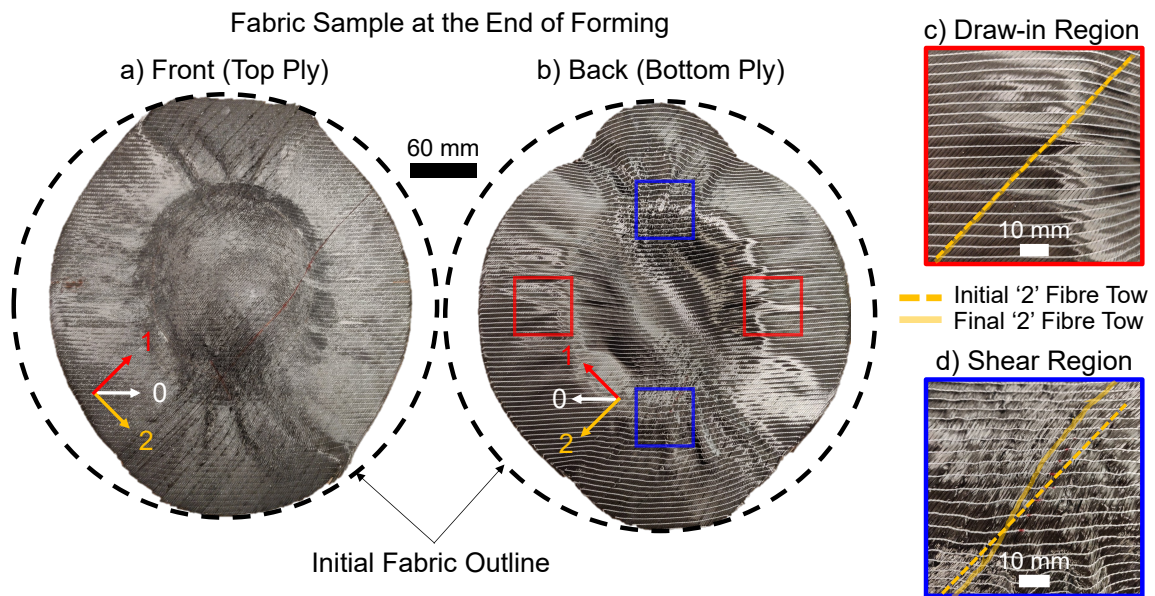
Fig. 3.6 The outline of a representative formed fabric sample relative to the initial fabric outline: a) the front surface of the fabric (facing the DIC cameras), b) the back surface of the fabric (facing away from the DIC cameras), showing regions of shear (in blue) and draw-in (in red), c) a close-up image of one of the draw-in regions of the fabric where an exemplar fibre tow (in orange) experiences minimal distortion, indicating minimal shearing, and d) a close-up image of one of the shear regions of the fabric where an exemplar fibre tow (in orange) experiences large distortion, indicating significant shearing.

Comparison of observations with other benchmark geometries
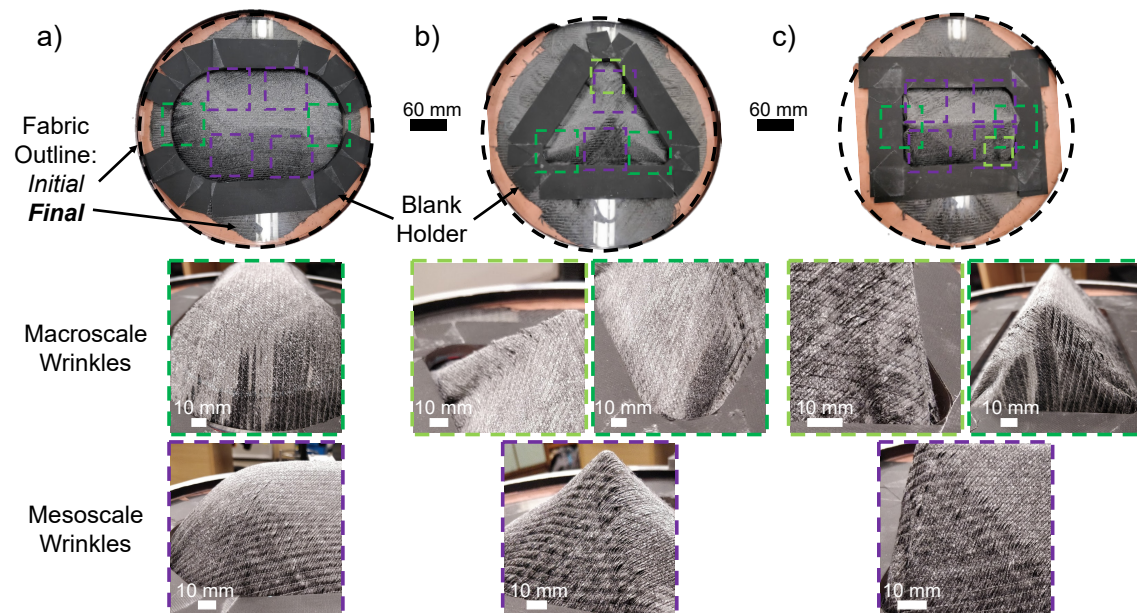
Fig. 3.7 Representative fabric samples (single biaxial NCF in each case) at the end of forming, shown relative to the initial fabric outline (dashed line), for three punch geometries and the with the resultant wrinkling defects and their locations on the formed fabric surface highlighted (shown using the colour coded squares: purple, light green and dark green): a) double dome, b) tetrahedron and c) triangular prism. Note that two different types of macroscale wrinkles are observed on the visible surface for the tetrahedron and the triangular prism.

The double dome, the tetrahedron and the triangular prism forming cases for this NCF, shown in Figure 3.7, all display the two wrinkle types seen with the hemispherical punch, with the tetrahedron and triangular prism additionally displaying a notably different type of macroscale wrinkling in regions where mesoscale wrinkles also occur. For the double dome results shown in Figure 3.7a, macroscale wrinkles are visible in the fabric along the two curved edges of the geometry while mesoscale wrinkles are seen along the long edges of the geometry. For the tetrahedron, macroscale wrinkles are observed over the two bottom corner edges while macroscale and mesoscale wrinkles are seen over the top corner edge, with mesoscale wrinkles also shown on the bottom face (Figure 3.7b). The triangular prism, in Figure 3.7c, displays significant macroscale wrinkles along the two vertical faces of the shape with mesoscale wrinkles on the two angled faces. Additional smaller macroscale wrinkling can also be seen the bottom left angled face (Figure 3.7c).

Due to the fabric architecture of this biaxial NCF, the material draw-in behaviour during forming is similarly unequal around the perimeter for the three geometries in Figure 3.7, with significantly more draw-in (and likely less shear) along the left and right-hand sides of the fabric. For example, the material draw-in is especially significant for the triangular prism in Figure 3.7c, in which the outline of the fabric is barely visible along the left and right edges and as such, these are regions of minimal shear (from Figure 3.6c). Furthermore, for the tetrahedron in Figure 3.7b, there is negligible draw-in along the top and bottom regions of the fabric, suggesting that these correspond to the significant shear regions in Figure 3.6d.

3.3.2   Wrinkle development during hemispherical forming

The wrinkling of the NCF is measured to be predominantly in regions of minimal shear, where the wrinkles grow linearly in amplitude and area after a clear onset point, as seen from Figure 3.8. The progression of the representative 'maximum' absolute wrinkle amplitude ($|a_w|_{max}$) with PD as shown in Figure 3.8a and the Wrinkle area (A_w) development with PD is similarly plotted in Figure 3.8b. Based on an average of five repeated samples for hemispherical forming, $|a_w|_{max}$ and A_w both grow linearly after a clear wrinkling onset point at PD = 25 mm before plateauing at PD = 50 mm. The surface distributions of $|a_w|_{max}$ and A_w shown in the insets in Figure 3.8a & b respectively, show that the wrinkling is concentrated to the left and right regions, which were shown to have minimal shearing in Figure 3.6.
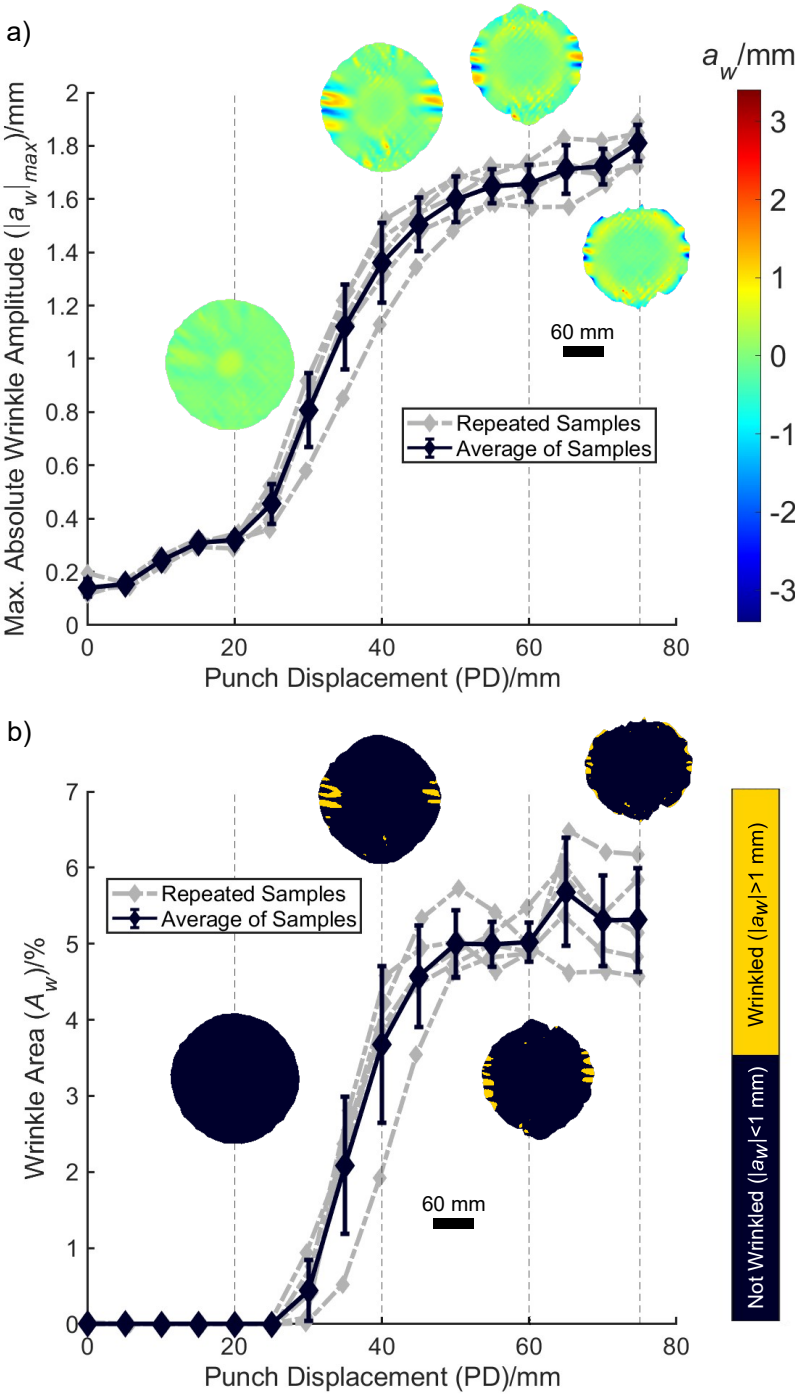
Fig. 3.8 The global development of wrinkles with increasing punch displacement (PD) during hemispherical forming, based on an average of five repeated samples with measurements taken every 5 mm of PD (the error bars correspond to the standard deviation between the five samples): a) representative 'maximum' absolute wrinkle amplitude, with wrinkling amplitude surfaces shown at PD = 20, 40, 60 & 75 mm, and b) wrinkle area, with wrinkle area surfaces shown at PD = 20, 40, 60 & 75 mm.

3.3.3 Shear angle development during hemispherical forming

As shown in Figure 3.9, shearing in the positive shear regions is restricted at an early stage while shearing in the negative shear regions is much more significant. This is seen from the development of the representative 'maximum' (γ_{max}) and 'minimum' (γ_{min}) shear angles with PD in Figure 3.9a. The maximum shear angle grows to a maximum of 10° and approaches a plateau at PD = 40 mm, after which no further positive shearing occurs. The minimum shear angle grows at a much faster rate and continues to grow beyond PD = 40 mm, reaching its peak of −35° at PD = 60 mm, decreasingly slightly after that. Figure 3.9b highlights that the positive shear (PS) regions correspond to the minimal shearing regions, and the negative shear (NS) regions to the significant shearing regions, which were previously established in Figure 3.6. From Figure 3.9c, the shearing of the fabric is shown to be largest at the edges of the visible fabric and thus is expected be largest near the blank holder (outside the visible region at the end of forming).
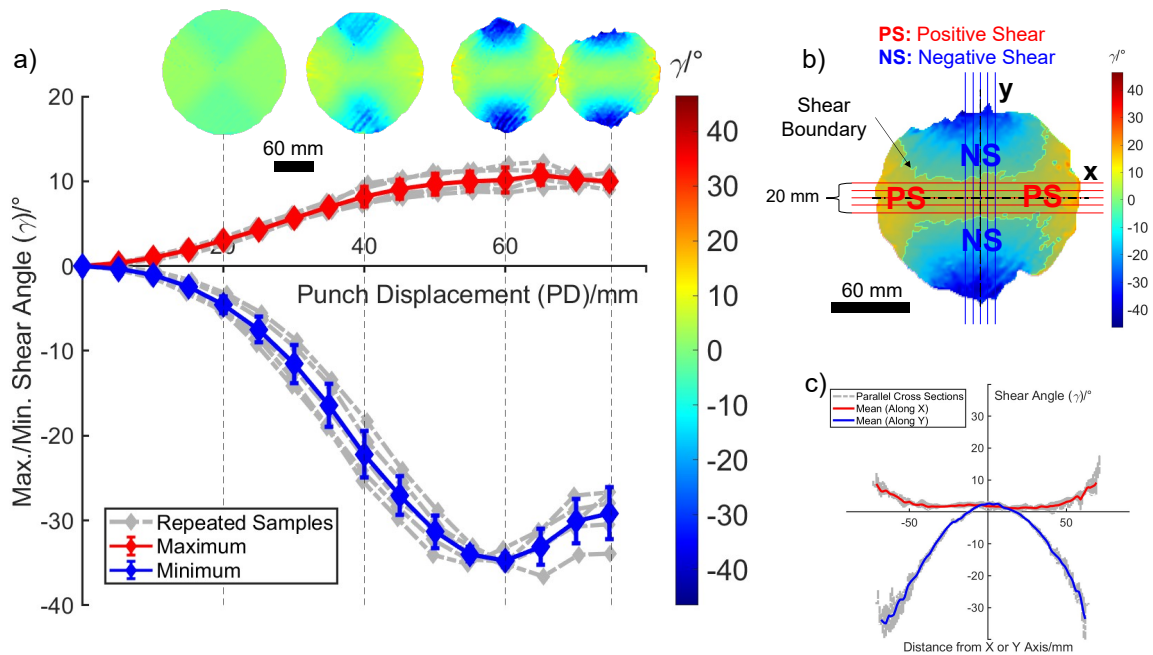
Fig. 3.9 a) The global development of the representative 'maximum' and 'minimum' shear angle with punch displacement (PD) for a representative sample during hemispherical forming (the local shear angle surfaces are shown for PD = 20, 40, 60 & 75 mm), b) the local shear angle distribution at the end of forming, defining the positive (PS) and negative shear (NS) regions, and c) the mean of the local shear angles calculated along the five vertical and horizontal parallel cross-sections (5 mm apart) shown in b), plotted against the distance from the X or Y axis.

3.3.4 Stitch and fibre tow strain development during hemispherical forming
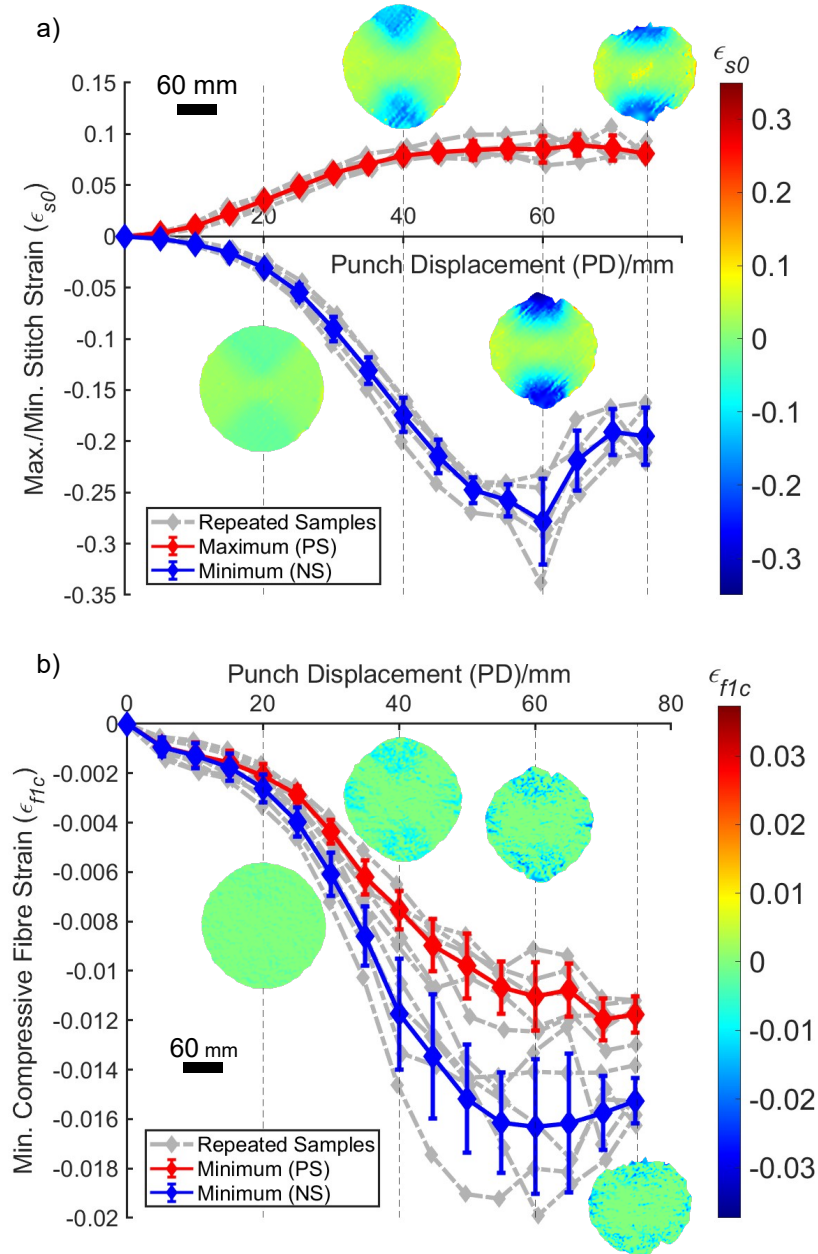
Fig. 3.10 a) The development of the 'maximum' and 'minimum' stitch strain in the positive (PS) and negative shear (NS) regions respectively, with punch displacement (PD) for a representative sample formed over a hemisphere. Surface distributions of stitch strain are shown for PD = 20, 40, 60 & 75 mm. b) The development of the 'minimum' compressive (negative-only) fibre strain in the PS and NS regions with PD for a representative sample formed over a hemisphere. Surface distributions of compressive fibre strain are shown for PD = 20, 40, 60 & 75 mm.

The strain along the polyester stitches of the NCF is large (up to 30% in compression from Figure 3.10a) and grows in a similar manner to the shear angle in the PS and NS regions respectively (comparing Figure 3.10a with Figure 3.9a). Stitch tension in the fabric is seen to correlate with positive shear and stitch compression with negative shear. This behaviour is expected based on the fabric architecture (Figure 3.1a).

The compression along the carbon fibre tows, which is suggested to cause mesoscale wrinkling, occurs in both the PS and NS regions, as seen in Figure 3.10b. The magnitude of the representative minimum compressive fibre strain ($\varepsilon_{f1c,min}$) is up to 1.7% in the NS regions and 1.2% in the PS regions.

3.3.5 Macroscale and mesoscale wrinkle development during hemispherical forming
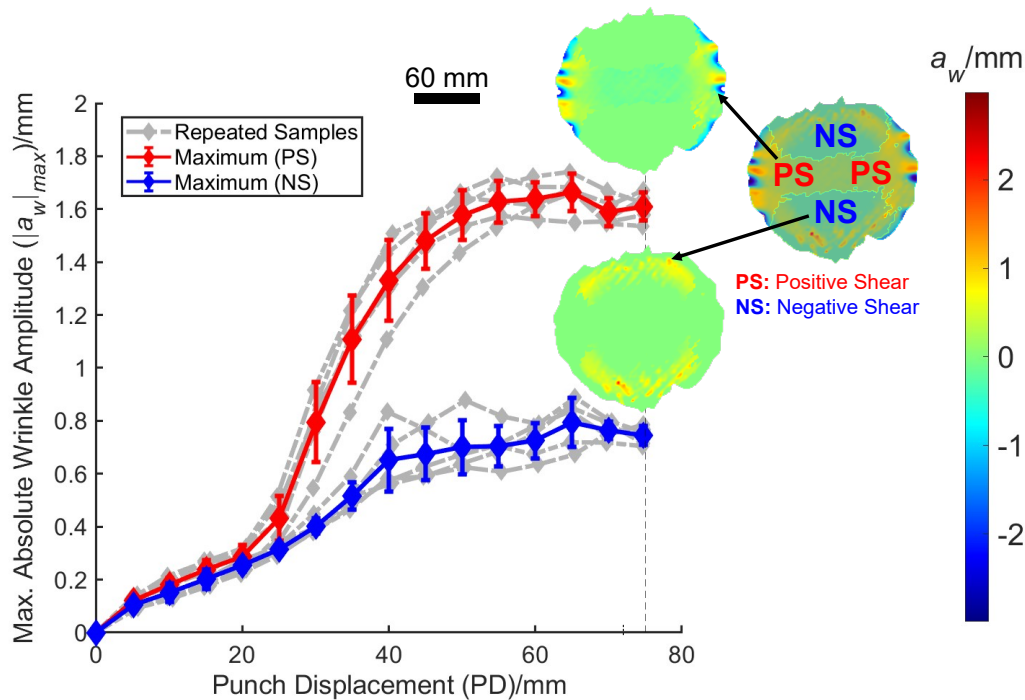
Fig. 3.11 The development of the representative 'maximum' absolute wrinkle amplitude in the positive (PS) and negative shear (NS) regions with punch displacement (PD). The wrinkle amplitude surface at the end of forming is shown for each of the regions, along with the global wrinkle amplitude distribution. The wrinkles in the positive shear region correspond to macroscale wrinkles and the wrinkles in the negative shear region correspond to mesoscale wrinkles. Note that in the NS region, only positive amplitude wrinkles are considered to eliminate erroneous data at the end of forming.

From Figure 3.11, the macroscale wrinkles in the PS regions are shown to be at least twice as large in amplitude as the mesoscale wrinkles in the NS regions. By considering the wrinkle amplitude in the PS and NS regions separately (based on Figure 3.9b), allows the development of macro and mesoscale wrinkles to be separated for hemisphere case, as shown in Figure 3.11. This shows that macroscale wrinkles predominantly occur in PS regions while the mesoscale wrinkles occur in NS regions. These wrinkle types appear to initiate around the same time (PD = 25 mm) but the mesoscale wrinkles reach a lower amplitude.

3.3.6 Relationships between wrinkling, strains and shear angle

The mesoscale wrinkle amplitude over the course of forming can be linearly correlated ($r^2 = 0.98$) with the growth of the compressive fibre strain in negative shear, as seen in Figure 3.12a. This suggests that tow compression causes mesoscale wrinkles. However compressive fibre strains are also shown to occur in positive shear regions (Figure 3.10b), where no mesoscale wrinkles develop so the correlation appears only to apply under specific conditions.

Figure 3.12b shows that the overall wrinkling amplitude of this NCF displays no consistent trend with shear angle and wrinkling initiates much before the locking angle for this fabric (57°, based on [16]) is reached.

As inferred from Figure 3.10a and as expected from the fabric architecture that aligns the stitching along the shearing direction, Figure 3.12c shows a linear relationship ($r^2 = 0.99$) between the stitch strain and shear angle of the fabric over the course of forming, with a consistent trend in both PS and NS regions.

In contrast to the stitch strain, the compressive fibre strain over the course of forming shows differing behaviour with respect to the shear angle in positive and negative shear (Figure 3.12d). In negative shear, a linear correlation between the compressive fibre strain and shear angle is noted, while in positive shear, the compressive strain increases at a higher rate compared to the shear angle.
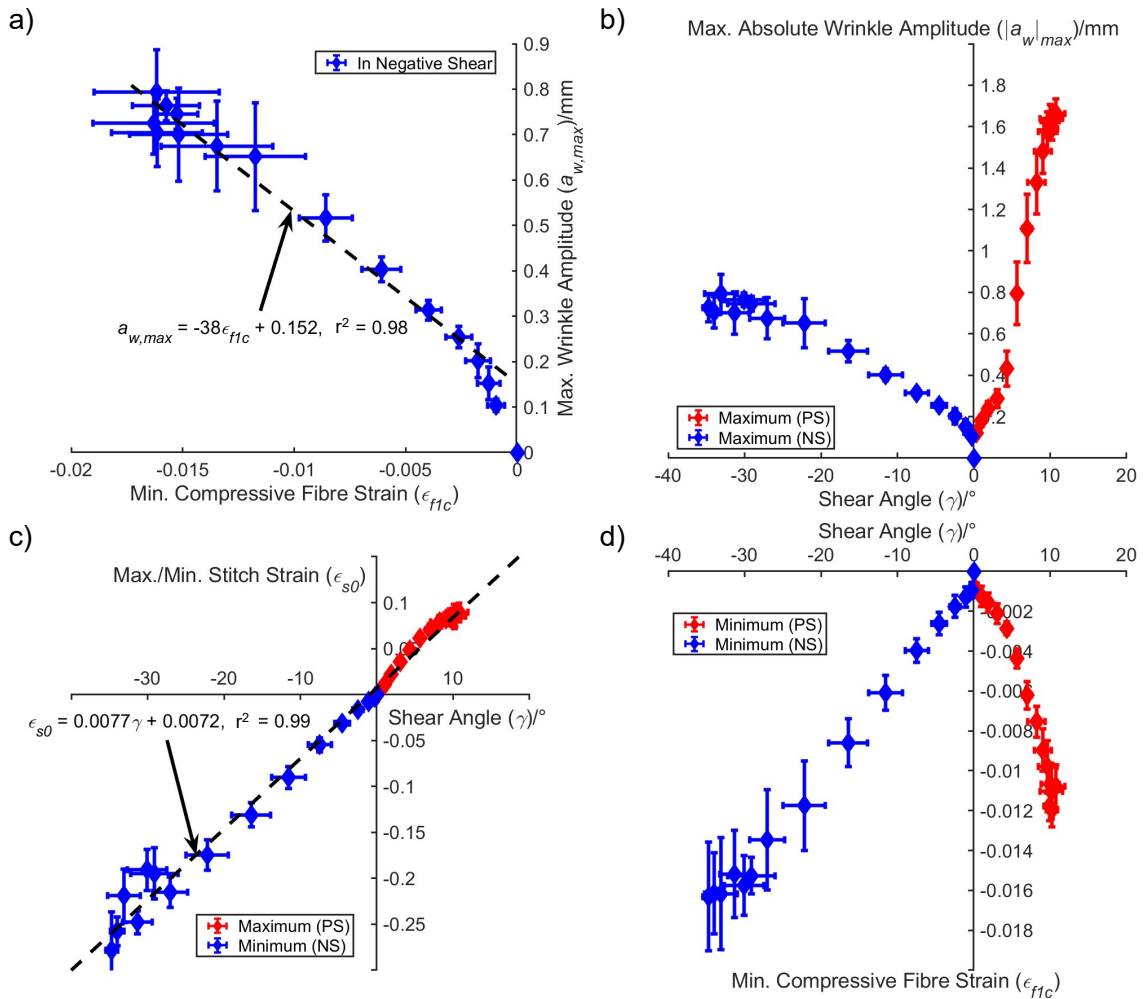
Fig. 3.12 a) The development of the representative 'maximum' mesoscale wrinkle amplitude and the representative 'minimum' compressive fibre strain in the negative shear region, over the course of the forming process. b) The development of the 'maximum' absolute wrinkle amplitude in positive and negative shear regions with shear angle, over the course of the forming process. c) The linear relationship between the 'maximum and 'minimum' stitch strain and the 'maximum and 'minimum' shear angle in both positive and negative shear regions over the course of the forming process. d) The compressive fibre strain plotted against shear angle, in both the positive and negative shear regions. Note that all data is averaged over five repeated samples formed over a hemisphere.

3.3.7 Wrinkling characterisation over four benchmark geometries
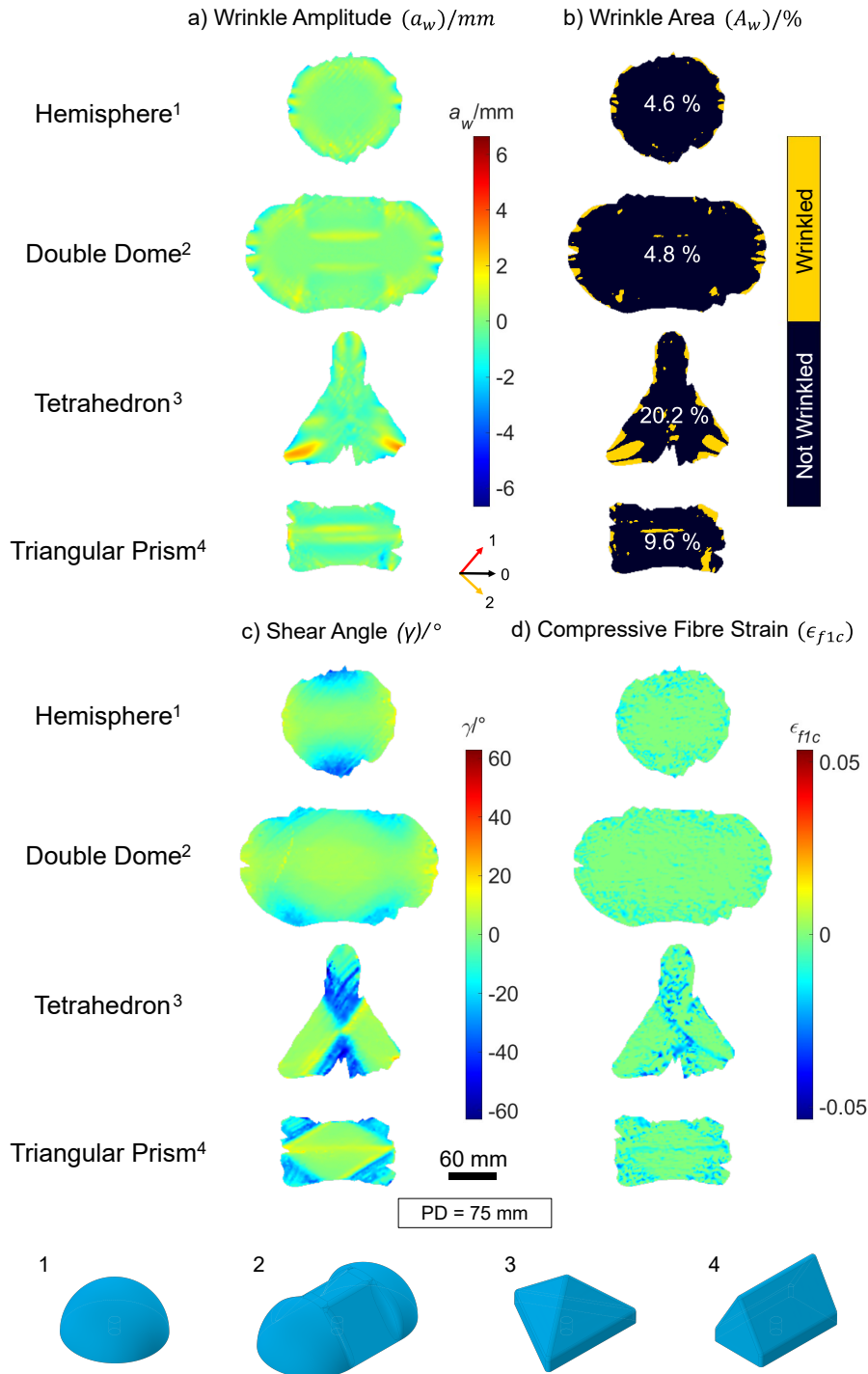
Fig. 3.13 A quantitative comparison of the wrinkling severity and surface strains for representative fabric samples formed over the four punch geometries investigated (hemisphere, double dome, tetrahedron and triangular prism), measured at the end of forming (punch displacement (PD) = 75 mm): a) wrinkle amplitude surface, b) wrinkle area surface, c) shear angle surface, and d) compressive fibre strain surface along the top layer of the fabric.

As seen from Figure 3.13, the wrinkling behaviour of the fabric over the four geometries tested differ significantly in amplitude and spread but the locations of wrinkling follow similar trends relative to the fabric straining, suggesting that the wrinkling mechanisms are consistent across different geometries. For all shapes, the largest wrinkles in Figure 3.13a are recorded in the PS regions (Figure 3.13c). Note that, for the triangular prism, the largest wrinkles on the vertical edges of the shape (observed in Figure 3.7) could not be tracked but these are expected to be in positive shear based on Figure 3.13c. The tetrahedron and the triangular prism are the only geometries that exhibit macroscale wrinkling in the negative shear regions, which are smaller in amplitude compared to those in PS regions (Figure 3.13a &c).

Some differences are noted in the compressive fibre strain distributions between the four geometries in Figure 3.13d with the tetrahedron and the triangular prism showing more larger, more localised compressive strains in the negative shear regions compared to the hemisphere and double dome, for which the strains are lower and more evenly distributed on the fabric surface.

Based on the 'spider diagram' in Figure 3.14, the double dome is shown to be the most formable geometry in terms of wrinkling whereas the tetrahedron displays the least formability. The five key wrinkling metrics that are evaluated in the 'spider diagram' are defined and their relevance explained in Table 3.4. Although closely matched by the hemisphere, the double dome has the lowest wrinkle amplitude and area, the latest wrinkle onset while also displaying the lowest shear angle and compressive fibre strain. The tetrahedron and triangular prism are significantly worse in almost all categories, which suggests that sharp edged geometries are more difficult to form than rounded geometries.
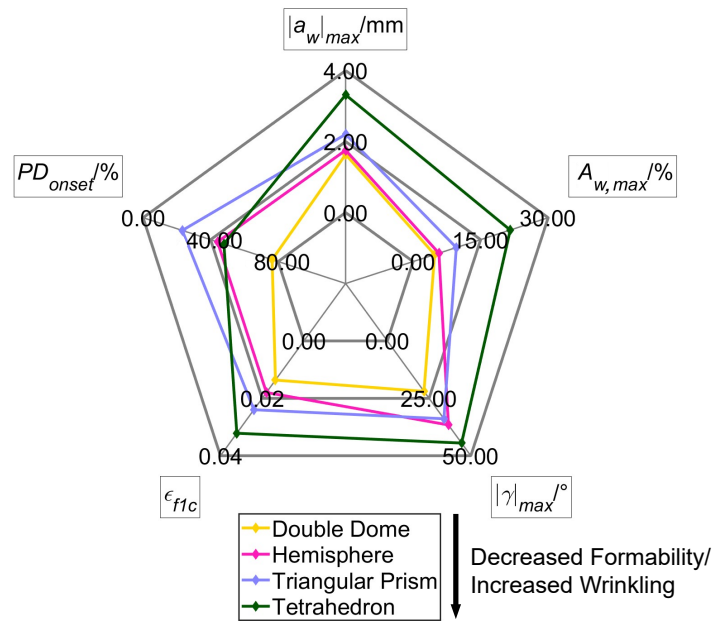
Fig. 3.14 A 'spider diagram' of the five wrinkling-related metrics, for the same fabric formed over four punch geometries. The parameters have been arranged such that the centre of the spider diagram represents maximum formability and minimum wrinkling. In order of decreasing formability, the four punch geometries are the double dome, hemisphere, triangular prism and tetrahedron.

Table 3.4 A description of the metrics plotted in Figure 3.14 and their respective relevance to wrinkling.

Symbol/unit	Description	Relevance to wrinkling
$|a_w|_{max}$/mm	the maximum absolute wrinkle amplitude on the visible fabric surface during the forming process	indicates the size of macroscale wrinkling
$A_{w,max}$/%	the maximum wrinkle area (wrinkle = $|a_w| > 1$ mm) measured during forming process	indicates the spread of macroscale wrinkling
PD_{onset}/%	the punch displacement (as a % of the final punch displacement) at the onset of wrinkling (when $|a_w| > 1$ mm)	indicates how early wrinkling occurs
$|\gamma|_{max}$/°	the maximum absolute shear angle measured across the visible fabric surface during the forming process	indicates initiation of shear macroscale wrinkling
$|\varepsilon_{f1,c}|_{max}$	the maximum absolute compressive fibre strain along the '1' direction measured across the visible fabric surface during the forming process	indicates likelihood of mesoscale wrinkling

3.4 Discussion

3.4.1 Wrinkling mechanisms
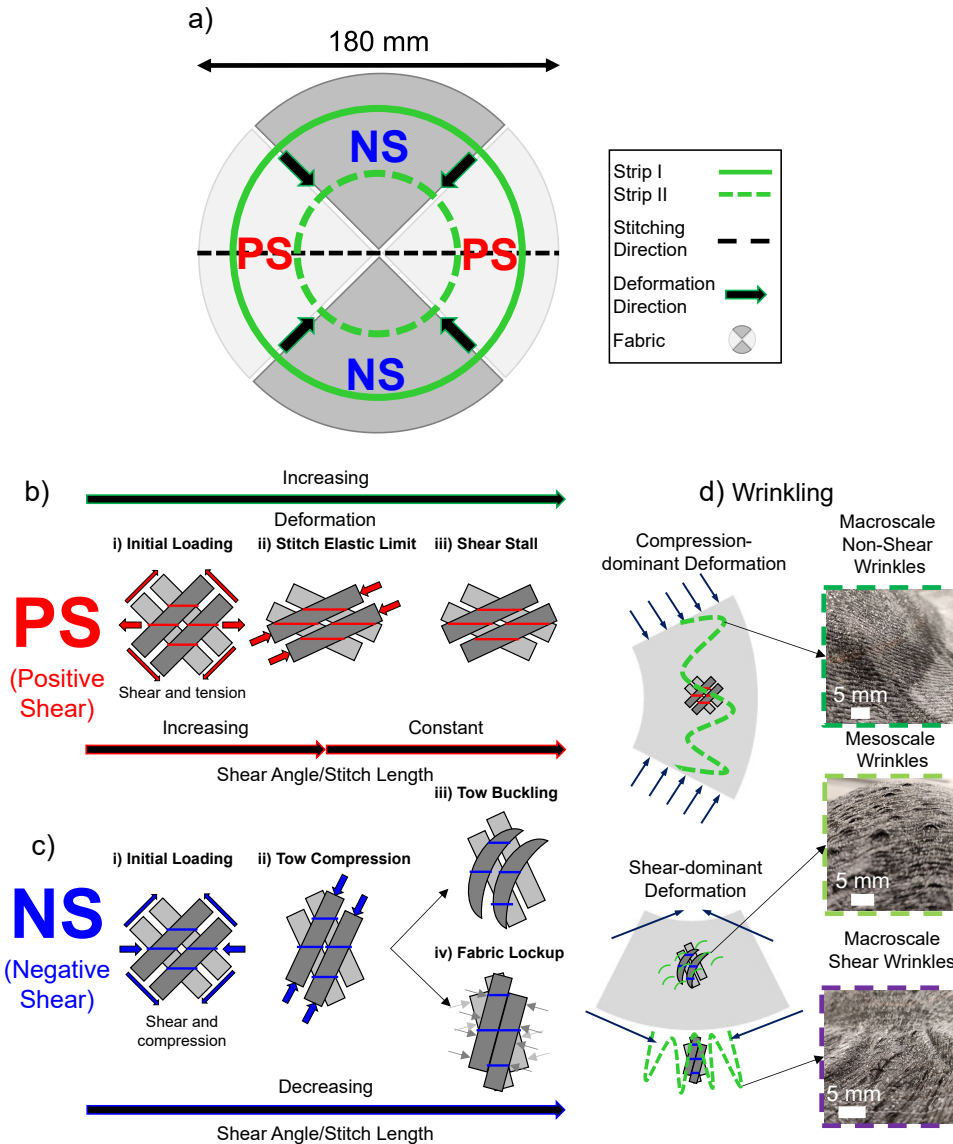
Fig. 3.15 A diagram, using hemispherical forming as an example, that highlights the two local shear deformations and the three wrinkling mechanisms that can be observed in this biaxial non-crimp fabric with a $\pm 45°$ fabric architecture: a) a schematic of the fabric sample when formed over a hemisphere, highlighting the circumferential reduction of length required of a hypothetical Strip I to be able to form into Strip II during forming, b) the shear deformation seen in the positive shear (PS) regions, showing that shearing initially occurs (i) but is then restricted by the stitches in tension reaching their elastic limit (ii), after which no shear is possible (iii), leading to material draw-in and causing macroscale non-shear wrinkles, c) the shear deformation seen in negative shear (NS) regions, showing initial shear and stitch compression (i), with the fibre tows also becoming compressed during shearing (ii), leading to either fibre tow buckling (mesoscale wrinkles) (iii) or further shearing and eventual lockup (macroscale shear wrinkles) (iv), and d) the three types of wrinkles possible to occur during the forming of this NCF and their relative locations, with images of each wrinkle type as shown in Figure 3.5.

Macroscale wrinkling in textile reinforcements can occur via two mutually exclusive and competing mechanisms: due to tow compression at shear lock-up (i.e. lateral tow-to-tow compression) or due to lateral fabric compression when the fabric is prevented from shearing owing to the tow architecture or the stitch pattern. These two mechanisms can clearly be identified and separated out for the particular NCF studied and are outlined for the case of hemispherical forming in Figure 3.15, but are equally applicable to other forming geometries, as seen from Figure 3.13. As depicted in Figure 3.15a, a prerequisite for a fabric to successfully form over a hemisphere is that a hypothetical strip of fabric ('Strip I') must reduce its circumferential length to that of 'Strip II' by the end of the process as it is drawn in. This reduction in length is facilitated by the local deformation of the fabric which in turn determines the likely wrinkling mechanism. For this NCF, the distinct deformation modes in the positive shear (PS) and negative shear (NS) regions highlight two ways for this reduction of length to occur for this fabric (Figure 3.15a). In the NS regions, the fabric deforms primarily via shear while in the PS regions, the fabric deforms via material draw-in.

Macroscale shear wrinkling occurs when shearing is the dominant fabric deformation mode and the fabric has sheared to its limit leading to the adjacent tows locking up. For this NCF, this occurs in the NS regions where shearing is unrestricted and allowed to reach the shear lockup stage. The shear angle of the fabric in the NS regions increases with increasing punch displacement (PD). In the initial stage of shear deformation, the shear resistance of the fabric is low due to low frictional forces between the tow layers. With continuing deformation, the shear resistance of the fabric increases more rapidly as inter-tow gaps vanish on each tow layer and adjacent parallel tows begin to press onto each other laterally, while held together by stitching (Figure 3.15c). This is the initiation of a lockup or jamming regime (Figure 3.15c). As shear deformation of the fabric increases, the pressure between adjacent parallel tows rises. This contact pressure corresponds to an in-plane compressive force that triggers the formation of wrinkles, which is referred to as *macroscale shear wrinkling* [69, 70]. The experimental investigation reveals that the critical lock-up angle is only reached for the tetrahedron and the triangular prism, which require large amounts of shear to be formed, resulting in macroscale shear wrinkles of around 1-2 mm in amplitude (Figure 3.13 and Figure 3.7). No macroscale shear wrinkling is seen in the NS regions for the hemisphere or the double dome with lower shear angles, except in the non-critical area underneath the blank holder (Figure 3.5), where the shear angle is expected to reach its peak (Figure 3.9c). Although shear wrinkling is said to be of primary concern when designing composites using textiles [21], this study suggests that the macroscale shear wrinkles are significant only in geometries with sharp corners and edges.

As previously discussed by Skordos et al. [73] for a rate-dependent prepreg textile, when the shearing of a fabric is restricted, the fabric is likely to wrinkle due to lateral fabric compression. For this NCF, in the PS regions, shearing is restricted to a minimum by the stitching (Figure 3.9a), leading to macroscale wrinkles as the fabric needs to reduce its circumferential length by lateral compression, which then induces *macroscale non-shear wrinkling* (Figure 3.15b & d). As a result, large wrinkles of up to 6 mm in amplitude form in these regions of the preform for all geometries tested (Figure 3.14a). These wrinkles are shown not to be related to the shearing of the fabric (Figure 3.12b). Furthermore, these wrinkles can initiate very early on during forming (Figure 3.8) and there appears no simple way of mitigation when shearing cannot be encouraged. Thus these wrinkles present a significant concern when manufacturing any doubly curved component using this fabric and in any particular forming situation that restricts shear deformation.

Mesoscale wrinkling in textile reinforcements occurs when fibre tows are loaded in compression along their length and not restricted from buckling in their locality. This was shown to be likely, as a linear relationship was found between the growth of mesoscale wrinkle amplitude and the growth of compressive fibre strain (Figure 3.12) and the locations of the compressive strains could be correlated with the locations of mesoscale wrinkling in the NS regions (Figure 3.10b & Figure 3.5). This matches the observations in [16] for the same material. However, even though compressive fibre strains occur across the fabric surface (Figure 3.10b), mesoscale wrinkling only occurs in negative shear regions of the fabric (Figure 3.6). This is because the tensioned stitching in positive shear not only restricts shearing but also prevents the tows from buckling by acting physically as an anti-buckling guide across the top of the tows - restricting the effective buckling length of tow to the stitching distance (Figure 3.15b). In negative shear, where the stitching is in compression and the fibre compression increases linearly with shear angle (Figure 3.15d), the stitching is unable to prevent this buckling leading to mesoscale wrinkles (Figure 3.15c). The mesoscale wrinkles are significantly smaller in amplitude compared to the macroscale wrinkles (Figure 3.11). However, since they are shown to develop over large areas of the formed surface of the fabric for all geometries (Figure 3.5 & Figure 3.7), they represent a potentially detrimental defect in terms of damaging the in-plane mechanical properties of the final manufactured component.

3.4.2   Deformation modes and wrinkling behaviour

The wrinkling behaviour of textile reinforcements is directly linked to the competing deformation modes (in-plane shear and material draw-in) of the fabric and the resultant local

deformation depends on the fabric's local shear resistance. For most dry textile reinforcements, the shear resistance is relatively low throughout the forming process, meaning that in-plane shear is the dominant deformation mode and macroscale shear wrinkles are the most likely defect [19]. However, in the case of this NCF, the stitching is aligned along the shearing direction of the fibre tows (at 45° to each tow - Table 3.1) and thus it becomes the restrictive element in PS regions when the stitch is in tension [16], preventing further shearing once it is taut (Figure 3.9b and Figure 3.15b). Thus, in those shear restricted regions, rather than forming like a pin-jointed net, the fabric locally forms like a sheet metal that deforms mainly by lateral compression during forming [144]. Similar behaviour is observed for woven prepregs by Skordos et al. [73] and this explains the similar wrinkling previously observed by Lee et al. [27] in regions of low shear during a hemispherical forming on an NCF with a similar architecture. As a result, the possible deformation modes of any NCF should be identified in order to understand and optimise its wrinkling behaviour.

3.4.3   Fabric architecture and wrinkling behaviour

The fabric architecture rather than the geometry dictates the wrinkling mechanisms exhibited by the fabric during forming. For all the forming geometries tested, the same types of wrinkling are observed to occur (Figure 3.5 & Figure 3.7) within the expected shear regions of the fabric (Figure 3.13) based on the mechanisms outlined in Figure 3.15. For this NCF, the interaction of the stitching with the fabric's shearing behaviour during forming controls the types of wrinkling that can form in the positive (PS) and negative shear (NS) regions, respectively. As shown in Figure 3.12c, there is a linear relationship between shearing of the fabric and strain along the stitches, with positive shear correlating with stitch tension and negative shear correlating with stitch compression. This matches the findings of Chen et al. [16] for this exact NCF and the analytical stitch model developed by Krieger et al. [31]. In PS regions, the taut stitching encourages macroscale wrinkles due to lateral compression (macroscale non-shear wrinkling) but prevents mesoscale wrinkling by physically preventing buckling. While in NS regions, the compressed stitches allow excessive shearing and tow compression leading to macroscale wrinkling due to shear lockup (macroscale shear wrinkling) and mesoscale wrinkling.

This pattern of wrinkling, in terms of where particular types of wrinkles are located, is consistent for all geometries tested using the same fabric, as shown in Figure 3.13. Thus, to identify the wrinkling types and mechanisms for a particular textile reinforcement, it does not necessarily need to be tested over multiple complex geometries.

3.4.4   Effect of geometry on wrinkling behaviour

The severity and the extent of fabric wrinkling are heavily influenced by the particular tool geometry, while the types of wrinkles observed are generally consistent for complex geometries. The variation in severity of wrinkling for different geometries can be clearly seen from Figure 3.14a, which shows how the tetrahedron results in much larger wrinkles relative to the other three geometries. This is equally true in terms of the spread of wrinkling, which is seen from Figure 3.14b, with the tetrahedron having a wrinkle area that is at least twice as large as the next largest (triangular prism). In general, the more rounded geometries with fewer sharp corners are shown to wrinkle less significantly and thus are more formable, as seen from Figure 3.13 and Figure 3.14 for the double dome and the hemisphere. In particular, shapes with more sharp corners (e.g. the tetrahedron and the triangular prism) are more likely to require larger amounts of fabric shear, meaning they are more likely to exceed the fabric's critical shear angle leading to macroscale shear wrinkling (Figure 3.7). However, as shown by Krieger et al. [31] for two biaxial NCFs, the extent of shearing over a geometry without circular symmetry is also dependent on the relative orientation of the fabric with the geometry. Figure 3.13d highlights that sharp-edged geometries are shown to cause larger compressive strains on the fabric surface, which have been correlated with mesoscale wrinkles. However, based on observation in Figure 3.5 and Figure 3.7, all the geometries tested result in similar size mesoscale wrinkles, spread across the negative shear regions. Thus, as long as any amount of tow compression occurs in regions where buckling is not restricted, mesoscale wrinkles are likely to develop.

3.4.5   Optimisation of wrinkling

The results from this study suggest that locally controlling forming process conditions could improve the formability of NCFs and minimise macroscale wrinkling by addressing local variations in deformation behaviour. This optimisation can be done at either the design stage or at the preforming process stage.

At the design stage, selecting a biaxial NCF with the stitching not parallel to the shearing direction and optimising the geometry to minimise sharp corners would help mitigate macroscale wrinkling. When the stitching is aligned with the shearing direction, local shear resistance is increased leading to non-shear macroscale wrinkles (Figure 3.15b), and thus other fabric architectures are preferred (e.g. a 0°/90° biaxial NCF). Furthermore, more rounded geometries in this study are shown to result in smaller wrinkles and reduced shear than those with sharper corners (Figure 3.13). Finally, although not explored in this study, the layup in multi-layer

forming and the relative orientation of the ply relative to the tool geometry are expected to have a significant effect on wrinkling through variations in frictional behaviour [103] and local shear behaviour [97].

At the process stage, optimisation of the blank holder force application and locally controlling the shear and frictional behaviour are critical for mitigating wrinkling behaviour. Generally, higher blank holder forces reduce the amplitude of the resultant shear wrinkles [27] by reducing in-plane shear. However, for NCFs such as the one studied, local shear behaviour should not be completely restricted during forming so as not to introduce macroscale wrinkles due to compression in the positive shear regions. Thus the BHF should be delicately optimised and ideally be locally varied around the fabric to avoid any adverse effects and control local shear behaviour [102]. Alternative promising techniques for locally controlling shear behaviour include applying local resin patches [106] and the additional of risers at certain key locations around the blank [104]. Finally, controlling the inter-NCF frictional behaviour, which can significantly exacerbate resultant wrinkles, can be done by adding metal sheets in between each NCF in the layup and actively vibrating these sheets [102].

3.4.6 Benefits and limitations of method

While the experimental approach taken has many benefits such as allowing wrinkling-strain relationships to be investigated and providing validation data for forming simulations, it has some limitations that should be addressed. Firstly, the 3D-DIC cameras are only able to track parts of the blank that are originally visible to them (shown in Figure 3.2) and thus no data can be obtained on the sections of the fabric that are initially under the blank holder, resulting in the visualised surface decreasing in size throughout the process (e.g. in Figure 3.8a). Secondly, due to limited depth of the field of the cameras and because the speckle pattern starts breaking down in certain regions due to excess in-plane shear, some data loss can occur at large punch displacements (e.g. for the tetrahedron in Figure 3.13). Thirdly, while the effect of the speckle pattern has been minimised to as large an extent as possible, the graphite sprayed onto the fabric to provide a speckle pattern does still have some effect (see Appendix C), as also shown by Harrison et al. [50]. Finally, because it is a visual approach, it can only be employed in open mould forming arrangements where the top ply is visible and is unable to track plies below the top surface (e.g. in multi-ply forming cases).

Although it is expected that the forming results represent the general behaviour of this NCF, the particular test conditions and setup used for the forming tests (Figure 3.2) can have a certain influence on the development of wrinkles on the NCF during preforming. In particular,

key variables that could have a certain influence are the blank holder force (affecting wrinkle amplitude), the alignment of the punch geometry (affecting the location of wrinkles), the inner fillet radius of the top blank holder (affecting in-plane shearing) and the material of the top and bottom blank holders (affecting frictional conditions). Comparison of the measured shear angle distribution on the fabric with an alternative hemispherical forming setup for the same NCF [16], suggest that the results are comparable and the aforementioned factors are minimal, at least in terms of shear. Finally, in contrast to [16], the open mould setup in this study changes the appearance of mesoscale wrinkles in particular as they develop out-of-plane instead of in-plane.

The wrinkling characterisation approach in Figure 3.14 is useful in identifying five key parameters that contribute towards the three types of wrinkles identified, including their severity and extent in the case of macroscale wrinkles. This allows for comparisons between the four geometries to be made. However, this is approach is somewhat limited in that single values cannot necessarily convey the exact wrinkling behaviour and the parameters do not capture the extent of mesoscale wrinkles, which cannot be accurately measured using the presented method.

3.5 Conclusions

This study leads to the following conclusions:

- The 3D-DIC approach can be successfully used to characterise the development of wrinkling during forming and relate the wrinkling behaviour to the strains in the fabric.

- The linear stitch-strain relationship in $\pm 45°$ biaxial NCFs controls their deformation and wrinkling behaviour, leading to both macroscale and mesoscale wrinkles.

- Typically, textile reinforcements deform via in-plane shear but, as is shown for this NCF, they also can deform via material draw-in when the shearing of the fabric is restricted.

- Macroscale wrinkles occur in textile reinforcements during forming via two competing mechanisms, depending on the local shear resistance of the fabric: lateral tow compression at fabric shear lockup (macroscale shear wrinkling) and lateral fabric compression (macroscale non-shear wrinkling).

- For this NCF, macroscale non-shear wrinkles, occurring in the regions of minimal shear, are shown to be severe and in more critical locations than macroscale shear wrinkles.

- In forming situations where the fabric's local shear resistance is high, using the maximum shear angle in the fabric (relative to the locking angle) is not a suitable indicator of wrinkling onset or severity.

- The severity of wrinkling defects during press forming of this biaxial NCF with a pillar stitch is shown to be highly influenced by component geometry but the wrinkling mechanisms of a particular fabric are shown to be independent of geometry.

Building on the conclusions, it is imperative that the effect of tool geometry on wrinkling is further investigated for other geometries beyond those used here in order to gain more confidence in the conclusions made and a more fundamental understanding of how wrinkling severity is affected by particular geometrical features. However, experimental testing of all possible geometry variations is clearly not practically feasible due to high tooling costs. Thus, simulation-based approaches, that incorporate the wrinkling mechanisms highlighted in this chapter are necessary for a more exhaustive study of the effect of tool geometry on wrinkling severity. This will be attempted in Chapter 5.

Chapter 4

Characterisation of wrinkling variability

4.1 Introduction

As highlighted in Chapter 2, the wrinkling of textile reinforcements has been shown to be subject to significant variability: unexpected differences in wrinkling under identically designed production protocols. This variability was also noted in the forming experiments of Chapter 3, where representative wrinkle amplitude values are used to obtain more consistent trends in wrinkle growth (Subsection 3.2.2) and yet noticeable variations in wrinkle amplitude between repeated samples are observed throughout the forming process (Figure 3.8). This variability detrimentally impacts experimental studies into fabric wrinkling as well as makes the validation of wrinkling models more challenging. However, there has yet to be investigations looking into quantitatively characterising this wrinkling variability. This variability is a function of the material variability and the preforming process variability. As summarised in Chapter 2, previous studies have only considered the as-produced variability of the undeformed fabric material but have not tried to measure the variability in the resultant preform, which is subject to change based on preforming conditions. In order to address this, the specific objectives of this chapter are as follows:

- To develop a novel variability calculation method that can decouple the wrinkling variability of fabrics in terms of wrinkle amplitude and wrinkle location.

- To apply this variability calculation method to characterise the experimental variability in the wrinkling defects of a preformed biaxial NCF compared against other materials, and with contrasting preforming conditions and layups.
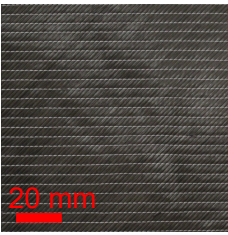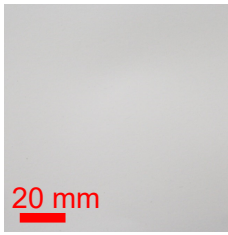
4.2 Materials and methods

4.2.1 Material characterisation

The three materials used in this study are characterised in Table 4.1: specifically a biaxial carbon fibre NCF (referred to in this chapter as 'Bi-NCF'), a triaxial carbon fibre NCF ('Tri-NCF') and standard printing paper ('paper'). In a contrast to the biaxial NCF, the Tri-NCF was selected due to its poor formability and its tendency for severe wrinkling [25], which would allow the wrinkling variability method to be thoroughly evaluated. Additionally, the paper was selected as a second comparison as it lacks the predefined structure of NCFs and thus it is expected to form large wrinkles in a nonuniform and unconstrained manner. It then allows an examination into the effect of the fabric architecture on wrinkling variability. The Bi-NCF and the Tri-NCF are both manufactured by Hexcel, under the trade names 'FCIM359' and 'FCIM358', respectively. They have the same polyester pillar-chain stitching and a similar fabric architecture except for an additional layer of tows along the $0°$ (stitch) direction and the $45°$ and $-45°$ directions being flipped. As a result of the added layer, the Tri-NCF is more than 1.5 times heavier and thicker than the Bi-NCF. The paper is lighter and thinner than both fabrics with an areal weight of 164 gm^{-2} and a thickness of 0.2 mm.

All the three materials are cut into circular samples of 380 mm in diameter using a rotary cutter and Perspex template, similarly to [25]. The paper is cut from A1 size sheets, controlling for the machine direction of each sheet, while the fabrics are cut from 1.6 m wide production rolls. Each sample is then applied with a speckle pattern to be compatible with the 3D-DIC system used for capturing the wrinkled surface. In the case of the paper, the speckle pattern is applied using solely a graphite spray, while for the fabrics, a graphite spray is used to make a black base layer that removes any reflections from the carbon, before a flaw detector spray is used to apply the white speckles. The detailed method for speckle pattern application is described in Appendix C.

Table 4.1 Characterisation of the three materials used in this study: a biaxial NCF ('Bi-NCF'), a triaxial NCF ('Tri-NCF') and standard printing paper ('paper').

Material name	Biaxial NCF ('Bi-NCF')	Triaxial NCF ('Tri-NCF')	Paper
Commercial name	Hexcel 'FCIM359'	Hexcel 'FCIM358'	N/A
Thickness/mm ($\pm$ 0.01 mm)	0.51	0.89	0.2
Areal weight /g m^{-2}	441 $\pm$ 22	749 $\pm$ 38	164
Tow orientations/°	-45/45	45/0/-45	N/A
Fibre material	Carbon fibre	Carbon fibre	Cellulose
Stitch material	Texturised polyester	Texturised polyester	N/A
Stitch type	Pillar	Pillar	N/A
Front/back of material	20 mm	20 mm	20 mm

4.2.2 Experimental forming method and wrinkle calculation

The forming tests, from which the variability data is derived, are all carried out using the forming rig shown in Figure 4.1a, using the same method detailed in Chapter 3, with the values and uncertainties in process parameters shown in Table 4.2. The wrinkle amplitude surface at the end of forming is calculated using the approach detailed in Chapter 3, that compares the deviation from the ideal formed shape along the surface normal in order to calculate absolute wrinkle amplitude ($|a_w|$) across the fabric surface. Before the wrinkle amplitudes are calculated, the fabric coordinates at the end of forming are used to fit a surface on a square grid of size 300 mm $\times$ 300 mm with 1 mm spacing using *gridfit* [145]. The fabric surface edges are bounded to the outermost tracked (*x,y*) fabric coordinates using the *boundary* function in MATLAB. A summary of this wrinkle calculation method is given in Figure 4.1b.
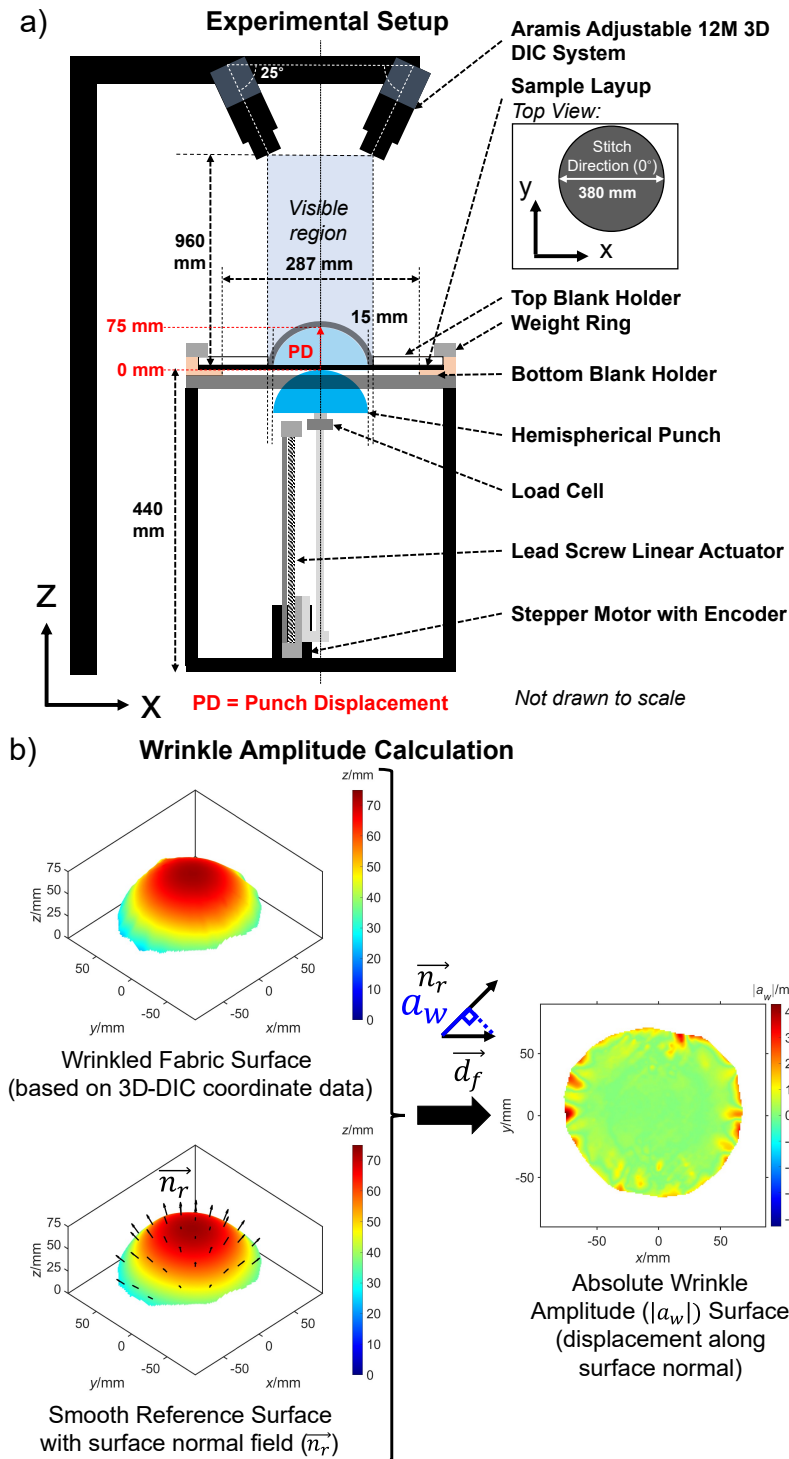
Fig. 4.1 Experimental setup and wrinkle calculation method: a) experimental rig used for preforming process, consisting of a preforming rig and a 3D-DIC system, and b) wrinkle amplitude surface calculation method based on data acquired from the 3D-DIC system. Note that $\vec{d_f}$ refers the outward displacement vectors from the reference surface to the fabric surface and $\vec{n_r}$ refers to the outwardly normal vectors of the reference surface. The setup and calculation method are the same as used in Chapter 3.

Table 4.2 The process parameters associated with the experimental rig and the preforming process, including the uncertainty associated with each of them.

Process parameter/unit	Value (±)
Circular sample diameter/mm	380 ± 1
Forming speed/mm s^{-1}	1 ± 0.01
Hemispherical punch radius/mm	75 ± 0.01
Maximum forming height/mm	75 ± 0.1
Blank holder force/N	$(59 - 179) \pm 1$
Circular top blank holder inner diameter/mm	180 ± 1 or 287 ± 1
Circular bottom blank holder diameter/mm	287 ± 1

4.2.3 Sources of variability and variability control during preforming tests

The proposed experimental preforming method consists of multiple sources of potential wrinkle variability that need to be closely controlled and minimised, such that any variability in the preforms can be primarily accounted for by the material variability and the preforming variability, which are of primary interest in this study. Table 4.3 provides a description of all the sources of variability identified for this experimental method, their relative potential effect on variability (evaluated on the scale 1-3 where 3 is the maximum relative effect) as well as the control techniques introduced to minimise these effects and their effectiveness (evaluated on the scale 1-3 where 3 is maximum variability control effectiveness). Based on this, it is suggested that the potential effect of all the controlled sources of variability are minimised such that they are unlikely to contribute significantly towards the observed wrinkling variability.

The controlled sources of variability associated with the preforming process (Table 4.3) relate to cutting each sample as well as placing and loading each sample into the forming rig. As these steps are done manually during testing, which increases the potential for variability [120], stringent control measures are implemented in order to mitigate potential effects, with consistency between samples verified at each stage. For example, the mass of each cut sample is measured and ensured that this is within the fabric areal weight production tolerance (5%) of the expected mass of 50.01 g for the Bi-NCF. It was found that all the Bi-NCF samples were within 1% of the expected mass.

The 3D-DIC measurement used to capture the wrinkled shape of the fabric introduces additional sources of variability, namely the required speckle pattern application and the

inherent error in tracking positions using DIC, and these need to be suitably controlled as well (Table 4.3). With regards to the speckle pattern application, it is important that the potential effects of the graphite spray on fabric deformation and bending stiffness, as previously highlighted by Harrison et al. [50], are minimised. This is achieved by accurate control of the spray process (see Table 4.3) and through careful optimisation to minimise the amount of graphite applied (see Appendix C). To evaluate the effect and variability of the application, the speckled samples are weighed and the added mass determined. For the Bi-NCF samples tested in this study, the mean added mass from the speckle pattern was 0.53 g, corresponding to a 1% increase in mass, still falling within production tolerances. However, some variability in the spraying is noted with a standard deviation of 0.21 g in the added mass, which is due to the manual application of the spray.

Additionally, the DIC approach is subject to some variability in its accuracy as previously noted by, for example, Alsayednoor et al. [146], who found that the strain accuracy is particularly dependent on the selection of suitable facet size, which needs to be large enough to be easy to track while also small enough to capture the heterogeneity of the displacement fields at the right length scale. For this investigation, the facet size was selected to be 26 pixels, while facet separation is set to 20 pixels, resulting in a pixel side length of 0.1 mm. This meant that the resolution was fine enough to capture the fabric's macroscale wrinkles of interest, while also not losing track of the deformed fabric at the end of forming. Additionally, the strain measurements from this 3D-DIC system and experimental preforming setup were previously validated by comparison to direct measurement using a Vernier caliper, with differences in strains being within the uncertainty of direct measurement (see Table 3.3 in Chapter 3). For full details of the DIC system (GOM ARAMIS 12M) and the specific experimental DIC parameters, refer to Table 3.2 in Chapter 3.

Table 4.3 Sources of potential variability at each stage of the experimental preforming setup, including both the sources associated with the preforming process ('Process') and the 3D-DIC method ('Measurement'). The sources related to the process are divided into 'uncontrolled' (those that are investigated) and 'controlled' (those that are mitigated) sources while the sources related to measurement are all controlled. The techniques used to mitigate the effects of the controlled sources are detailed under 'Control technique(s)'. The effect on variability ('Effect') and the control effectiveness ('Control') columns are evaluated on a scale from 1 to 3 where 3 is the maximum relative effect or effectiveness.

Type	Process step	Variability source(s)	Potential effect(s)	Effect (E) [1,3]	Control technique(s)	Control (C) [1,3]	E-C
Process (uncontrolled)	Material production	• Tolerances in fibre production • Tolerances in fabric assembly	• Irregular fibre tow orientations • Variations in sample mass	3	• Not controlled – investigated in study	N/A	3
	Material forming	• Deformation modes • Dynamic effects • Frictional behaviour	• Changes in preformed shape • Changes in wrinkle behaviour	3	• Not controlled – investigated in study	N/A	3
Process (controlled)	Sample cutting	• Sample dimensions	• Variations in sample dimensions and/or geometry • Variation in sample mass	1	• Use cutting template to get consistent geometry • Apply weights onto template to prevent sliding	3	-2
	Sample cutting	• Lateral alignment of template	• Variations in fibre tow locations on the sample	1	• Using stitching as guide when aligning cutting template • Apply weights onto template to prevent sliding	3	-2
	Sample placement	• Alignment of sample relative to blank holder	• Variations in initial fibre tow orientations	1	• Use the fixed grooves on blank holder to align stitch direction • Use ruler and protractor to ensure correct rotation	3	-2
	Sample loading	• Inconsistent weight loading	• Irregular blank holder force application	1	• Avoid local loading variations between the 4 weight hooks on the weight ring	2	-1
	Sample loading	• Inconsistent weight ring alignment	• Irregular blank holder force application	1	• Place weight ring on blank holder such that the opposing hooks are directly in line with the fixed grooves	1	0
Measurement (controlled)	Speckle pattern application	• Irregular or excessive application of graphite	• Local variations in sample mass • Local variations in bending behaviour	2	• Using spray can gun to control spray pressure • Keep spraying distance consistent at 500 mm	3	-1
	Digital image correlation	• Fabric coordinate measurement subject to errors • 3D tracking calibration	• Inconsistent tracking of fabric coordinates between samples • Variations in wrinkle amplitudes	1	• Optimisation of facet size to maximise accuracy of fabric tracking • Validation of strain measurements from DIC	3	-2

4.2.4   Outline of testing
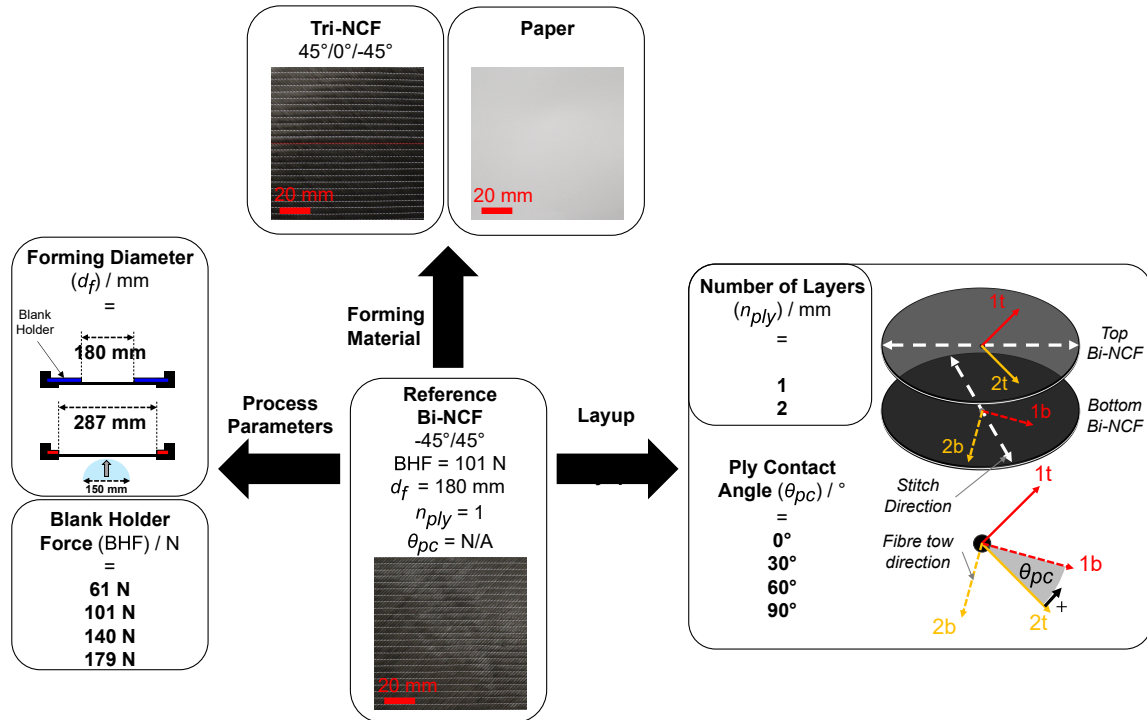
Fig. 4.2 Outline of the experimental testing conducted to investigate the effect of varying the material, process parameters and layup on the wrinkling variability after preforming. These tests are all compared relative to the prescribed reference ('Ref') case for the forming of a single ply of a biaxial NCF ('Bi-NCF') with a blank holder force of 101 N and forming diameter of 180 mm. For each variation relative to the reference, the forming test is repeated 7 or 8 times (16 for the paper) under those particular conditions in order to characterise the wrinkling variability for that sample set. Note that the forming diameter (d_f) is defined as the inner diameter of the circular top blank holder while the ply contact angle (θ_{pc}) is defined as the initial angle between the fibre tows on the top layer of bottom NCF (2t) and the bottom layer of top NCF (1b).

As outlined in Figure 4.2, the variability of the wrinkling behaviour during preforming is explored with regards to three key areas: the effect of process parameters, materials and layup. For each area, two particular changes are explored with the respect to the reference ('Ref') case of a single Bi-NCF is formed with a blank holder force (BHF) of 101 N, a forming diameter (d_f) of 180 mm, with the stitching (0°) direction aligned along the global X direction (see Figure 4.1a). For process parameters, four different blank holder forces (BHF = 61 N, 101 N, 141 N and 179 N) and two forming diameters (inner diameter of the top blank holder: d_f = 180 mm and 287 mm) are explored. In terms of investigating forming material effects, two

contrasting materials (Tri-NCF and paper) are compared against the Bi-NCF. For the paper, to discount the potential effect of forming anisotropy [147], 8 tests each are conducted with the paper 'grain direction' (along the long edge of the sheet) parallel and perpendicular to the global X direction, with these samples all compared against each other within one sample set of 16 samples. Finally, the effect of the layup is investigated by comparing the single-layer Bi-NCF forming to two-layer Bi-NCF forming, with the initial orientation of the second, bottom NCF at four different angles relative to the fixed top NCF (ply contact angle (θ_{pc}) = 0°, 30°, 60° and 90°).

All forming tests are conducted with a hemispherical punch made of modelling board with a radius 75 mm, a circular Perspex blank holder, a forming speed of 1 mm s^{-1} and a total forming height of 75 mm. For full details regarding the forming test procedure, refer to Appendix B. For each sample set, the forming test is repeated 7 or 8 (16 for the paper) times. The results from these are then used to characterise the wrinkling variability within that sample set using the approach outlined in Subsection 4.2.5.

4.2.5 Method for wrinkling variability characterisation

The novel method for characterising the variability in wrinkle amplitude and wrinkle location is outlined in Figure 4.3. The method is used to calculate the magnitude differences between every possible pair in a wrinkle surface sample set. A sample set is defined as a set of experimental samples of the same material that have been formed under the same prescribed forming conditions. The variability characterisation method is implemented in MATLAB, taking advantage of the Image Processing Toolbox. As the surfaces are compared as images, the method is generalisable to any type of surface data and this surface data can be acquired via any feasible method.
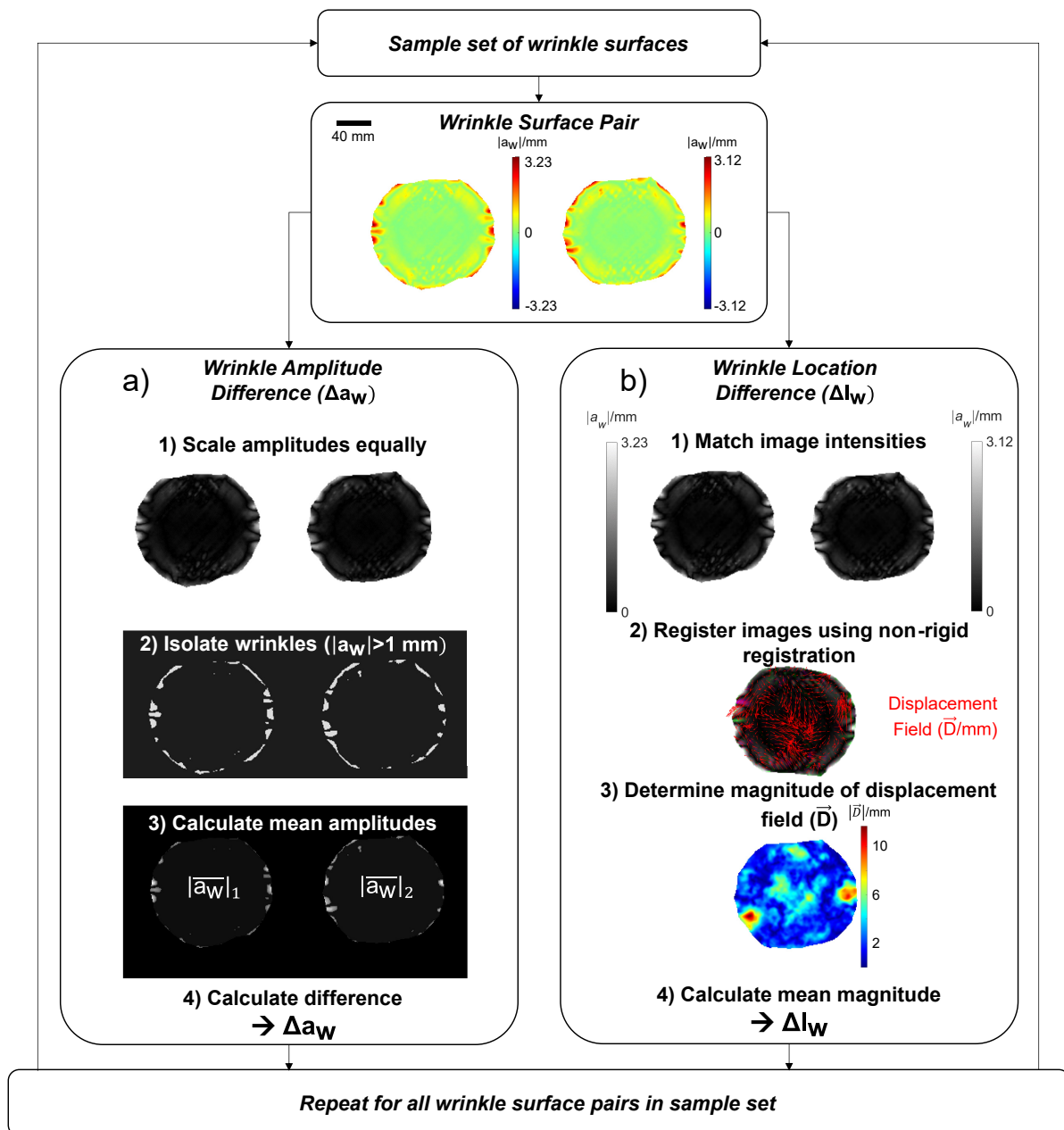
Fig. 4.3 Outline of wrinkling variability calculation method for a given sample set of wrinkle surfaces from repeated forming tests: a) calculation of the wrinkle amplitude difference between each wrinkle surface pair to characterise wrinkle amplitude variability, and b) calculation of the wrinkle location difference between each wrinkle surface pair to characterise wrinkle location variability.

Wrinkle amplitude variability

Figure 4.3a outlines the calculation of the wrinkle amplitude difference, Δa_w, which characterises the variability in wrinkle amplitude:

1. The wrinkle surface pairs are converted to grayscale images and the intensity scaled such that the maximum corresponds to the largest wrinkle amplitude within the entire set: $|a_w|_{max,set}$.

2. The image pairs are processed through edge detection and filtering to isolate just the wrinkles in each image.

   - Edge detection to identify the edges of the wrinkle surface is done using the Sobel operator, which identifies the surface edges based on maximum gradients.

   - Filtering to isolate just the wrinkles on the surface is done by applying a mask that locates all image pixels where the intensity equivalent wrinkle amplitude exceeds a specified filter amplitude. The filter amplitude is chosen to be 1 mm, consistent with the threshold used for 'Wrinkle Area' in Chapter 3.

   - All other pixel intensities, beyond these wrinkled regions, are set to NaN.

3. The mean wrinkle amplitude of each image, $|\overline{a_w}|$, is calculated by converting the mean intensity in pixels into a mean amplitude in mm:

$$|\overline{a_w}|[mm] = \bar{I} \times \frac{|a_w|_{max,set}}{I_{max}} \tag{4.1}$$

   where $\bar{I}$ is the mean intensity of the filtered image and $I_{max} = 255$.

4. The absolute difference in the means between the two images is calculated to determine Δa_w (step 4):

$$\Delta a_w[mm] = ||\overline{a_w}|_i - |\overline{a_w}|_j| \tag{4.2}$$

   where $|\overline{a_w}|_i$ and $|\overline{a_w}|_j$ are mean wrinkle amplitudes of the ith and j[th] images in the sample set respectively.

The wrinkle amplitude difference is decoupled from the effect of wrinkle location by taking the mean amplitude of the wrinkles of each image before taking the difference. Note that, for the generated wrinkle surfaces in the benchmark study (Figure 4.4) where large differences in wrinkle location are imposed, it was necessary to apply a rigid registration to align the two images before Δa_w is calculated in order to minimise the fictitious differences in amplitude arising from representing sinusoidal wrinkles of varying orientations using square pixels.

To eliminate this error, the wrinkle patterns were first aligned so that the wrinkles and thus amplitude difference was consistent and as expected.

Wrinkle location variability

Figure 4.3b outlines how the wrinkle location difference, Δl_w, is separately calculated to characterise the variability in the wrinkle locations:

1. The maximum image intensities between two images are matched by scaling them independently to the maximum amplitude of each particular sample: $|a_w|_{max}$.

   - Additionally, the histograms between the two images are matched using the *imhist-match* function to ensure equal intensity distributions.

2. The two images are registered using non-rigid registration in order to determine the displacement field ($\vec{D}$) from one wrinkle surface to another, with the local displacement vectors corresponding to differences in wrinkle locations in pixels.

   - The non-rigid registration is performed using the 'Demons' registration algorithm [148] as implemented in the *imregdemons* function. This function determines the displacement field required to align a particular image to be registered ('moving') with a 'fixed' reference image.

   - For the wrinkle surfaces considered, the optimal parameters for the variables associated with the *imregdemons* function, that produce the maximum similarity between the registered images, were found to be:

     - *PyramidLevels* $= 3$
     - *N* (number of iterations at each pyramid level): $= [200\ 100\ 50]$
     - *AccummulatedFieldSmoothing* $= 1$

3. The magnitudes of the displacement field in millimetres, $|\vec{D}|$, are determined by converting the D_x and D_y components from pixels to millimetres, and calculating the vector magnitude:

$$|\vec{D}|[mm] = \sqrt{(D_x \times c)^2 + (D_y \times c)^2} \qquad (4.3)$$

where c is the conversion factor from pixels to millimetres and equals 1 mm px^{-1} in this case.

4. The wrinkle location difference, Δl_w, is calculated by taking the mean of $|\vec{D}|$:

$$\Delta l_w[mm] = \overline{|\vec{D}|} \qquad (4.4)$$

Variability within each sample set

The variability within each sample set is quantified by calculating the mean wrinkle amplitude difference ($\overline{\Delta a_w}$) and the mean wrinkle location difference ($\overline{\Delta l_w}$) between all the pairs of that set, thus describing the overall wrinkling variability under the particular conditions of the sample set. In addition, the uncertainty in the overall variability is characterised by the sample standard deviation of the wrinkle amplitude difference ($s_{\Delta a_w}$) and the wrinkle location difference ($s_{\Delta l_w}$) respectively. For experimental measurements, this allows for the spread in the variability measurements to be evaluated: i.e. how repeatable the observed variability is.

Statistical significance of variability

One-way ANOVA analysis, followed by a multiple comparisons test, is used to evaluate the statistical significance of differences in variability of all the tested sample sets relative to a specified reference set. This is done in order to understand whether the imposed change for that sample set has a significant impact on the observed wrinkling variability or whether the mean result is within the uncertainty for the reference set. This analysis is completed using the *anova1* and *multcompare* functions, separately applied to the wrinkle amplitude difference and wrinkle location difference respectively. The significance level chosen for the multiple comparisons test to evaluate significance is the 95% confidence interval ($p < 0.05$).

Benchmark study

In order to validate the variability calculation method and give context to the experimental results of the study, a series of fictitious benchmark wrinkle surface cases are generated and their variability calculated against a reference case (Figure 4.4). The benchmark wrinkles cases ('Reference' and Cases 1-9) in Figure 4.4 are all generated using MATLAB and are loosely based on the hemispherical forming of a biaxial NCF. The 'Reference' wrinkle surface consists of four equal-sized sinusoidal wrinkles, with a maximum absolute amplitude ($|a_w|_{max}$) of 1 mm and a maximum wrinkle width of 11.25 mm, that are equally positioned around the circumference of the fabric surface (diameter = 180 mm) such that the wrinkles are all aligned along the *x* and *y* axes. The benchmark cases are all variations on this reference surface with changes made to the number, the width, the orientation and the amplitude of the wrinkles in various combinations. The benchmark study additionally aids to assess whether the non-rigid registration is able to successfully determine the location difference between surfaces with differing wrinkle patterns. Additional details regarding the wrinkle generator used to create the

fictitious wrinkle patterns, the reference benchmark wrinkle surface and the validation of the variability calculation method are provided in Appendix D.
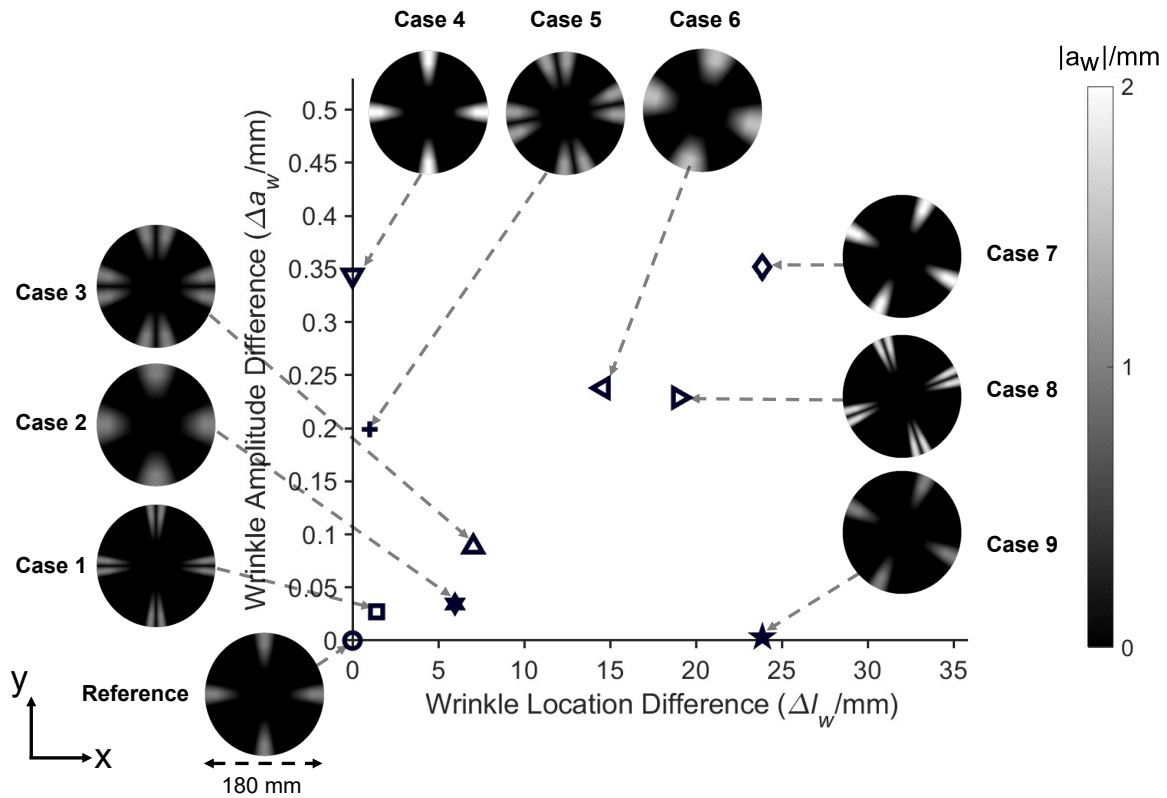
Fig. 4.4 Benchmark study of the wrinkle variability characterisation method using fictitious wrinkle patterns: the wrinkle variability of nine generated wrinkle surfaces (Cases 1-9) are compared against a generated reference wrinkle surface ('Reference') with the calculated wrinkle amplitude differences and wrinkle location differences shown. Each case is specified to be uniquely different to the reference in terms of the wrinkle pattern, amplitude and/or location. The results give context to, but are not directly related to, the experimental results in Figure 4.5. They also validate the decoupling in amplitude and location difference for the proposed method (shown by Cases 4, 7 and 9).

The benchmark results in Figure 4.4 show that amplitude and location differences calculated are fully decoupled by the method which produces variability results that are consistent with what would be expected from observation. The decoupling of Δa_w and Δl_w is confirmed by how the variability data points of the Reference, Cases 4, 7 and 9 (in Figure 4.4), fall at the corners of a rectangle. This confirms that the calculated amplitude and location variability components for the coupled Case 7 are equal to the corresponding components for cases where amplitude (Case 4) or location (Case 9) differences are independently imposed. Additionally, the benchmark

study shows that the calculated Δa_w and Δl_w are consistent even when the compared wrinkle patterns are inherently different. For example, Case 1 with twice the number of wrinkles that are half the size relative to the reference is shown to be very close to the reference in both amplitude and location (near 0 mm). In comparison, for Case 8 where increased amplitude and rotation are imposed relative to the surface in Case 1, larger values of Δa_w and Δl_w of 0.225 mm and 19 mm respectively are observed. However, counter-intuitively, the location difference of Case 3 with no imposed rotation is significantly larger than that of Case 5, which is both higher in amplitude by 0.25 mm and rotated by 10° relative to the reference. This is explained by observing that with this imposed rotation, 4 of the 8 wrinkles in Case 5 are already near-perfectly aligned, meaning no further registration is done between the images.

4.3   Results

4.3.1   Overview of variability results
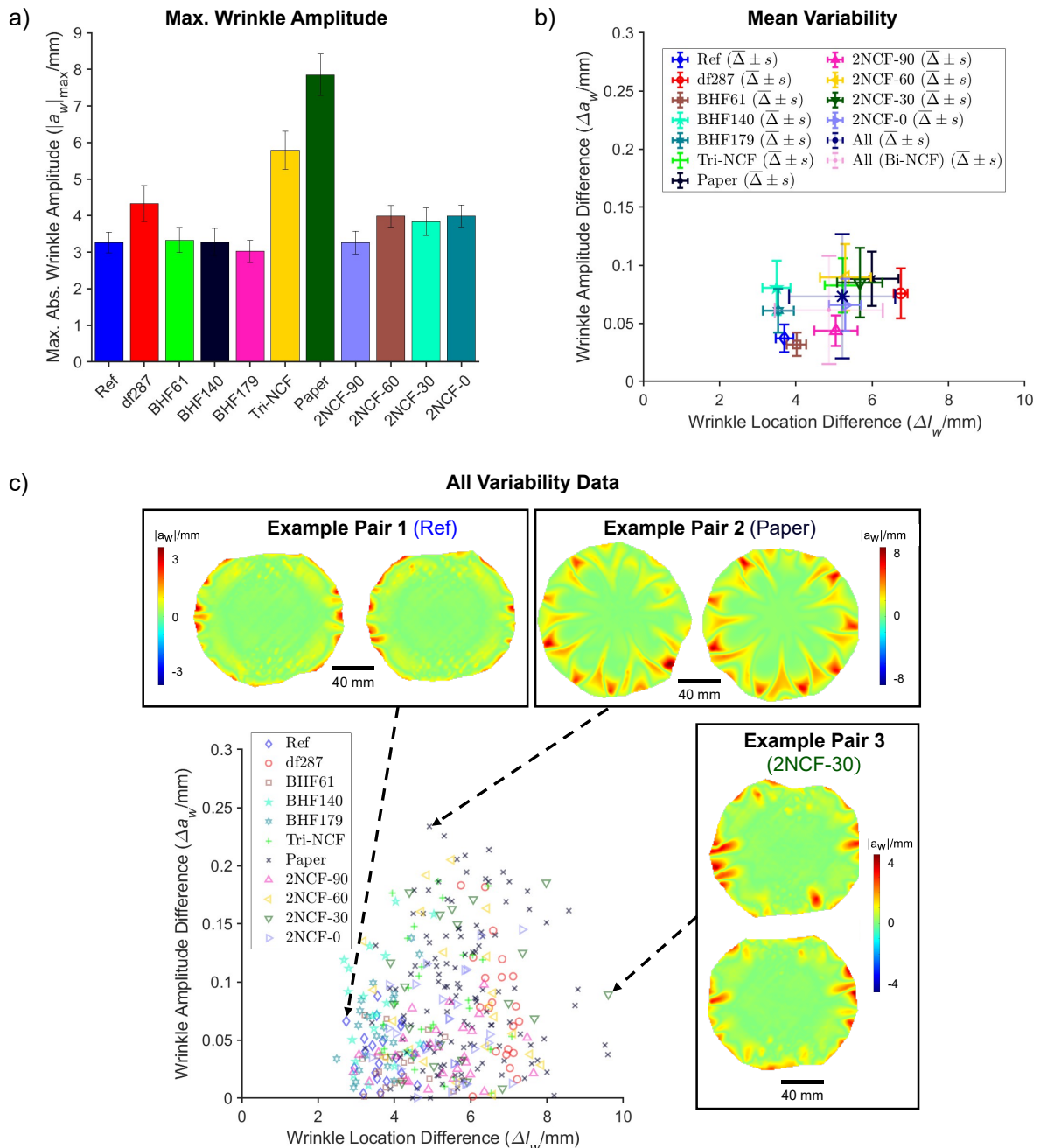
Fig. 4.5 Overview of the experimental variability results for all the tested sample sets: a) the mean values of the maximum absolute wrinkle amplitude recorded within each sample set with the standard deviation shown as error bars, b) the mean ($\overline{\Delta}$) and standard deviation (s) in wrinkle variability for each sample set, including estimates of the mean and standard deviation for all the sample sets combined and just all the biaxial NCF ('Bi-NCF') sample sets (excluding 'Tri-NCF' and paper), and c) all the variability data points measured between samples in each sample set, based on which the mean values in b) are calculated. Additionally, three example wrinkle surface pairs are shown in c) for data points at the extremes of the overall distribution.

To give context to the variability results in Figure 4.5b & c, Figure 4.5a shows the maximum wrinkle amplitudes for each respective sample set, highlighting some considerable differences between them. In particular, the largest wrinkles are observed in the Tri-NCF (5.9 mm) and the paper (7.9 mm) sample sets, while the Bi-NCF sample sets have smaller maximum amplitudes ranging from 3 mm to 4.5 mm.

The mean and the standard deviation of the data points in each sample set are shown in Figure 4.5b, highlighting noticeable differences between sample sets and suggesting that the wrinkle variability in both amplitude and location is sensitive to changes in material, process conditions and layup. From the sample set with the lowest amplitude variability ('BHF61') to the largest ('2NCF-60'), $\overline{\Delta a_w}$ triples from 0.03 mm to 0.09 mm. Similarly, $\overline{\Delta l_w}$ nearly doubles at the extremes from 3.5 mm to 6.7 mm. The overall mean and standard deviation for the variability of all the data points is 0.07 ± 0.05 mm in amplitude and 5.2 ± 1.4 mm in location, while for just the Bi-NCF sample sets the wrinkle amplitude and location variability are 0.06 ± 0.05 mm and 4.8 ± 1.4 mm respectively.

Figure 4.5c shows that the magnitude of wrinkling amplitude variability observed for all sample sets ranges from 0 mm to 0.25 mm while the magnitude of the wrinkle location variability is between 2 mm and 10 mm. Three example surface pairs are shown in Figure 4.5c, which correlate to data points at three extremes of all the data points, highlighting the differences that lead to particular amplitude and location variability measurements. Example 1 from the 'Ref' sample set, shows two wrinkle surfaces that are visually quite similar and lead to relatively low values of Δa_w and Δl_w: 0.067 mm and 2.7 mm respectively. Example 2 from the paper sample set has the largest Δa_w of any two samples at 0.23 mm and this is explained by the large difference in wrinkle amplitudes in the top-left regions of these samples. Example 3 from the '2NCF-30' sample set, in contrast, is the data point with the largest Δl_w, which is visually verified by the two samples having wrinkles in very contrasting locations.

In the subsequent sections, the effect on the variability of specific changes relative to the reference set will be analysed, with the variability data points and mean values for each set shown together in the subsequent figures.

4.3.2 Effect of changing material

As shown in Figure 4.6a, the chosen forming material has a significant effect on wrinkling variability, with the Bi-NCF ('Ref') being the least variable in both amplitude ($\overline{\Delta a_w} = 0.04$ mm) and location ($\overline{\Delta l_w} = 3.7$ mm) out of three materials considered. In contrast, the Tri-NCF and paper are similar in amplitude difference ($\overline{\Delta a_w} = 0.08$ mm and $\overline{\Delta a_w} = 0.09$ mm respectively) while the paper is overall slightly more variable in location (by 0.8 mm) than the Tri-NCF (5.2 mm). The standard deviation in variability is also the highest for the paper ($s_{\Delta a_w} = 0.02$ mm and $s_{\Delta l_w} = 0.7$ mm), which has a significantly larger spread in data points, particularly in comparison to the reference Bi-NCF case. This suggests that the Bi-NCF is more consistent in the level of variability observed between repeated samples compared to the other two materials tested.

Additionally, Figure 4.6b highlights the representative differences in wrinkle patterns for the three materials with the paper wrinkling all the way around the sample circumference, while the Bi-NCF and the Tri-NCF both only form wrinkles in particular regions according to the constraints of their fabric architecture. This could help explain their lower variability compared to the paper. Furthermore, this gives justification for the higher variability in the Tri-NCF among the two NCFs as the Bi-NCF only forms significant wrinkles in two locations while the Tri-NCF forms wrinkles in six separate locations. Finally, as shown in Figure 4.5a, the Bi-NCF overall exhibits significantly smaller wrinkle amplitudes ($|a_w|_{max} = 3.2$ mm) compared to the Tri-NCF ($|a_w|_{max} = 5.9$ mm) and the paper ($|a_w|_{max} = 7.9$ mm) and thus has less potential for variability in wrinkle amplitude.
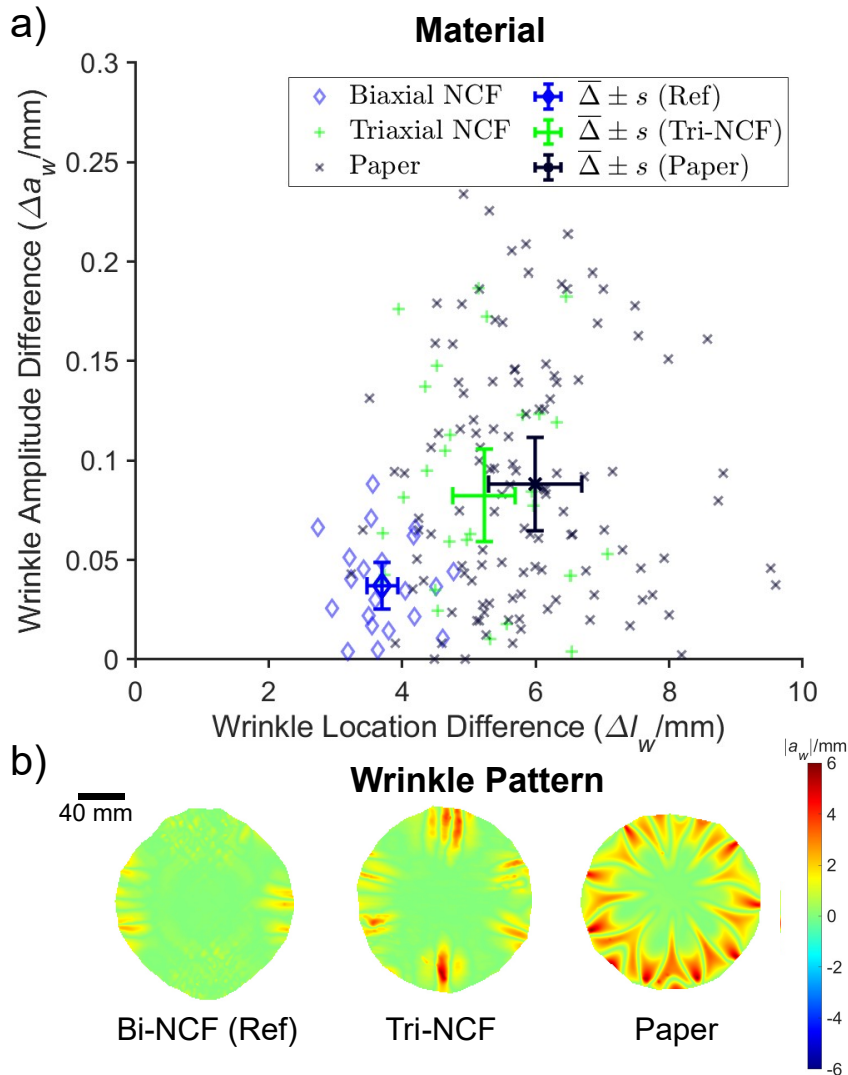
Fig. 4.6 a) The wrinkling variability in terms of amplitude difference (Δa_w) and location difference (Δl_w) for three different materials at the end of preforming: a biaxial NCF ('Ref'), a triaxial NCF and paper. b) The wrinkle amplitude surface shown for each of these materials at 2/3 through the total forming process (punch displacement = 50 mm), showing the distinctly different wrinkle patterns and respective amplitudes. Note that each data point corresponds to the difference between a wrinkle surface pair within the sample set and that $\overline{\Delta} \pm s$ refers to the mean and standard deviation of the sample set in terms of both Δa_w and Δl_w.

4.3.3 Effect of forming parameters

Figure 4.7a shows that increasing the blank holder force (BHF) applied during the preforming process has a negligible effect on the location variability of wrinkling: the mean $\overline{\Delta l_w}$ ranging from 3.5 mm for BHF = 179 N to 4.0 mm for BHF = 61 N. The differences in variability are within the respective uncertainties for all the four sample sets considered.

In terms of amplitude variability, an increase in $\overline{\Delta a_w}$ and a larger uncertainty ($s_{\Delta a_w}$) is observed for the two larger BHF sample sets, compared to the two lower BHF sample sets, suggesting that potentially BHF can increase wrinkle amplitude variability. However, given that the largest variability is for BHF = 140 N rather than BHF = 179 N suggest that there is no clear trend. It is possible that these slight differences could be due to the additional bending moments introduced onto the weight ring (Figure 4.1a) as a result of unbalanced dead-weight loading. Further work is needed to understand whether these differences in variability become more significant at larger BHF.

Increasing the forming diameter (d_f) from 180 mm to 287 mm is shown in Figure 4.7b to have a large effect on the wrinkle location variability. The wrinkle amplitude variability is also affected but, due to greater uncertainty in the wrinkle amplitude variability, it is not clear whether this effect is significant. The mean wrinkle location difference ($\overline{\Delta l_w}$) nearly doubles from 3.7 mm for d_f = 180 mm to 6.7 mm for d_f = 287 mm with a very small uncertainty as measured by $s_{\Delta l_w}$. Similarly, $\overline{\Delta a_w}$ also doubles from 0.04 mm to 0.08 mm respectively but is also associated with a doubling in the standard deviation ($s_{\Delta a_w}$) from 0.01 mm to 0.02 mm. In any case, this result suggests that when the fabric is less constrained during the preforming process, there is greater variation and uncertainty in the amplitude and location of the resultant wrinkle defects, leading to a larger level of unpredictability in the final preforming result. As such, this result justifies the practice of minimising the distance between the tool and the blank holder during forming to constrain the deformation of the fabric.
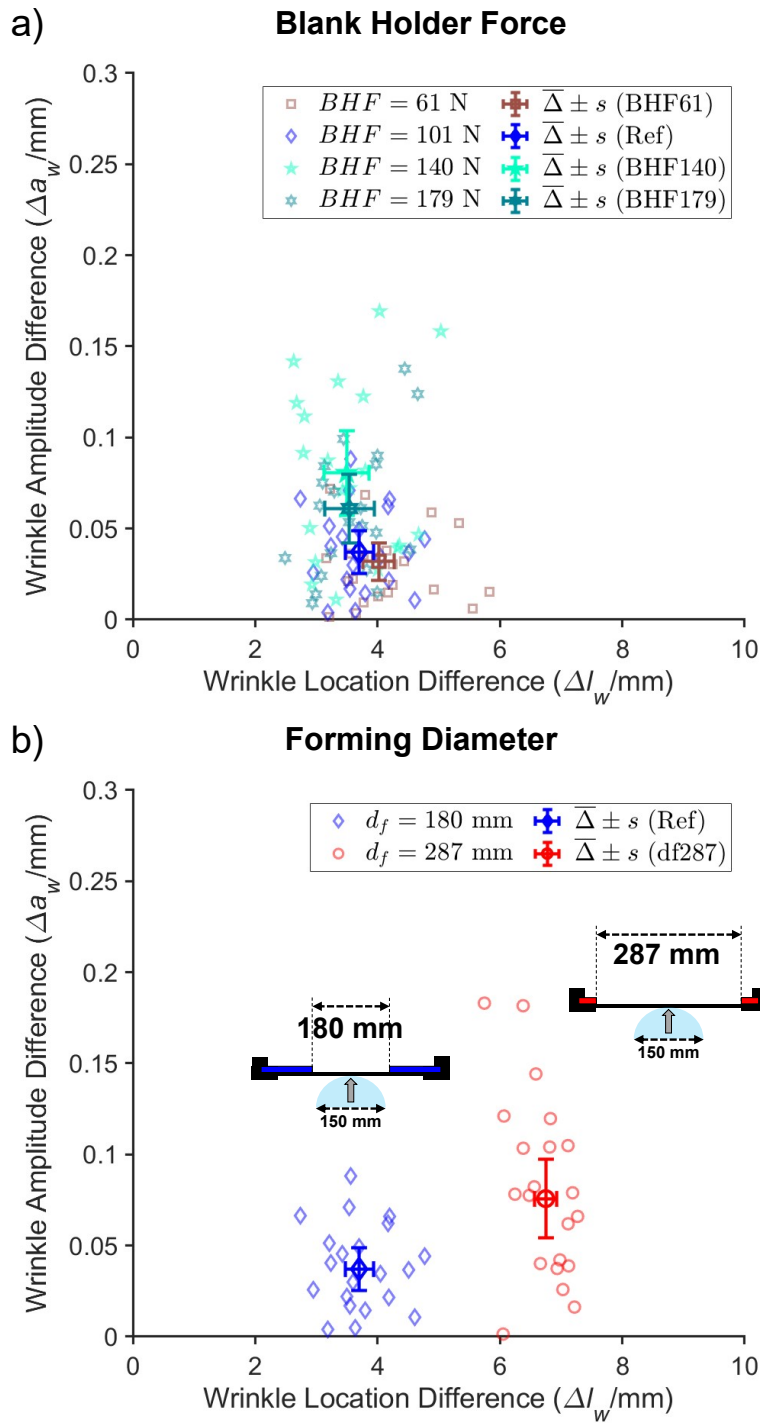
Fig. 4.7 The effect of changing particular preforming process parameters on the wrinkling variability, both in terms amplitude (Δa_w) and location (Δl_w), of a biaxial NCF: a) the effect of changing the blank holder force (BHF) where BHF = 101 N is the reference ('Ref') case, b) the effect of changing the forming diameter (d_f) where $d_f = 180$ mm is the reference case. Note that each data point corresponds to the difference between a wrinkle surface pair within the sample set and that $\overline{\Delta} \pm s$ refers to the mean and standard deviation of the sample set in terms of both Δa_w and Δl_w.

4.3.4   Effect of forming layup

As highlighted in Figure 4.8a, forming two Bi-NCFs simultaneously is more variable in terms of wrinkle location compared to single-NCF forming (the reference 'Ref' case). Comparing the reference case to the two-NCF case (with $\theta_{pc} = 90°$ corresponding to two Bi-NCFs in the same orientation placed atop one another), there is no increase in wrinkle amplitude difference but there is a noticeable increase in the mean wrinkle location difference (by 1.3 mm) and its uncertainty (by 0.4 mm). This suggests that the additional inter-ply friction between the NCF layers has an effect on the variability in the wrinkling defects observed.

In Figure 4.8b, four different ply contact angles (θ_{pc}) for the two-NCF layup are considered, showing that while location variability is similar for all these two-NCF sample sets (between $\overline{\Delta l_w} = 5 - 5.7$ mm with $s_{\Delta l_w}$ up to 0.7 mm), the mean wrinkle amplitude difference is largest for $\theta_{pc} = 30°$ & $60°$ ($\overline{\Delta a_w} = 0.09$ mm for both), which is more than double that of the reference single-NCF case under the same conditions. However, once the bottom ply is rotated such that the contacting plies are initially aligned ($\theta_{pc} = 0°$), the wrinkling amplitude variability drops but is still higher than for $\theta_{pc} = 90°$ and for the reference. This highlights that the wrinkle amplitude variability that results from this preforming rig is influenced by the particular layup of the fabric plies. This observation could be due to the additional uncertainty in manually laying up NCFs at angles that are not perpendicular or parallel to each other (Table 4.3). However, it is more likely to be due to the inter-ply friction, which varies depending on the relative tow orientations and thus highly non-uniform and subject to local variability [138, 149]. Additionally, this inter-ply friction has been shown to be strongly linked to additional wrinkling modes during multi-ply forming, thus contributing to their variability [84].
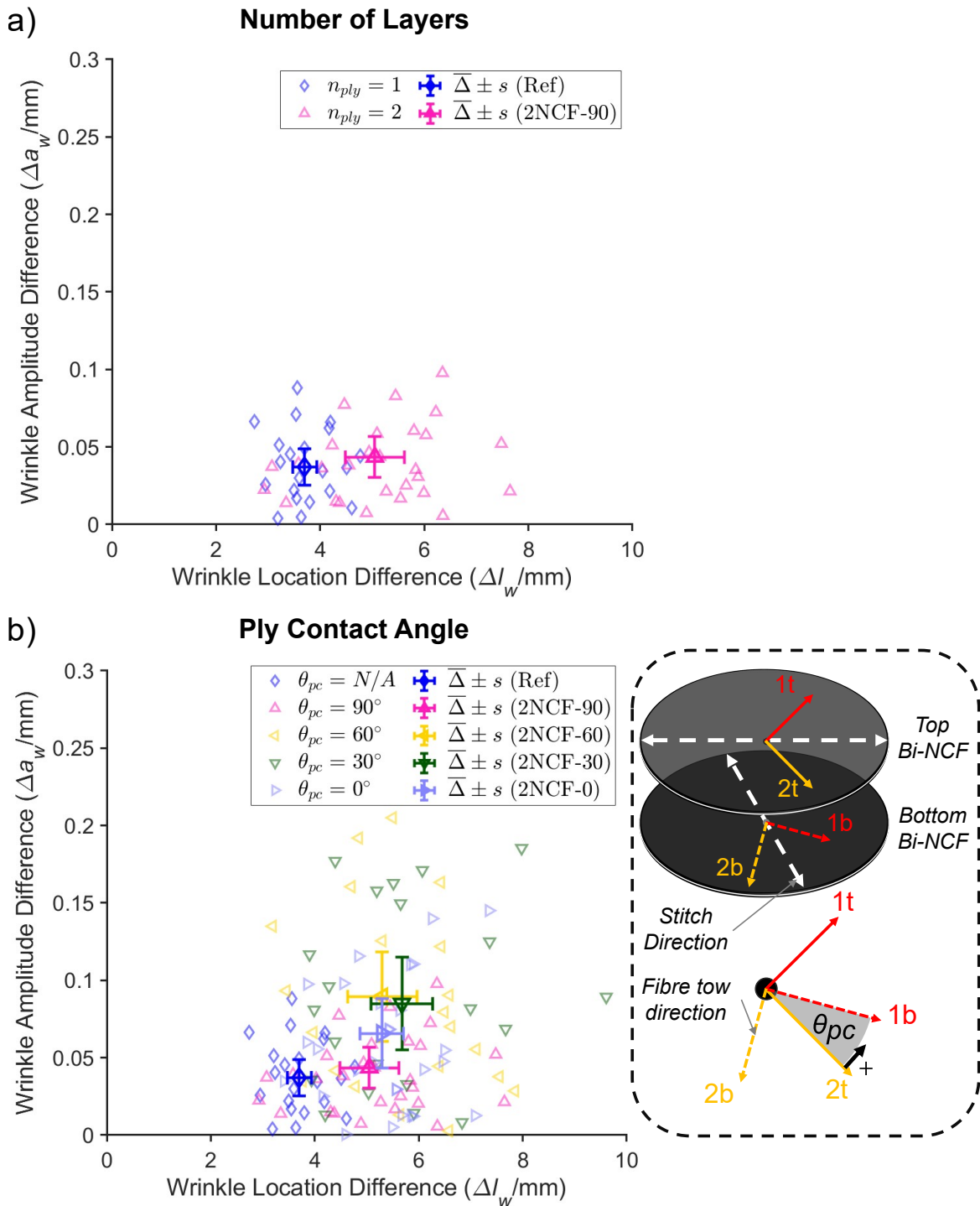
Fig. 4.8 The effect of changing the preforming layup on the wrinkling variability, both in terms amplitude (Δa_w) and location (Δl_w), of a biaxial NCF: a) the effect of changing the number of plies in the layup (n_{ply}) where $n_{ply} = 1$ is the reference ('Ref') case, b) the effect of changing the forming layup, measured in terms of the ply contact angle (θ_{pc}) for two-NCF forming, with four different θ_{pc} (90°, 60°, 30° and 0°) tested with respect to the single-ply ('Ref') reference. Note that each data point corresponds to the difference between a wrinkle surface pair within the sample set and that $\overline{\Delta} \pm s$ refers to the mean and standard deviation of the sample set in terms of both Δa_w and Δl_w.

4.3.5   Statistical significance of differences between sample sets

As an evaluation of the significance of the changes in wrinkling variability due to the factors investigated, the one-way analyses of variance (ANOVA1) and multiple comparison tests in Figure 4.9 present differing results for Δa_w and Δl_w. Only three (shown in red in Figure 4.9c) out of the 10 sample sets are statistically different in wrinkle amplitude difference (Δa_w) compared to the reference sample set at a 95% confidence level. In comparison, seven of the sample sets (shown in red in Figure 4.9cd) lead to a statistically significant change in wrinkle location difference (Δl_w) relative to the reference. The only three cases that lead to both a significant change in Δa_w and Δl_w are the two alternative materials (Tri-NCF and paper) as well as the two-NCF case with a $\theta_{pc} = 30°$ ('2NCF-30'). It is noted that the '2NCF-60' sample set is also very close to being statistically different in both amplitude and location but is not significantly different in amplitude to a 95% confidence level, only 92% ($p = 0.08$). The two-NCF cases with the tows either perpendicular ('2NCF-90') or perpendicular ('2NCF-0') are significantly different to the reference only in location but not in amplitude, suggesting that the 'off-axis' cases are more critical for variability. At a 95% confidence level, the results also show that BHF has no significant effect on either the amplitude variability or the location variability of wrinkles. Finally, the results show that while increasing d_f results in the largest and most significant change in wrinkle location relative to the reference out of all the sample sets, the change in wrinkle amplitude difference is not significant at a 95% confidence level ($p = 0.16$). It is important to note that an underlying assumption of the ANOVA analysis is that the variances in each data set are equal and although this criterion is not explicitly met with some sets exhibiting larger variance than others (Figure 4.5b), the differences are deemed not to be significant enough to affect the inferences drawn regarding statistical significance.
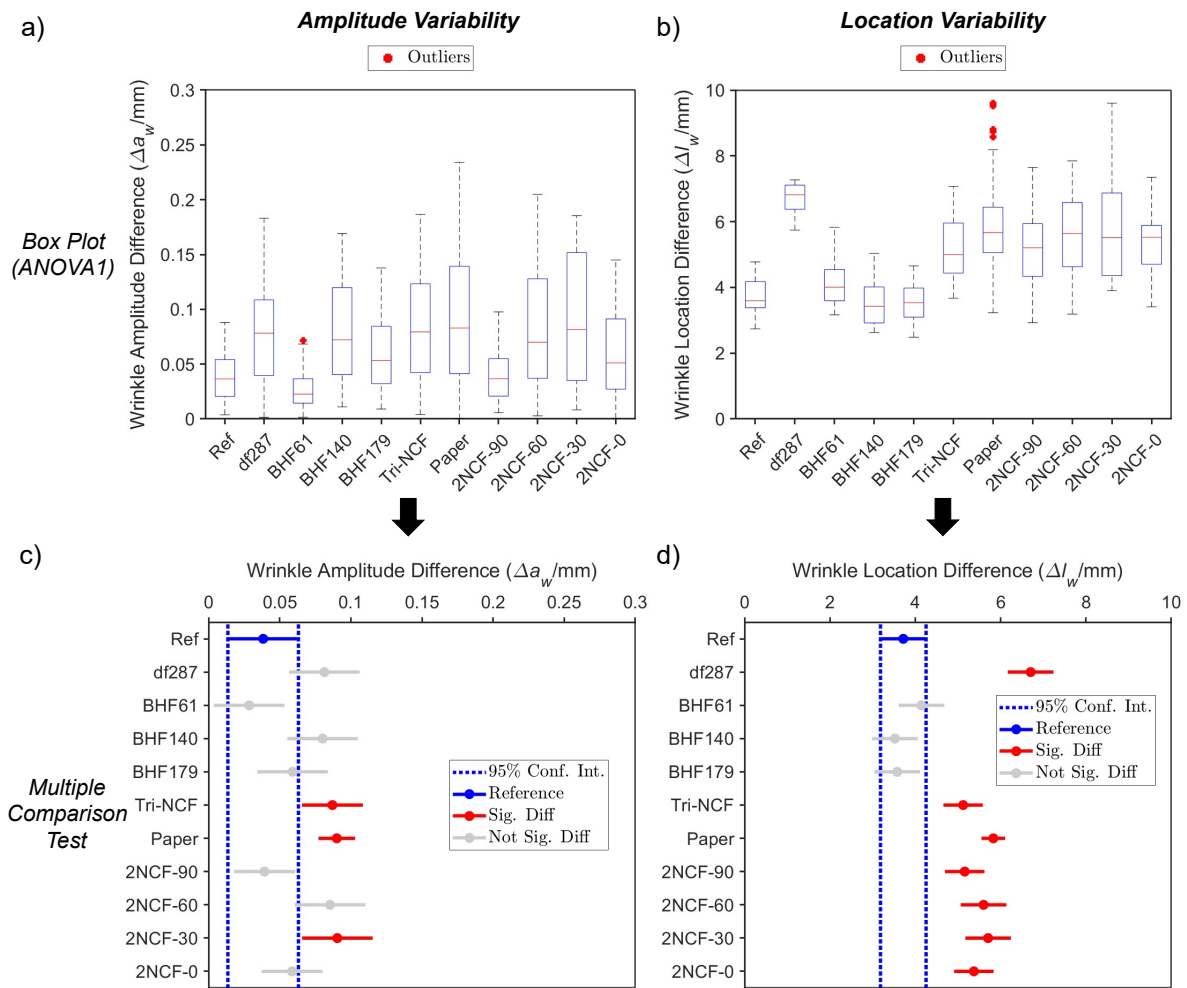
Fig. 4.9 Analysis of the statistical significance of the differences in variability between the reference ('Ref') set and the other sample sets: a) box plot acquired through one-way analysis of variance (ANOVA1) for the wrinkle amplitude difference (Δa_w) for all the surfaces pairs in each of the sample sets (outliers shown in red), b) box plot acquired through one-way analysis of variance (ANOVA1) for the wrinkle location difference (Δl_w) for all the surfaces pairs in each of the sample sets (outliers shown in red), c) multiple comparison test for the results from a) showing the statistical significance of the mean values for each of the sample sets relative to the reference (in blue), and d) multiple comparison test for the results from b) showing the statistical significance of the mean values for each of the sample sets relative to the reference (in blue). Data points in red correspond to a statistically significant difference (at a 95% confidence interval) compared to the reference, while gray data points are not significant.

4.4   Discussion

4.4.1   Wrinkle amplitude variability and wrinkle location variability

The experimental variability observed between samples (Figure 4.5) is relatively small, suggesting that the wrinkling variability for the forming process is not large enough to fundamentally change the wrinkling behaviour observed between samples. The relatively small variability is shown by the fact that the $\overline{\Delta a_w}$ and $\overline{\Delta l_w}$ for all experimental cases are 0.07 mm and 5.2 mm (Figure 4.5b) respectively, and therefore comparable to Cases 1-3 from the benchmark study (Figure 4.4), which are only different to the reference in their wrinkle patterns. In contrast, the experimental $\overline{\Delta a_w}$ and $\overline{\Delta l_w}$ are much less than the calculated variability for Cases 4-9 (Figure 4.4) which have significant amplitude and/or location differences imposed relative to the reference.

Nevertheless, the measured variability in wrinkling is large enough to suggest that it should be taken into account during industrial production, particularly in terms of the variation in wrinkle location. While the mean wrinkle amplitude difference for all the Bi-NCF cases is only 0.06 mm, relative to a mean $|a_w|_{max}$ of 4.3 mm, the mean wrinkle location difference is 4.8 mm, which represents a significant shift in location over a hemisphere tool of radius 75 mm (Figure 4.5). Particularly for the manufacturing of complex components where wrinkles cannot be avoided and significant wrinkles are directed into a particular location, such a level of variability could potentially be detrimental to the final component.

Importantly, the study also showed that the level of variability observed is influenced by the particular material, forming process and the layup configuration, leading to significant changes in variability, particularly in terms of wrinkle location. Relative to the reference case for a single Bi-NCF, Figure 4.9 shows that the wrinkle location difference (Δl_w) is significantly affected by changes in forming diameter, material and additional NCFs in the layup, regardless of the relative orientation of the plies in the layup. Thus this wrinkle location variability is highly sensitive to changes in the underlying process and should be carefully characterised for particular preforming setups or processes. In contrast, the wrinkle amplitude difference (Δa_w) is more constant across the various cases tested with only the Tri-NCF, the paper and one of the multi-NCF forming cases resulting in a significantly larger Δa_w when compared to the reference (Figure 4.9). Thus it is suggested that, at least for NCFs, the wrinkle amplitude is less sensitive to variability than the wrinkle location so it is more important to characterise the severity of the wrinkling and potential changes in location rather than its amplitude variability.

While the results for variability in this study are presented in absolute terms (in millimetres), in certain circumstances it could be useful to normalise the wrinkle amplitude difference and wrinkle location difference and express them as a percentage. Doing this for all the Bi-NCF cases tested (excluding the Tri-NCF and the paper) and normalising the amplitude difference (Δa_w) relative to the maximum wrinkle amplitude in each sample set (Figure 4.5c), results in a mean relative amplitude difference of 1.6%. Similarly for the wrinkle location difference, if normalised relative to the hemispherical punch radius of 75 mm, this results in a mean relative location difference for all the NCF cases of 6.3%. Normalisation is beneficial to compare the relative significance of the variations in amplitude and location, which again suggests that the location variability is more significant.

4.4.2 Factors affecting preforming variability

The particular forming material affects the resultant preforming variability significantly (Figure 4.9) and the differences in variability between the materials tested are found to be due to their underlying material architecture. This is evident from the Bi-NCF forming, which results in less wrinkling variability (Figure 4.6a) and with wrinkles smaller and constrained into fewer locations on the material surface (Figure 4.6b) compared to the Tri-NCF. Chapter 3 showed that the two wrinkling regions of the Bi-NCF correspond to the positive shear regions and are a direct consequence of the NCF fabric architecture. In contrast, due to the additional tow layer and inter-tow friction, the Tri-NCF has significantly larger wrinkles in six symmetric locations (Figure 4.6b), still correlated to its architecture (wrinkle locations are approximately perpendicular to its tow directions ($45°/0°/-45°$)). As a result, the Tri-NCF has greater variability than the Bi-NCF. However, it has lower wrinkle location variability than the paper, which has no distinctly defined fibre architecture and thus wrinkles all around the circumference of the sample, resulting in a larger $\overline{\Delta l_w}$ and a larger associated uncertainty ($s_{\Delta l_w}$) (Figure 4.6).

The results show that there is a significant contribution to wrinkling variability from the preforming process itself, that cannot be accounted for by characterising just the material variability in the produced roll, as has been done previously by e.g. Skordos and Sutcliffe [112]. Given that the biaxial and triaxial fabrics tested are produced in the same plant, it is likely that their production tolerances in terms of global material variability are similar (Table 4.1). Thus their statistically significant differences in wrinkle amplitude and location variability (Figure 4.9d) are due to their differences in deformation (dictated by their fabric architecture), becoming evident at the preforming stage.

The composite component layup also has a significant effect on preforming variability, while it is also expected that the component geometry would also have an influence on variability. Figure 4.8 indicates clearly that the addition of a second ply has an effect on preforming variability and this effect becomes more significant for particular ply contact angles ($\theta_{pc} = 30°$ and 60°), suggesting that the layup design, which dictates the relative orientation of the plies, has a significant influence on the variability observed at the preforming stage. Thus this result suggests that when textile composite layups are designed, perpendicularly contacting plies ($\theta_{pc} = 90°$) should be prioritised as these result in the lowest amount of wrinkling variability and thus most confidence in the repeatability of the manufacturing process. However, further work is needed to concretise this finding for alternative fabrics and for other common ply contact angles such as $\theta_{pc} = 45°$.

In terms of preforming parameters, the results suggest certain parameters have a greater effect on wrinkling variability than others. This is demonstrated by how the effect of blank holder force on variability is found to be negligible (Figure 4.7a and Figure 4.9). In contrast, it is shown that increasing the forming diameter from 180 mm to 287 mm results in a significant increase in wrinkle location variability (Figure 4.7b and Figure 4.9). However, the latter case of $d_f = 287$ mm represents a somewhat unrealistic forming situation where there is a large 68.5 mm gap between the tool and the blank holder and this increase in Δl_w is found to be linearly proportional to the increase in this gap. Therefore, this result supports the established practice of minimising this gap in industrial preforming processes.

4.4.3   Optimisation for minimal variability

To minimise the variability in wrinkling behaviour of NCFs during forming and make it more predictable, this study suggests that NCFs with simpler architectures should be prioritised (fewer tow layers), the forming diameter should be minimised relative to the geometry, and the contacting tow layers should be laid up parallel or orthogonal where possible. Following these approaches allows the unpredictability in wrinkling variability to be minimised as much as possible, allowing for localised approaches for wrinkling mitigation to be more successfully implemented. Localised approaches have the advantage over global approaches (e.g. modifying the global BHF) of being able to target just the fabric regions in which defects are likely to occur, thus improving the effectiveness of the mitigation and reducing the chances of unwanted effects. Examples of such approaches for local wrinkling mitigation include local resin patches [106], clamping of individual layers [102], springs to locally vary tension around the blank [104] and stitch removal [63], which could all be improved via minimising wrinkling variability.

4.4.4 Implications for wrinkle mitigation with realistic composite layups

The results of this study provide some insights into what the implications are for mitigating wrinkling and its variability during the manufacturing of realistic composite components using LCM processes. The wrinkle locations generated for a single layer of Bi-NCF are relatively low in variability compared to the paper. However, as shown for a two-NCF layup (Figure 4.8), this variability can be increased with additional NCF layers, with wrinkling becoming more prominent due to the inter-ply frictional effects [84, 83] and thus more prone to variability, as the local frictional conditions can vary greatly within the layup. This variation in frictional conditions is due to the inter-ply friction being highly sensitive to tow orientation [139] and level of intra-ply shear [103], which both become more non-uniform during the preforming process. Thus, further study is needed to understand how this wrinkling variability correlates for more industrially relevant, thicker layups and to better understand the effects of frictional conditions on variability, with a view to understanding how this variability could be minimised to achieve repeatable results.

Considering industrial-level manufacturing conditions where multi-NCF layups are required together with often complex geometries, this study shows that forming in these conditions is likely to cause significant wrinkling variability and result in production issues. In particular, the results suggest that layups where the contacting tows are neither parallel nor perpendicular are more variable in wrinkle amplitude (Figure 4.8b). Thus, given the typical layup design practices (and component strength requirements) that often require tows to laid up at $\theta_{pc} = 45°$, it is likely that the increase in variability from these layups need to be addressed using further process adjustments. However, the compounding effect of the different variables has not been studied here and it is also not clear how the variability would be affected by the addition of more NCFs to the layup but it is suggested that this will likely create further variability. Furthermore, each preforming process will have its own additional sources of variability that need to be taken into account (Table 4.3). Finally, the effect of component geometry on wrinkling variability should also be investigated given the wide range of geometries that are manufactured in industry and that the tool geometry has already been shown to have a critical effect on wrinkle patterns and their severity (Chapter 3). Thus further work is needed to understand the exhaustive implications for industrial preforming.

4.4.5 Implications for process simulation

Analysing the results presented in this study for wrinkling variability during preforming suggests that any process simulation attempting to capture the wrinkling behaviour of fabrics

needs to incorporate some variability within the model, in order to account for the preforming variability. Stochastic process models incorporate material variability through a characterisation of the as-produced fabric that is then defined within a Monte Carlo scheme, with Skordos and Sutcliffe [112] concluding that the measured geometric variability has a significant effect on the variability of wrinkling due to tow buckling, based on simulating local wrinkling strain. However, current models that attempt to capture the true shape of fabrics after preforming [39, 63, 150], have thus far not incorporated any variability within their models, with the exception of [76]. This is despite it being clear from the work by Thompson et al. [39] that their predicted wrinkle paths do not exactly align with those achieved from experimental testing. Incorporating a level of variability or uncertainty in these models would allow for more confidence in the model's predictions relative to experimental results. In order to improve upon this, the previous stochastic characterisation of fibre tow angles could be extended to incorporate the dimensional and spatial variability of the key parameters associated with the material and the forming process into existing forming models.

4.4.6   Evaluation of variability characterisation method

The proposed method for variability characterisation has certain strengths that make it useful for analysing variability in a wide variety of scenarios. In particular, it allows for the characterisation of defect amplitude difference and location difference independently (Figure 4.4), making the method rather robust and widely applicable. Furthermore, given that the inputs for variability calculation are grayscale images representing spatial distributions of data, it is generalisable for use in a variety of contexts. These include other forming cases, other full-field measurement methods, other sources of data and other defect types. As a result, this method has a number of potential applications beyond the specific focus of this study.

Firstly, is envisioned that this method can be extended to consider the variability in other defects or surface parameters that can be measured during the preforming process of fabrics. These include the shear angle, fibre compression, mesoscale wrinkles etc. On this basis, such a method could become a benchmarking tool for assessing the repeatability of a particular preforming setup by quantifying the consistency of repeated tests. This is particularly important for textile reinforcements, for which previous benchmarking has shown that results from shear characterisation tests across institutions can vary significantly for the same material [151] due to variations in equipment.

Secondly, the method can be equally applied when using alternative full-field measurement methods such as 'shape-from-focus' [25] or structured white light scanning [63]. Furthermore,

the characterisation method can be applied to other forming processes such as double diaphragm forming or matched tool forming, and to consider the effect of tool geometry on wrinkling variability.

Finally, the calculation approach could be applied to data from finite element (FE) simulations of the preforming process, allowing investigation of the sensitivity of forming models in terms of the resultant wrinkles. The latest forming models that include non-linear bending stiffness of NCFs have been shown to be able to accurately replicate fabric wrinkling behaviour [63] and additionally Zimmerling et al. [152] have shown how FE forming results can be represented as 2D grayscale images [152]. Thus such an approach holds a lot of promise to analyse the robustness and sensitivity of forming results from simulations.

Despite the advantages and potential of the proposed method, it has certain limitations that should be discussed. Firstly, some error in the calculated Δa_w could occur in cases where wrinkles are at significantly different locations. This is because the pixelated image approximations of the surface data change based on the orientation of the surface and so can result in unexpected differences. From testing on the benchmark reference image (Figure 4.4), this can result in errors in Δa_w of up to 15% from the expected result. Thus for wrinkle surfaces that are significantly different in terms of where the wrinkles are located, it is important to apply a rigid registration to align the images before the amplitude difference is calculated. This was done in the benchmark study (Figure 4.4) where large rigid transformations were imposed. While for the experimental cases tested, it was found that this rigid registration made no difference.

Secondly, although the method is generalisable to any surface data, to achieve accurate characterisation results, it is necessary that the image registration parameters are optimised for each particular set of images. Particularly for the calculation of location difference, this ensures suitable displacement fields and thus accurate values for Δl_w that actually correspond to the mean distance to map one set of wrinkles to the other.

Additionally, the location difference based on non-rigid registrations has a few potential limitations. As highlighted by Case 3 and Case 5 of the benchmark study (Figure 4.4), in certain cases where the surfaces are different in terms of the numbers of wrinkles, the registration will not give the expected result.

Finally, from analysis using the benchmark cases, it was found that, if the prescribed difference in wrinkle locations is too large (beyond an imposed pattern rotation of 25°), the non-rigid registration fails to properly register the two images, resulting in an incorrect displacement field and thus an unreliable value for Δl_w. The limit of 25° was found to be consistent for a variety of generated wrinkle surfaces. This suggests that the wrinkle location difference method

becomes less accurate for cases where the two wrinkle surfaces are highly different in location, thus potentially limiting it to surfaces with some degree of similarity.

4.4.7 Challenges of variability characterisation

While this study highlights the importance of considering variability within the composite manufacturing process, it also highlights the associated difficulties with investigating variability. Firstly, variability in wrinkling is particularly sensitive to the specific material and the forming process considered, and any changes in these could have a consequential effect on the variability. Thus it makes comparisons between similar investigations difficult and means that variability is often considered in qualitative [17], rather than quantitative terms [153].

Additionally, the particular experimental method used to capture the shape of the preforming fabric can create potential limitations in terms of the accuracy of the variability data and its usefulness. The limitations of the 3D-DIC approach for wrinkle characterisation have previously been analysed (Chapter 3) and particularly for variability analysis, it is limited because it cannot capture the entire fabric shape at the end of forming. Thus, alternative surface capturing methods applied at the end of forming could provide a more thorough characterisation of the whole wrinkled surface.

4.5 Conclusions

From the results of this chapter, the following conclusions can be drawn:

- A novel image-based analysis method is able to characterise the variability in both wrinkle amplitude and wrinkle location for fabrics at the end of preforming.

- The material architecture and the specific layup are shown to have a significant influence on the wrinkling variability, both in terms of amplitude and location.

- Increasing the gap between the blank holder and the tool geometry significantly increases the absolute wrinkle location variability in a biaxial NCF.

- Increasing the fibre tow layers in the fabric architecture of an NCF is shown to increase the variability in amplitude and location of the resultant wrinkles in the preform.

- The wrinkling variability in both amplitude and location of a biaxial NCF is shown to be lower compared to paper formed under the same conditions.

- Forming two biaxial NCF layers is shown to be statistically more variable in wrinkling than a single biaxial NCF formed under the same conditions.

- The proposed variability characterisation method has the potential to be applied as a benchmarking tool to characterise process defects in a wide variety of scenarios.

Chapter 5

Rapid prediction of fabric wrinkling for a given tool geometry

5.1 Introduction

The recent development of deep learning networks called 'fully convolutional networks' (FCNs) have considerable potential for use as surrogate models in improving aspects of composites manufacturing, including for the mitigation of wrinkling defects during the preforming process.

As previously discussed in Chapter 2, a key factor affecting the presence of wrinkling defects in the resultant preform is the geometrical features of the tool over which the fabric layup is formed [17] but this factor has also been largely overlooked in the literature in favour of investigating factors that can be modified at the preforming process stage. However, it has been noted that the geometrically-induced wrinkling cannot be mitigated solely through changes to the preforming process and conditions [154]. Hence, it is critical that design for manufacture principles are implemented into the composite component design process along with the development of functional tools that can predict the effect on the manufactured component of particular changes to the geometry.

Furthermore, as summarised in Chapter 2, existing simulation tools for predicting the formability of a fabric layup over a given geometry are not suitable for design optimisation. They are either too simplistic to accurately capture the occurrence of wrinkles or too computationally costly to produce the rapid results necessary for optimisation purposes.

Deep learning surrogate models offer an attractive solution that could, in theory, provide the low computational cost of kinematic or simplistic mechanistic models while maintaining a level of accuracy comparable to the 'parent' model that it was trained on (Figure 5.1). Thus

such a model could be feasibly used for the iterative optimisation of a preforming process for minimal wrinkling defects.
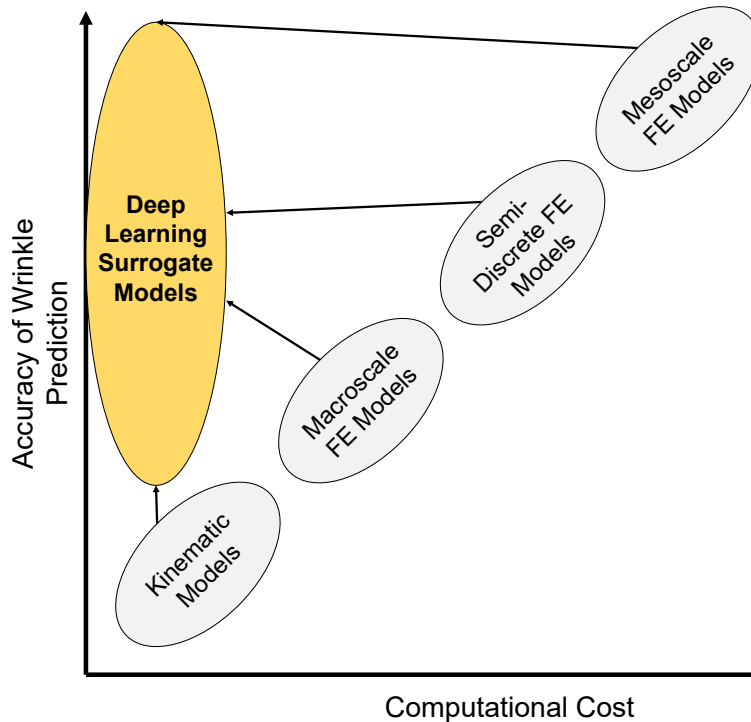
Fig. 5.1 A schematic of the accuracy of wrinkle prediction versus the computational cost for various modelling approaches. The grey models represent the conventional modelling approaches that require a higher computational cost to achieve higher accuracy. In contrast, the deep learning surrogate models (in yellow), have the potential of achieving very high accuracy with low computational cost.

While a surrogate model can be trained to make predictions for any set of variables, the aforementioned gap in understanding regarding the effect of tool geometry on wrinkling motivates the development of a surrogate model for predicting the wrinkling behaviour for a given tool geometry. This is because the model development process also provides an avenue for gaining further insight into the relationship between the component geometry and the resultant wrinkle after preforming.

As a result of the above, the specific objectives of this chapter are the following:

- To develop a deep learning surrogate model to rapidly predict the wrinkling severity for a given convex tool geometry during double diaphragm forming for a biaxial NCF.

- Based on the simulated data used to develop the surrogate model, to investigate the relationship between geometrical characteristics of the tool geometry and the severity of wrinkling.

The chapter is arranged as follows: firstly, a short literature review, that extends upon Chapter 2, is presented to provide context to deep learning neural networks and surrogate models, and to further motivate the objectives. Secondly, the method for developing the deep learning surrogate model and for assessing the effect of tool geometry is outlined, before the results of the investigation are presented. The chapter ends with a discussion of the results and some conclusions.

5.2 Literature review: deep learning neural networks

5.2.1 Background to neural networks

Artificial neural networks (ANN) are computer-based networks made up of sequentially connected neurons that are inspired by the workings of the human brain. They typically fit within the domain of deep learning, which is a subfield of machine learning, all of which sits within the larger domain of artificial intelligence [155]. ANNs consist of multiple layers with an input layer, output layer and a number of hidden layers whose weights are progressively optimised during the training of the network such that they learn the relationship between given inputs and outputs. This represents a type of *supervised learning* where the network is given a particular output and is used to solve regression or classification problems, whereas in *unsupervised learning* only input data is provided and this is used to solve association and clustering problems. The key difference between deep learning and machine learning is that in deep learning the features to be extracted from the input data are not predefined by the user but learned by the algorithm, thus making it more powerful than machine learning tools for solving complex problems where the significant features are not self-evident [156]. Deep learning ANNs differ in structure from machine learning ANNs by having more than one hidden layer, with typically a larger number of layers resulting in higher predictive performance. For an examination of the different types of machine learning beyond ANNs, refer to the review by Chauhan and Singh [157].

Deep convolutional neural networks (CNNs) differ primarily from other ANNs by being designed to be used with image-based data, as first proposed by LeCun et al. [158] in 1998. CNNs typically consist of successive convolution layers (identifying key features in data), pooling layers (reducing data dimensions based on key features) in various arrangements

and end with a fully connected layer that provides the probability of the given input image belonging to each of the pre-defined set of classes [155]. The layers of the CNN are sometimes collectively referred to as an 'encoder' (Figure 5.2). A key feature of CNNs is that with each successive network layer the resolution (length and height) of the feature maps gets smaller as the input images are broken down into finer features with the resulting output (after the classifier - Figure 5.2) being a scalar from which the most probable class can be inferred. CNNs have found a multitude of applications with their most common use being for image classification [159]: classifying images into particular classes. For example in Figure 5.2, the CNN is able to identify that the input image is likely to contain a dog or a cat.
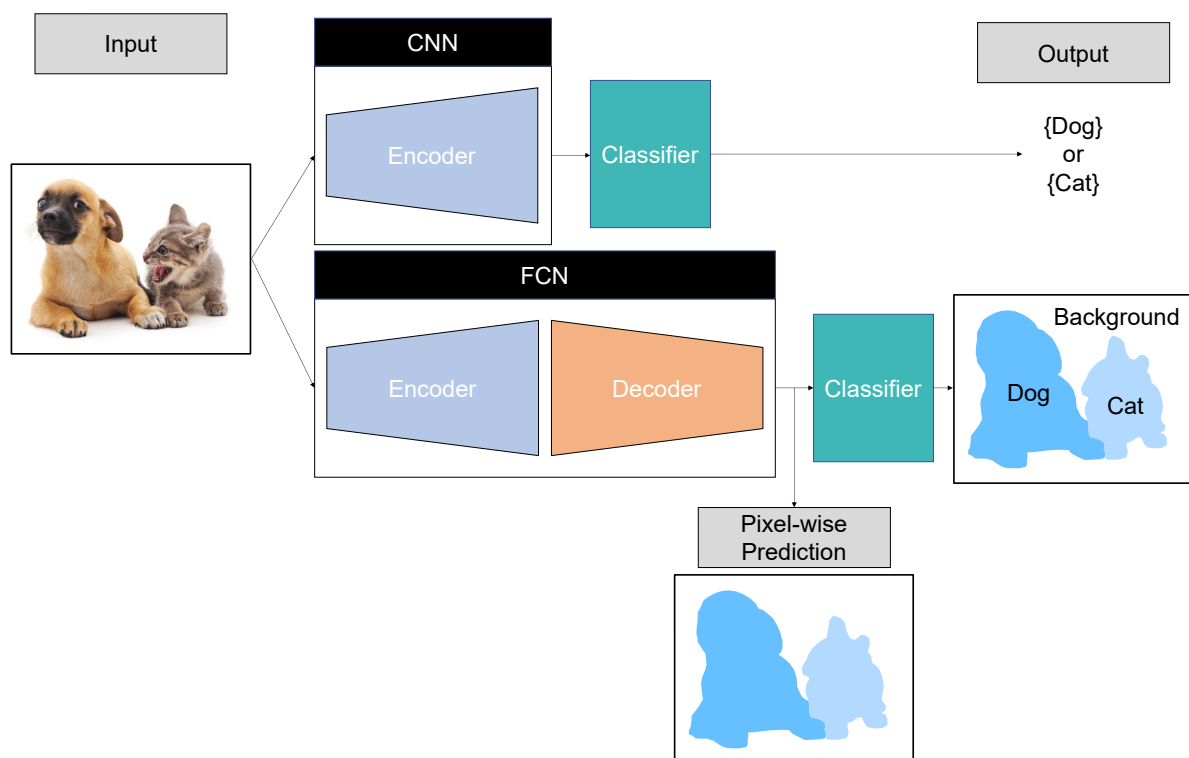
Fig. 5.2 A diagram highlighting the differences in structure and utility between a convolutional neural network (CNN) and a fully convolutional network (FCN). Both networks are fed an input image of a dog and a cat, with the CNN being able to associate the image with the labels 'Dog' or 'Cat' (image classification) while the FCN can locate and label the positions of the dog and the cat within the image (image segmentation). Images adapted from [160].

Fully convolutional networks (FCNs) are an extension of CNNs that have images at both the input and the output (Figure 5.2) and were first introduced by Long et al. [161] in 2015. In addition to the initial 'encoder' part from the CNN, these networks include an additional 'decoder' (also called the 'upscaling' or the 'deconvolutional' phase). Within the decoder,

the initial operations are reversed (often mirrored) to then obtain equal-sized image(s) at the output of the network [162]. As a result, there is typically a one-to-one connection between the input image pixels and the output image pixels [163]. The input images are first broken down into high-level feature representations before the decoder interprets these features to generate a pixel-wise prediction at the output. Several variants of FCNs have been proposed and these will be discussed in Subsection 5.2.2. These networks have been particularly used for image segmentation [164]: to divide images into patches of particular features. For example in Figure 5.2, the FCN is able to identify the outlines of the dog and the cat from the background of the image. This image segmentation capability of FCNs has various real life engineering applications, including for improving the capabilities of autonomous vehicles for detecting features on the road based on video footage [165]. When used without a classifier (Figure 5.2), the pixel-wise predictions of FCNs have also been shown to be particularly suited for use as image-based surrogate models that learn the phenomenological relationships between pairs of (input, output) images that have been derived from a physically relevant model [152, 166]. Based on this capability, an FCN-based surrogate model is developed for wrinkling prediction in this chapter.

5.2.2   Development of FCNs for image segmentation

Since their initial introduction in 2015 [161], various FCN architectures have been proposed, each attempting to improve upon what came previously. The original FCN by Long et al. [161] was the first work to convert an existing CNN structure for pixel-wise prediction and thus it opened up a whole new avenue of possibilities for deep learning networks and their applications. It also introduced skip connections into the network for improved predictive capabilities. However, this initial network lacked any real deconvolution (transposed convolution) layers, making use of an upsampling layer instead, and thus its performance for image segmentation was insufficient [159]. Noh et al. [167] improved upon this by developing the 'DeconvNet', an FCN that added a deconvolutional phase, made up of deconvolution layers and unpooling layers, to the end of an existing CNN ('VGG16 - [168]), creating the mirrored structure that is now a common feature of most FCNs. Recently, a less memory-intensive version of [167] was developed by Badrinarayanan et al. [169] and called 'SegNet'. This network removes the superfluous fully connected layers between the convolutional and deconvolutional phase of [167], thus reducing the number of trainable parameters by 90% and thus improving model efficiency.

An alternative mirrored network structure that became very popular and spawned various iterations, is the 'UNet', developed by Ronneberger et al. [170]. This network consists of a mirrored convolutional-deconvolutional network similar to [167] but additionally contains the skip connections from [161], that transmit higher level context information between the convolution and deconvolution layers, thus resulting in a 'U' shaped network structure. This network has inspired a number of modified and more complex networks including the 'ResUNet' [171], the 'ResUNet++' [172], the 'ResUNet-a' [173] and the 'Res-SE-UNet' [166]. The key addition in all of these networks is the addition of residual ('Res') units to create a mapping between the inputs and outputs of each convolution/deconvolution layer. These residual units have been shown to improve learning capability in certain cases, particularly for deeper networks [174].

While these more advanced and deeper FCNs have been developed in recent years for the task of image segmentation, it does not necessarily mean that these should be automatically selected for a particular alternative application. In fact, it is suggested that the networks perform the best when they are only as complex as the corresponding application [155]. In the case of preforming prediction, it was previously found that a simpler version of the 'DeconvNet' was sufficient for shear angle predictions [152] and thus based on this, a similar network architecture is utilised in this work for wrinkle prediction, taking into account key features from both the 'DeconvNet' and the 'SegNet'.

5.2.3 Applications of neural networks for composites

The use of deep learning neural networks such as FCNs is being more widely considered within the composites community, with potential uses for improving manufacturing processes and designing components for better manufacturability. This fast-growing attention towards using these networks for addressing some of the unresolved problems in the field is enabled by the increasing amount of data collected throughout industry [156], the continual increases in computing power for generating simulated data and the increased network training speeds provided by GPUs [175].

As reviewed thoroughly by Wang et al. [156], deep learning has huge potential for improving manufacturing in various ways: for example, through automated defect detection. Sacco et al. [176] showed that an FCN could be successfully used for pixel-wise classification of defects during the automated fibre placement (AFP) process: giving the exact size, shape and location of defects on any component. They also proved that such a solution could be easily integrated within the AFP process software, making it a feasible reality for the industrial

operator. However, they also estimated that more than 1000 images of defects will be needed to achieve sufficient accuracy such that operator intervention is not necessary. Given that this translates to hundreds of scrapped components, generating such a dataset experimentally becomes very costly. This points to one of the drawbacks of using FCNs for defect identification: they require large amounts of data from defective samples to be effective and producing these samples is expensive and thus not necessarily industrially viable [156].

While using FCNs for defect monitoring is limited by expensive data, within component design there is tremendous potential to apply deep learning tools to reduce the likelihood of defects in the first place through optimisation based on manufacturing outcomes. A key way that FCNs can enable this design optimisation is through using them as surrogate models to phenomenologically replicate the results of high-fidelity models and therefore significantly reduce the computational cost of repeated predictions. For example, rapid topology optimisation of structures has been shown to be feasible using such an approach, with Banga et al. [177] reporting reductions in overall computation time of up to 40% while maintaining similar levels of accuracy compared to physics-based modelling. Gu et al. [178] additionally showed how neural networks could be incorporated within an efficient optimisation scheme to optimise the geometric design of composites for maximum theoretical strength and toughness. Similar approaches could equally be used to optimise designs for minimal manufacturing defects and thus maximise the final as-manufactured strength of components.

Deep learning surrogate models also have significant potential for improving the fabric preforming process, for which process optimisation has typically been limited to the use of simple models [92, 104] that do not sufficiently capture physics of fabric deformation, in particular wrinkling formation. The pioneers in applying FCNs to composite forming are Zimmerling et al. [152], who showed that a surrogate FCN could be trained based on 9000 generated geometries to predict the shear angle distributions of a woven fabric formed over a given tool geometry. This work was novel because it incorporated predictions of full shear strain fields rather single scalar values of their previous work [179, 180], making it much more powerful and useful tool for engineers compared to using scalar-based optimisation. They later extended this work to perform an optimisation of the variable gripper forces [141], material draw-in [181] to achieve optimal shear angle patterns as well as using such a surrogate model to optimise component design [107]. However, in terms of formability and defect prediction, the accuracy of their proposed surrogate models are still limited by either the use of a kinematic forming model for training [152] and/or the reliance on the shear locking angle for identifying the onset of wrinkles [107]. As explained in Chapter 2, the shear locking angle is not a sufficient predictor of shear wrinkling in regions of significant shear [55] and as shown in Chapter 3, it

cannot predict the non-shear wrinkling of in regions of restricted shear. Furthermore, it can give no indication of wrinkling severity, which is crucial for complex geometries where wrinkling cannot be fully avoided. Hence for a more suitable surrogate model, the physically relevant wrinkling patterns should be simulated directly instead and used to train the model. In this chapter, such an FCN-based surrogate model for predicting the wrinkle pattern for a given tool geometry is developed.

5.2.4 Using neural networks to investigate effect of tool geometry

Machine learning approaches have allowed breakthroughs in developing new ways to investigate the geometrical effects on defect development during manufacturing. As an example in sheet metal forming, Wang and Cao [99] were able to develop a feed-forward neural network for predicting the possibility of wrinkling from a set of geometrical variables. Additionally and more recently, Hamouche and Loukaides [100] trained various deep neural networks to identify the best metal forming process for a given geometry based on a description of the component's mean and Gauss curvature.

In terms of the effect of geometry on composites fabric forming in particular, the investigations by Zimmerling et al. [152, 107] are the most relevant but these are insufficient in a critical way. In [152] they employ a geometry parametrisation scheme, made up of six independent parameters, to generate a set of 9000 convex shapes with varying topologies to represent the tool geometry in forming while in [107], they use a similar approach to generate various doubly curved corner features within a larger component. However, the derived understanding from these studies about how geometry influences formability is limited because no characterisation of geometries (e.g. of their surface curvatures) is carried out to understand how these characteristics relate to the resultant forming behaviour. Particularly when considering thousands of geometries, this would allow a more fundamental understanding of the geometrical effects and the potential development of design guidelines. To address this limitation, in this work all the generated geometries are characterised and these characteristics are linked to the resultant wrinkling severity to assess their effect.
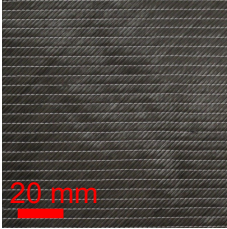
5.3   Material, process and FE model

This investigation is conducted using a large dataset of simulated data, based on forming a layup of biaxial NCFs via the double diaphragm forming (DDF) process over a range of tool geometries. This dataset is used to investigate the effect of tool geometry on wrinkling as well as to develop the deep learning surrogate model. While there are no experimental tests conducted in this study, the finite element model used to model the DDF process has previously been validated using an analogous experimental forming rig [57, 45]. The details of the material, the process and the FE model are outlined below.

5.3.1   Material, layup and forming process

The fabric material that is investigated in this study is outlined in Table 5.1. It is a carbon fibre biaxial ±45° NCF with a pillar stitch ('FCIM-359', manufactured by Hexcel), for which the effect of geometry was previously investigated experimentally in Chapter 3.

Table 5.1 Details related to the material used in this chapter: a biaxial ±45° non-crimp fabric (NCF) manufactured by Hexcel. *The thickness of this NCF was previously measured to be 0.51 mm in Chapter 4 but the lower value of 0.4 mm is used here to be consistent with previous modelling efforts using this material at the University of Nottingham [16].

Fabric	
Type	Biaxial NCF
Commercial name	Hexcel 'FCIM359'
Thickness/mm (± 0.01 mm)	0.4*
Areal weight (GSM)/ g m^{-2}	441 ± 22
Tow orientation/°	-45/45
Fibre material	Carbon fibre
Stitch material	Texturised polyester
Stitch type	Pillar
Front/back of fabric	

For the purposes of this numerical investigation, two plies of this NCF with square sample dimensions of 200 mm × 200 mm and a layup of $[0°/90°, 0°/90°]$ are used (Table 5.2). The bottom NCF closest to the tool is referred to as 'NCF1' while the top NCF of the layup is referred to as 'NCF2'. The pillar stitching on the plies is orientated such that it is at 45° to the global X direction (see Table 5.2). A two-layer NCF layup is chosen, in this case, in order to better replicate realistic forming situations where the interply frictional effects are included, that have been found to have a significant effect on wrinkling behaviour and severity [84].

Table 5.2 Details related to the fabric layup that is investigated in this chapter and how the non-crimp fabric (NCF) plies within the layup relate to the forming tool. The NCF ply closest to the tool is referred to as 'NCF1', while the other ply is referred to as 'NCF2'. The '0' direction corresponds to stitch direction, while the '1' and '2' directions correspond to the fibre tow directions.

Layup	
Layup/°	[0/90,0/90]
Sample size/mm × mm	200 × 200
Sample shape	Square
Stitch orientation (relative to the global X direction)/°	45
Representation of the layup relative to the tool	

Table 5.3 Details related to the double diaphragm forming process that is simulated in this chapter, including a diagram highlighting the key components and dimensions of the process.

Forming process	
Forming process type	Double diaphragm forming (DDF)
Vacuum pressure/kPa	100
Diaphragm material	Stretchlon HT-350 (thermoplastic)
Diaphragm thickness/mm	0.08
Base dimensions/m × m	1.8 × 1.5
Diagram of forming process	

As outlined in Table 5.3, the forming process that is investigated in this study is the double diaphragm forming (DFF) process. The dimensions of the simulated process are based on the laboratory scale DDF rig with dimensions of 1.8 m × 1.5 m, which was developed at the University of Nottingham. Further details regarding the specifics of this rig can be found in [38]. The diaphragm material used is the 'Stretchlon HT-350', made of thermoplastic and with a thickness of 0.08 mm. The maximum vacuum pressure imposed onto the plies during the process is 100 kPa. As the focus of this investigation is on the effect of the tool geometry on wrinkling, the tool geometry used to form this layup is variable but in order to allow for a more effective comparison between geometrical features, the forming height of the tool is kept constant at 50 mm. Male tooling is used specifically because previous analysis has shown that using male tooling rather than female tooling during DDF is more likely to result in wrinkling [182], which is the defect of interest in this investigation. All other parameters related to the forming process beyond the shape of the tool geometry are kept constant throughout the investigation.

5.3.2 Finite element model

Table 5.4 Key details relating to the macroscale material model used to describe the biaxial non-crimp fabric within the finite element (FE) forming simulation of the double diaphragm forming process. For additional information related to the FE forming model, refer to [45].

Material model used in FE forming model	
Type	Superimposed shell-membrane macroscale model
Abaqus subroutine	VFABRIC
In-plane/out-of-plane decoupling	Achieved via decomposing each NCF ply into 3 layers using Abaqus 'composites layup' [63]:
	Layer 1: out-of-plane bending
	Layer 2: in-plane tension and shear
	Layer 3: out-of-plane bending
Layer 2 element type	Membrane - M3D4R
Layer 1 and 3 element type	Shell - S4R
Element edge size/mm	3
Fabric thickness/mm	0.4
Volumetric density/kg m^{-3}	1200
Tensile modulus/GPa	3
Shear behaviour: asymmetric	
Normalised shear force (F_{norm} in N m^{-1}) as a function of shear angle (γ in radians)	$F_{norm} = F_{yarn} + F_{stitch}$ [16]
F_{yarn} is the shear force due to the fibre yarns/N m^{-1}	$F_{yarn} = 29.56\gamma^5 + 5.56\gamma^4 + 137.07\gamma^3 + 94.73\gamma^2 + 112.19\gamma$
F_{stitch} is the shear force due to the stitching/N m^{-1}	$F_{stitch} = \begin{cases} 2000\gamma - 120 & \text{if } 0.06 \leq \gamma \leq 0.50 \\ -3520\gamma - 2640 & \text{if } 0.50 \leq \gamma \leq 0.75 \\ 0 & \text{otherwise} \end{cases}$
Bending: linear, non-orthogonal	
Bending stiffness per unit width along fibre direction (B_{fi})/Nm	0.00228

The development of a surrogate model for wrinkling prediction necessitates the use of a 'parent' model from which the expected output ('ground truth') data for a given input can be obtained and used to determine the phenomenological relationship between the input and the output.

Different finite element modelling techniques for capturing the wrinkling behaviour of textile reinforcements were reviewed in Chapter 2 and based on this, an established hypoelastic macroscale material model of the biaxial NCF forming using superimposed shell-membrane elements is chosen to provide the ground truth wrinkling behaviour for this investigation [63, 45, 57]. The key details of this material model are outlined in Table 5.4.

The membrane-based fabric material model was initially developed by Chen et al. [16] and this model was extended by Yu et al. [63] to include superimposed shell elements to model the fabric's bending stiffness. The model is implemented in Abaqus/Explicit with the non-orthogonality of the fabric captured via the 'VFABRIC' subroutine. Reduced quadrilateral elements (M3D4R and S4R) of element edge size of 3 mm are used for the fabric. This mesh size was found to be sufficient for modelling the forming behaviour of this NCF through mesh sensitivity studies performed previously by Chen et al. [16] and Yu et al. [45]. The decoupled in-plane and out-of-plane behaviour of the fabric model, achieved through the use of Abaqus 'composites layup', ensures that the large shear stiffness and relatively low bending stiffness of the NCF can be accurately captured [63]. The asymmetric in-plane shear material behaviour was previously characterised through a picture frame test and implemented into the model through polynomial functions that combine the shear behaviour of the carbon fibre yarns and the polyester stitch respectively (Table 5.4) [16].

The thermoplastic diaphragm material (from Table 5.3) was previously characterised using uniaxial tensile, equibiaxial tensile and planar shear tests [45]. The two diaphgrams in the process are modelled using a Marlow material model based on this experimental data, with reduced quadrilateral shell elements (S4R) used for meshing them [45]. The element size for the shell elements is varied between 3 mm and 7.5 mm, with the smaller 3 mm elements used in regions where diaphragms are in contact with the layup and the tool. For more details regarding the diaphragm characterisation and modelling, refer to [45].

The contact interactions between the fabrics and the diaphragms are modelled using the Abaqus penalty contact algorithm with Coulomb friction [45]. The friction coefficients used have been derived experimentally by Yu et al. [45] and are 0.51, 0.40 and 0.36 respectively for the tool-diaphragm, fabric-diaphragm and fabric-fabric interfaces.

The shell-membrane model has been experimentally validated for both the press forming [57] and double diaphragm forming processes [45]. Additionally, it has been shown to be able to capture the two distinct wrinkling mechanisms in positive and negative shear for this $\pm 45°$ NCF [57].

While both non-linear and linear bending stiffness characterisations for this model have been proposed [57], with the non-linear characterisation achieving improved accuracy, a linear

model is adopted here for the sake of computational efficiency with the linear bending model being 25% faster. This is justified because in this study, thousands of simulations are run using this model and thus this reduces the total run-time of the simulations by several weeks. Additionally, although achieving sufficient accuracy of the wrinkling behaviour is important to allow for comparisons of the tool geometry effect, the surrogate modelling method proposed is equally applicable to be used with any 'parent' model and the choice of the model does not affect the validation of the surrogate modelling approach for wrinkling prediction.

For this investigation, the bending stiffness of the NCF is modelled with a constant bending stiffness per unit width along the fibre direction (B_{fi}) of 0.00228 Nm (Table 5.4). This B_{fi} value used for this study is 40% lower than the mean experimentally derived value of 0.0035 Nm for this NCF (based on the cantilever test - [57]) but since they of the same order of magnitude, this does not drastically change the wrinkling behaviour [65]. Based on a direct comparison of simulations using the two values of B_{fi}, it was found there was on average a 10% difference in wrinkling severity using the lower B_{fi} value with the wrinkles somewhat exaggerated but the patterns comparable. Thus using the lower value allows for any trends related to the effect of geometry to be more clearly identified without compromising the validity of the observations.

Within this explicit simulation, the quasi-static double diaphragm forming process is modelled as three distinct steps: (1) applying pressure on the diaphragms, (2) moving the tool relative to the fabric layup and (3) removing the pressure on the bottom diaphragm to force the fabric layup to form over the tool [45]. Different levels of mass scaling are used in each step to reduce the overall computational cost. In the first step, a fixed mass scaling factor of 10000 is used, while this factor is reduced to 200 and 20 for steps 2 and 3 respectively. The actual forming of the layup and thus the formation of wrinkles occurs in step 3. Therefore the reduced mass scaling factor in this step minimises the potential of dynamic effects impacting the formed fabric shape. Previous analysis by Yu et al. [45] has shown that the kinetic energy of the simulation remains below 5% of the total strain energy throughout and thus the effect of the mass scaling on the forming result can be concluded to be negligible.

5.4   Method
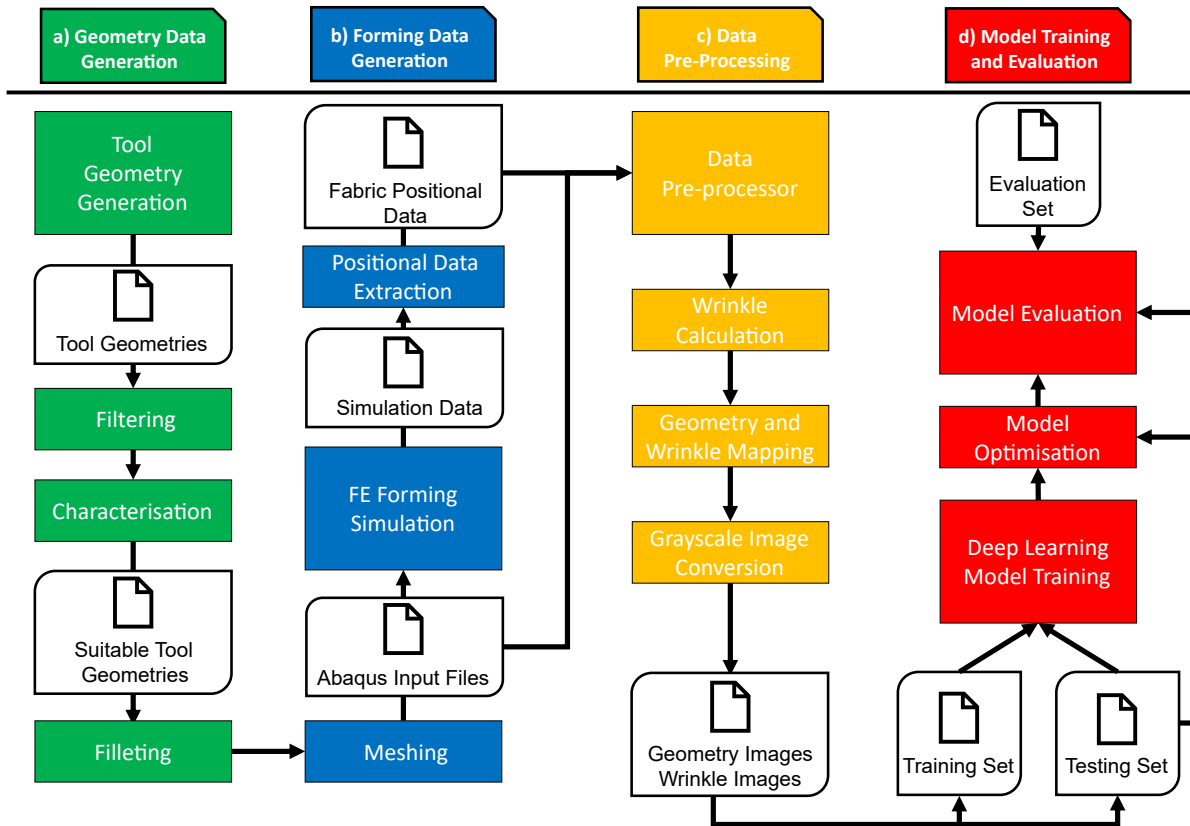
Fig. 5.3 Outline of the method for the development of the deep learning surrogate model for wrinkle prediction. The method consists of four key stages: a) geometry data generation, b) forming data generation, c) data pre-processing and d) model training and evaluation.

The method for the development of the deep learning (DL) surrogate model for rapid wrinkle prediction is outlined in Figure 5.3, consisting of four key stages:

a) Tool geometry generation (Subsection 5.4.1): generating and characterising a large set of varying tool geometries.

b) Forming data generation (Subsection 5.4.2): simulating the forming of NCF layup over each tool geometry using the finite element model to obtain fabric positional data from which the ground truth wrinkle data can be obtained.

c) Data pre-processing (Subsection 5.4.3): processing the geometry and wrinkling data into 2D grayscale images that are suitable to train a deep learning model.

d) Model training and evaluation (Subsection 5.4.4): training the deep learning network and evaluating its performance relative to the ground truth finite element simulation.

Each of these stages is further detailed in this section. As well as the resulting deep learning model, by characterising each generated geometry based on a number of geometrical characteristics, it allows the generalised effect of the tool geometry to be investigated by comparing the characteristics against the severity of the obtained wrinkled patterns.

5.4.1   Geometry data generation

Geometry data generation is the first stage of the method in which the sampled geometry space for this investigation is created. Thus it determines the range of geometries that are used as input data to train the deep learning surrogate model and also to investigate the effect of geometry on wrinkling severity. This stage consists of generating a large set of differing tool geometries, characterising each of these geometries, filtering out all geometries that are unsuitable for forming and filleting the edges of the suitable geometries. In the end, 1818 suitable geometries are taken forward to the next stage of wrinkle data generation.

Tool geometry generation
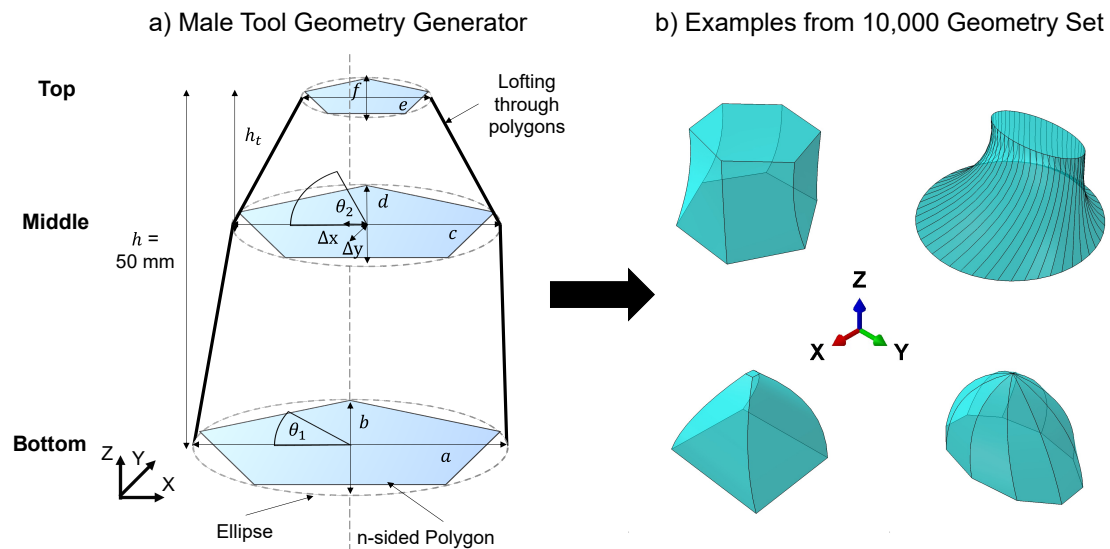
Fig. 5.4 a) Outline of the code-based geometry generator used to generate the geometry set of male (globally convex) geometries and b) examples of geometries from the initial set of 10,000 geometries.

Table 5.5 Outline of the variable input parameters used for the geometry generator and the corresponding parameter ranges. The ranges are manually selected for each parameter while the combinations of parameter values for each geometry are randomly assigned from these ranges, subject to certain conditions (eqs. (5.1) to (5.3)). The referenced ellipses and polygons are defined in Figure 5.4a.

Symbol/unit	Description	Parameter range
n	Sides (number of sides for each polygon)	[3, 4, 5, 6, 8, 10, 30, 50]
h_t/mm	Top height (height between top and middle polygon)	[1,2…30]
a/mm	Bottom ellipse major axis	[50,51…99,100]
b/mm	Bottom ellipse minor axis	[50,51…99,100]
c/mm	Middle ellipse major axis	[25,26…99,100]
d/mm	Middle ellipse minor axis	[25,26…99,100]
e/mm	Top ellipse major axis	[0.25…100]
f/mm	Top ellipse minor axis	[0.25…100]
g	Top ellipse/middle ellipse length ratio	[1/100, 1/10,1/4,1/2,3/4,7/8,1]
θ_1/°	Bottom polygon rotation anticlockwise relative to x axis	[-90,-45,0,45,90]
θ_2/°	Middle polygon rotation anticlockwise relative to x axis	[-90,-45,-30,-15,0,15, 30, 45, 90]
Δx & Δy/mm	Middle polygon shift in x and y, relative to centre of bottom polygon	[-18.75…18.75]

In order to meet the significant data requirements for deep learning models and to be able to gather sufficient data for analysis of the relation between geometries and wrinkling, a rapid method for generating a large number of different geometries is necessary. A code-based CAD geometry generator is developed (Figure 5.4a) and used to generate an initial set of 10,000 male tool geometries (Figure 5.4b). The generator is loosely inspired by previous works of [107, 152] but differs in its implementation and sampling. As shown in Figure 5.4a, the generator consists of three polygons that are fitted within ellipses and then lofted together through their vertices. The number of polygon sides (n), major and minor axes of each ellipse (a, b, c, d, e, f), the relative height between them (h_t) and their relative rotation (θ_1, θ_2,) and lateral shift (Δx, Δy) are all modifiable parameters (Table 5.5), This allows the generation of vastly different geometries, as shown by the examples in Figure 5.4b. Note that the same n is used for the three polygons within one geometry in order to ensure they can be successfully lofted together. Furthermore, the overall height of the tool (h) geometry is kept at constant at 50 mm (as was

done in [107]) in order to accommodate more direct comparisons between geometrical features in terms of the resulting wrinkling behaviour. The generator is implemented in a Python script using the parametric CAD module 'CadQuery' (v 2.0), based on the PythonOCC development framework [183].

For generating the initial geometry set of 10,000 geometries, a semi-random approach for input parameter selection is utilised, with each parameter value randomly picked from within manually specified parameter ranges that are outlined in Table 5.5. The parameter ranges are selected so as to produce the widest possible distribution of geometry characteristics (Figure 5.4.1). A simple random sampling approach is preferred to a parametric approach that considers every possible combination of parameters because it allows for a larger breadth of combinations to be covered within a fewer total number of geometries. While a more robust random sampling method - 'latin hypercube sampling' (LHS) - has previously been used [152, 166] to sample the parameter space, it was found not to improve the distribution of geometrical characteristics in the generated geometry set (Figure 5.6) and thus not employed in this case. This is partly because LHS assumes that all input parameters are independent of each other [184] (which does not apply in this case), and because the input parameters do not directly correlate with the geometrical characteristics (which are of primary interest in this study).

During the semi-random parameter selection process, the following constraints are imposed between the 13 input parameters in order to ensure that every geometry has a globally convex (male) shape (eq. (5.1)), that the top and middle ellipse maintain the same aspect ratio (eq. (5.2)) and that the likelihood of undercuts is minimised (eq. (5.3)):

$$a \geq b \geq c$$
$$b \geq d \geq f \tag{5.1}$$

$$\frac{c}{e} = g$$
$$\frac{d}{f} = g \tag{5.2}$$

$$\Delta x \leq (a - c)$$
$$\Delta y \leq (b - d) \tag{5.3}$$

However, the presence of undercuts cannot be fully avoided due to the inclusion of relative twisting and thus any generated shapes with undercuts are removed out at the filtering stage.

Filtering

Filtering of the geometries is necessary in order to ensure they meet the requirements of the specific forming process to be simulated. Based on applying the five filters outlined in Table 5.6, the initial 10,000 geometries are reduced to a final set of 1818 geometries. The filtering metrics (ΔX, ΔY, ΔZ, $N_{z,min}$, r_A and $\theta_{d,min}$) are defined in Appendix E and are used to identify suitable geometries from the initial set. To exemplify the filtering process, Figure 5.5 shows examples in red of rejected geometries corresponding to each of the five filters as well as an example in green of a geometry that passed all filters.

The five filters are shown to filter out the initial geometry set to differing extents. The dimensions of the ellipses that constitute each geometry are chosen so that they meet automatically the requirements of the first three filters (Table 5.5) but due to the lofting operation connecting the polygons in Figure 5.4, it is plausible for these filters to be exceeded as curved edges are fitted through the polygon vertices. As a result, 301, 308 and 923 geometries are rejected by the 'max length', 'max width' and 'max height' filters respectively (Table 5.6). Furthermore, the 'sharp points' filter, as described by a combination of $\theta_{d,min}$ and r_A, eliminates 1025 geometries (Table 5.6) that are too pointy to be realistically simulated without fabric penetration and could even lead to piercing the diaphragm during forming trials. However, the most important critical filter from a forming perspective is the 'undercuts' filter that rejected 7779 geometries that have downward-pointing surfaces (Table 5.6). This is also the most critical filter from a forming perspective because such geometries cannot be successfully formed without excessive bridging in the case of DDF or tool collision during matched tool forming [152]. Furthermore, having no undercuts is required such that the tool geometry can be mapped onto a 2D surface without loss of detail (see Subsection 5.4.3). In theory, if the minimum z component of all the surface normal vectors on the geometry ($N_{z,min}$) is negative, then the surface contains at least one undercut region and should be eliminated. However, to account for unrepresentative outliers, the filter requirement is set at $N_{z,min} > -0.1$. Applying all the filters together results in 8288 rejected and 1818 suitable ('Accepted') geometries (Table 5.6), with the latter taken forward to the characterisation stage and subsequent simulation.

Table 5.6 Details for the five filters used to identify suitable geometries for preforming and how many geometries were accepted and rejected by each filter, along with summary based on applying all filters simultaneously. The $()'$ notation denotes the complement of the set defined within the brackets.

Filter number	Filter name	Filter condition	Accepted	Rejected
1	Max length	$\Delta X \leq 100$ mm	9699	301
2	Max width	$\Delta Y \leq 100$ mm	9692	308
3	Max height	$\Delta Z \leq 50.1$ mm	9077	923
4	Undercuts	$N_{z,min} > -0.1$	2221	7779
5	Sharp points	$(\theta_{d,min} < 45° \cap r_A < 0.01)'$	8975	1025
	All		1818	8282
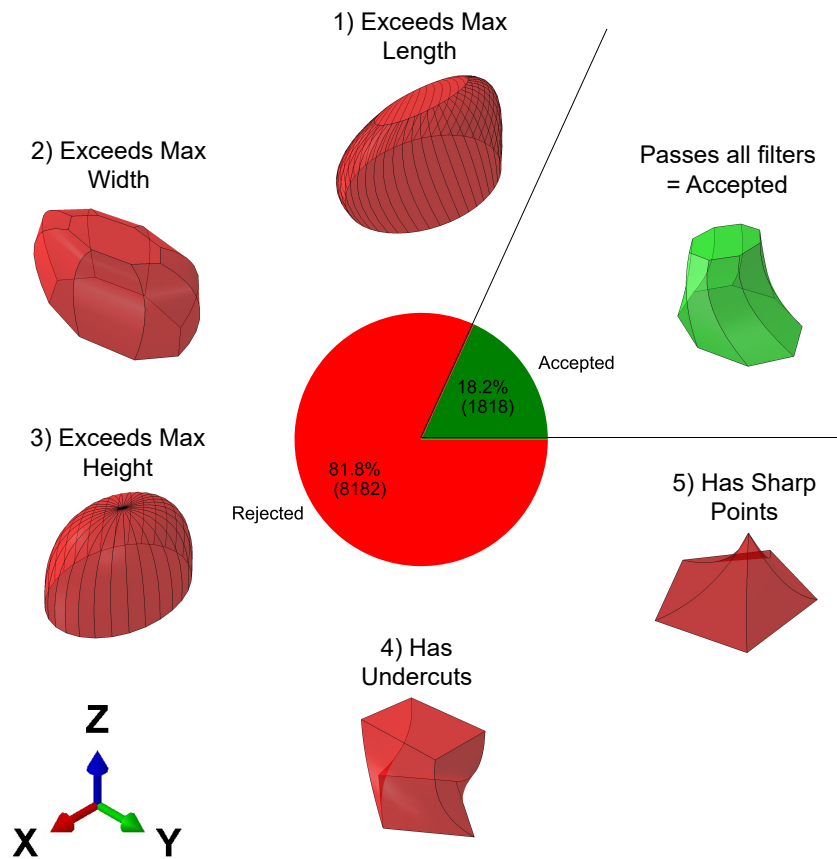
Fig. 5.5 Pie chart showing the number of geometries that were accepted and rejected at the filtering stage. Examples of geometries that were rejected by each of the five filters and one example of a geometry that passed all filters are shown.

Characterisation

The characterisation of the accepted tool geometries is necessary to enable the diversity within the geometries to be evaluated, to categorise them within particular groups and subsequently to understand how these characteristics correlate with the resultant wrinkling severity. All of the geometries are characterised based on eight metrics, which are defined in Appendix E. Figure 5.6 shows the probability density distribution and five-bin histograms across the range of each metric with example geometries shown for three of the five histogram bins to provide context. The eight metrics and the associated characteristics (in **bold**) that have been developed for the characterisation of the geometries are the following:

- r_A (area ratio) (Range: [0,1]) characterises the **'Area Ratio'** of the geometry with r_A approaching 0 resulting in a pointed geometry while r_A equal to 1 is a flat-topped geometry with vertical sides. Figure 5.6a shows the distribution of r_A is concentrated at the lower end of the range, suggesting more pointed than blunt shapes.

- r_V (volume ratio) ([0,1]) characterises the **'Volume Ratio'** of the geometry relative to its bounding box and thus describes to what extent the geometry fills out its bounding box, with a $r_V = 1$ corresponding to a cuboid the same size as the bounding box. Figure 5.6b shows that most of the geometries are between $0.4 < r_V < 0.6$, with very few geometries at the extremes of the distribution.

- $\overline{\theta_{do}}/°$ (mean overall draft angle) ([0,45]) characterises the **'Conicity'** of the geometry with a larger draft angle ($\overline{\theta_{do}}$), for a fixed tool height, corresponding to a more conical geometry with greater tapering while a $\overline{\theta_{do}}$ approaching to 0 has vertical sides and thus no draft. As a result, this characteristic is somewhat related to r_A, albeit inversely. Figure 5.6d shows that the geometries are approximately normally distributed with the mode between 18° and 27° (3rd bin).

- $\overline{\theta_{int}}/°$ (mean interior angle) ([60,180]) characterises the **'Angularity'** of the geometry with a large $\overline{\theta_{int}}$ tending to approximately curved edges in the limit while the smallest $\overline{\theta_{int}} = 60°$ corresponds to a triangular geometry that is distinctly angular. Figure 5.6d shows that the geometries tend to be more curved than angular with a majority of geometries in the last two bins. Additionally, the distribution can be seen to be discrete due to being directly linked to the number of polygon sides (Appendix E)

- $|d_o|/$mm (offset distance) ([0,6]) characterises the **'Asymmetry'** of the geometry with a larger $|d_o|$ corresponding to a greater degree of asymmetry. Figure 5.6e shows that the geometries tend more towards symmetric, which is expected given that excessive

asymmetry is likely to cause undercuts in the geometry, which were eliminated during filtering.

- $\overline{\theta_{tt}}/°$ (mean true twist angle) ([0,35]) characterises the **'Tortuosity'** of the geometry with a larger $\overline{\theta_{tt}}$ corresponding to larger relative twist within the geometry. Figure 5.6f shows that the distribution is discrete and that most geometries have relatively small amounts of twist (between 0-7°), which is expected given the large number of geometries with large $\overline{\theta_{int}}$ that minimises the true twist and how increasing twist is likely to cause undercuts for smaller values of $\overline{\theta_{int}}$.

- H_r/mm^{-1} (representative mean curvature) ($[-3.5, 1.5] \times 10^{-2}$) characterises the **'Mean Curvature'** of the geometry, calculated based on the mode of the local mean curvature (H) distribution across the geometry surface (see Appendix E). When $H_r < 0$, the geometry tends to curve away from the outward surface normals (see the example for bin 1 in Figure 5.6g) while when $H_r > 0$, the geometry tends to curve towards the outward surface normals (see the example for bin 5). Based on Figure 5.6g, the majority of geometries are concentrated in bin 4 between $[-0.5, 0.5] \times 10^{-2}$ mm^{-1} (thus having minimal mean curvature). Furthermore, there are more negative H_r geometries than positive H_r geometries, showing that the geometries tend to curve away from the normals.

- K_r/mm^{-2} (representative Gauss curvature) ($[-3.5, 1.5] \times 10^{-3}$) characterises the **'Gauss Curvature'** of the geometry, is calculated similarly to H_r: based on the mode of the local Gauss curvature (K) distribution (Appendix E), where K corresponds to the product of the principal curvatures k_1 and k_2. Thus when $K_r < 0$, the sides of the geometry tend to bulge inwardly, $K = 0$ describes a single curvature geometry with (k_1 or $k_2 = 0$) and $K_r > 0$ corresponds to a dome-like shape. The distribution of K_r in Figure 5.6h, is concentrated around 0 (bin 4) suggesting that although most of the geometries exhibit some level of double-curvature, there is not a large amount of variability in the extent of this curvature, with relatively few geometries at the extremes of the range.
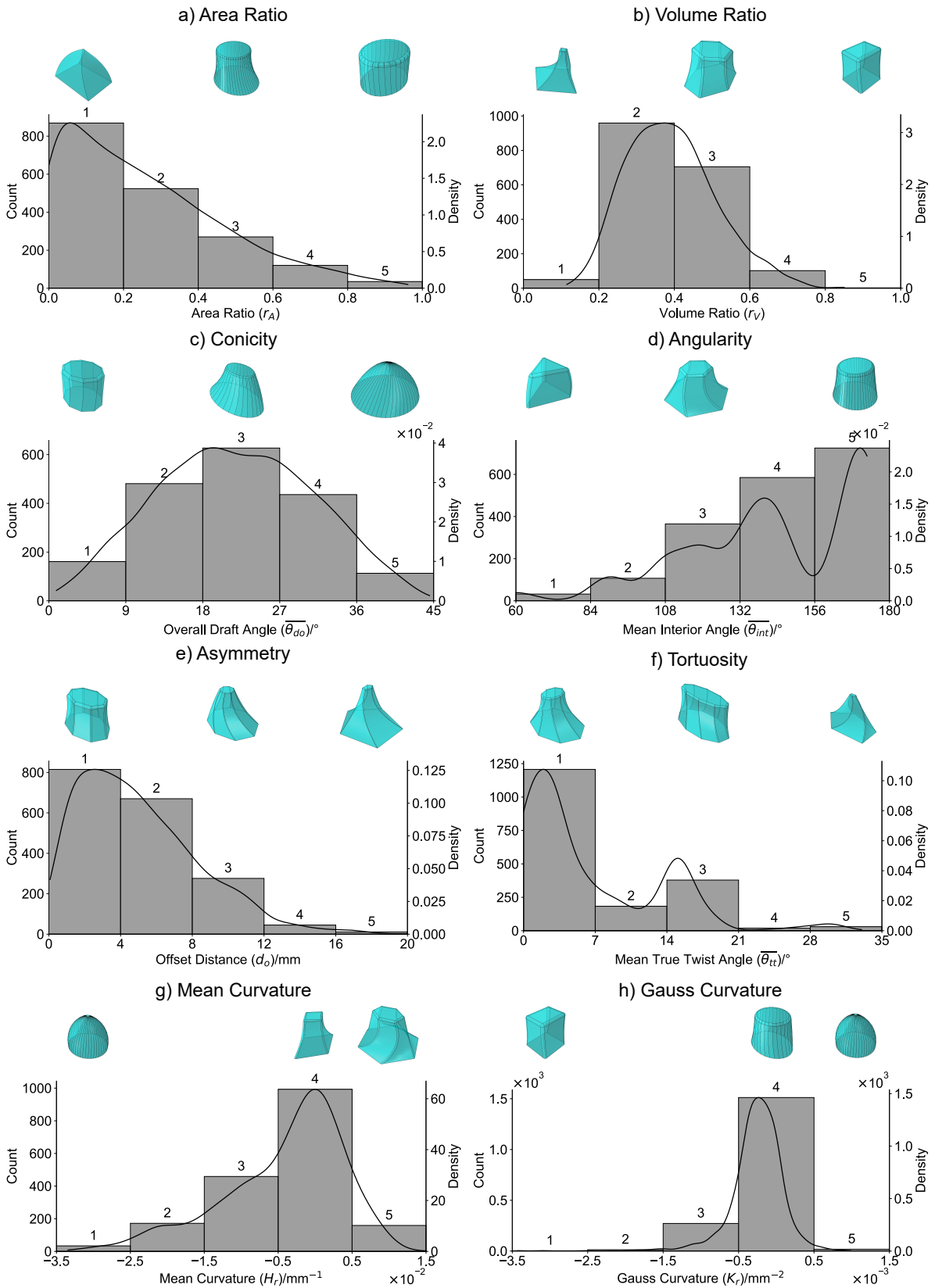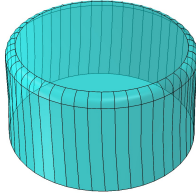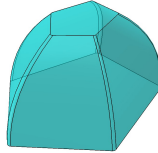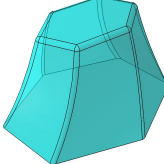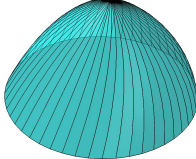
Fig. 5.6 Probability density distributions and 5-bin histograms, based on all suitable 1818 tool geometries, for all eight geometry characteristics considered: a) Conicity, b) Area Ratio, c) Volume Ratio, d) Angularity, e) Asymmetry, f) Tortuosity, g) Mean Curvature and h) Gauss Curvature.

Filleting

Table 5.7 Details for the automated filleting algorithm used to apply fillets to the tool geometry edges ahead of the simulation stage.

Type	Condition	Example	Quantity (% of total)
Top fillet only	$\theta_{d,min} < 35° \cap \theta_{int,min} \geq 135°$		747 (41)
Side fillet only	$\theta_{int,min} < 135° \cap \theta_{d,min} \geq 35°$		48 (3)
Top and side fillet	$\theta_{d,min} < 35° \cap \theta_{int,min} < 135°$		894 (49)
No fillet	$(\theta_{d,min} \geq 35° \cap \theta_{int,min} \geq 135°)$ $\cup f < 1$ mm		129 (7)

Engineering components typically have filleted radii in order to minimise stress concentrations. Thus in order to make the generated geometries as realistic as possible and to minimise contact penetrations during simulations, a filleting algorithm (detailed in Table 5.7), which determines whether fillets are required in two key locations of the geometry, is applied to all suitable geometries. The algorithm is implemented in CadQuery [183], with the fillet radius (r_f)

calculated based on the minor axis length of the top polygon (f - see Figure 5.4) as follows:

$$r_f = \begin{cases} 1, & \text{if } \frac{f}{15} < 1 \\ \frac{f}{15}, & \text{if } 1 \leq \frac{f}{15} \leq 5 \\ 5, & \text{if } \frac{f}{15} > 5 \end{cases} \qquad (5.4)$$

The minimum draft angle ($\theta_{d,min}$) and the minimum interior angle ($\theta_{int,min}$), as defined in Appendix E, are used to identify whether to apply fillets for each geometry in two general locations of each geometry where fillets might be needed. These two locations are along the edges of the top polygon ('top fillet'), or along the lofted edges that connect the polygons ('side fillet') (see Table 5.7). A top fillet is applied if $\theta_{d,min} < 35°$, a condition which is empirically found to correspond to sharp edges for at least one of the top vertices. A side fillet is applied if $\theta_{int,min} < 135°$ that likewise suggests that at least one of the lofted edges is sharp. As a result, the geometries had either a top fillet, a side fillet, both or neither with the quantities for each category shown in Table 5.7. Most of the geometries required a top fillet (90%) to be applied, with approximately half (52%) needed a side fillet.

5.4.2 Forming data generation
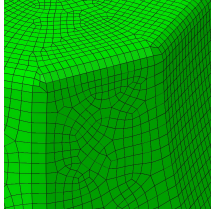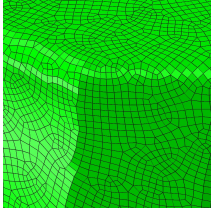
Using the 1818 suitable geometries generated, the corresponding wrinkle data for each tool geometry is created by simulating the wrinkling behaviour of a two-NCF layup over each one during DDF using the FE model detailed in Section 5.3.

Tool meshing

The generated tool geometries need to be meshed in a systematic manner that maintains, as much as possible, the true topology of each geometry. To achieve this, the meshing approach detailed in Table 5.8 is applied. This approach consists of using the 'Free' meshing algorithm in Abaqus with a target element side length of 1 mm, and mostly quadrilateral rigid elements ($R3D4$) with some triangular elements included in the difficult-to-mesh regions ($R3D3$). As it is known that highly distorted elements can cause simulations to abort prematurely, the minimum interior angle of all the triangular elements ($\theta_{m,min}$) is calculated to identify geometries with highly distorted elements of near-zero area in the mesh. For those geometries for which the minimum angle ($\theta_{m,min}$) is less than 0.1° (5% of all meshed geometries), the virtual topology that stringently defines the points through which the mesh nodes need to pass through, is removed and the geometry is re-meshed. While this theoretically reduces the accuracy of the

mesh in representing the geometry, the fine mesh size means that deviations from the true shape are kept to a minimum (see example in Table 5.8).

Table 5.8 Details for the meshing of the generated tool geometries, including the conditions for removing the virtual topology of the geometry in cases of highly distorted elements.

Element types	R3D4, R3D3		
Mesh size/mm	1		
Abaqus mesh algorithm	Free – advancing front (quad-dominated)		

Type	Condition	Example	Quantity (% of total)
With virtual topology	$\theta_{m,min} \geq 0.1°$		1724 (95)
Without virtual topology	$\theta_{m,min} < 0.1°$		94 (5)

Optimised simulation process

The running time for one finite element (FE) simulation of the linear bending membrane-shell model used in this study is on the order of several hours [57] and thus for the efficient simulation of 1818 geometries, it is important to optimise the simulation process to minimise the total run time. All the FE simulations are run using a high-end CPU: the Intel i9-10980XE @3.0GHz with 18 total cores and 64GB of RAM, which is able to at most run 16 simulations in parallel. Based on this setup, it was determined that the most time-efficient method for simulating all geometries was to run 16 simulations in parallel using 1 CPU core each, as compared to running each simulation with 2, 4, 8 or 16 CPUs each with maximum parallelisation (Figure 5.7). The average runtime for the completed simulations, based on the mass scaling described in Subsection 5.3.2, was found to be 11.5 h (hours) and all the simulations were completed in just less than two months (1307 h or 54 d (days)). Out of the 1818 simulations that were attempted, 16 were found to have aborted prematurely and thus those geometries were eliminated at this

stage from the investigation. The rest of the 1802 simulations are further processed to obtain the tool height, shear angle and wrinkle amplitude maps for each corresponding tool geometry.
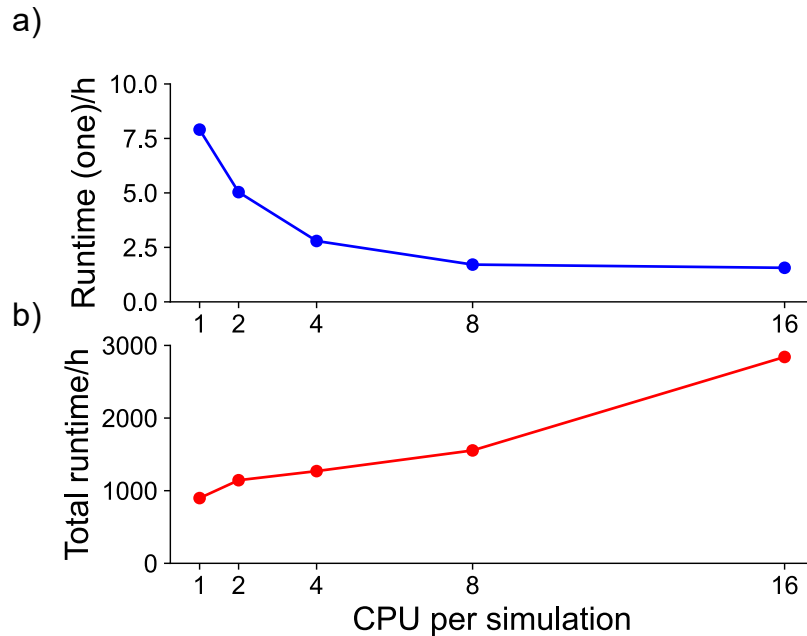
Fig. 5.7 Optimisation of the total runtime for running 1818 finite element forming simulations with respect to the number of CPU cores used for each simulation: a) the measured runtime for one forming simulation against the number of cores used, and b) the expected total runtime for all 1818 simulations, calculated based on the runtime for one simulation (a) and assuming that a total of 16 CPU cores can be used at any one time.

5.4.3 Data pre-processing

Positional and strain data are extracted from the simulations and processed in MATLAB in order to obtain sets of grayscale images corresponding to the tool height surfaces, shear angle surfaces and wrinkle amplitude surfaces respectively for each simulation (Figure 5.8). The pre-processing stage consists of first calculating the wrinkle amplitudes at each position on the deformed fabric and then mapping the wrinkling and the corresponding shear angle results back onto the initially flat, undeformed fabric, such that there is no data loss when these surfaces are turned into 2D grayscale images. The tool geometry coordinates are translated into a contour map of the same dimensions as the undeformed fabric and then turned into a grayscale image, with the local tool height represented by the intensity of the image. The tool height and wrinkle amplitude images are used to train the deep learning surrogate model and the shear angle

images are used to compare the wrinkling behaviour in the positive shear (PS) and negative shear (NS) regions respectively.
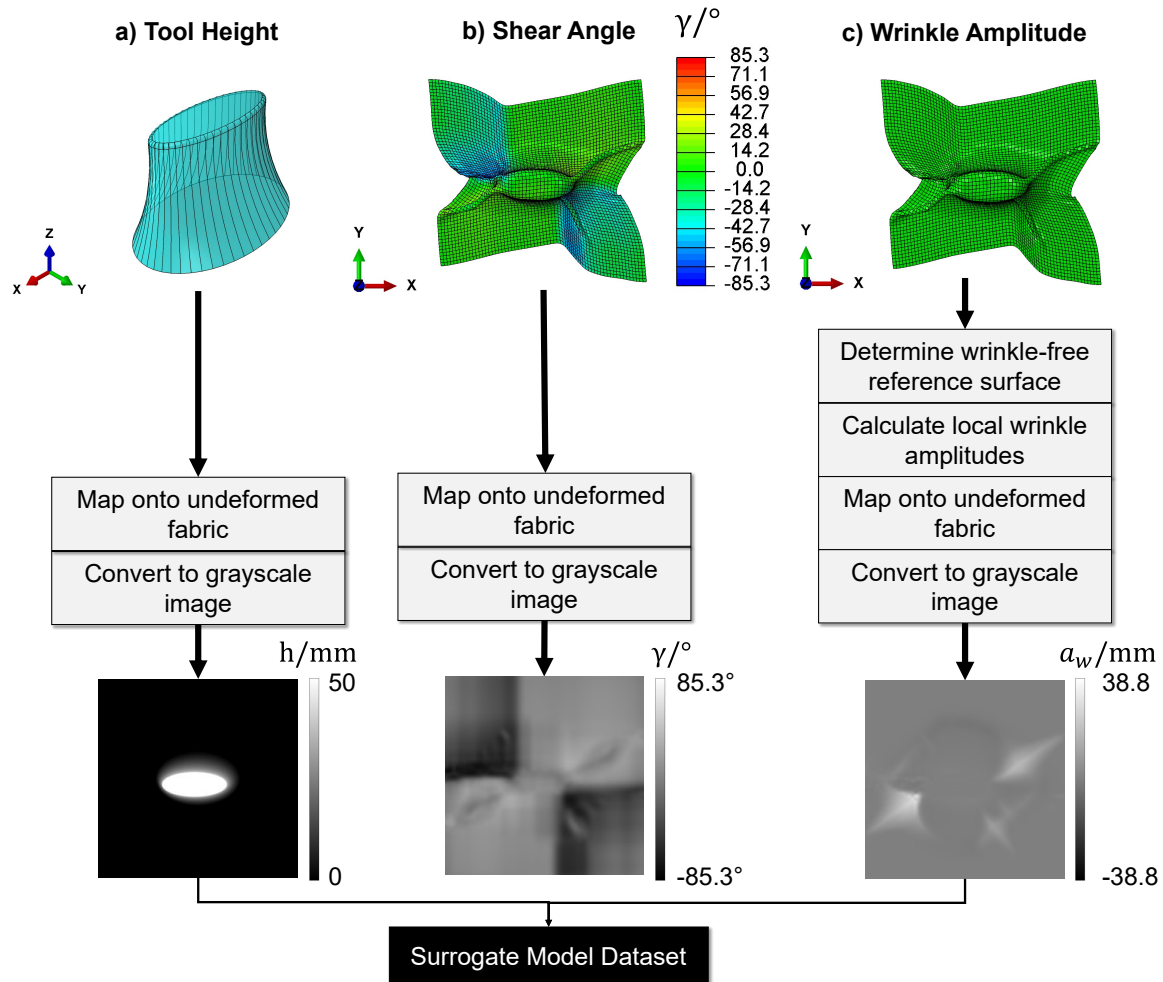
Fig. 5.8 Outline of the method for obtaining grayscale images for the tool height (a), the shear angle (b) and the wrinkle amplitude (c) from the finite element simulation data. Note that only the tool height and wrinkle images are used to train the surrogate model.

Wrinkle calculation

The wrinkle amplitude surfaces are calculated based on the same method outlined in Chapter 3 where the wrinkle amplitude (a_w) is defined to be the magnitude of the out-of-plane displacement of the deformed fabric surface in the direction of the surface normal of a wrinkle-free 'reference surface'. The only difference in the method is that now with thousands of varying geometries for processing, an automated method was developed for determining the wrinkle-free reference surface (Figure 5.9).

After the DDF process, the bridging and wrinkling defects are often superimposed on top of each other and thus it is important for the bridging to be discounted as part of the reference surface so that all measurements are related to actual fabric wrinkling. The reference surface (grey in Figure 5.9) is calculated by determining the mean paths of the fabric from the point at which the fabric breaks away from the tool surface ('breakaway point' in Figure 5.9) and combining this with the sections of the tool geometry that are in contact with the fabric. To find the mean paths, firstly the mean heights ($\bar{h}$) of the deformed fabric around the tool geometry perimeter for a range of incremental mean radii ($\bar{r}$) away from the tool centre are calculated (see Figure 5.9). Then the paths are found by setting all the fabric heights around the perimeter at each $\bar{r}$ equal to $\bar{h}$ and fitting a 2D surface through these points. This surface containing the mean paths is combined with the top section of the tool geometry (above the 'breakaway point' in Figure 5.9) and the boundaries of the deformed fabric to obtain the reference surface for each tool geometry. As a result, the reference surface does not contain any wrinkles as these have been eliminated by taking the mean fabric heights but the bridging is maintained by determining the path through these mean heights (as shown in Figure 5.9). The wrinkle amplitude $a_w(x, y)$ surface is then calculated as per eq. (3.1), based on the deformed fabric surface and the reference surface.
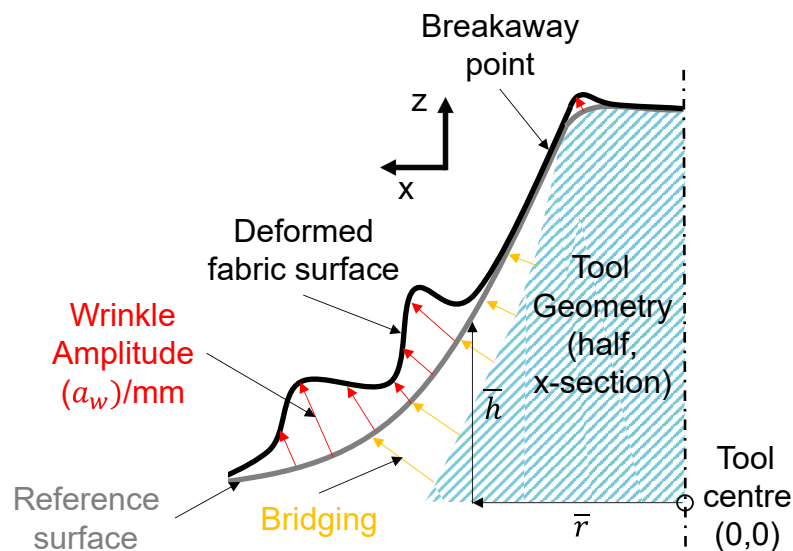
Fig. 5.9 Schematic outlining how the wrinkle-free reference surface, that is used to calculate local wrinkle amplitudes, is obtained automatically for each tool geometry. This reference surface incorporates the bridging of the fabric from the tool surface so that the bridging can be decoupled from wrinkling. The wrinkle amplitudes are calculated with respect to the particular reference surface for each tool geometry and the actual formed fabric surface.

Mapping onto undeformed fabric

The mapping of the wrinkle amplitudes of the deformed fabric surface onto the undeformed fabric is necessary to avoid data loss when translated to a 2D grayscale image. This mapping is inspired by a previous study where this was done for a shear angle distribution [152]. To achieve the mapping, a linear interpolation is made from the grid coordinates of the deformed fabric surface to the wrinkle amplitudes of the deformed fabric at each grid coordinate (X, Y). Then this interpolation is applied to the nodal coordinates (x, y, z) of the deformed fabric at the end of forming to obtain the wrinkle amplitudes at each fabric surface node coordinate (x, y). Using the nodal information, the wrinkle amplitudes can then be mapped to the initial nodal positions (x_i, y_i) to obtain the 'undeformed' wrinkle map.

The shear angle (γ) distribution across the NCF surface, is also mapped onto the undeformed fabric in a similar way (Figure 5.8b). This allows the shear angle distributions to be directly compared with the wrinkling behaviour and thus allows the wrinkling severity to be differentiated based on the wrinkling mechanism.

For the tool geometries, as they do not contain any undercuts, a height map $h(x, y)$ viewed from above can describe them without any loss of detail [152]. The tool height map is obtained by fitting a 2D surface through the tool coordinates on a grid the size of the undeformed fabric.

Grayscale image conversion and scaling

The undeformed wrinkle map, shear angle map and tool height map are converted to grayscale images (see bottom of Figure 5.8) such that the intensity of the image corresponds to the local wrinkle amplitude (a_w), local shear angle (γ) and local tool height (h) respectively. The images are scaled such that the extremes of the grayscale range, black and white, correspond to the largest possible values across all the simulations, in order to allow for direct comparisons and wrinkling severity evaluation based on each image. For the tool height, the limits are constant between 0 mm (black) and 50 mm (white) and for the shear angle the largest magnitude shear angle was found to be $-85.3°$ and thus the limits were set at $[-85.3, 85.3]°$. Finally, for the wrinkle amplitude, the maximum amplitude was found to be 38.8 mm and thus the limits are set at $[-38.8, 38.8]$ mm. The resulting images of size 201 px (pixels) $\times$ 201 px are resized to a size of 256 px $\times$ 256 px so that they are compatible with the requirements of CNNs, which necessitate that image dimensions be multiples of two for best performance.

Wrinkling metrics

As a result of the equal scaling of the grayscale images and correlation of the intensity with wrinkle amplitude, the wrinkling severity for each tool can be directly evaluated from these images based on various metrics. For this work, three wrinkling metrics are used: the maximum absolute wrinkle amplitude ($|a_w|_{max}$), the wrinkle area (A_w) and the mean absolute wrinkle amplitude ($\overline{|a_w|}$). These metrics respectively describe how large the most severe wrinkles are, how much of the preform are they cover and what is the average size of the wrinkles. Thus, when used together, the three metrics are able to provide an exhaustive assessment of wrinkling severity.

The following description outlines how the metrics are calculated: based on the linear relationship between the local intensities of the image ($I(i)$) and the wrinkle amplitude at any given point ($a_w(i)$), the absolute wrinkle amplitude map ($|a_w(i)|$) from each image can be obtained as follows:

$$|a_w(i)|[mm] = |\frac{2a_{w_{max,set}}}{I_{max}}I(i) - a_{w_{max,set}}| \tag{5.5}$$

where i is the ith pixel of the image, $a_{w_{max,set}} = 38.8$ mm and $I_{max} = 255$. From this, three wrinkling metrics can be calculated as follows:

- Max wrinkle amplitude:

$$|a_w|_{max}[mm] = max(|a_w(i)|) \tag{5.6}$$

- Wrinkle area:

$$A_w[\%] = \frac{N_{|a_w(i)|>1mm}}{N} \tag{5.7}$$

- Mean wrinkle amplitude:

$$\overline{|a_w|}[mm] = \overline{|a_w(i)|_{>1mm}} \tag{5.8}$$

where $N_{|a_w(i)|>1mm}$ is the number of pixels with an absolute wrinkle amplitude greater than 1 mm, N is the total number of pixels in the image and $|a_w(i)|_{>1mm}$ corresponds to all image pixels with an absolute wrinkle amplitude greater than 1 mm. These metrics are used to compare the wrinkling severity between the simulated geometries, to relate the wrinkling severity to the geometrical characteristics and to evaluate the wrinkling prediction performance of the surrogate model.

5.4.4 Model training and evaluation

The final stage of the method consists of splitting the processed data into subsets, selecting a suitable neural network architecture and training the surrogate model using optimised hyperparameters. Subsequently, the wrinkle predictions from the surrogate model are evaluated by comparing them against the 'ground truth' (or expected results) from the finite element model.

Training, test and evaluation sets

The total dataset is divided into two subsets: the training set and the test set. Approximately 90% (1616) of the total dataset (1802) is used for the training set, with 10% of the data reserved for the test set (186). As the numbered geometries are already ordered randomly based on the generation process (Subsection 5.4.1), the last 186 geometries chronologically are selected as the training set, while being representative of the larger training set. The test set is used to optimise the performance of the model for maximum accuracy, and evaluate the distributions in model predictions. While it is common to include a third validation set in addition to the training and test sets [155], in this study, the test and validation sets are combined together in order to maximise the size of the training set. Also because a separate evaluation set is used, there is less of a need for a third, unseen validation set for evaluation purposes.

Table 5.9 The respective sizes of the total, training, test and evaluation datasets used with the surrogate model. Each dataset consists of pairs of tool geometry and wrinkle amplitude images.

Dataset	Dataset size (% of total)
Total dataset	1802 (100)
Training set	1616 (90)
Test set	186 (10)
Evaluation set	10

The evaluation set consists of ten realistic benchmark tool geometries, which are shown in Figure 5.10. Four of these geometries (hemisphere, double dome 1, triangular prism and tetrahedron) are similar to those used in Chapter 3 for press tool forming with six others also selected to highlight a wide variety of benchmark geometries, some of which fall outside the generated geometry space ('extrapolations'). Like all the generated geometries used for training and testing, all of the evaluation geometries are scaled to have a maximum height of 50 mm. Furthermore, all of them are simulated using the FE forming model in order to allow for the surrogate model predictions to be evaluated relative to the ground truth. This evaluation set

is used to evaluate the generalisability of the trained model: how well the model can predict wrinkling for new, previously unseen tool geometries.
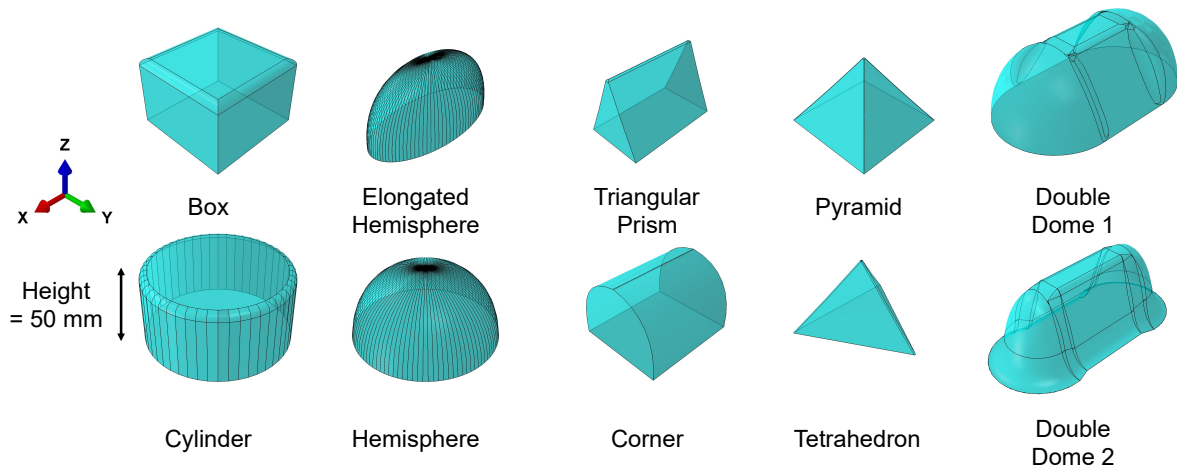
Fig. 5.10 The 10 geometries, making up the evaluation set, that are used to evaluate the performance of the deep learning surrogate model.

Network architecture
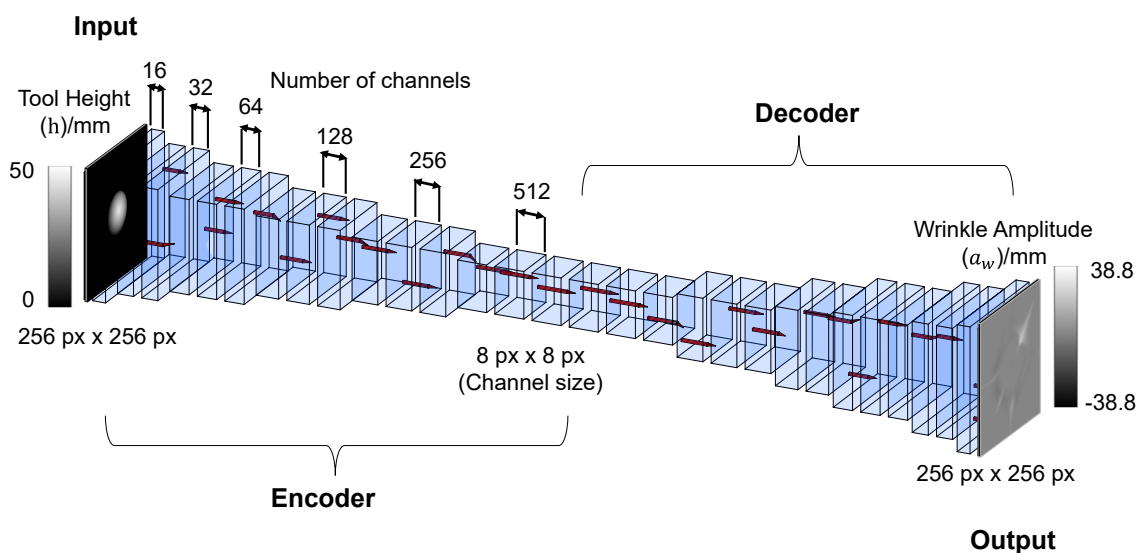
Fig. 5.11 Outline of the fully convolutional network (FCN) used for the wrinkling prediction surrogate model with an example pair of tool geometry and wrinkle pattern images at the input and output respectively.

Table 5.10 Details relating to the fully convolutional network used for the surrogate model, including the specific hidden layers (and their quantity) used within the encoder and decoder stages, the min/max channel sizes, the min/max number of channels and the number of trainable parameters. Note that 'px' refers to pixels.

Network detail	Value/description
Type	Fully convolutional network (FCN)
Input channel size (px $\times$ px)	256 $\times$ 256
Encoder	16$\times$Conv2D 6$\times$MaxPool2D 16$\times$Relu2D
Fully connected layers	None
Minimum channel size (px $\times$ px)	8 $\times$ 8
Decoder	16$\times$Conv2DTranspose 6$\times$MaxUnpool2D 16$\times$Relu2D
Output channel size (px $\times$ px)	256 $\times$ 256
Min channels	16
Max channels	512
Trainable parameters	15,705,185

The deconvolutional network architecture utilised for the deep learning model (shown in Figure 5.11, with additional details in Table 5.10) is developed based on some of the existing, proven-to-work FCNs architectures reviewed in Section 5.2 for image segmentation. A similar but shallower deconvolutional network has previously been shown to be fit for purpose for use as a preforming surrogate model by Zimmerling et al. [152]. The selection and quantity of particular network layers for best performance is not straightforward as neural networks are difficult for humans to interpret and thus empirical investigations were conducted to identify the most optimal network architecture with respect to the most accurate wrinkle predictions. The architecture is primarily inspired by the 'DeconvNet' [167] and the 'SegNet' [169], which are FCN versions of the original 'VGG16' CNN [185]. The network consists of the following key features, with the similarities and differences to these networks highlighted:

- **Input and output layer size**: a layer size of 256 px $\times$ 256 px is used instead of the 224 px $\times$ 244 px in [167, 169, 185]. This provides a higher level of detail in each image at the cost of higher data requirements.

- **Encoder**: the encoder, which divides the input image into an increasing number of smaller feature images, is the same as the 'VGG16' from [185] except that an additional convolution block (3× Conv2D layers, 3× ReLu layers and 1× MaxPool2D layer) has been added to account for the input larger image size. Furthermore, the initial channel size is set to 16 instead of 64.

- **Fully connected layers**: the network contains no fully connected layers as first proposed by [169] as they found it significantly reduces the number of trainable parameters in the model and makes it easier to train. Empirically, removing the fully connected layers was also found to improve the accuracy of the wrinkle predictions.

- **Decoder**: the decoder, which recreates the output image based on the input feature images, is the same as the decoder in [169] except that an additional deconvolution block (3× Conv2DTranspose layers, 3× ReLu layers and 3× MaxUnPool2D layer) has been added. Furthermore, the channel size in the last block is 16 instead of 64 to make the decoder structure symmetric to the encoder.

- **Batch normalisation**: batch normalisation ('BatchNorm') layers are often used after every Conv2D or Conv2DTranspose layer to normalise layer inputs and improve training speed [186] and thus are included in most conventional FCNs such as [167, 169]. However, these were found empirically to have a detrimental effect on wrinkle pattern predictions for this application and thus were removed in this network.

The model contains a total of more than 15 million parameters (Table 5.10) that need to be iteratively trained based on the training set such as to achieve maximum performance on the test set.

Model performance metrics

The model performance for wrinkling patterns and wrinkling severity is assessed during training by means of two contrasting metrics (Table 5.11): a global image comparison metric based on structural image similarity ('image accuracy') and a local pixel-based comparison metric based on the mean wrinkle amplitude difference ('wrinkle error').

The 'image accuracy' metric is used to holistically assess the model performance during training and evaluate how well the predicted wrinkle patterns align with the expected patterns in terms of their shapes and locations. As reviewed by Ding et al. [187], there are a number of ways to assess the similarity between two images, with the most state-of-the-art methods being based on neural networks trained on dedicated image datasets. However, these metrics are

computationally expensive and are trained on real-life photographs and thus not suited for the grayscale, generated images used in this work. Likewise, error-sensitivity measures such as the mean absolute error (*L*1) or the mean squared error (*MSE*), while easy to calculate and interpret, have been shown to not correlate with perceived visual quality [188, 187] and are deemed not suitable for assessing wrinkle patterns because they are too strongly influenced by the 'non-wrinkle' background within any particular image. Furthermore, due to their assumption of pixel independence, they are not able to contextually compare two similar wrinkle patterns that are somewhat offset relative to each other. Instead, a structural metric, which considers the image similarity between image features rather than just pixel-wise similarity, is preferred in this study as it offers an established method for easily assessing the similarity between two images.

As a result, the 'image accuracy' metric chosen in this study is the multi-scale structural similarity metric (*MS* − *SSIM*) [189], which improves upon the default single-scale *SSIM* [188] by considering image details at multiple scales. *MS* − *SSIM* is calculated as the product of the relative luminance (*l*), contrast (*c*) and structure (*s*) of two images (*x* and *y*), where *c* and *s* are calculated at 'M' scales of filtering (by default *M* = 5):

$$MS - SSIM = l_M(x,y) \sum_{j=1}^{M} c_j(x,y) s_j(x,y) = \frac{2\mu_x \mu_y}{\mu_x^2 + mu_y^2 + C_1} \sum_{j=1}^{M} \frac{2\sigma_{xy} + C_2}{\sigma_x^2 + \sigma_y^2 + C2} \qquad (5.9)$$

where $\mu_{x/y}$ refers to the mean of either image *x* or *y*, $\sigma_{x/y}$ refers to the variance of one image and σ_{xy} is the co-variance of both images. Furthermore, $C_1 = (K_1 L)^2$ and $C_2 = (K_2 L)^2$ where *L* is the dynamic range of the image (= 255 for 8-bit image), $K_1 = 0.01$ and $K_1 = 0.03$. In practice, *MS* − *SSIM* is calculated iteratively over patches of the two images using a convolutional filter with kernel size *K* (*K* = 11 by default), with the mean of these reported. *MS* − *SSIM* is implemented as per the 'PIQ' metric library [190].

To calculate the 'image accuracy', the *MS* − *SSIM* is calculated between the 'predicted' wrinkle pattern image from the surrogate model and the 'expected' wrinkle pattern image from the finite element model. From empirical testing on the wrinkle pattern predictions, *MS* − *SSIM* was found to be able to discern between highly similar and dissimilar wrinkle patterns, whereas *SSIM* was less successful. *MS* − *SSIM* conveniently produces a normalised result between 0 and 1, with 1 corresponding to two identical images, making it an easy metric to interpret.

In contrast to the 'image accuracy' which assesses globally how well the two wrinkle pattern images compare, the 'wrinkle error' ($\Delta \overline{|a_w|}$) metric is used to evaluate how well on average the model captures the wrinkling severity for a given expected wrinkle pattern. $\Delta \overline{|a_w|}$ is calculated based on the absolute difference in mean wrinkle amplitudes for the predicted (*p*)

and expected (e) wrinkle images as follows:

$$\Delta \overline{|a_w|}[mm] = \left| \overline{|a_w|}_p - \overline{|a_w|}_e \right| \tag{5.10}$$

While this metric is similar to just simply taking the mean absolute error of image pixels ($L1$), it is different in a key way that makes it a more reliable measure of wrinkling prediction capability. Namely, the image pixels are filtered out to only include regions of the fabric with $|a_w| > 1$ mm. Thus the influence of the background pixels is negated, which could otherwise produce misleading results for the mean amplitude difference. Note that the filtering is applied before the difference is taken and thus the wrinkled regions are calculated independently for the predicted and expected wrinkle images. This is a similar approach that was previously used to quantify the wrinkle amplitude variability in Chapter 4.

Table 5.11 Details relating to the two metrics used to evaluate the performance of the surrogate model for wrinkle prediction. The 'image accuracy' metric is used as the primary metric for the model hyperparameter optimisation.

Metric	Name/unit	Range	Objective
Image accuracy	Multi-scale structural similarity index ($MS-SSIM$)	[0,1]	Maximise
Wrinkle error	Mean wrinkle amplitude difference ($\Delta \overline{|a_w|}$)/mm	[0,∞]	Minimise

Loss function

A loss function is used to direct the training process towards minimising a particular function. The loss function drives the optimisation of network parameters during the training process and thus its selection is crucial for a successful model. Although, in theory, any differentiable function tending to zero can be used as the loss function, in reality, simpler functions have become the norm. The most common loss functions used in training deep learning models are the mean absolute error (L_{L1}) or the mean squared error (L_{MSE}), calculated as follows:

$$L_{L1} = \sum_{i=1}^{P} |x_1(i) - x_2(i)| \tag{5.11}$$

$$L_{MSE} = \sum_{i=1}^{P} x_1(i)^2 - x_2(i)^2 \tag{5.12}$$

where x_1 and x_2 are the two images to be compared, i is the index of the image pixels and P is the total number of pixels in each image. Due to its simplicity and robustness, particularly L_{MSE} has become the default option for most regression optimisation problems [171, 191]. However, the squaring of the error has also been shown to lead the optimisation towards blurred images [171, 192]. Using L_{L1} results in no such blurring and it has also previously been shown to be superior as a loss function in some tasks compared to L_{MSE} [191].

However, Zhao et al. [191] has shown that, while L_{L1} can achieve good results in terms of intensity, it can be insufficient for identifying high contrast regions and proposed that superior results are achieved by combining L_{L1} with a loss function based on $MS-SSIM$, $L_{MS-SSIM}$, as follows:

$$L_{MS-SSIM-L1} = \alpha L_{MS-SSIM} + (1-\alpha)L_{L1} \tag{5.13}$$

where

$$L_{MS-SSIM} = 1 - (MS-SSIM) \tag{5.14}$$

This loss function ($L_{MS-SSIM-L1}$) is adopted in this work as it was found to achieve superior image accuracy results over using $L_{MS-SSIM}$, L_{L1} or L_{MSE} independently (Appendix F). The optimal α was found to be 0.4 (Appendix F) but in order to ensure the best performance for the model, other hyperparameters need to also be chosen carefully.

Model hyperparameters

The hyperparameters related to the deep learning model are selected for maximum accuracy on the test set (Table 5.12) and then used to train the final optimal model (Figure 5.12). The optimisation process is detailed further in Appendix F along with results for each hyperparameter.

Table 5.12 The chosen hyperparameter values for the surrogate model, chosen based on the optimisation results in Appendix F. Note that 'early stopping' refers to stopping the training of the model when the loss function stops decreasing.

Hyperparameter	Value/description
Loss function	$L_{MS-SSIM-L1}$
Alpha (α)	0.4
Learning rate (lr)	2×10^{-4}
Batch size (b)	16
Weight decay (w_d)	0
Epochs (ep)	Early stopping

During training, pairs of input (x) and output (y) images are fed to the network in batches of 'batch size' (b - hyperparameter). The input batch of images is forward propagated through the nodes of the network until a predicted output ($\hat{y}$) is obtained used to calculate the loss (L) relative to the expected output batch of images (y). For this model, the optimal b was found to be 16. This agrees with previous work showing that lower b results in better model accuracy over the typical b values employed [193, 194], at the expense of data parallelism and increased computational time.

After forward propagation, the loss for the batch is then 'backpropagated' through the network in order to calculate the gradients of the node weights with respect to the loss [155]. Based on these gradients, the model weights (parameters) are updated based on a particular optimisation algorithm, that aims to minimise the loss with the 'learning rate' (lr - hyperparameter) specifying the step size of this optimisation. In this case, the model is trained using the popular 'Adam' algorithm [195] that uses adaptive learning rates to robustly reach a global minimum based on the initial lr. The initial lr is one of the most important hyperparameters to select, with too high a lr meaning you do not reach the global minimum and too low a lr meaning the training is too slow to be effective [196]. Based on Appendix F, the optimal initial lr for this model was found to be 2×10^{-4}. Additionally, often a penalty function ('weight decay') with a scaling term w_d is added to the loss function in order to improve generalisability of the model and prevent overfitting [197], but for this application, it was found not to improve performance with $w_d = 0$ being the optimal value for maximum accuracy on the test set (Appendix F).

The above process of forward and backward propagation is repeated in batches for multiple cycles of all images in the training set (epochs) and thus the final hyperparameter to optimise is how many epochs (ep) the model should be trained for such that it is neither overfitted (only performing well on the training set) or underfitted (lower than optimal performance on both training and test sets). To avoid needing to optimise this, and following accepted convention [196, 180], an 'early stopping' algorithm is used to identify the point at which the loss on the test no longer reduces over a p number of epochs, where p is selected, in this case, to be 24.

Training of optimal model

The changes in loss function ($L_{MS-SSIM-L1}$), image accuracy ($MS-SSIM$) and wrinkle error ($\Delta\overline{|a_w|}$) with training time (epochs) for the final optimised model are shown in Figure 5.12, with the red line indicating the epoch from which the final 'optimised' model parameters are taken.
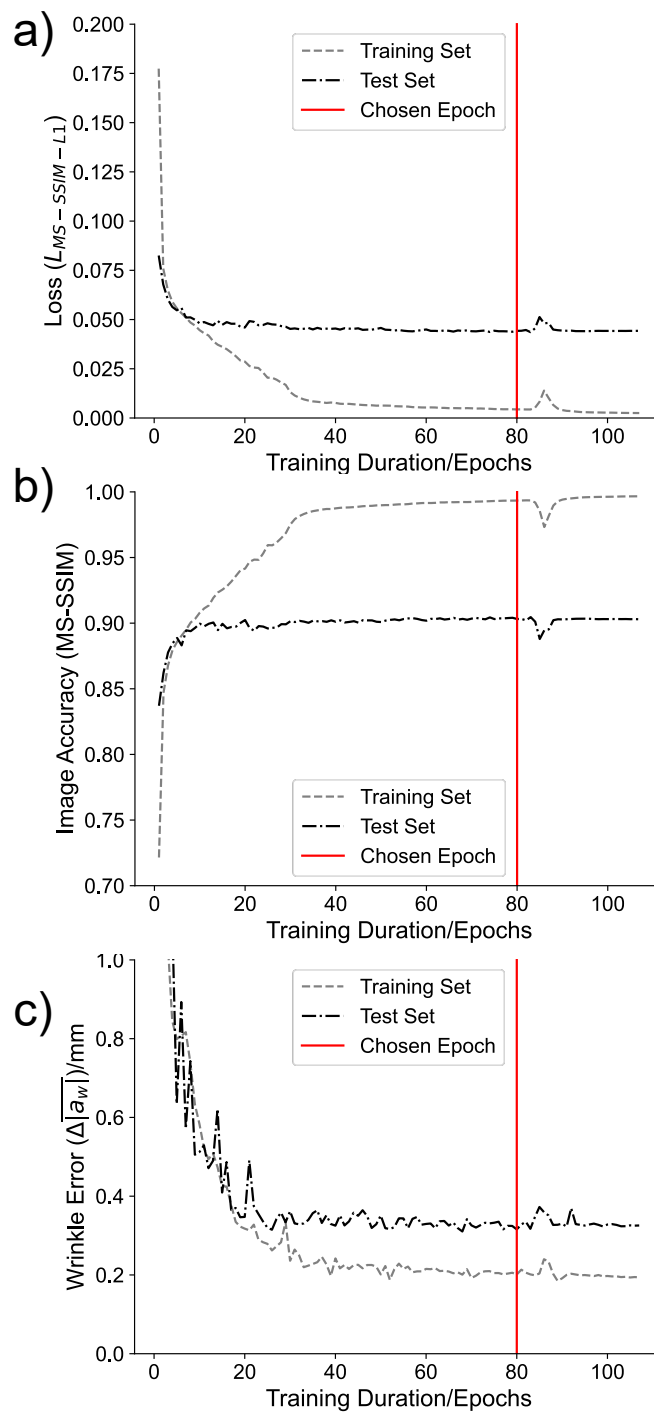
Fig. 5.12 The progression in the loss function (c), the 'image accuracy' (b) and the 'wrinkle error' (c) over the course of training the optimised surrogate model. One epoch corresponds to one full cycle of all the images in the training set. The model parameters that were used to make predictions for the evaluation of the model are from epoch 80 (red line).

Figure 5.12a shows that the loss converges quite quickly towards an optimal solution, after which only iterative improvements are made on the test set, while training set loss continues to decrease further. The early stopping algorithm is activated at around epoch 80 and then the training continues for another 24 epochs before terminating.

The image accuracy in Figure 5.12b is shown to follow a similar but reverse trend to the loss, as would be expected as the loss is partially based on $1 - (MS - SSIM)$. The test set reaches a maximum image accuracy of 0.9, at which it remains for most of the training period, while the training set achieves a maximum accuracy closer to 1. Although ideally there would be a smaller gap between the training and test sets in order to achieve better generalisability, it was found to not be possible to exceed this performance with alternative networks or hyperparameters (Appendix F), suggesting that this limit could only be surpassed by improving the underlying dataset, as will be discussed in Section 5.6.

The wrinkle error in Figure 5.12c is shown to change more erratically during training compared to the image accuracy, which is suggested to be because it is not directly optimised by the chosen loss function, whereas image accuracy is. However, the wrinkle error is still shown to reduce with decreasing loss, suggesting some correlation between the two. It reaches a minimum of around 0.3 mm on the test set but continues to fluctuate around this for the subsequent epochs. Due to these fluctuations, the epoch at which this wrinkle error is a minimum in this plateau phase is chosen as the one for which the model performance is evaluated. Thus, the model parameters at 80 epochs (red line in Figure 5.12) are selected and used in the results of this chapter.

Wrinkle prediction evaluation

The wrinkle predictions of the optimised model are evaluated both on the test set and the evaluation set, with the test set used to better understand the distributions in prediction quality while the evaluation set is used to assess generalisability to new geometries.

In order to quantitatively evaluate how well the model wrinkle predictions (p) compare with the expected (e) ground truth from the FE simulation, the wrinkling metrics from Subsection 5.4.3 are applied to both sets of images. The relative wrinkle errors based on each of the wrinkle metrics are then calculated as follows:

- Max wrinkle error:

$$\frac{\Delta|a_w|_{max}}{|a_w|_{max}}[\%] = \frac{||a_w|_{max_p} - |a_w|_{max_e}|}{|a_w|_{max_e}} \tag{5.15}$$

- Wrinkle area error:

$$\frac{\Delta A_w}{A_w}[\%] = \frac{|A_{w_p} - A_{w_e}|}{A_{w_e}} \tag{5.16}$$

- Mean wrinkle error:

$$\frac{\Delta \overline{|a_w|}}{\overline{|a_w|}}[\%] = \frac{|\overline{|a_w|}_p - \overline{|a_w|}_e|}{\overline{|a_w|}_e} \tag{5.17}$$

where p corresponds to the predicted image and e corresponds to the expected image. These error metrics are used to evaluate the predictive capabilities of the deep learning model. Note that the mean wrinkle error is the relative version of the 'wrinkle error' metric introduced previously in Table 5.11.

In addition to calculating the relative prediction error based on each wrinkle metric, the coefficient of determination (R^2) is calculated to compare how well the predicted values match up to expected values for each wrinkle metric. Based on fitting a line $y_p = y_e$ over all predictions from the test set, R^2 for metric y can be found as follows:

$$R^2 = 1 - \frac{SS_{res}}{SS_{tot}} = 1 - \frac{\sum(y_e - y_p)}{\sum(y_e - \overline{y_p})} \tag{5.18}$$

where $\overline{y_p}$ is mean of y_p and $y = |a_w|_{max}$, A_w or $\overline{|a_w|}$.

5.4.5   Wrinkling-geometry correlation

To analyse the effect particular geometrical characteristics of the tool have on the wrinkling behaviour of the preform, correlation analysis is performed to evaluate the linear coefficient of correlation (r^2) between each characteristic (Figure 5.6) and each wrinkling severity metric. Additionally, the analysis is separately conducted for the wrinkling behaviour in the positive shear (PS) and negative shear (NS) regions.

After fitting a line of best fit $\tilde{y} = mx + b$ between a characteristic x, and a wrinkling metric y, r^2 is obtained as follows:

$$r^2 = 1 - \frac{SS_{res}}{SS_{tot}} = 1 - \frac{\sum(y - \tilde{y})}{\sum(y - \overline{y})} \tag{5.19}$$

where $\overline{y}$ is mean of y. As r^2 is based upon the best fit line through the data, it provides a measure of how well the characteristic and wrinkling metric correlate to another, with $r^2 = 1$ corresponding to a perfect linear correlation and $r^2 = 0$ corresponding to no correlation.

5.5   Results

5.5.1   Typical wrinkling behaviour obtained from FE simulation
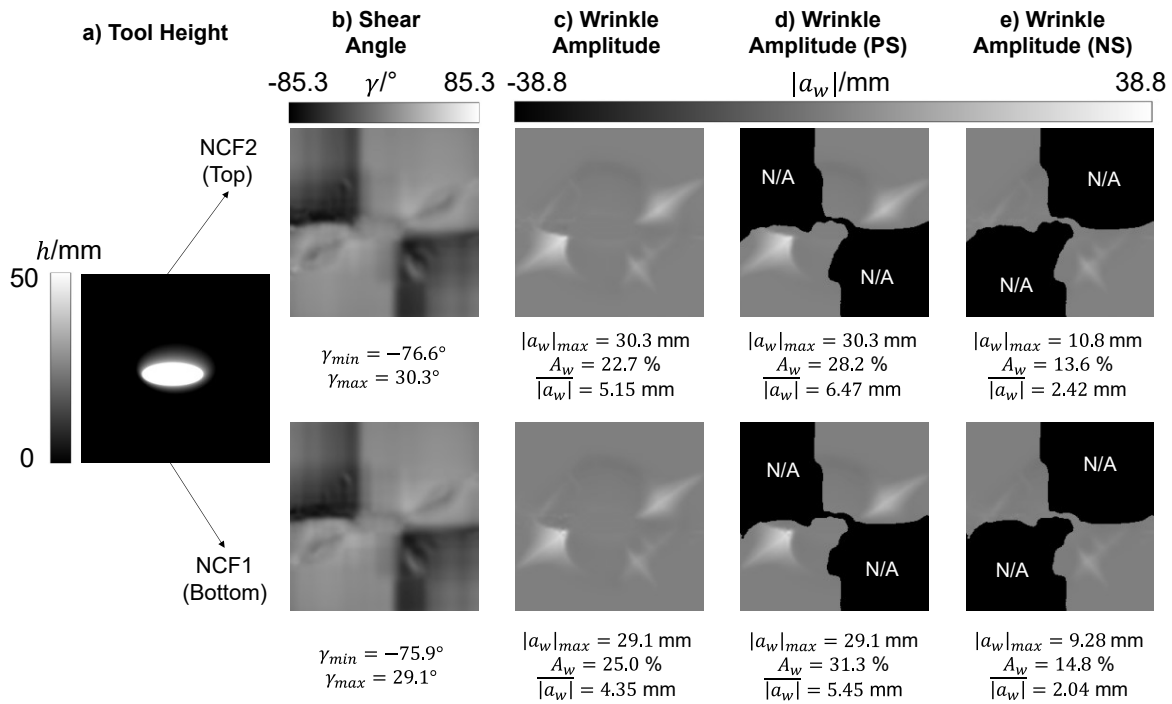
Fig. 5.13 Tool height, wrinkle amplitude and shear angle images for one geometry from the geometry set, shown for both NCF plies ('NCF1' and 'NCF2') within the layup: a) tool height image, b) shear angle image, c) overall wrinkle amplitude distribution image, d) wrinkle amplitude distribution image for just the positive shear (PS) region, and e) wrinkle amplitude distribution image for just the negative shear (NS) region. The values for the max wrinkle amplitude ($|a_w|_{max}$), wrinkle area (A_w) and mean wrinkle amplitude ($\overline{|a_w|}$) are reported under each wrinkle amplitude image while the maximum (γ_{max}) and minimum (γ_{min}) shear angles are reported underneath the shear angle images.

Based on the FE simulation results, the formed NCF layup is shown to result in significant wrinkling of comparable severity in both NCF plies with the largest wrinkles concentrated typically in the positive shear (PS) region of the fabrics. Figure 5.13 shows the simulated wrinkle amplitude patterns for the two layers of the NCF layup obtained for one representative tool geometry (Figure 5.13a), with the corresponding shear angle distribution used to divide the wrinkle patterns into the wrinkle amplitude in positive shear (PS) and the wrinkle amplitude in negative shear (NS).

The shear distribution in Figure 5.13b shows that the simulation successfully captures the asymmetric shear behaviour, with $\gamma_{min} = -75.9°$ and $\gamma_{max} = 30.3°$ for NCF1 (and similar for NCF2). This asymmetry results from the stitching of the NCF being orientated along the shear direction and is crucial in explaining the macroscale wrinkling behaviour of this NCF (Chapter 3). In PS, shearing is limited due to the stitching becoming taut early on in the forming process and thus this NCF tends to wrinkle via lateral compression, while in NS the NCF wrinkles via excess shear once the shear locking angle (γ_l) has been reached.

The wrinkle patterns in Figure 5.13c show that the max wrinkle amplitude is large ($|a_w|_{max}$ = 29.1 and 30.3 mm for NCF1 and NCF2 respectively). Additionally, in spite of the locking angle for this material ($\gamma_l = 57°$) being exceeded in the NS regions, Figure 5.13d-e show that the largest wrinkles are located in the PS region with the wrinkles in the NS region being three-fold smaller in comparison ($|a_w|_{max} = 9.28$ and 29.1 mm for the NS and PS regions of NCF1 respectively). Furthermore, Figure 5.13 suggests that the differences in wrinkling severity between NCF1 and NCF2 of the layup are rather minimal. Regardless, these observations will be further investigated in the next section based on all the simulated tool geometries.

5.5.2   Effect of geometry on NCF wrinkling

Global wrinkling distributions

Considering the distributions of three wrinkling characteristics for all 1802 simulated geometries (Figure 5.14) shows that while the extent of wrinkling is consistently similar for the two NCFs in the layup, the resultant wrinkling severity for both depends significantly on the tool geometry being formed. The distribution of wrinkling characteristics for the tool geometries is approximately normally distributed with a large range for all three metrics and both NCFs (Figure 5.14). The max wrinkle amplitude ($|a_w|_{max}$), plotted in Figure 5.14a, ranges from around 5 mm to 38 mm for all the geometries with a median value between $20-21$ mm for both NCFs. Similarly, the wrinkle area (A_w) distributions for NCF1 and NCF2 in Figure 5.14b are similar in shape and median value but both extend over a large range (from 5% to 60%). Finally, there is more a noticeable difference in the mean wrinkle amplitude ($\overline{|a_w|}$) in Figure 5.14c between the two NCF plies with the top NCF2 having a median $\overline{|a_w|}$ of 4.1 mm that is 0.6 mm greater than the bottom NCF1. However, this difference is not deemed significant enough for the two NCF plies to be treated separately in this study, particularly because the shapes of the distribution are comparable. Therefore, in the subsequent sections and for the training of the surrogate deep learning model, only the data relating to NCF1 is used but the findings are equally applicable to NCF2.
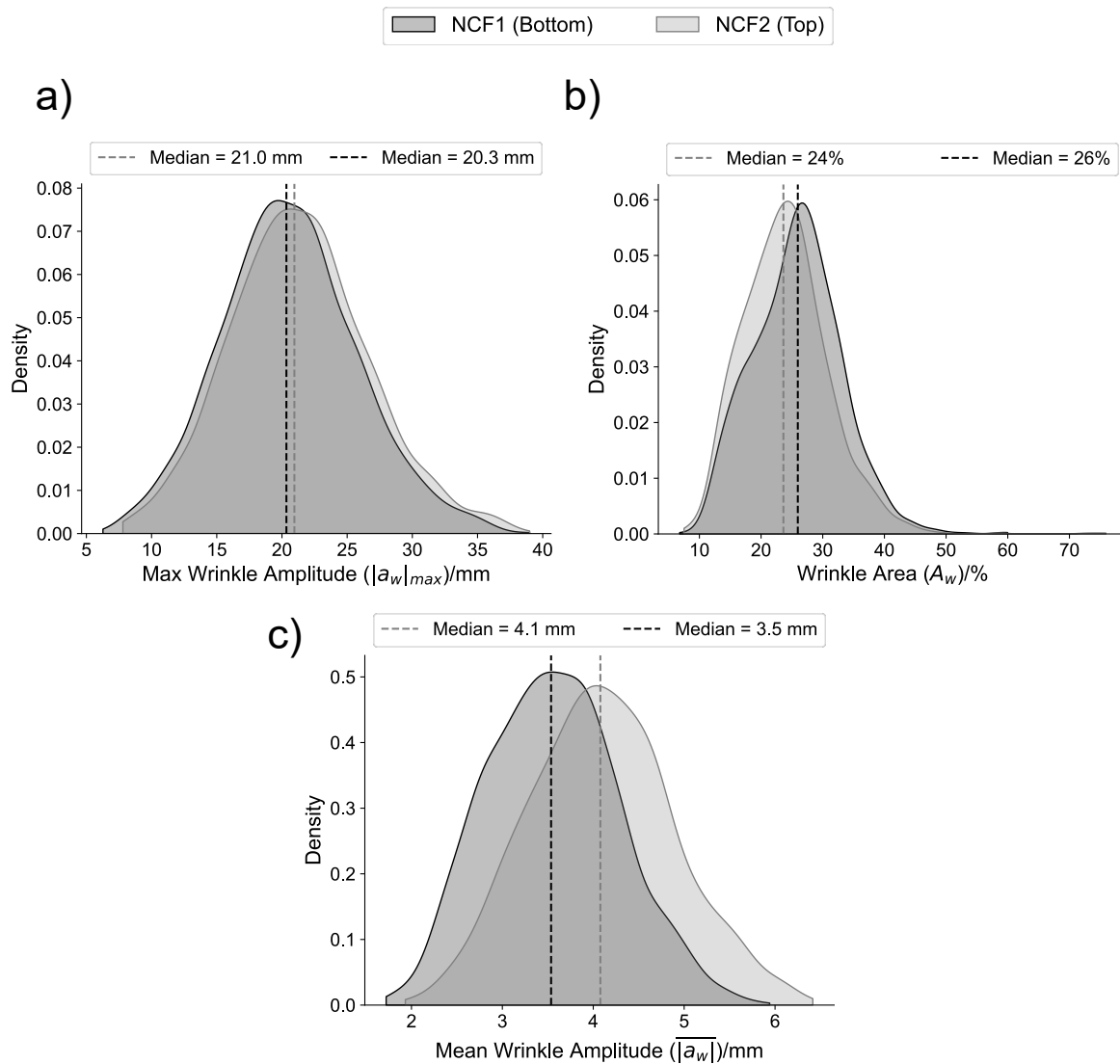
Fig. 5.14 Comparison of the probability density distributions, based on all 1802 simulated tool geometries, of the wrinkling severity between the two NCFs in the layup ('NCF1' and 'NCF2'): a) the distribution of the max wrinkle amplitude, b) the distribution of the wrinkle area, and c) the distribution of the mean wrinkle amplitude. The median values for each distribution are reported.

Comparison of effect on wrinkling by shear region

As shown in Figure 5.15, the wrinkling of the NCF layup is statistically much more severe in the PS regions than the NS regions of the fabric for all the tool geometries investigated, something which can be related back to the two differing wrinkling mechanisms of the fabric. The mechanisms can be inferred from Figure 5.15a, which shows the maximum absolute shear angles ($|\gamma|_{max}$) in each region relative to the known locking angle (γ_l) for this NCF [16]. This

shows that the shear locking angle is predominantly exceeded in NS but not in PS, suggesting that any wrinkles in the PS regions are not due to excessive shearing (most common for textile reinforcements), but rather lateral compression (as described in Chapter 3).
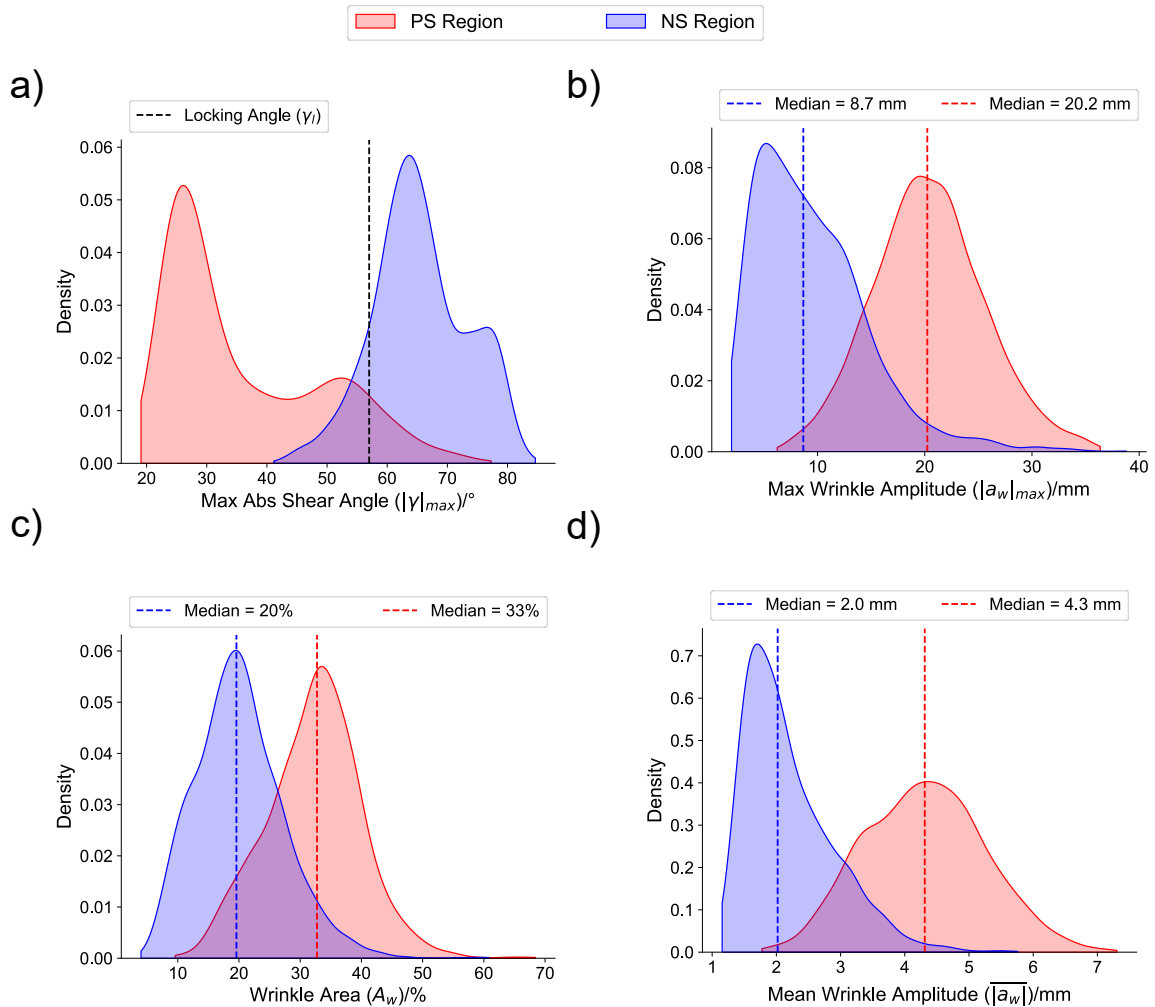
Fig. 5.15 Probability density distributions, based on all 1802 simulated tool geometries, of the shear angle and wrinkling severity in the positive shear (PS) and negative shear (NS) regions of the bottom NCF in the layup ('NCF1'): a) the maximum absolute shear angle distribution for both PS and NS with the shear locking angle for this NCF ($\gamma_L = 57°$ [16]) shown, b) the distribution of the max wrinkle amplitude in PS and NS regions, c) the distribution of the wrinkle area in PS and NS regions, and d) the distribution of the mean wrinkle amplitude in PS and NS regions. The median values for each distribution are reported.

The contrasting wrinkle severity in each region is shown in Figure 5.15b-d, which show that the wrinkling is more severe in PS regions based on all three metrics. For example, the median of the mean wrinkle amplitude ($\overline{|a_w|}$) distribution in Figure 5.15d is more than twice as large

in the PS regions (4.3 mm compared to 2.0 mm) compared to the NS regions. Similarly, the max wrinkle amplitude is on average more than twice as large in PS than in NS (Figure 5.15b), with the wrinkle area also being statistically larger (Figure 5.15c). Albeit resulting in different levels of severity, the effect of the tool geometry is still significant for the wrinkles in both shear regions with the metrics distributions extending over similarly wide ranges (Figure 5.15b-d). As a result, the observations made for the representative tool geometry in Figure 5.13 appear to hold true for all the geometries in the set. Due to the contrasting severity and mechanisms in PS and NS regions, the correlations between the geometrical characteristics and the wrinkling behaviour will be investigated separately for PS and NS wrinkling in the next section.

Correlations between geometry characteristics and wrinkling severity

Figure 5.16 contains plots relating the mean wrinkle amplitude to each of the eight geometry characteristics that were measured for each tool geometry. The figure shows that certain characteristics are significantly correlated with the resulting wrinkling severity while some characteristics have little to no correlation with wrinkling severity. It was found that there are generally few differences between the respective correlations calculated for the three wrinkle severity metrics ($|a_w|_{max}$, A_w and $\overline{|a_w|}$) and thus only the lines of best fit for the mean wrinkle amplitude ($\overline{|a_w|}$) are shown for simplicity.

Based on Figure 5.16a, the mean wrinkle amplitude ($\overline{|a_w|}$) is most strongly correlated ($r^2 = 0.53$) with the Conicity of the geometry, as measured by the mean overall draft angle ($\overline{\theta_{do}}$). This is a negative correlation and thus geometries that are more cone-like (with a higher $\overline{\theta_{do}}$) tend to result in lower mean wrinkles amplitudes. Based on the line of best fit and 95% prediction intervals, $\overline{|a_w|}$ can drop from 4.9 ± 1 mm for $\overline{\theta_{do}} = 0°$ to 2.9 ± 1 mm for $\overline{\theta_{do}} = 45°$, representing a 40% drop in mean severity. Additionally, the Area Ratio (r_A) is shown to be positively correlated with wrinkle severity ($r^2 = 0.38$ from Figure 5.16b). Therefore, results suggest that convex geometries with smaller initial contact points with the fabric lead to less severe wrinkling. However, it is noted that as r_A approaches 0, the correlation becomes weaker. Despite this, given the correlation with the draft angle in Figure 5.16a, this correlation is not surprising as the geometries with a smaller r_A also tend to also have a larger draft angle ($\overline{\theta_{do}}$).

In contrast to the Conicity and the Area Ratio, the Volume Ratio (Figure 5.16c, $r^2 = 0.17$) and Gauss Curvature (Figure 5.16d, $r^2 = 0.18$) are found to be weakly correlated with wrinkling severity. Firstly, increasing the Volume Ratio (r_V), meaning the geometry approaches a cuboid, is shown to lead towards larger wrinkling severity (Figure 5.16c). Secondly, based on Figure 5.16d, geometries with negative Gauss Curvature (inwardly curving) tend to wrinkle more than those with positive K_r (outwardly curving) but the confidence in this correlation is

dampened by the large 95% confidence intervals for $K_r < 1.5 \times 10^{-3}$ mm^{-2}, as most geometries are concentrated close to $K_r = 0$ mm^{-2}. The four remaining characteristics investigated show little to no correlation with overall wrinkling severity. These include Asymmetry (Figure 5.16f, $r^2 = 0.08$), Mean Curvature (Figure 5.16e, $r^2 = 0.03$), Tortuosity (Figure 5.16g, $r^2 = 0.00$) and Angularity (Figure 5.16h, $r^2 = 0.00$).

The correlation analysis is extended in Figure 5.17 to consider the wrinkling in positive (PS) and negative (NS) regions separately, showing that generally similar trends from Figure 5.16 apply for both PS and NS but for certain correlated characteristics, the correlation is more significant for NS than for PS. Most notably, in terms of Area Ratio, r^2 for wrinkling in PS is 0.23 compared to 0.60 in NS (Figure 5.17b). This observation that the correlation is stronger in NS than PS is equally noted for Conicity (Figure 5.17a, $r^2 = 0.39$ (PS) and $r^2 = 0.49$ (NS)). Furthermore, the correlation between Volume Ratio and wrinkling severity is greater in NS ($r^2 = 0.36$) than PS ($r^2 = 0.08$) (Figure 5.17c).
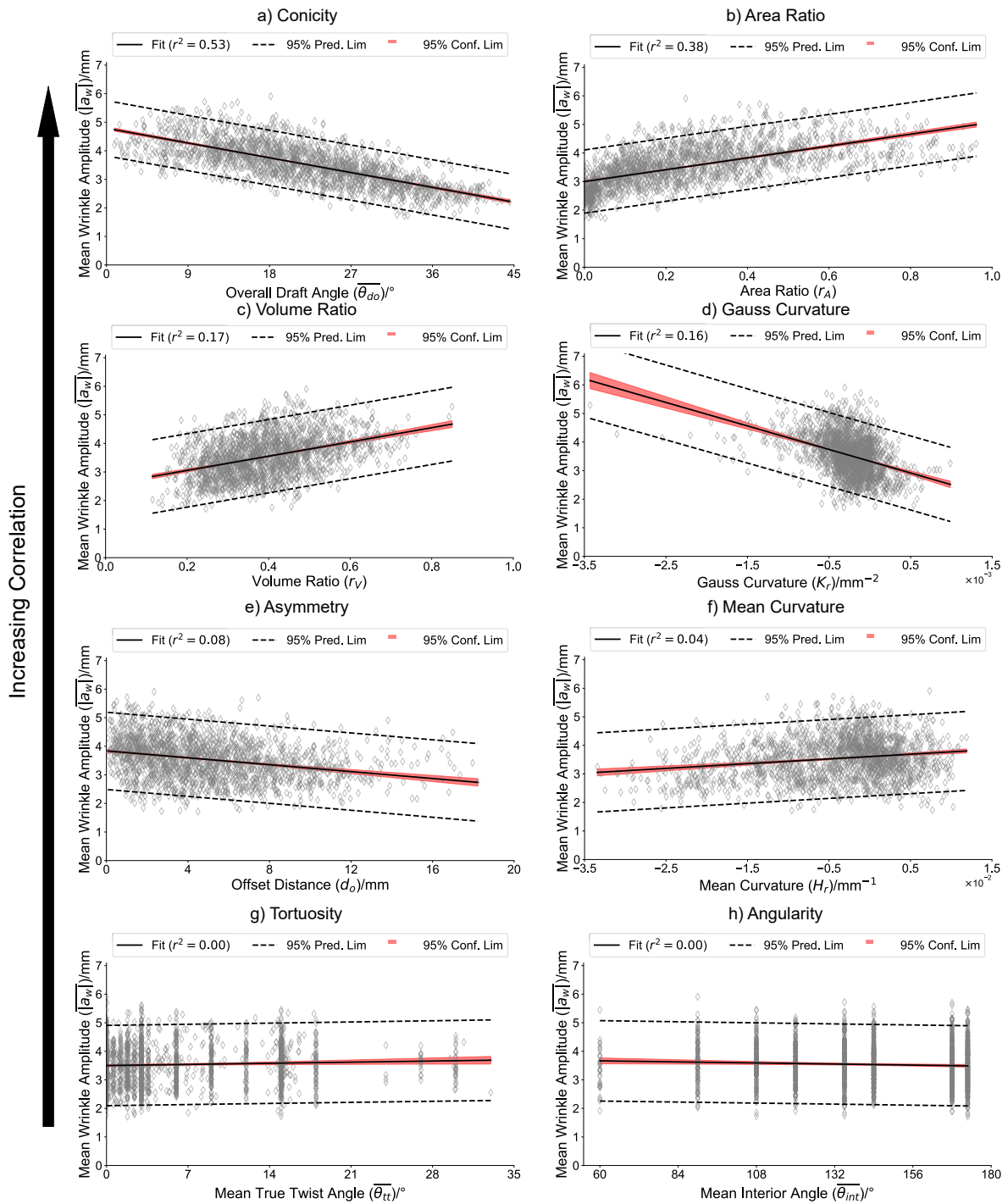
Fig. 5.16 The linear correlation between the eight tool geometry characteristics and the mean wrinkle amplitude, ordered in descending order of the squared coefficients of correlation (r^2): a) Conicity, b) Area Ratio, c) Volume Ratio, d) Gauss Curvature, e) Asymmetry, f), mean curvature, g) Tortuosity and h) angularity. For each correlation, the 95% prediction limits and the 95% confidence limits are also calculated.
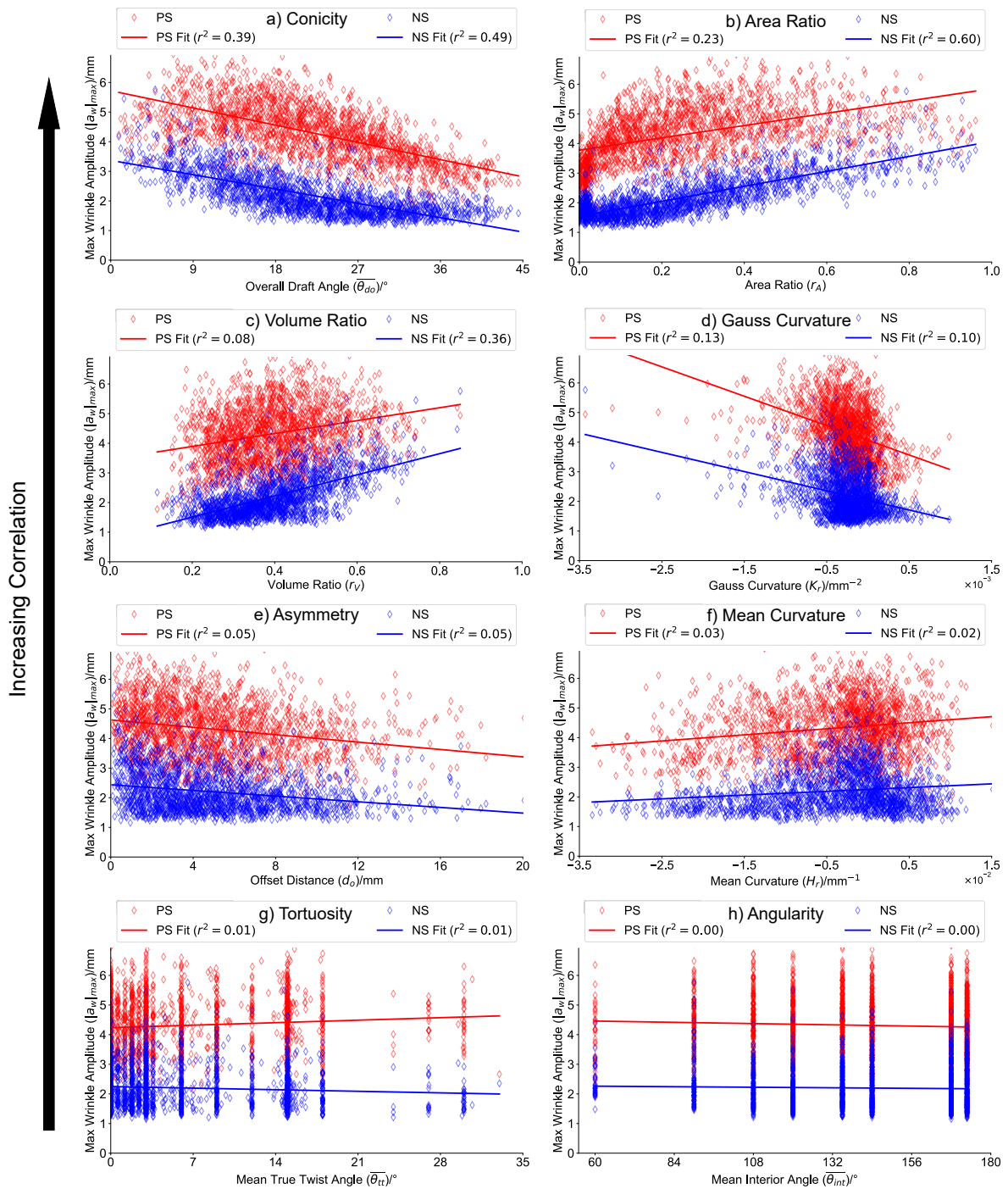
Fig. 5.17 The linear correlation between the eight tool geometry characteristics and the mean wrinkle amplitude in the positive shear (PS) and negative shear (NS) regions, ordered similarly to Figure 5.16: a) Conicity, b) Area Ratio, c) Volume Ratio, d) Gauss Curvature, e) Asymmetry, f), Mean Curvature, g) Tortuosity and h) Angularity.

5.5.3   Surrogate model performance

The analysis of the simulated forming data highlighted some interesting trends in terms of the effect of tool geometry on wrinkling severity. The forming data is also used to train the deep learning surrogate model, and the performance of this model for wrinkling predicting is analysed in this section. This is done by considering the following: the effect of training dataset size on model accuracy, the model predictions on the test set when using all available training data, and the model predictions for the 10 evaluation geometries as compared to the ground truth from the FE model.

Effect of training set size on model accuracy

The effect of training set size (m_{tr}) on the surrogate model image accuracy was evaluated in Figure 5.18, based on a constant test set size ($m_{te} = 186$). It shows that there are diminishing returns for $m_{tr} > 1000$ as the image accuracy converges towards a maximum. This suggests that the number of samples used for training could be almost halved while achieving the same levels of prediction accuracy, thus potentially allowing for the data generation (and training) time to be considerably reduced for this particular task. As there was no previous reference of the amount of data required for effective wrinkle prediction, proceeding with more samples than necessary was a good approach. However, this result is helpful for future work in providing better guidance for how much data is necessary to achieve convergence for such a model.
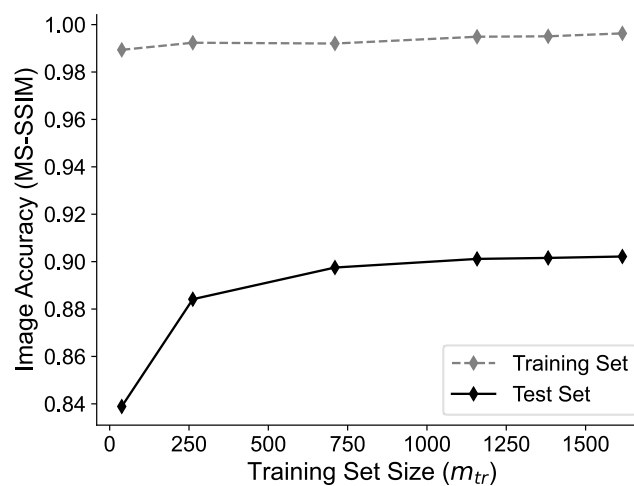
Fig. 5.18 The effect of increasing the training set size on the maximum 'image accuracy' obtained, as measured for the training and test sets respectively. The test set size is kept constant at 186 throughout.

Image accuracy and wrinkle error on test set

The performance of the surrogate model based on predicting the wrinkle amplitude patterns for the 186 geometries in the test set is relatively good with a vast majority of geometries being predicted with high levels of image accuracy and low levels of relative wrinkle error compared to the finite element results.

Figure 5.19a, containing the probability distribution of the image accuracy for all tool geometries in the test set, shows that the predicted images for the test set have a high level of accuracy with 75% of the predictions having a $MS-SSIM > 0.86$ and a median accuracy of 0.93. Figure 5.19b shows examples of wrinkle predictions from each of the six percentile domains (i-vi) in Figure 5.19a with the tool geometry ('Input'), the FE ground truth wrinkle pattern ('Exp. Output'), the surrogate model wrinkle prediction ('Pred. Output') and the inverted pixel-wise error ('Diff') shown. It shows that the predictions with $MS-SSIM > 0.86$ correspond visually to a very good prediction (iii) with only small details missing from the predicted wrinkle image. These predictions get visually better for iv)-vi) with the latter predicted image with $MS-SSIM = 0.99$ being near indistinguishable from the expected ground truth. As such, Figure 5.19 also shows that $MS-SSIM$ is an effective metric for discriminating across the spectrum of 'good' and 'bad' wrinkle pattern predictions.
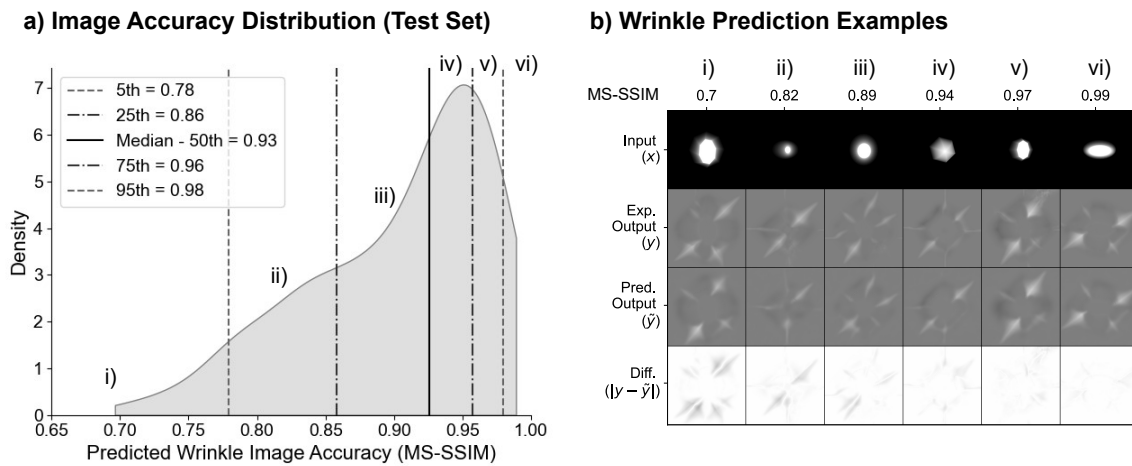
Fig. 5.19 a) The probability density distribution of the image accuracy across the 186 test set geometries with the 5th, 25th, 50th (median), 75th and 95th percentiles shown and b) examples of wrinkle predictions from each of the regions (i-vi) bounded by the percentiles in a), with the image accuracy reported for each prediction. For each example, the tool geometry ('Input'), the FE ground truth wrinkle pattern ('Exp. Output'), the surrogate model wrinkle prediction ('Pred. Output') and the inverted pixel-wise error ('Diff') between the ground truth and prediction are shown.
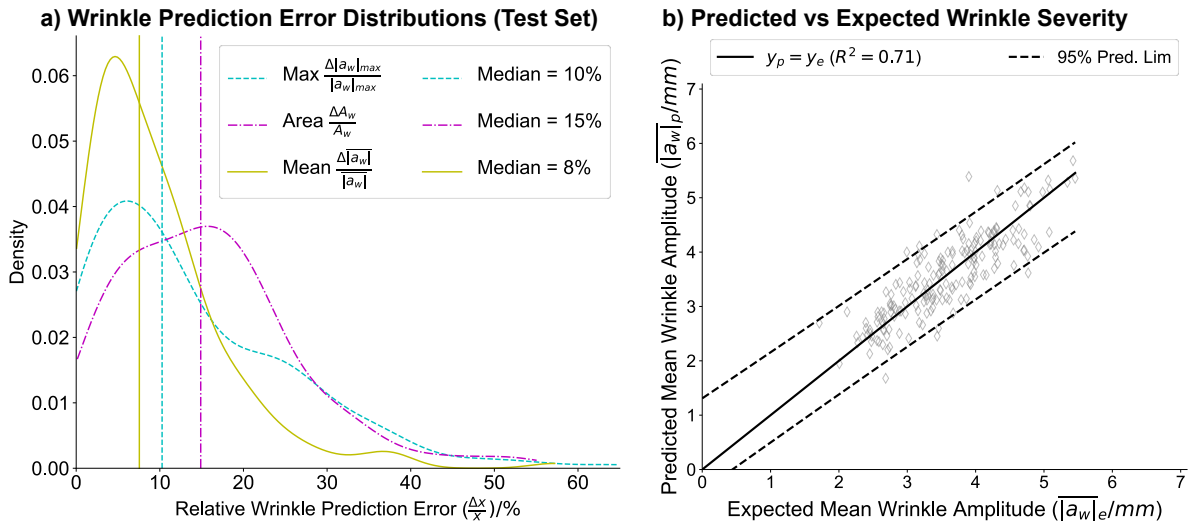
Fig. 5.20 a) The probability density distributions of the wrinkle prediction error for the geometries in the test set, evaluated for the three relative wrinkle error metrics (max wrinkle error, wrinkle area error and mean wrinkle error). The median values for each distribution are also shown. b) The predicted mean wrinkle amplitude vs. the expected mean wrinkle amplitude for all the geometries in the test set with the coefficient of determination (R^2) of the data with respect to the line $y_p = y_e$ reported. The 95% prediction limits of the data are additionally shown.

Figure 5.20 shows that the high image accuracy values observed in Figure 5.19 correspond to low levels of wrinkle error, with the surrogate model doing particularly well in predicting the mean wrinkle amplitudes for each geometry in the test set. However, it is shown to be less accurate with predictions for the max wrinkle amplitude and the wrinkle area. Figure 5.20a displays the probability distributions and median values for the max wrinkle error ($\frac{\Delta |a_w|_{max}}{|a_w|_{max}}$), the wrinkle area error ($\frac{\Delta A_w}{A_w}$) and the mean wrinkle error ($\frac{\Delta \overline{|a_w|}}{\overline{|a_w|}}$) with the median relative error values for the mean wrinkle amplitude being the lowest at 8%, while the wrinkle area had the largest relative error with a median of 15%. Additionally, Figure 5.20b shows that the mean wrinkle amplitude is well predicted by the model with a coefficient of determination (R^2) of 0.71 with respect to the expected values from the finite element model and the line $y_p = y_e$ falling within the 95% prediction limits. While not shown, it was found that the model was less accurate in its predictions of the max wrinkle amplitude ($R^2 = 0.53$) and the wrinkle area ($R^2 = 0.53$), which are both somewhat under-predicted by the model. However, the surrogate model predictions are still sufficient as first estimates of wrinkling severity. This is because the relative differences between tool geometries can be established based on these predictions and therefore the tool geometries resulting in the lowest wrinkling severity can be identified.

Model wrinkle predictions for evaluation set
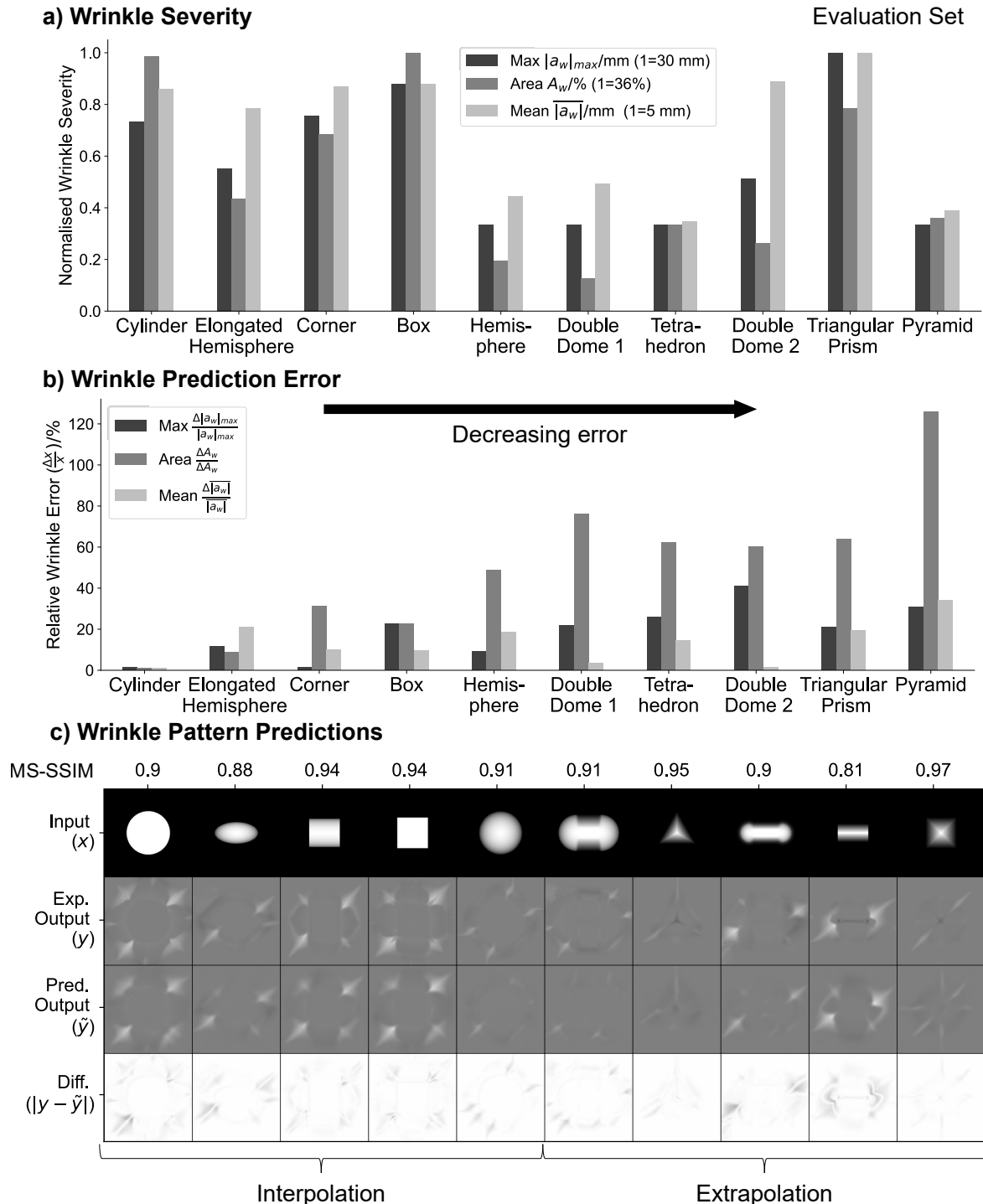
Fig. 5.21 a) The normalised wrinkling severity for the 10 evaluation geometries based on the wrinkling data from the finite element simulation, b) the relative wrinkle prediction error (based on the max wrinkle error, the wrinkle area error and the mean wrinkle error) for the 10 evaluation geometries, arranged from left to right descending in prediction error (based on the mean of the three relative wrinkle error metrics), and c) the wrinkle pattern predictions for all evaluation geometries from the surrogate model ('Pred. Output') compared to the ground truth from the finite element model ('Exp. Output'), with the tool geometry images ('Input') and the inverted pixel-wise difference of the wrinkle patterns ('Diff') also shown.

The model predictions for the previously unseen evaluation set, shown in Figure 5.21, highlight that the surrogate model can successfully predict the wrinkling patterns to a good level of accuracy for certain geometries but for geometries that are clearly outside the boundaries of the training set, it is less accurate.

Figure 5.21a shows the normalised wrinkling severity of the ground truth wrinkle patterns for each evaluation geometry based on three wrinkling severity metrics, showing that the cylinder, corner, box, triangular prism and elongated hemisphere have the highest wrinkling severity out of the ten geometries.

The corresponding error in the wrinkle predictions of the surrogate model for each evaluation geometry is shown in Figure 5.21b, with the geometries arranged in order of decreasing relative prediction error (the mean of the three relative error metrics) from left to right. Thus it shows that the cylinder is predicted with the lowest error and the pyramid is predicted with the largest error. There is a significant range in the measured errors across the geometries with, for example, the wrinkle area error ($\frac{\Delta A_w}{A_w}$) ranging from near 0% for the cylinder to over 120% for the pyramid. Also, the trained model is shown to be better at predicting the mean wrinkle amplitude rather than the wrinkle area or the max wrinkle amplitude, given that the mean wrinkle error ($\frac{\Delta \overline{|a_w|}}{\overline{|a_w|}}$) is generally smaller across the 10 geometries than the other two error metrics.

The predicted wrinkle patterns for each evaluation geometry ('Pred. Output') and the ground truth wrinkle patterns ('Exp. Output') are shown in Figure 5.21c. This figure allows the predictions to be qualitatively evaluated and shows that the first four wrinkle patterns from the left (cylinder, elongated hemisphere, corner and box) are visually well predicted while more noticeable errors in the location and/or numbers of wrinkles are present for the other six geometries. For example, the predicted pattern for the hemisphere has only one noticeable wrinkle whereas four were expected, although that one wrinkle is of the expected size and amplitude. The last five geometries (double dome 1, tetrahedron, double dome 2, triangular prism and pyramid) are also less well predicted, each in their own particular way. For example, for the pyramid, six wrinkles are predicted when only two wrinkles were expected, thus resulting in the very large difference in wrinkle area seen in Figure 5.21c. These last five geometries were expected to be less well predicted as they represent geometries that fall outside of the types of geometries the surrogate model was trained on. Thus they are 'extrapolations' whereas the first five geometries are 'interpolations'. It is notable that the hemisphere should be better predicted by the surrogate model given that it represents an interpolation.

Another observation from Figure 5.21 is that the geometries with better predictions are generally those with more severe wrinkling. This can be attributed to the fact that the model

is optimised based on improving the image accuracy of predicted wrinkle image relative to the ground truth. However, for less severely wrinkled patterns, a high image accuracy can be achieved easier due to the greater influence of the 'non-wrinkle' background of the image (as seen from the high $MS - SSIM$ scores for the triangular prism and the pyramid in Figure 5.21c). This suggests that the image accuracy ($MS - SSIM$) is not always sufficient for identifying high levels of wrinkling accuracy, particularly for these wrinkle patterns of lower severity.

Variability in expected wrinkle patterns for certain geometry types
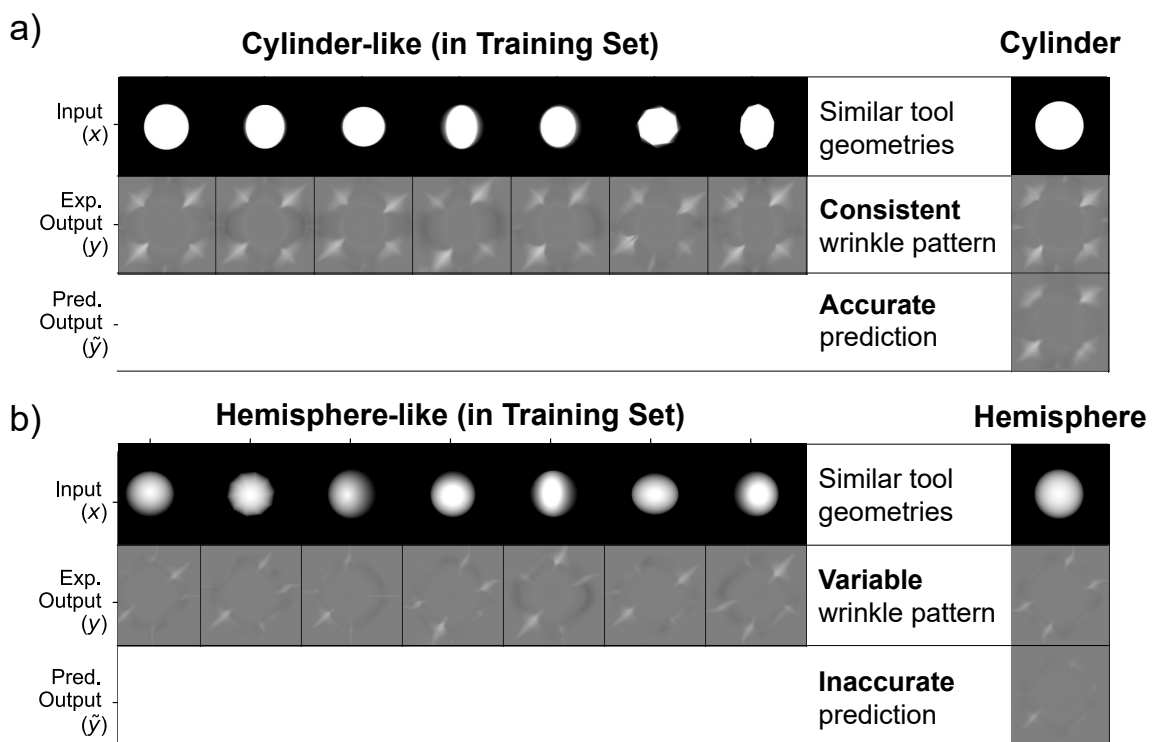
Fig. 5.22 a) A selection of most cylinder-like geometries (based on their $MS - SSIM$ relative to the cylinder) from the training set and their corresponding simulated wrinkle patterns ('Exp. Output') compared against the surrogate model prediction ('Pred. Output') for the cylinder from the evaluation set. b) A selection of the most hemisphere-like geometries (based on their $MS - SSIM$ relative to the hemisphere) from the training set and their corresponding simulated wrinkle patterns ('Exp. Output') compared against the surrogate model prediction ('Pred. Output') for the hemisphere from the evaluation set.

The accuracy of the surrogate model predictions is potentially affected by numerical variability in the wrinkle patterns obtained from the finite element simulations for certain similar geometries, such as the hemisphere. This is seen from Figure 5.22, which compares the surrogate

model predictions for the cylinder (a) and the hemisphere (b), and presents the most similar training set geometries to each of them respectively. The figure shows that the cylinder-like geometries in the training set result consistently in similar wrinkle patterns (four large wrinkles with one in each corner) in the NCF while for the hemisphere-like geometries in the training set, the ground truth wrinkle patterns are more variable with changes in the number of wrinkles and their locations. As also highlighted previously in Figure 5.21, the wrinkle prediction for the cylinder is accurate while the hemisphere prediction is inaccurate. Thus, it is plausible that the differences in the prediction outcomes can be accounted to the variability in the wrinkle patterns for hemisphere-like geometries. This suggests that there is some level of numerical variability within the finite element simulation that can lead to large changes in wrinkle pattern for only small changes in input geometry. The implications of this are further discussed in Section 5.6.

Computational cost of surrogate model

Table 5.13 The computational cost of wrinkle prediction using the trained surrogate model compared against using the equivalent finite element model, based on one tool geometry.

Model type	CPU details	Computational cost/h (% of total)
Macroscale FE model	Intel i9-10980XE @3.0GHz (64GB) - 18 cores	1.33 (16 cores)
Pre-trained deep learning surrogate model	Intel i7-1051OU @1.8GHz (16GB) - 4 cores	0.000215

As shown in Table 5.13, the computational cost of using the trained surrogate model to get wrinkle predictions for one tool geometry is many orders of magnitude lower than the alternative of running the equivalent finite element model of comparable accuracy. The average computational cost for one image prediction using the surrogate model is less than 1 second (0.7 s or 0.000215 h) using a conventional CPU while the cost of running the FE model with a high-performance CPU and parallelised over 16 cores is 1.33 h. Thus the surrogate model achieves approximately a 6000 times reduction in prediction time compared to the FE model.

Table 5.14 The computational cost of developing and using the surrogate model used in this investigation, including the data generation, model training and prediction stages.

Stage	CPU/GPU details	Computational cost/h (% of total)
Simulated data generation using FE model	**CPU**: Intel i9-10980XE @3.0GHz (64GB) - 18 cores	1307 (99.3)
Surrogate model training	**GPU**: NVIDIA GeForce RTX 2070 Super (8GB)	9 (0.7)
Prediction	**CPU**: Intel i7-1051OU @1.8GHz (16GB) - 4 cores	0.000215 (0)
All		1316 (100)

In contrast, Table 5.14 shows that the development of this deep learning surrogate model has significant computational costs due to, primarily, the need to run thousands of simulations to generate the wrinkling dataset for training. The generation of the wrinkling data using finite element simulations for 1802 geometries is calculated to be approximately 99.3% of the total development cost of 1316 h (or 55 d). The training of the surrogate model is only 0.7% of the total time at 9 h, while the cost of predictions is negligible in comparison.

5.6 Discussion

The discussion is divided in the context of the two objectives: assessment of the effect of geometry on wrinkling and the development of a deep learning surrogate model for wrinkling prediction.

5.6.1 NCF wrinkling and tool geometry

Significance of geometry effect

The results of this investigation show that the shape of the tool geometry has a significant global effect on the wrinkling severity of this biaxial NCF during DDF, with this being independent of the underlying wrinkling type within the positive and negative shear regions respectively. The large variations in wrinkling severity for the 1802 widely contrasting geometries investigated are seen in Figure 5.14. More specifically not only does the tool geometry affect the amplitude

of the wrinkles but also their width, quantity and relative positions on the fabric (see for example Figure 5.19 and Figure 5.21), thus resulting in highly contrasting wrinkle patterns. The independence of this significant geometrical effect with wrinkling type for this NCF is observed in Figure 5.15: the distributions in wrinkle severity are similarly widespread in both PS and NS regions, each corresponding to different wrinkle mechanisms respectively (as discussed in Chapter 3).

Furthermore, it is also shown that wrinkling severity across all the tool geometries investigated is more than twice as large for the non-shear wrinkles in the PS regions than the shear wrinkles in the NS regions (Figure 5.15). This finding is in agreement with what was found for the same NCF during experimental press forming tests in Chapter 3 and more comprehensively suggests that for this $\pm 45°$ NCF, it is the non-shear wrinkles in PS regions that are of primary concern for the manufacturing of $\pm 45°$ biaxial NCFs. Thus they should be the primary focus with respect to wrinkling mitigation. This conclusion is in agreement with the findings of Yu et al. [45] for DDF using the same NCF, where the wrinkles in positive shear were more prominent.

However, while the large variation in wrinkling severity suggests that there is potential for modifying the underlying geometry to *reduce* wrinkling severity, it is also noted that these wrinkles formed are still significant for all geometries (the lowest maximum amplitude recorded across all geometries is 7 mm - Figure 5.14). Therefore, when dealing with difficult-to-form male geometries with double curvatures [182], modifications to the geometry cannot fully remove wrinkles and forming process optimisation tools need to also be implemented to address this issue.

The link between geometry characteristics and wrinkling severity

While the global effects of geometry on wrinkling are significant, this study also suggests that certain geometrical characteristics of the geometry contribute more strongly than others towards the resultant wrinkling severity in the final preform, with these trends being broadly similar for the wrinkling in the two distinct shear regions of this biaxial NCF. Based on Figure 5.16 and Figure 5.17, it was found particularly that the Conicity, Area Ratio, Gauss Curvature and Volume Ratio correlate to some extent with wrinkling severity while the Asymmetry, Mean Curvature, Angularity and Tortuosity were found to not be correlated at all with wrinkling severity. The strongest correlation was found to be with Conicity (Figure 5.16a) and this negative correlation suggests that more conical geometries (with higher draft angle) that are more tapered along the vertical axis of the tool (e.g. hemisphere) are likely to result in less severe wrinkling than those with abrupt edges and no tapering (such as a box or cylinder). This

is further supported by the (weaker) correlation with Volume Ratio (Figure 5.16c), where a larger Volume Ratio tends towards a more 'boxy' geometry. Furthermore, the strong negative correlation with Area Ratio (Figure 5.16b) is suggested to emphasize a similar conclusion as a lower Area Ratio also tends to have more tapered sides (Figure 5.6). As this correlation is found to not apply for very small area ratios ($r_A < 0.01$), it suggests that the initial contact area with the geometry is less significant than the mean angle formed by the top and bottom areas relative to the vertical axis (mean overall draft angle - Conicity). The aforementioned three characteristics that have the highest correlation with wrinkling severity all describe, to some extent, how abruptly or gradually the topology of the tool geometry changes along its vertical direction. Thus it suggests that this is the most important design feature to optimise for wrinkling mitigation purposes. This effect is exemplified in (Figure 5.21) by how the tetrahedron, the hemisphere and the pyramid have significantly lower wrinkle amplitudes compared to the box and the cylinder. However, Figure 5.17 also showed that for those three characteristics, the correlation is stronger for wrinkles in NS regions and therefore it suggests that increasing the Conicity of the geometry is more likely to reduce the shear wrinkles in negative shear than non-shear wrinkles in positive shear, with the latter found to be of greater severity (Figure 5.15). This is likely to be because the more conical geometries result in lower levels of in-plane shear and thus do not necessarily reach the shear locking angle in NS, whereas in PS the non-shear wrinkles are more difficult to avoid as they are observed at very low levels of shear ($\gamma = 8°$ based on [63]).

The mild correlation of wrinkle severity with Gauss Curvature (K_r, $r^2 = 0.16$) but not with the Mean Curvature (H_r, $r^2 = 0.03$) is an interesting finding and suggests that the product of the local principal curvatures is more critical than their sum for affecting wrinkling. Based on this, geometries with positive K_r (locally convex, outwardly curving e.g. hemisphere) are suggested to wrinkle less than geometries with negative K_r (locally concave, inwardly curving). While no comparable study exists in the literature, this suggestion is supported by the experimental press forming findings in Chapter 3 and by the DDF simulations for the evaluation geometries (Figure 5.21a): the hemisphere, the two double domes and the elongated hemisphere all wrinkle less severely than the geometries of zero Gauss Curvature (cylinder, box and triangular prism). However, it is also noted that the Conicity has a more significant role in wrinkling than the Gauss Curvature given that the high Conicity, zero Gauss Curvature geometries of the tetrahedron and the pyramid result in the lowest levels of wrinkling severity from the evaluation geometries (Figure 5.21a).

The lack of correlation between the mean interior angles of the geometries (Angularity) and wrinkling severity (Figure 5.16h) is a rather surprising finding given how you might expect

more angular shapes (e.g. a triangular cylinder) to be more difficult to form than a more rounded geometry (e.g. regular cylinder). However, this suggests that the sharpness of the angles along the sides of the geometry is not significant for wrinkling, and is further exemplified by how the cylinder and the box have very similar wrinkle patterns in Figure 5.21c, despite highly contrasting levels of Angularity. Furthermore, given that the Angularity has no effect, it also explains why the Tortuosity (or twisting about the vertical axis) has no effect (Figure 5.16g) because essentially this just reorientates the vertices of the top and middle polygons, which have been shown to not to contribute towards the wrinkling severity.

Lastly, it is interesting to note that (Figure 5.21a) suggests that the tetrahedron wrinkles less severely compared to the triangular prism and to a similar level to the hemisphere and the double dome, which is in contrast to Chapter 3 where the tetrahedron is found to wrinkle most severely based on press forming of the same fabric. This suggests that the observations made regarding the effect of the tool geometry found in this study for DDF cannot necessarily be extended to other preforming processes without verification. As a result, this prompts the need to compare the effect of tool geometry for different preforming processes.

Implications for mitigating wrinkling through component design

Based on the correlation analysis (Figures 5.16-5.17), certain practical guidelines for designing components or tooling to achieve minimal wrinkling in the final component can be suggested. Firstly and most critically, more tapered, conical tool geometries tend to wrinkle less during double diaphragm forming and thus introducing a larger overall draft angle into the tool geometry is likely to be beneficial from a manufacturing point of view. For predefined designs with limited scope for changes, a similar improvement in terms of wrinkling defects could potentially thus also be achieved by introducing larger fillets or chamfers onto component top edges such that transitions along the geometry topology are more gradual. Furthermore, introducing positive Gauss curvature i.e. outwardly curving surfaces are suggested to reduce wrinkling and thus introducing dome-like features instead of inner radii could be beneficial. Finally, in terms of what does not affect wrinkling, the study suggests that having asymmetrical features, twisted features along the height of geometry or having angular sides to the geometry have no effect and thus are less critical from a design for manufacturing perspective. While these observations are limited to convex, standalone geometries, they can equally be applied in more complex industrially applicable geometries where often geometrical features are located far enough apart such that they can be thought of independently from a forming perspective [107]. However, as shown by Krebs et al. [182], the wrinkling resulting from a female tool during DDF is significantly different and thus these guidelines do not necessarily apply in those

cases, or for other preforming processes as previously mentioned. In any case, further work is required to validate these guidelines for a wider array of geometries and forming situations.

Limitations of geometry analysis method

The method used to investigate the effect of geometry on wrinkling severity is unique within composites manufacturing due to the large of geometries involved and thus it provides useful insights, but nevertheless, it has certain limitations.

Firstly, the large number of geometries means that it is more challenging to analyse the nuanced differences in effect between similar tool geometries, which would be more feasible with fewer geometries. Instead, the analysis is more broad stroke, based on global characteristics, which cannot fully describe any one geometry on their own, but rather are simplified approximations that describe the average value for one particular aspect of the geometry. For example, the mode of the local curvature distribution (Appendix E) does not necessarily capture local regions of extreme curvature , which could have a significant contribution to wrinkling.

This highlights the second limitation in that the correlations are analysed separately for each characteristic (Figures 5.16-5.17) but given how each geometry has a unique set of measured characteristics, these observed trends can hide within them contributions from the other characteristics. For example, the Area Ratio appeared to correlate well with wrinkling severity up to a certain point but it was found that this trend was actually more closely linked to the change in draft angle (Conicity) rather than the Area Ratio itself (Figure 5.5.2. This occurs because the characteristics are not fully independent of each other and because the effects of other characteristics are not controlled for in this study. As such, using more tightly controlled geometry sets where only one parameter or characteristic is changed in each case, might allow for more comprehensive conclusions to be drawn.

Thirdly, some of the characterisation metrics are limited by the precision of the method used to calculate them, in particular for the mean and Gauss curvature. Due to the generation method utilised (Figure 5.4), the curvatures had to be obtained from a surface fitted through the geometry coordinates (Appendix E) but a fully representative surface fit was not always possible for all geometries (particularly for the filtered geometries containing undercuts), which could have affected the final accuracy of H_r and K_r. Thus an alternative strategy for generating geometries that does not approximate curvatures radially around the tool would allow for more accurate curvature values to be obtained based on the true geometry.

Fourthly, the wrinkling severity observed in this study is slightly exaggerated by the use of a lower bending stiffness than measured experimentally and also by characterising the bending

stiffness as linear (Table 5.4), and thus for more accurate results, a non-linear bending model should be implemented [63, 57], although this would add significant computational cost.

Finally, this geometrical analysis could be affected by the asymmetrical wrinkling behaviour of this ±45° biaxial NCF. This means that the largest wrinkles tend to be focused in the PS regions irrespective of the underlying tool geometry and thus depending on the orientation of local features on a tool, its effect could be amplified or weakened. To negate this effect, two simulations for each geometry could be done with two layups that are rotated 90° relative to each other (e.g. [0°/90°, 0°/90°] and [90°/0°, 90°/0°]) such that each tool region is both in PS and NS. Alternatively, a fabric with symmetric shear behaviour could be utilised.

5.6.2 Surrogate model for wrinkling prediction

Assessment of model performance and usefulness

The deep learning surrogate model is assessed to perform well when interpolating to new geometries and its usefulness is aided by the potential to reduce the number of geometries for training but hindered by an apparent accuracy ceiling that cannot be exceeded for this wrinkling dataset. The results showing the performance of the surrogate model for wrinkling predictions (Figure 5.21 suggest that it provides good predictions for geometries that are similar but it is shown to become less accurate when extrapolating to new geometries far beyond the training set. With regards to the extrapolation geometries, the two double domes consist of two peaks that make simultaneous contact with the fabric while all the generated geometries only have one initial point of contact with the fabric, thus significantly affecting the shear distribution and wrinkling patterns in ways that the surrogate model cannot appreciate. Secondly, the tetrahedron and pyramid both consist of sharp peaks and these types of geometries had been eliminated from the training set at the filtering stage due to concerns about fabric penetration during simulation creating unrepresentative results (Figure 5.5). This limited extrapolation capability highlights the importance of selecting the initial dataset such that it is fit for the purpose of your application. This finding regarding limited extrapolation capabilities is in agreement with those of Zimmerling et al. [152] for the prediction of shear angle patterns, who found their FCN surrogate model was only effective on convex shapes but not on concave shapes, which were outside of the training set.

The usefulness of the surrogate model derives from how fast it is to obtain predictions from the trained model. The cost of predictions using this surrogate model is shown to be over 6000 times lower compared to running the equivalent FE model (Table 5.13) and thus it is highly useful in a number of academic and industrial applications. Furthermore, this shows that the

more complex the phenomenon that is being simulated, the higher the benefit of using a trained surrogate model as the surrogate model prediction cost will be near-constant irrespective of complexity while the parent model cost will increase with complexity and accuracy (Figure 5.1). Furthermore, the time for just training the model is on the same order of magnitude as running a FE model for wrinkle prediction (9 h), making it efficient to train new networks once you have a suitable dataset for training.

However, the usefulness of this wrinkling prediction surrogate model is currently held back by the high total computational cost ($\sim$ 2 months) for developing the model, of which generating the wrinkling data using a FE model takes up a vast majority (Table 5.14). This high initial cost of this wrinkling surrogate model illustrates why previous forming surrogate models [107, 152] have relied upon vastly computationally cheaper parent models, sacrificing accuracy for the sake of accessibility. However, the results (Figure 5.18) also show that the number of geometries used for training could be significantly reduced without affecting final model accuracy, thus making this approach more accessible and useful. In fact, the number of geometries could be reduced by about half (see Figure 5.18), thus reducing the total data generation time by close to a month (Table 5.14). Further reductions in computational cost could also be achieved by further optimising the runtime of the FE model (Figure 5.7).

Interestingly, the optimisation of the model network and hyperparameters for maximum accuracy (Figure 5.12 and Appendix F) suggest that there is an accuracy ceiling with regards to performance on the test set that cannot be exceeded, irrespective of the chosen network or parameters. Thus this implies that the underlying dataset limits the maximum performance, either due to the sampling of the geometries or due to inconsistencies in the wrinkling patterns for a given geometry, as was found for the hemisphere in Figure 5.22b.

Implications for using DL surrogate models for improving preforming and minimising wrinkling

The surrogate model developed extends understanding about the potential uses of surrogate models within composites manufacturing by showing that it is indeed possible to apply surrogate modelling for the study of wrinkling behaviour directly, without having to rely on the (insufficient) predictions of the shear angle distributions [152, 107]. As such, this work allows the scope of studies investigating the effect of the tool on wrinkling to be expanded, particularly for $\pm 45°$ biaxial NCFs with irregular wrinkling mechanisms. For example, knowing that the predictions from the trained model are sufficiently accurate, the correlation analysis could easily be extended to new sets of similar geometries in a computationally efficient way.

Due to the low computational cost of the deep learning (DL) surrogate model developed compared to its high-fidelity parent model (Table 5.13), it holds tremendous potential for component geometry optimisation. As a concrete example, by incorporating the DL surrogate model within an optimisation scheme consisting of a parametrised CAD model of the initial component design to be manufactured via RTM, all the potential parameter combinations can be iteratively tested until an optimal geometry is obtained that minimises the mean wrinkle amplitude ($\overline{|a_w|}$) during DDF. Such an approach was recently employed by Hao et al. [198] for the design optimisation of curvilinearly stiffened panels, showing that it achieved much-improved component performance at a lower computational cost compared to other surrogate-based optimisation methods. While the accuracy of the surrogate model is not quite as high as its parent model, it is sufficiently good that it can identify relative differences between potential geometries (Figure 5.10) and allows for a time-efficient exploration of the potential design space, as shown by Zimmerling et al. [107]. Once the optimal design has been found via the surrogate model, the predicted wrinkling behaviour can also be validated by running the FE model and/or via experimental testing.

Furthermore, in contrast to FE models that require significant levels of technical expertise for use for fabric forming, pre-trained DL surrogate models could become particularly useful within the composites manufacturing industry due to their ease of use and rapid predictions, and thus could replace the default methods of kinematic modelling, and trial and error testing. While this work focused on predictions based on changes in tool geometry, similar surrogate models can be trained based on changes in different forming process parameters [180]. These various factors affecting formability and wrinkling could also be incorporated within the same surrogate model by expanding dataset and model inputs, as has been done within metal forming [166], giving the engineers a simple tool to obtain rapid forming results for any given forming case without having to resort to expensive experimental testing.

Another potential area where such surrogate modelling could become particularly useful is for the simulation of large scale components on the scale of multiple metres where the defects occur within local regions of that component at a much smaller scale, as is common for aerospace components. Yu et al. [45] showed that a global-to-local modelling strategy could be used for this purpose to capture the wrinkling severity of the plies only in the key regions of interest where wrinkling is predicted to occur, thus reducing total computational time. However, assuming that the regions of wrinkling are far enough from each other to be independent in terms of behaviour [107], the FE sub-models could be replaced by a trained surrogate model that obtains predictions significantly faster. Such an approach was previously proposed by

Zimmerling et al. [107] but focusing solely on the shear distributions around the key locations of interest.

Limits to the wrinkling predictions of the surrogate model

No surrogate model will be equally as accurate as its parent model but for this application to wrinkling prediction, it was found that the maximum accuracy of the developed model was limited beyond a certain point (Figure 5.12 and Appendix F). This is in contrast to a previous study using a similar model for predicting shear angle distributions during forming, where higher levels of accuracy seemed to have been achieved [152]. While this also could potentially be due to unequal sampling in the training dataset, it is suggested that instead, predicting wrinkle patterns based on a phenomenological model is more challenging due to the underlying variability in simulating wrinkling (Figure 5.22). The capacity of any phenomenological model to accurately predict an output image based on an input image requires that the relationships between input and output are consistent for all sets of inputs and outputs. However, it is suggested that for this wrinkling surrogate model, this assumption does not always hold and thus potentially restricting the model from achieving higher levels of image accuracy. This is supported by how the surrogate model incorrectly predicts the wrinkle pattern and the number of wrinkles for the hemisphere despite there being numerous hemisphere-like geometries in the training set (Figure 5.22b). This is because, unlike for the cylinder-like geometries (Figure 5.22a), the hemisphere-like geometries result in widely different simulated wrinkle patterns, implying that these wrinkling patterns do not necessarily follow empirically from the input tool geometries, which are similar in this case. This indicates that the FE model is subject to numerical wrinkling variability that can make the simulated wrinkles patterns less reliable in certain cases. While experimental wrinkling trials are also subject to certain variability (Chapter 4), it is unclear whether the results for *all* tool geometries are representative of the 'real' fabric behaviour. Thus further work is necessary to analyse this numerical variability in the simulations by analysing the robustness of the model under various conditions and comparing the wrinkling predictions against experimental results.

Additionally, variability of the fabric wrinkle patterns exposes another limitation of this surrogate model's predictions. This is because the predictions are single deterministic results for a given tool geometry but in reality, as highlighted by Figure 5.22b and the results in Chapter 4, wrinkling variability cannot be avoided, neither numerically or experimentally. To address this, the full range of experimental wrinkling possibilities should be incorporated within the modelling framework, while the numerical variability should be minimised. While conventional deep learning surrogate models, like the one employed in this work, cannot incorporate

probabilistic outcomes, there is currently significant ongoing research into extending the capabilities of deep learning models, as reviewed by Masegosa et al. [199]. One method of implementing variability within the deep learning network would be to incorporate a 'variational auto-encoder', which produces a probabilistic distribution of values for a given input [199]. However, training such a probabilistic deep learning model and understanding its limits requires that probabilistic training data is available. Thus probabilistic FE forming simulations based on incorporating experimental variability are needed, as will be discussed further in Chapter 6.

Limitations of method

The method used to develop this surrogate model has certain limitations that should be addressed, namely with respect to the geometry space used, the high cost of data generation and the training approach.

Firstly, in terms of the geometry space, the usefulness of the model for predicting geometrical effects is limited by the types of geometries it was trained on and thus, despite its potential, it is unlikely to be directly useful for industrial use given that the geometry space used (Figure 5.4) is not representative of typical composite components in the aerospace or automotive industries, that are typically larger in scale and more complex in terms of their features (Figure 2.4). Therefore while the proposed model in its current form is useful for assessing wrinkling patterns for certain types of generic convex geometries and as a proof of concept for such an approach, alternative geometry sets would need to be developed for use with industrial applications, thus highlighting a key avenue for further work.

This leads to another key limitation of the method which is the high initial computational cost for generating the simulated data that is used to train the model (nearly two months of continuous computing for this task - Table 5.14), which makes it time-consuming to implement and cumbersome to make changes to the underlying approach. Despite this, based on the popular strategy of transfer learning [200], previously trained models can be retrained for a new task based on smaller sets of new data and thus the computational costs associated with developing an entirely new geometry dataset can be significantly reduced. Furthermore, by developing shared databases of simulated and experimental forming data across companies and institutions, the implementation costs of such models could be brought down even further.

Finally, while a saturated accuracy is reached based on the $MS-SSIM$ metric and guided by the $L_{MS-SSIM-L1}$ loss function, the key metrics of interest for wrinkling prediction are ultimately the wrinkling metrics but these do not directly decrease with loss (Figure 5.12). Thus potentially the model performance could be improved by implementing a custom loss function based on one or a combination of these wrinkling metrics. However, developing such

a function that performs robustly during training and tends reliably to a global minimum is a challenging task and one of the key reasons why in most cases L_{L1} or L_{MSE} are used.

5.7 Conclusions

The following conclusions can be made based on the work in this chapter:

- The effect of tool geometry on wrinkling severity during double diaphragm forming is large and is equally significant for the two types of macroscale wrinkles that occur for biaxial NCFs with a pillar stitch.

- The greater the tapering of a convex tool geometry is, the less severe the resultant wrinkling is likely to be.

- More outwardly curving geometries tends to form less severe wrinkles than zero curvature or inwardly curving geometries.

- The sharpness of the outside vertices of a tool geometry makes no contribution towards wrinkling severity.

- A deep learning surrogate model can be successfully developed for the prediction of wrinkling severity over a given tool geometry.

- The predictions of the surrogate model are found to be sufficiently accurate for geometries similar to those it was trained on but its ability to extrapolate to vastly different geometries is limited.

- The computational cost of obtaining a wrinkling prediction using the trained deep learning surrogate model is approximately 6000 times lower than the equivalent finite element model.

Chapter 6

Conclusions and future work

This thesis set out to characterise the mechanisms and variability of NCF wrinkling behaviour and to investigate the effect of tool geometry of wrinkling, and both of these aims were achieved. For each of these aims, a brief summary of the contributions made, a complete list of specific conclusions and suggestions for future work are provided.

6.1 Summary of contributions

6.1.1 Wrinkling characterisation

The wrinkling of a biaxial ±45° NCF with a pillar stitch was successfully characterised in terms of the underlying mechanisms, severity and variability. The use of 3D-DIC was shown to be an effective method for the characterisation of the mechanisms of macroscale wrinkling as it allowed the continuous measurement of wrinkling severity and the in-plane fabric strains throughout the forming process (Figures 3.8-3.10). From this, the two competing macroscale mechanisms of a ±45° biaxial NCF were identified (lateral fabric compression during material draw-in and tow compression at shear-lockup - see Figure 3.15) and related to the asymmetric shear behaviour of the fabric. The characterisation of wrinkling severity highlighted the significance of the lateral fabric compression wrinkles (macroscale non-shear wrinkles) that are caused in this NCF by the taut stitching in positive shear (Figure 3.12). It was also shown that mesoscale wrinkles form exclusively in regions of negative shear (Figure 3.11) and are caused by tow compression (Figure 3.15). Furthermore, the same experimental testing setup was used to characterise the variability in the resulting wrinkling defects at the end of forming by applying a novel image-based comparison method (Figure 4.3) for quantifying the differences in wrinkle amplitude and wrinkle location within a set of repeated forming

tests under the same conditions (Figure 4.2). This showed that the wrinkling variability is particularly significant during multi-layer forming (Figure 4.8) and subject to change depending on the forming conditions (Figure 4.9). While this study also made clear that using 3D-DIC is not the most effective approach exist for capturing the *final* wrinkled shape of preforms due to gradual data loss, the proposed variability characterisation method was found to hold tremendous potential as a benchmarking tool for assessing the variability in process defects in a wide variety of preforming scenarios. As a result, important contributions were made to comprehensively outline the plausible wrinkling mechanisms of biaxial NCFs and develop a novel method for characterising the inherent variability in fabric wrinkling.

6.1.2   Effect of tool geometry on wrinkling

The effect of geometry on the wrinkling severity of NCFs was shown to be significant and a deep learning surrogate model was proposed for the rapid prediction of this effect in order to allow for component design optimisation.

The effect of geometry on wrinkling severity was initially investigated through an experimental comparison of four benchmark geometries (Figures 3.13-3.14). While this demonstrated that the severity was highly variable depending on the geometry, the high costs of experimentally testing a wide range of geometries meant that more generalised conclusions about how certain geometrical features contribute to wrinkling could not be made. To address this, a dataset of forming simulations for nearly two thousand geometries was generated and used to relate the characteristics of these geometries with the resultant wrinkling severity (Figures 5.16-5.17). From this novel approach, certain guidelines for minimising wrinkling through design could be suggested that extend the boundaries of what was previously known about the geometrical effect on wrinkling. Particularly it showed the benefits of introducing tapering into the design for reducing wrinkling. However, while intuitive guidelines are useful to direct the initial design towards the defect-free solution, using automated optimisation tools present a superior avenue to navigate the complexities of the geometrical design space. For this purpose, the aforementioned dataset was used to train a deep learning neural network (Figure 5.11) for rapidly predicting the wrinkling patterns for a given tool geometry. The good level of prediction accuracy (Figures 5.19-5.21) demonstrated the potential for using deep learning surrogate models to optimise composite component designs for minimal wrinkling in a time-efficient manner (Table 5.13). As a result, critical contributions were made by extending the understanding of the effect of the tool geometry on wrinkling and developing a promising method by which component geometries can be optimised to minimise wrinkling.

6.2 Specific conclusions

6.2.1 Wrinkling characterisation

From Chapter 3 and Chapter 4, the following conclusions could be made:

- The 3D-DIC approach can be successfully used to characterise the development of wrinkling during forming and relate the wrinkling behaviour to the strains in the fabric.

- The linear stitch-strain relationship in $\pm 45°$ biaxial NCFs controls their deformation and wrinkling behaviour, leading to both macroscale and mesoscale wrinkles.

- Typically, textile reinforcements deform via in-plane shear but, as is shown for this NCF, they also can deform via material draw-in when the shearing of the fabric is restricted.

- Macroscale wrinkles occur in textile reinforcements during forming via two competing mechanisms, depending on the local shear resistance of the fabric: lateral tow compression at fabric shear lockup (macroscale shear wrinkling) and lateral fabric compression (macroscale non-shear wrinkling).

- For this NCF, macroscale non-shear wrinkles, occurring in the regions of minimal shear, are shown to be severe and in more critical locations than macroscale shear wrinkles.

- In forming situations where the fabric's local shear resistance is high, using the maximum shear angle in the fabric (relative to the locking angle) is not a suitable indicator of wrinkling onset or severity.

- A novel image-based analysis method is able to characterise the variability in both wrinkle amplitude and wrinkle location for fabrics at the end of preforming.

- The material architecture and the specific layup are shown to have a significant influence on the wrinkling variability, both in terms of amplitude and location.

- Increasing the gap between the blank holder and the tool geometry significantly increases the absolute wrinkle location variability in a biaxial NCF.

- Increasing the fibre tow layers in the fabric architecture of an NCF is shown to increase the variability in amplitude and location of the resultant wrinkles in the preform.

- The wrinkling variability in both amplitude and location of a biaxial NCF is shown to be lower compared to printer paper formed under the same conditions.

- Forming two biaxial NCF layers is shown to be statistically more variable in wrinkling than a single biaxial NCF formed under the same conditions.

- The proposed variability characterisation method has the potential to be applied as a benchmarking tool to characterise process defects in a wide variety of scenarios.

6.2.2   Effect of tool geometry on wrinkling

From Chapter 3 and Chapter 5, the following conclusions could be made

- The severity of wrinkling defects during press forming of this biaxial NCF with a pillar stitch is shown to be highly influenced by component geometry but the wrinkling mechanisms of a particular fabric are shown to be independent of geometry.

- The effect of tool geometry on wrinkling severity during double diaphragm forming is large and is equally significant for the two types of macroscale wrinkles that occur for this biaxial NCF with a pillar stitch.

- The greater the tapering of a convex tool geometry is, the less severe the resultant wrinkling is likely to be.

- More outwardly curving geometries tends to form less severe wrinkles than zero curvature or inwardly curving geometries.

- The sharpness of the outside vertices of a tool geometry makes no contribution towards wrinkling severity.

- A deep learning surrogate model can be successfully developed for the prediction of wrinkling severity over a given tool geometry.

- The predictions of the surrogate model are found to be sufficiently accurate for geometries similar to those it was trained on but its ability to extrapolate to vastly different geometries is limited.

- The computational cost of obtaining a wrinkling prediction using the trained deep learning surrogate model is approximately 6000 times lower than the equivalent finite element model.

6.3 Future work

6.3.1 Wrinkling characterisation

Characterisation of mesoscale wrinkling for NCFs

Future work could include attempting to more thoroughly characterise the secondary type of wrinkling that was observed consistently during the forming trials in Chapter 3: mesoscale wrinkling. While the macroscale wrinkling and its underlying two mechanisms for this biaxial NCF were characterised, the analysis was more limited for mesoscale wrinkles. From the fabric strain data, it was clear that this mesoscale wrinkling occurs due to compression along the fibre tow and that it occurs exclusively in negative shear regions (Figure 3.15). However, it is yet not understood exactly how this compression occurs in negative shear or how these potentially detrimental wrinkles might be avoided. Thus developing improved experimental methods for characterising this defect could provide greater understanding. For example, a shear-tension picture frame rig [78] could potentially be used to isolate mesoscale wrinkles in negative shear.

Mitigation of non-shear wrinkles

Developing methods for mitigating the non-shear macroscale wrinkles that occur in biaxial NCFs should be a priority in terms of future work. The results in Chapter 3 make clear that these wrinkles are almost inevitable when forming a $\pm 45°$ biaxial NCF with a pillar stitch because these wrinkles form so early in the process (Figure 3.8). In comparison to the shear wrinkles, which can be avoided by introducing tension and/or locally modifying the shearing behaviour (Chapter 2), it is not clear how these non-shear wrinkles could be mitigated for this material system. One plausible approach would be to partially remove stitching in positive shear regions so as to encourage further deformation rather than lateral compression but this suggestion needs to be further investigated while examining any potential adverse effects on the fabric's structural integrity.

Comparison of alternative and/or combination of surface measurement techniques

Future work could also include comparisons between the results obtained via 3D-DIC with wrinkling characterisations obtained via alternative and lower cost means such as structured white light scanning [63, 110] or photogrammetry [110, 36]. While the 3D-DIC system utilised was effective for characterising the growth in wrinkling severity and fibre strains during forming (Chapter 3), it was less effective for capturing the end state of the preform

(Chapter 4). This is due to the gradual loss in data that occurs at larger deformations as the speckle pattern disintegrates and the fact that the 3D-DIC cameras cannot track the fabric that emerges from under the blank holder. Thus it would be valuable to compare the results for wrinkling variability using 3D-DIC with results from alternative methods, where the full final wrinkled pattern can be captured. This would extend upon the work of Harrison and Gonzalez Camacho [110] which compared the effectiveness of structured white light scanning with photogrammetry. Furthermore, by combining 3D-DIC together with e.g. photogrammetry within a single workflow, it would allow for greater confidence in the measured wrinkling severity. Furthermore, it would potentially enable the two datasets to be combined, allowing the data loss from 3D-DIC to be compensated for from the photogrammetry data and thus more complete comparisons of the fabric strains with wrinkling severity. This would also permit the complete experimental fabric wrinkle patterns to be mapped onto the initial undeformed fabric surface, in a similar way that was done in Chapter 5 for simulated data (Figure 5.8). This would mean no data loss occurs during conversion to grayscale images thus making the resulting variability analysis more rigorous.

Characterisation of through-thickness wrinkling for multi-layer NCF layups

Future work should consider extending the characterisation in this thesis to investigate the severity of wrinkles through the thickness of multi-layer NCF layups. The proposed characterisation methods in Chapters 3-4 are optimised for the study of single fabric forming because the 3D-DIC can only measure the wrinkle patterns for the top-most NCF. Therefore in terms of multi-layer NCF forming, which is more representative of industrial preforming, it is not clear how the wrinkling severity would vary across the thickness of the layup. This could be experimentally investigated by capturing the deformed surfaces of each NCF layer at the end of forming through one of the aforementioned alternative surface scanning methods. Then by using the proposed wrinkle calculation approach (Figure 3.3), the wrinkle amplitudes for each layer could be obtained and compared. Such an investigation would additionally aid in better understanding the effect of inter-ply friction on wrinkling severity, which was partially explored in Chapter 4 and has received more attention in recent years (Chapter 2), but for which more study is needed.

Extension of characterisation to different NCF material systems

The method developed for the characterisation of wrinkling behaviour (Chapter 3) and its variability (Chapter 4) should be applied to NCF material systems beyond the particular biaxial

NCF (±45° NCF with a pillar stitch) that was predominantly investigated in this study. Thus future work could consider characterising other NCF material systems with different numbers of layers (e.g. UD-NCF), stitch types (e.g. tricot or tricot-pillar stitch), layer orientations (e.g. 0°/90°) etc. This would extend upon the work of Arnold et al. [25] that quantified the relative wrinkling severity for a range of NCFs and the work of Mei et al. [26] that qualitatively compared the defects between two biaxial NCFs.

From the results of Chapter 3 and Chapter 5, it was found that the mascroscale wrinkles occurring in positive shear, where shearing is restricted, are more severe than those in negative shear (Figure 5.15). As this restriction in shearing causes the asymmetric shear behaviour of this NCF, it is suggested that the more symmetric the fabric shear behaviour, the less severe the wrinkling is likely to be. A similar suggestion was made in the recent work of Krieger et al. [31]. Thus it would be of interest to do a direct comparison of the results of this study with a tricot-stitched biaxial NCF, which has been shown to be less asymmetric in shear [31] or a biaxial NCF with a 0°/90° architecture, which has been shown to have negligible asymmetry [26]. This would allow the identification of the optimal 'off-the-shelf' biaxial NCF architecture for minimal wrinkling.

Additionally, extending the characterisation to other NCFs will allow for the method to be tested with other NCFs, in particular how well the proposed 3D-DIC method in Chapter 3 works with alternative stitch patterns, for which the stitches are more prominent and thus could affect the performance of the 3D-DIC to track facets during forming. The novel strain calculation method (Figure 3.4) that was developed for biaxial NCFs in Chapter 3 should also be tested with UD-NCFs or triaxial NCFs to see if it can be adapted to calculate strains for these fabrics as well. If so, it could be used as a generalised strategy for strain calculations for NCFs, for which only one set of fibre tows can be tracked from one side (in contrast to woven fabrics). Finally, comparisons of the fibre strains and wrinkling amplitudes would provide important insights into the wrinkling mechanisms of UD-NCFs and triaxial NCFs, which have previously had limited attention in the literature, with the exception of the work by Schirmaier et al. [201, 202] for UD-NCFs.

6.3.2 Effect of tool geometry on wrinkling

Effect of geometry on wrinkling variability

The experimental investigation into wrinkling variability in Chapter 4 considered the effects of different process parameters (Figure 4.2) but did not include the effect of tool geometry. Thus the effect of differing tool geometries on wrinkling variability could be investigated as part of

future work, using a simulation-based approach and/or an experimental approach. As suggested above, a photogrammetry approach could be used to avoid the high costs of using 3D-DIC while capturing the full deformed fabric. To reduce the costs associated with tooling, additive manufacturing ('3D printing') could be utilised to develop a modular tool geometry to which features/blocks could be added or removed as necessary [203], allowing for various similar tool geometries with gradually changing features to be compared in terms of wrinkling variability and severity. Such an approach would allow for an efficient way to validate wrinkling forming models under different tool geometries, each of which could potentially trigger numerical instabilities that do not correlate with reality [110]. Furthermore, based on using such modular tooling and characterising each of the geometries that are tested, the findings from Chapter 5 regarding how different geometry characteristics affect wrinkling severity (Figures 5.16-5.17) could be validated against experimental results.

Expanding understanding into the effect of geometry

There are a number of ways in which the investigation into the effect of geometry in Chapter 5 could be expanded upon as future work. Firstly, the trained surrogate model could be implemented within an optimisation scheme for improving the design of a particular case study geometry within certain constraints. Then once the optimal design is found, the reduction in wrinkle severity and improvements in component structural integrity could be evaluated. Additionally, numerical comparisons could be made between the press forming and DDF processes with respect to the same range of tool geometries, to understand how generalisable the findings of Chapter 5 are. Lastly, a separate, more controlled study into the effect of each geometry characteristic (Figure 5.6) could be considered. This would be done by using different sets of geometries where within each set only one characteristic or geometrical parameter is gradually modified. Thus this avoids any potential secondary effects from other varying aspects of the generated geometries. Therefore, such an additional study could give more clarity and help validate the correlations observed between geometry characteristics and wrinkling severity.

Characterisation of numerical variability and robustness of wrinkling predictions

Combining the methods of Chapter 4 and Chapter 5 allows the numerical variability in wrinkling predictions to be investigated. By applying the variability characterisation method on the processed wrinkling images from the finite element simulations under slightly varied simulation conditions (e.g small pre-defined changes to the geometry), the numerical variability of the finite element simulations could be investigated. From this analysis, the noticeable variability

in the wrinkling patterns for hemisphere-like geometries (Figure 5.22b) can be analysed to understand what causes these unexpected changes in wrinkling behaviour. This builds on the findings on Harrison and Gonzalez Camacho [110] who noted that using their semi-discrete forming model, the growth direction of wrinkles could suddenly change during the forming process due to numerical instabilities and stressed the importance of evaluating the robustness of forming models, which is typically not done in the literature. Such an investigation would allow the robustness of the macroscale wrinkling model used in Chapter 5 [63] to be investigated while also potentially provide a method for improving the phenomenological predictions of the surrogate model developed.

Expanding the capabilities of the surrogate model

As the surrogate model for wrinkling prediction in Chapter 5 is a proof of concept, there are numerous ways in which its capabilities can be expanded to make it more useful for the purposes of improving composites forming. Firstly, the structure of the surrogate model (Figure 5.11) could be expanded by implementing additional input channels related to the fabric layup and process conditions, in order to build a more complete, simple-to-use geometry optimiser for industrial purposes. Furthermore, the potential of using 'transfer learning' [204] for improving the extrapolating performance of the model should be explored. This could be done by retraining the surrogate model using additional data related to a new class of geometry that would otherwise be poorly predicted and then examining the performance of the retrained model. Finally, the investigated geometry set used to train the surrogate model could be adapted based on an alternative geometry generator that is more closely related to larger industrially relevant components. For example, this could be a high aspect ratio spar geometry (Figure 2.4), that is common in the aerospace industry [45, 44].

Development of stochastic wrinkling simulations

The macroscale finite element model utilised in Chapter 5 has been shown to be able to model fabric wrinkling behaviour [63, 57], but the results of Chapter 4 show that in reality the resultant wrinkle patterns are subject to variability. Thus developing a forming simulation that is able to incorporate this wrinkling variability would be advantageous in order to quantify the uncertainty in model wrinkling predictions. This could be achieved through extending the stochastic modelling approaches outlined in Chapter 2 to material models capable of wrinkling prediction, such as the one used in Chapter 5. As an alternative approach, the latter simulations could be repeated with small variations in the material parameters to assess

how small fluctuations impact the resultant wrinkling patterns. Furthermore, the results from these simulations could be assessed in terms of wrinkling variability using the pre-processing steps (Figure 5.8) from Chapter 5 and the variability characterisation method (Figure 4.3) from Chapter 4. Through introducing variability into the material tow orientations and the simulation process parameters, it would ensure that the forming simulations accurately reflect the variability in the process, giving greater confidence in the results and identifying the worst-case scenarios. While this would undoubtedly result in computationally costly simulations [111], it could be a useful approach as a final validation step before proceeding to manufacture. However, for this approach to be viable, the observed numerical variability in the wrinkling simulations (Figure 5.22) needs to be first understood and minimised such that it can be decoupled from the material and process related variability.

Surrogate model-based design optimiser for mitigating wrinkling defects

The deep learning surrogate model developed for wrinkling prediction in Chapter 5 has tremendous potential. Such an approach could be extended to develop a composites component design tool that incorporates experimental and simulation data to be able to rapidly provide the predicted defect formations for any given proposed design based on a trained surrogate model. Thus this would allow engineers to efficiently identify the most promising designs from a manufacturing perspective [107]. As a result, it would no longer be necessary to run expensive FE forming simulations for each proposed design as the resulting deformed preform and wrinkling patterns could be obtained instantaneously. This could be implemented within an existing CAD software or an alternative graphical user interface, allowing design modifications to be made on the fly in an intuitive manner. Combined with other key design targets, such a deep learning surrogate model approach could enable an entirely new design process where given designs can be 'instantaneously' evaluated in terms of the final component performance with respect to these targets. Such a proprietary interface has already been proposed by a startup company Monolith AI for general engineering applications [205]. However, further work is required to make this approach functional within the composites design and manufacturing context where complexities associated with component layups, manufacturing routes, fabric variability and choice of resin need to all be additionally considered to assess overall component performance.

References

[1] H. Ritchie. Cars, planes, trains: where do CO2 emissions from transport come from?, 2020. https://ourworldindata.org/co2-emissions-from-transport. [Accessed: 2021-07-16].

[2] D. Walker. Electric planes are here – but they won't solve flying's CO2 problem, 2019. https://theconversation.com/electric-planes-are-here-but-they-wont-solve-flyings-co-problem-125900. [Accessed: 2021-07-17].

[3] C. A. Ambel. Aviation biofuels. Technical report, Transport and Environment, 2016. https://www.transportenvironment.org/sites/te/files/publications/2016_06_Aviation_biofuels_briefing_FINAL.pdf. [Accessed: 2021-09-16].

[4] M. Gorner. Electric vehicles, 2020. https://www.iea.org/reports/electric-vehicles. [Accessed: 2021-07-16].

[5] J. M. Luk, H. C. Kim, R. De Kleine, T. J. Wallington, and H. L. MacLean. Review of the fuel saving, life cycle GHG emission, and ownership cost impacts of lightweighting vehicles with different powertrains. *Environmental Science and Technology*, 51(15): 8215–8228, 2017. doi:10.1021/acs.est.7b00909.

[6] Material Property Charts, 2021. https://www.grantadesign.com/education/students/charts/. [Accessed: 2021-07-17].

[7] V. Giurgiutiu. Introduction. In *Structural Health Monitoring of Aerospace Composites*, pages 1–23. Elsevier Inc., 2016. ISBN 9780124096059. doi:10.1016/b978-0-12-409605-9.00001-5.

[8] S. Lomov. Introduction. In S. Lomov, editor, *Non-crimp fabric composites*, pages xvi–xix. Woodhead Publishing Limited, Cambridge, 2011. ISBN 1845697626.

[9] J. Lee, X. Ni, F. Daso, X. Xiao, D. King, J. S. Gómez, T. B. Varela, S. S. Kessler, and B. L. Wardle. Advanced carbon fiber composite out-of-autoclave laminate manufacture via nanostructured out-of-oven conductive curing. *Composites Science and Technology*, 166:150–159, 2018. doi:10.1016/j.compscitech.2018.02.031.

[10] P. Boisse. Textile composite forming simulations. In M. Aliabadi, editor, *Woven Composites*, chapter 7. Imperial College Press, London, 1st edition, 2015. ISBN 978-1-78326-617-3.

[11] J. Sloan. The making of the BMW i3, 2014. https://www.compositesworld.com/articles/the-making-of-the-bmw-i3. [Accessed: 2021-07-16].

[12] S. Chen. *Fabric forming simulation and process optimisation for composites*. PhD thesis, University of Nottingham, 2016.

[13] D. Cai, G. Zhou, X. Wang, C. Li, and J. Deng. Experimental investigation on mechanical properties of unidirectional and woven fabric glass/epoxy composites under off-axis tensile loading. *Polymer Testing*, 58:142–152, 2017. doi:10.1016/j.polymertesting.2016.12.023.

[14] U. Beier. *High-performance fibre-reinforced composites prepared by a novel preform manufacturing routine*. PhD thesis, University of Bayreuth, 2010.

[15] S. Bel, P. Boisse, and F. Dumont. Analyses of the deformation mechanisms of non-crimp fabric composite reinforcements during preforming. *Applied Composite Materials*, 19: 513–528, 2012. doi:10.1007/s10443-011-9207-x.

[16] S. Chen, O. P. L. McGregor, L. T. Harper, A. Endruweit, and N. A. Warrior. Defect formation during preforming of a bi-axial non-crimp fabric with a pillar stitch pattern. *Composites Part A: Applied Science and Manufacturing*, 91:156–167, 2016. doi:10.1016/j.compositesa.2016.09.016.

[17] K. D. Potter, B. Khan, M. R. Wisnom, T. Bell, and J. Stevens. Variability, fibre waviness and misalignment in the determination of the properties of composite materials and structures. *Composites Part A: Applied Science and Manufacturing*, 39(9):1343–1354, 2008. doi:10.1016/j.compositesa.2008.04.016.

[18] K. D. Potter. Understanding the origins of defects and variability in composites manufacture. In *17th International Conference on Composite Materials*, Edinburgh, 2009.

[19] T. Gereke, O. Döbrich, M. Hübner, and C. Cherif. Experimental and computational composite textile reinforcement forming: a review. *Composites Part A: Applied Science and Manufacturing*, 46:1–10, 2013. doi:10.1016/j.compositesa.2012.10.004.

[20] P. Bussetta and N. Correia. Numerical forming of continuous fibre reinforced composite material: A review. *Composites Part A: Applied Science and Manufacturing*, 113:12–31, 2018. doi:10.1016/j.compositesa.2018.07.010.

[21] P. Boisse, J. Colmars, N. Hamila, N. Naouar, and Q. Steer. Bending and wrinkling of composite fiber preforms and prepregs. A review and new developments in the draping simulations. *Composites Part B: Engineering*, 141:234–249, 2018. doi:10.1016/j.compositesb.2017.12.061.

[22] G. Bibo, P. Hogg, and M. Kemp. Mechanical characterisation of glass- and carbon-fibre-reinforced composites made with non-crimp fabrics. *Composites Science and Technology*, 57(9-10):1221–1241, 1997. doi:10.1016/S0266-3538(97)00053-5.

[23] H. Krieger, T. Gries, and S. E. Stapleton. Design of tailored non-crimp fabrics based on stitching geometry. *Applied Composite Materials*, 25:113–127, 2018. doi:10.1007/s10443-017-9603-y.

[24] A. Schnabel and T. Gries. Production of non-crimp fabrics for composites. In S. Lomov, editor, *Non-crimp fabric composites*, chapter 1, pages 3–41. Woodhead Publishing Limited, Cambridge, 2011.

[25] S. E. Arnold, M. P. F. Sutcliffe, and W. L. A. Oram. Experimental measurement of wrinkle formation during draping of non-crimp fabric. *Composites Part A: Applied Science and Manufacturing*, 82:159–169, 2016. doi:10.1016/j.compositesa.2015.12.011.

[26] M. Mei, Y. He, X. Yang, K. Wei, Z. Qu, and D. Fang. Shear deformation characteristics and defect evolution of the biaxial ±45° and 0/90° glass non-crimp fabrics. *Composites Science and Technology*, 193:108137, 2020. doi:10.1016/j.compscitech.2020.108137.

[27] J. S. Lee, S. J. Hong, W. R. Yu, and T. J. Kang. The effect of blank holder force on the stamp forming behavior of non-crimp fabric with a chain stitch. *Composites Science and Technology*, 67(3):357–366, 2007. doi:10.1016/j.compscitech.2006.09.009.

[28] K. Tanaka, R. Ushiyama, T. Katayama, S. Enoki, and H. Sakamoto. Formability evaluation of carbon fiber NCF by a non-contact 3D strain measurement system and the effects of blank folder force on its formability. *WIT Transactions on the Built Environment*, 137:317–326, 2014. doi:10.2495/HPSM140301.

[29] A. J. Thompson, B. El Said, J. P. Belnoue, and S. R. Hallett. Modelling process induced deformations in 0/90 non-crimp fabrics at the meso-scale. *Composites Science and Technology*, 168:104–110, 2018. doi:10.1016/j.compscitech.2018.08.029.

[30] Multiaxial Reinforcements, 2021. https://www.hexcel.com/Resources/DataSheets/MultiaxialReinforcements. [Accessed: 2021-09-08].

[31] H. Krieger, T. Gries, and S. E. Stapleton. Shear and drape behavior of non-crimp fabrics based on stitching geometry. *International Journal of Material Forming*, 11:593–605, 2018. doi:10.1007/s12289-017-1368-1.

[32] J. Sirtautas, A. K. Pickett, and P. Lépicier. A mesoscopic model for coupled drape-infusion simulation of biaxial non-crimp fabric. *Composites Part B: Engineering*, 47:48–57, 2013. doi:10.1016/j.compositesb.2012.09.088.

[33] A. K. Pickett, G. Creech, P. D. Luca, A. K. Pickett, G. Creech, and P. D. Luca. Simplified and advanced simulation methods for prediction of fabric draping methods for prediction of fabric draping. *Revue Européenne des Éléments*, 14(6-7):677–691, 2005. doi:http://dx.doi.org/10.3166/reef.14.677-691.

[34] A. Mallach, F. Härtel, F. Heieck, J.-P. Fuhr, P. Middendorf, and M. Gude. Experimental comparison of a macroscopic draping simulation for dry non-crimp fabric preforming on a complex geometry by means of optical measurement. *Journal of Composite Materials*, 51(16):2363–2375, 2017. doi:10.1177/0021998316670477.

[35] L. Li, Y. Zhao, H.-G.-N. Vuong, Y. Chen, J. Yang, and Y. Duan. In-plane shear investigation of biaxial carbon non-crimp fabrics with experimental tests and finite element modeling. *Materials and Design*, 63:757–765, 2014. doi:10.1016/j.matdes.2014.07.007.

[36] R. Jagpal, R. Butler, and E. G. Loukaides. Towards flexible and defect-free forming of composites through distributed clamping. *Procedia CIRP*, 85:338–343, 2020. doi:10.1016/j.procir.2019.09.008.

[37] G. Bardl, A. Nocke, M. Hübner, T. Gereke, M. Pooch, M. Schulze, H. Heuer, M. Schiller, R. Kupke, M. Klein, and C. Cherif. Analysis of the 3D draping behavior of carbon fiber non-crimp fabrics with eddy current technique. *Composites Part B: Engineering*, 132: 49–60, 2018. doi:10.1016/j.compositesb.2017.08.007.

[38] S. Chen, O. P. McGregor, A. Endruweit, M. T. Elsmore, D. S. De Focatiis, L. T. Harper, and N. A. Warrior. Double diaphragm forming simulation for complex composite structures. *Composites Part A: Applied Science and Manufacturing*, 95:346–358, 2017. doi:10.1016/j.compositesa.2017.01.017.

[39] A. J. Thompson, J. P. Belnoue, and S. R. Hallett. Modelling defect formation in textiles during the double diaphragm forming process. *Composites Part B: Engineering*, 202 (August):108357, 2020. doi:10.1016/j.compositesb.2020.108357.

[40] L. I. Long, Z. Yan, L. I. U. Gang, Z. Xiaoran, S. Jiupeng, and G. Ming. Draping behavior of carbon non-crimp fabrics and its effects on mechanical performance of the hemispherical composites. *Journal of Wuhan University of Technology-Mater. Sci. Ed.*, 33:720–728, 2018. doi:10.1007/s11595-018-1884-y.

[41] J. Shury. GKN creates composite wing structure using new manufacturing process, 2013. https://www.compositestoday.com/2013/05/gkn-creates-composite-wing-structure-using-new-manufacturing-process/. [Accessed: 2021-08-25].

[42] P. Hallander, T. Grankäll, M. Eriksson, M. Petersson, and M. Åkermo. Using tailored temperature variations to obtain flawless forming of multi-stacked uni-directional prepreg. *Journal of Composite Materials*, 54(26):3999–4009, 2020. doi:10.1177/0021998320924714.

[43] G. Nica. BMW i3 might be cheaper to live with due to carbon fiber construction, 2013. https://www.autoevolution.com/news/bmw-i3-might-be-cheaper-to-live-with-due-to-carbon-fiber-construction-73054.html. [Accessed: 2021-08-25].

[44] K. J. Johnson, R. Butler, E. G. Loukaides, C. Scarth, and A. T. Rhead. Stacking sequence selection for defect-free forming of uni-directional ply laminates. *Composites Science and Technology*, 171:34–43, 2019. doi:10.1016/j.compscitech.2018.11.048.

[45] F. Yu, S. Chen, L. Harper, and N. Warrior. Double diaphragm forming simulation using a global-to-local modelling strategy for detailed defect detection in large structures. *Composites Part A: Applied Science and Manufacturing*, 147:106457, 2021. doi:10.1016/j.compositesa.2021.106457.

[46] Woven Composites Benchmark Forum, 2008. http://www.wovencomposites.org. [Accessed: 2013-07-13].

[47] H. Yin, X. Peng, T. Du, and Z. Guo. Draping of plain woven carbon fabrics over a double-curvature mold. *Composites Science and Technology*, 92:64–69, 2014. doi:10.1016/j.compscitech.2013.12.013.

[48] A. G. Prodromou and J. Chen. On the relationship between shear angle and wrinkling of textile composite preforms. *Composites Part A: Applied Science and Manufacturing*, 28 (5):491–503, 1997. doi:10.1016/S1359-835X(96)00150-9. arXiv:arXiv:1112.6158v1.

[49] H. Shen, P. Wang, X. Legrand, and L. Liu. Characterisation and optimisation of wrinkling during the forming of tufted three-dimensional composite preforms. *Composites Part A: Applied Science and Manufacturing*, 127:105651, 2019. doi:10.1016/j.compositesa.2019.105651.

[50] P. Harrison, M. F. Alvarez, and D. Anderson. Towards comprehensive characterisation and modelling of the forming and wrinkling mechanics of engineering fabrics. *International Journal of Solids and Structures*, 0:1–17, 2017. doi:10.1016/j.ijsolstr.2016.11.008.

[51] P. Boisse, J. Huang, and E. Guzman-Maldonado. Analysis and modeling of wrinkling in composite forming. *Journal of Composites Science*, 5(3), 2021. doi:10.3390/jcs5030081.

[52] J. S. Lightfoot, M. R. Wisnom, and K. Potter. Defects in woven preforms: formation mechanisms and the effects of laminate design and layup protocol. *Composites Part A: Applied Science and Manufacturing*, 51:99–107, 2013. doi:10.1016/j.compositesa.2013.04.004.

[53] S. Mukhopadhyay, M. I. Jones, and S. R. Hallett. Compressive failure of laminates containing an embedded wrinkle; experimental and numerical study. *Composites Part A: Applied Science and Manufacturing*, 73:132–142, 2015. doi:10.1016/j.compositesa.2015.03.012.

[54] J. P. Belnoue and S. R. Hallett. A rapid multi-scale design tool for the prediction of wrinkle defect formation in composite components. *Materials and Design*, 187:108388, 2020. doi:10.1016/j.matdes.2019.108388.

[55] S. Allaoui, P. Boisse, S. Chatel, N. Hamila, G. Hivet, D. Soulat, and E. Vidal-Salle. Experimental and numerical analyses of textile reinforcement forming of a tetrahedral shape. *Composites Part A: Applied Science and Manufacturing*, 42(6):612–622, 2011. doi:10.1016/j.compositesa.2011.02.001.

[56] C. Zimmerling, C. Poppe, and L. Kärger. Estimating optimum process parameters in textile draping of variable part geometries - A reinforcement learning approach. *Procedia Manufacturing*, 47(2019):847–854, 2020. doi:10.1016/j.promfg.2020.04.263.

[57] F. Yu, S. Chen, L. T. Harper, and N. A. Warrior. Simulating the effect of fabric bending stiffness on the wrinkling behaviour of biaxial fabrics during preforming. *Composites Part A: Applied Science and Manufacturing*, 143, 2021. doi:10.1016/j.compositesa.2021.106308.

[58] D. Dörr, T. Joppich, F. Schirmaier, T. Mosthaf, L. Kärger, and F. Henning. A method for validation of finite element forming simulation on basis of a pointwise comparison of distance and curvature. *AIP Conference Proceedings*, 1769(1):170011, 2016. doi:10.1063/1.4963567.

[59] Y. K. Hamidi and M. C. Altan. Process induced defects in liquid molding processes of composites. *International Polymer Processing*, 32(5):527–544, 2017. doi:10.3139/217.3444.

[60] S. P. Haanappel, R. H. Ten Thije, U. Sachs, B. Rietman, and R. Akkerman. Formability analyses of uni-directional and textile reinforced thermoplastics. *Composites Part A: Applied Science and Manufacturing*, 56:80–92, 2014. doi:10.1016/j.compositesa.2013.09.009.

[61] A. C. Long, B. J. Souter, F. Robitaille, and C. D. Rudd. Effects of fibre architecture on reinforcement fabric deformation. *Plastics, Rubber and Composites*, 31(2):87–97, 2002. doi:10.1179/146580102225001391.

[62] B. J. Souter. *Effects of fibre architecture on formability of textile preforms*. PhD thesis, University of Nottingham, 2001.

[63] F. Yu, S. Chen, J. V. Viisainen, M. P. F. Sutcliffe, L. T. Harper, and N. A. Warrior. A macroscale finite element approach for simulating the bending behaviour of biaxial fabrics. *Composites Science and Technology*, 191, 2020. doi:10.1016/j.compscitech.2020.108078.

[64] ASTM D1388-14. Standard test method for stiffness of fabrics. Technical report, ASTM International, West Conshohocken, PA, 2014. http://www.astm.org/cgi-bin/resolver.cgi?D1388-14.

[65] B. Liang, N. Hamila, M. Peillon, and P. Boisse. Analysis of thermoplastic prepreg bending stiffness during manufacturing and of its influence on wrinkling simulations. *Composites Part A: Applied Science and Manufacturing*, 67:111–122, 2014. doi:10.1016/j.compositesa.2014.08.020.

[66] M. Christ, A. Miene, and U. Mörschel. Measurement and analysis of drapeability effects of warp-knit NCF with a standardised, automated testing device. *Applied Composite Materials*, 24(4):803–820, 2017. doi:10.1007/s10443-016-9555-7.

[67] S. Rothe, E. Wendt, S. Krzywinski, M. Halász, P. Bakonyi, P. Tamás, and A. Bojtos. Investigation of shear-induced deformation of reinforcing textiles by optical measurement devices. *Materials*, 12(7), 2019. doi:10.3390/ma12071029.

[68] S. Allaoui, G. Hivet, A. Wendling, D. Soulat, and S. Chatel. Experimental approach for optimizing dry fabric formability. In *14th European Conference On Composite Materials*, Budapest, 2010.

[69] A. Hosseini, M. H. Kashani, F. Sassani, A. S. Milani, and F. K. Ko. Identifying the distinct shear wrinkling behavior of woven composite preforms under bias extension and picture frame tests. *Composite Structures*, 185:764–773, 2018. doi:10.1016/j.compstruct.2017.11.033.

[70] A. Hosseini, M. H. Kashani, F. Sassani, A. S. Milani, and F. Ko. A mesoscopic analytical model to predict the onset of wrinkling in plainwoven preforms under bias extension shear deformation. *Materials*, 10(10), 2017. doi:10.3390/ma10101184.

[71] W. F. Hosford and J. L. Duncan. Sheet metal forming: A review. *JOM*, 51(11):39–44, 1999. doi:10.1007/s11837-999-0221-5.

[72] A. Hosseini. *A multiscale analysis of forming induced wrinkles in woven composite preforms*. PhD thesis, University of British Columbia, 2018.

[73] A. A. Skordos, C. Monroy Aceves, and M. P. F. Sutcliffe. A simplified rate dependent model of forming and wrinkling of pre-impregnated woven composites. *Composites Part A: Applied Science and Manufacturing*, 38(5):1318–1330, 2007. doi:10.1016/j.compositesa.2006.11.005.

[74] P. Ouagne, D. Soulat, J. Moothoo, E. Capelle, and S. Gueret. Complex shape forming of a flax woven fabric; analysis of the tow buckling and misalignment defect. *Composites Part A: Applied Science and Manufacturing*, 51:1–10, 2013. doi:10.1016/j.compositesa.2013.03.017.

[75] C. Tephany, J. Gillibert, P. Ouagne, G. Hivet, S. Allaoui, and D. Soulat. Development of an experimental bench to reproduce the tow buckling defect appearing during the complex shape forming of structural flax based woven composite reinforcements. *Composites Part A: Applied Science and Manufacturing*, 81:22–33, 2016. doi:10.1016/j.compositesa.2015.10.011.

[76] W. R. Yu, P. Harrison, and A. C. Long. Finite element forming simulation of NCF considering natural variability of fiber direction. In *Proceedings of the 8th International ESAFORM Conference on Materials Forming*, Cluj-Napoca, 2005.

[77] P. Harrison, F. Abdiwi, Z. Guo, P. Potluri, and W. R. Yu. Characterising the shear-tension coupling and wrinkling behaviour of woven engineering fabrics. *Composites Part A: Applied Science and Manufacturing*, 43(6):903–914, 2012. doi:10.1016/j.compositesa.2012.01.024.

[78] F. Nosrat-Nezami, T. Gereke, C. Eberdt, and C. Cherif. Characterisation of the shear-tension coupling of carbon-fibre fabric under controlled membrane tensions for precise simulative predictions of industrial preforming processes. *Composites Part A: Applied Science and Manufacturing*, 67:131–139, 2014. doi:10.1016/j.compositesa.2014.08.030.

[79] W. R. Yu, P. Harrison, and A. Long. Finite element forming simulation for non-crimp fabrics using a non-orthogonal constitutive equation. *Composites Part A: Applied Science and Manufacturing*, 36(8):1079–1093, 2005. doi:10.1016/j.compositesa.2005.01.007.

[80] A. R. Mehrabadi. *Towards mitigation of wrinkles during forming of woven fabric composites: an experimental characterization*. Master's thesis, University of British Columbia, 2016.

[81] S. Bel, N. Hamila, P. Boisse, and F. Dumont. Finite element model for NCF composite reinforcement preforming: Importance of inter-ply sliding. *Composites Part A: Applied Science and Manufacturing*, 43(12):2269–2277, 2012. doi:10.1016/j.compositesa.2012.08.005.

[82] R. Sourki, B. Crawford, R. Vaziri, and A. S. Milani. Orientation dependency and hysteresis nature of inter-ply friction in woven fabrics. *Applied Composite Materials*, 28:113–127, 2021. doi:10.1007/s10443-020-09846-y.

[83] J. Huang, P. Boisse, N. Hamila, I. Gnaba, D. Soulat, and P. Wang. Experimental and numerical analysis of textile composite draping on a square box. Influence of the weave pattern. *Composite Structures*, 267:113844, 2021. doi:10.1016/j.compstruct.2021.113844.

[84] E. Guzman-Maldonado, P. Wang, N. Hamila, and P. Boisse. Experimental and numerical analysis of wrinkling during forming of multi-layered textile composites. *Composite Structures*, 208:213–223, 2019. doi:10.1016/j.compstruct.2018.10.018.

[85] S. Allaoui, G. Hivet, and C. Cellard. Effect of inter-ply sliding on the appearance of defects for multilayered composite shaping. In *19th International Conference on Composite Materials*, Montréal, 2013.

[86] K. Vanclooster, S. V. Lomov, and I. Verpoest. On the formability of multi-layered fabric composites. In *17th International Conference on Composite Materials*, Edinburgh, 2009.

[87] B. Zhu, T. X. Yu, H. Zhang, and X. M. Tao. Experimental investigation of formability of woven textile composite preform in stamping operation. *International Journal of Material Forming*, 1:969–972, 2008. doi:10.1007/s12289-008-0219-5.

[88] S. Allaoui, G. Hivet, D. Soulat, A. Wendling, P. Ouagne, and S. Chatel. Experimental preforming of highly double curved shapes with a case corner using an interlock reinforcement. *International Journal of Material Forming*, 7(2):155–165, 2014. doi:10.1007/s12289-012-1116-5.

[89] G. Creech and A. K. Pickett. Meso-modelling of non-crimp fabric composites for coupled drape and failure analysis. *Journal of Materials Science*, 41(20):6725–6736, 2006. doi:10.1007/s10853-006-0213-6.

[90] A. R. Labanieh, C. Garnier, P. Ouagne, O. Dalverny, and D. Soulat. Intra-ply yarn sliding defect in hemisphere preforming of a woven preform. *Composites Part A: Applied Science and Manufacturing*, 107:432–446, 2018. doi:10.1016/j.compositesa.2018.01.018.

[91] P. Harrison, R. Gomes, and N. Curado-Correia. Press forming a 0/90 crossply advanced thermoplastic composite using the double-dome benchmark geometry. *Composites Part A: Applied Science and Manufacturing*, 54:56–69, 2013. doi:10.1016/j.compositesa.2013.06.014.

[92] S. Chen, L. Harper, A. Endruweit, and N. Warrior. Formability optimisation of fabric preforms by controlling material draw-in through in-plane constraints. *Composites Part A: Applied Science and Manufacturing*, 76:10–19, 2015. doi:10.1016/j.compositesa.2015.05.006.

[93] V. N. Khiêm, H. Krieger, M. Itskov, T. Gries, and S. E. Stapleton. An averaging based hyperelastic modeling and experimental analysis of non-crimp fabrics. *International Journal of Solids and Structures*, 1(12), 2017. doi:10.1016/j.ijsolstr.2016.12.018.

[94] M. A. Khan, T. Mabrouki, E. Vidal-Sallé, and P. Boisse. Numerical and experimental analyses of woven composite reinforcement forming using a hypoelastic behaviour. Application to the double dome benchmark. *Journal of Materials Processing Technology*, 210(2):378–388, 2010. doi:10.1016/j.jmatprotec.2009.09.027.

[95] E. Capelle, P. Ouagne, D. Soulat, and D. Duriatti. Complex shape forming of flax woven fabrics: design of specific blank-holder shapes to prevent defects. *Composites Part B: Engineering*, 62:29–36, 2014. doi:10.1016/j.compositesb.2014.02.007.

[96] A. Shanwan and S. Allaoui. Different experimental ways to minimize the preforming defects of multi-layered interlock dry fabric. *International Journal of Material Forming*, 12:69–78, 2018. doi:10.1007/s12289-018-1407-6.

[97] J. Pazmino, V. Carvelli, S. V. Lomov, B. Van Mieghem, and P. Lava. 3D digital image correlation measurements during shaping of a non-crimp 3D orthogonal woven E-glass reinforcement. *International Journal of Material Forming*, 7(4):439–446, 2013. doi:10.1007/s12289-013-1139-6.

[98] L. Kärger, S. Galkin, C. Zimmerling, D. Dörr, J. Linden, A. Oeckerath, and K. Wolf. Forming optimisation embedded in a CAE chain to assess and enhance the structural performance of composite components. *Composite Structures*, 192:143–152, 2018. doi:10.1016/j.compstruct.2018.02.041.

[99] X. Wang and J. Cao. On the prediction of side-wall wrinkling in sheet metal forming processes. *International Journal of Mechanical Sciences*, 42(12):2369–2394, 2000. doi:10.1016/S0020-7403(99)00078-8.

[100] E. Hamouche and E. G. Loukaides. Classification and selection of sheet forming processes with machine learning. *International Journal of Computer Integrated Manufacturing*, 31(9):921–932, 2018. doi:10.1080/0951192X.2018.1429668.

[101] U. Breuer, M. Neitzel, V. Ketzer, and R. Reinicke. Deep drawing of fabric-reinforced thermoplastics: wrinkle formation and their reduction. *Polymer Composites*, 17(4): 643–647, 1996. doi:10.1002/pc.10655.

[102] F. Nosrat Nezami, T. Gereke, and C. Cherif. Active forming manipulation of composite reinforcements for the suppression of forming defects. *Composites Part A: Applied Science and Manufacturing*, 99:94–101, 2017. doi:10.1016/j.compositesa.2017.04.011.

[103] F. Nosrat Nezami, T. Gereke, and C. Cherif. Analyses of interaction mechanisms during forming of multilayer carbon woven fabrics for composite applications. *Composites Part A: Applied Science and Manufacturing*, 84:406–416, 2016. doi:10.1016/j.compositesa.2016.02.023.

[104] S. Chen, O. P. McGregor, L. T. Harper, A. Endruweit, and N. A. Warrior. Optimisation of local in-plane constraining forces in double diaphragm forming. *Composite Structures*, 201:570–581, 2018. doi:10.1016/j.compstruct.2018.06.062.

[105] A. Rashidi and A. S. Milani. Passive control of wrinkles in woven fabric preforms using a geometrical modification of blank holders. *Composites Part A: Applied Science and Manufacturing*, 105:300–309, 2018. doi:10.1016/j.compositesa.2017.11.023.

[106] M. A. Turk, B. Vermes, A. J. Thompson, J. P. Belnoue, S. R. Hallett, and D. S. Ivanov. Mitigating forming defects by local modification of dry preforms. *Composites Part A: Applied Science and Manufacturing*, 128:24–28, 2020. doi:10.1016/j.compositesa.2019.105643.

[107] C. Zimmerling, D. Dörr, F. Henning, and L. Kärger. A machine learning assisted approach for textile formability assessment and design improvement of composite components. *Composites Part A: Applied Science and Manufacturing*, 124:105459, 2019. doi:10.1016/j.compositesa.2019.05.027.

[108] I. Giorgio, P. Harrison, F. Dell'Isola, J. Alsayednoor, and E. Turco. Wrinkling in engineering fabrics: a comparison between two different comprehensive modelling approaches. *Proceedings of the Royal Society A: Mathematical, Physical and Engineering Sciences*, 474(2216), 2018. doi:10.1098/rspa.2018.0063.

[109] A. Endruweit, A. C. Long, F. Robitaille, and C. D. Rudd. Influence of stochastic fibre angle variations on the permeability of bi-directional textile fabrics. *Composites Part A: Applied Science and Manufacturing*, 37(1):122–132, 2006. doi:10.1016/j.compositesa.2005.04.014.

[110] P. Harrison and L. F. Gonzalez Camacho. Deep draw induced wrinkling of engineering fabrics. *International Journal of Solids and Structures*, 212:220–236, 2021. doi:10.1016/j.ijsolstr.2020.12.003.

[111] T. S. Mesogitis, A. A. Skordos, and A. C. Long. Uncertainty in the manufacturing of fibrous thermosetting composites: a review. *Composites Part A: Applied Science and Manufacturing*, 57:67–75, 2014. doi:10.1016/j.compositesa.2013.11.004.

[112] A. A. Skordos and M. P. F. Sutcliffe. Stochastic simulation of woven composites forming. *Composites Science and Technology*, 68(1):283–296, 2008. doi:10.1016/j.compscitech.2007.01.035.

[113] F. Abdiwi, P. Harrison, I. Koyama, W. R. Yu, A. C. Long, N. Corriea, and Z. Guo. Characterising and modelling variability of tow orientation in engineering fabrics and textile composites. *Composites Science and Technology*, 72(9):1034–1041, 2012. doi:10.1016/j.compscitech.2012.03.017.

[114] S. Bickerton, P. Šimáček, S. E. Guglielmi, and S. G. Advani. Investigation of draping and its effects on the mold filling process during manufacturing of a compound curved composite part. *Composites Part A: Applied Science and Manufacturing*, 28(9):801–816, 1997. doi:10.1016/S1359-835X(97)00033-X.

[115] G. B. McGuinness and C. M. Ó Brádaigh. Development of rheological models for forming flows and picture-frame shear testing of fabric reinforced thermoplastic sheets. *Journal of Non-Newtonian Fluid Mechanics*, 73(1):1–28, 1997. doi:10.1016/S0377-0257(97)00040-2.

[116] J. Wang, J. R. Page, and R. Paton. Experimental investigation of the draping properties of reinforcement fabrics. *Composites Science and Technology*, 58(2):229–237, 1998. doi:10.1016/S0266-3538(97)00115-2.

[117] H. Montazerian, A. Rashidi, M. Hoorfar, and A. S. Milani. A frameless picture frame test with embedded sensor: Mitigation of imperfections in shear characterization of woven fabrics. *Composite Structures*, 211:112–124, 2019. doi:10.1016/j.compstruct.2018.11.096.

[118] M. Haghi Kashani, A. Hosseini, F. Sassani, F. K. Ko, and A. S. Milani. The role of intra-yarn shear in integrated multi-scale deformation analyses of woven fabrics: a critical review. *Critical Reviews in Solid State and Materials Sciences*, 43(3):213–232, 2018. doi:10.1080/10408436.2017.1342597.

[119] M. A. Sutton, J. J. Orteu, and H. W. Schreier. *Image Correlation for Shape, Motion and Deformation Measurements: Basic Concepts, Theory and Applications*. Springer Publishing Company, New York City, 1st edition, 2009.

[120] T. S. Mesogitis, A. A. Skordos, and A. C. Long. Non-crimp fabrics geometrical variability and its influence on composites cure. In *16th European Conference on Composite Materials*, Seville, 2014. ISBN 9780000000002.

[121] M. Karahan, S. V. Lomov, A. E. Bogdanovich, D. Mungalov, and I. Verpoest. Internal geometry evaluation of non-crimp 3D orthogonal woven carbon fabric composite. *Composites Part A: Applied Science and Manufacturing*, 41(9):1301–1311, 2010. doi:10.1016/j.compositesa.2010.05.014.

[122] P. Harrison, W.-R. Yu, and A. C. Long. Modelling the deformability of biaxial non-crimp fabric composites. In S. V. Lomov, editor, *Non-Crimp Fabric Composites*, chapter 7, pages 144–165. Woodhead Publishing Limited, Cambridge, first edition, 2011.

[123] K. Weissenberg. The use of a trellis model in the mechanics of homogeneous materials. *Journal of the Textile Institute Transactions*, 40(2):T89–T110, 1949. doi:10.1080/19447024908659443.

[124] R. E. Robertson, E. S. Hsiue, E. N. Sickafus, and G. S. Yeh. Fiber rearrangements during the molding of continuous fiber composites. I. Flat cloth to a hemisphere. *Polymer Composites*, 2(3):126–131, 1981. doi:10.1002/pc.750020309.

[125] T. M. McBride and J. Chen. Unit-cell geometry in plain-weave fabrics during shear deformations. *Science*, 51:345–351, 1997. doi:10.1016/S0266-3538(96)00136-4.

[126] P. Boisse, M. Borr, K. Buet, and A. Cherouat. Finite element simulations of textile composite forming including the biaxial fabric behaviour. *Composites Part B: Engineering*, 28(4):453–464, 1997. doi:https://doi.org/10.1016/S1359-8368(96)00067-4.

[127] P. Harrison. Modelling the forming mechanics of engineering fabrics using a mutually constrained pantographic beam and membrane mesh. *Composites Part A: Applied Science and Manufacturing*, 81:145–157, 2016. doi:10.1016/j.compositesa.2015.11.005.

[128] P. Boisse, Y. Aimène, A. Dogui, S. Dridi, S. Gatouillat, N. Hamila, M. A. Khan, T. Mabrouki, F. Morestin, and E. Vidal-Sallé. Hypoelastic, hyperelastic, discrete and semi-discrete approaches for textile composite reinforcement forming. *International Journal of Material Forming*, 3:1229–1240, 2010. doi:10.1007/s12289-009-0664-9.

[129] D. Durville. Simulation of the mechanical behaviour of woven fabrics at the scale of fibers. *International Journal of Material Forming*, 3:1241–1251, 2010. doi:10.1007/s12289-009-0674-7.

[130] A. C. Long, B. J. Souter, F. Robitaille, and C. D. Rudd. Effects of fibre architecture on reinforcement fabric deformation. *Plastics, Rubber and Composites*, 31(2):87–97, 2002. doi:10.1179/146580102225001391.

[131] Q. Steer, J. Colmars, and P. Boisse. Modeling of tricot stitch non crimp fabric in forming simulations. *AIP Conference Proceedings*, 2113(1):020004, 2019. doi:10.1063/1.5112509.

[132] L. Ma, J. Tudor, and J. Zawisza. An evaluation of the *FABRIC material model in ABAQUS/EXPLICIT for composite preforming analysis suitability. In *American Society for Composites Thirty-First Technical Conference*, Williamsburg, 2016. ISBN 9781605953168.

[133] M. Y. Matveev, A. Endruweit, N. A. Warrior, D. S. De Focatiis, and A. C. Long. Modelling wrinkling onset in textile forming using membrane elements. In *21st International Conference on Composite Materials*, Xi'an, 2017.

[134] M. H. Kashani, A. Hosseini, F. Sassani, F. K. Ko, and A. S. Milani. Understanding different types of coupling in mechanical behavior of woven fabric reinforcements: a critical review and analysis. *Composite Structures*, 179:558–567, 2017. doi:10.1016/j.compstruct.2017.06.069.

[135] M. Komeili and A. S. Milani. On effect of shear-tension coupling in forming simulation of woven fabric reinforcements. *Composites Part B: Engineering*, 99:17–29, 2016. doi:10.1016/j.compositesb.2016.05.004.

[136] P. Boisse, N. Hamila, E. Vidal-Sallé, and F. Dumont. Simulation of wrinkling during textile composite reinforcement forming. Influence of tensile, in-plane shear and bending stiffnesses. *Composites Science and Technology*, 71(5):683–692, 2011. doi:10.1016/j.compscitech.2011.01.011.

[137] P. Boisse, N. Hamila, and A. Madeo. The difficulties in modeling the mechanical behavior of textile composite reinforcements with standard continuum mechanics of Cauchy. Some possible remedies. *International Journal of Solids and Structures*, 154: 55–65, 2018. doi:10.1016/j.ijsolstr.2016.12.019.

[138] B. Cornelissen, B. Rietman, and R. Akkerman. Frictional behaviour of high performance fibrous tows: friction experiments. *Composites Part A: Applied Science and Manufacturing*, 44:95–104, 2013. doi:10.1016/j.compositesa.2012.08.024.

[139] D. M. Mulvihill, O. Smerdova, and M. P. F. Sutcliffe. Friction of carbon fibre tows. *Composites Part A: Applied Science and Manufacturing*, 93:185–198, 2017. doi:10.1016/j.compositesa.2016.08.034.

[140] E. I. Avgoulas, D. M. Mulvihill, A. Endruweit, M. P. F. Sutcliffe, N. A. Warrior, D. S. De Focatiis, and A. C. Long. Frictional behaviour of non-crimp fabrics (NCFs) in contact with a forming tool. *Tribology International*, 121:71–77, 2018. doi:10.1016/j.triboint.2018.01.026. arXiv:1008.2734.

[141] C. Zimmerling, J. Pfrommer, J. Liu, J. Beyerer, F. Henning, and L. Kärger. Application and evaluation of meta-model assisted optimisation strategies for gripper assisted fabric draping in composite manufacturing. In *18th European Conference on Composite Materials*, Athens, 2018. ISBN 9781510896932.

[142] A. A. Skordos, M. P. F. Sutcliffe, J. W. Klintworth, and P. Adolfsson. Multi-objective optimisation of woven composite draping using genetic algorithms. In *27th International Conference SAMPE Europe*, Paris, 2006.

[143] A. Bhosekar and M. Ierapetritou. Advances in surrogate based modeling, feasibility analysis, and optimization: a review. *Computers and Chemical Engineering*, 108: 250–267, 2018. doi:10.1016/j.compchemeng.2017.09.017.

[144] C. T. Wang, G. Kinzel, and T. Altan. Wrinkling criterion for an anisotropic shell with compound curvatures in sheet forming. *International Journal of Mechanical Sciences*, 36(10):945–960, 1994. doi:10.1016/0020-7403(94)90056-6.

[145] J. D'Errico. Surface Fitting using gridfit, 2021. https://uk.mathworks.com/matlabcentral/fileexchange/8998-surface-fitting-using-gridfit. [Accessed: 2021-09-16].

[146] J. Alsayednoor, P. Harrison, M. Dobbie, R. Costantini, and F. Lennard. Evaluating the use of digital image correlation for strain measurement in historic tapestries using representative deformation fields. *Strain*, 55(2), 2019. doi:10.1111/str.12308.

[147] L. Salminen. *Aspects of fracture processes in paper*. PhD thesis, Helsinki University of Technology, 2003.

[148] J. P. Thirion. Image matching as a diffusion process: An analogy with Maxwell's demons. *Medical Image Analysis*, 2(3):243–260, 1998. doi:10.1016/S1361-8415(98)80022-4.

[149] M. Tourlonias, M. A. Bueno, G. Fassi, I. Aktas, and Y. Wielhorski. Influence of friction angle between carbon single fibres and tows: experimental analysis and analytical model. *Composites Part A: Applied Science and Manufacturing*, 124:105478, 2019. doi:10.1016/j.compositesa.2019.105478.

[150] P. Boisse, N. Hamila, and A. Madeo. Modelling the development of defects during composite reinforcements and prepreg forming. *Philosophical Transactions of the Royal Society A: Mathematical, Physical and Engineering Sciences*, 374:20150269, 2016. doi:10.1098/rsta.2015.0269.

[151] J. Cao, R. Akkerman, P. Boisse, J. Chen, H. S. Cheng, E. F. de Graaf, J. L. Gorczyca, P. Harrison, G. Hivet, J. Launay, W. Lee, L. Liu, S. V. Lomov, A. Long, E. de Luycker, F. Morestin, J. Padvoiskis, X. Q. Peng, J. Sherwood, T. Stoilova, X. M. Tao, I. Verpoest, A. Willems, J. Wiggers, T. X. Yu, and B. Zhu. Characterization of mechanical behavior of woven fabrics: Experimental methods and benchmark results. *Composites Part A: Applied Science and Manufacturing*, 39(6):1037–1053, 2008. doi:10.1016/j.compositesa.2008.02.016.

[152] C. Zimmerling, D. Trippe, B. Fengler, and L. Kärger. An approach for rapid prediction of textile draping results for variable composite component geometries using deep neural networks. *AIP Conference Proceedings*, 2113(1):020007, 2019. doi:10.1063/1.5112512.

[153] J. M. Gan, S. Bickerton, and M. Battley. Quantifying variability within glass fibre reinforcements using an automated optical method. *Composites Part A: Applied Science and Manufacturing*, 43(8):1169–1176, 2012. doi:10.1016/j.compositesa.2012.03.024.

[154] T. Gereke, F. N. Nezami, M. Hübner, O. Döbrich, and C. Cherif. Active control of textile forming processes. In *20th International Conference on Composite Materials*, Copenhagen, 2015.

[155] I. Goodfellow, Y. Bengio, and A. Courville. *Deep Learning*. MIT Press, 2016.

[156] J. Wang, Y. Ma, L. Zhang, R. X. Gao, and D. Wu. Deep learning for smart manufacturing: methods and applications. *Journal of Manufacturing Systems*, 48:144–156, 2018. doi:10.1016/j.jmsy.2018.01.003.

[157] N. K. Chauhan and K. Singh. A review on conventional machine learning vs deep learning. In *2018 International Conference on Computing, Power and Communication Technologies*, pages 347–352, Greater Noida, 2018. IEEE. doi:10.1109/GUCON.2018.8675097.

[158] Y. LeCun, L. Bottou, Y. Bengio, and P. Haffner. Gradient-based learning applied to document recognition. *Proceedings of the IEEE*, 86(11):2278–2323, 1998. doi:10.1109/5.726791.

[159] H. Wu, Q. Liu, and X. Liu. A review on deep learning approaches to image classification and object segmentation. *Computers, Materials and Continua*, 60(2):575–597, 2019. doi:10.32604/cmc.2019.03595.

[160] A. Zhang, Z. C. Lipton, M. Li, and A. J. Smolar. Semantic segmentation and the dataset, 2021. https://d2l.ai/chapter_computer-vision/semantic-segmentation-and-dataset.html. [Accessed: 2021-08-06].

[161] J. Long, E. Shelhamer, and T. Darrell. Fully convolutional networks for semantic segmentation. In *Proceedings of the IEEE Computer Society Conference on Computer Vision and Pattern Recognition*, pages 431–440, Boston, 2015. IEEE. doi:10.1109/CVPR.2015.7298965.

[162] C. Chen, C. Qin, H. Qiu, G. Tarroni, J. Duan, W. Bai, and D. Rueckert. Deep learning for cardiac image segmentation: a review. *Frontiers in Cardiovascular Medicine*, 7, 2020. doi:10.3389/fcvm.2020.00025. arXiv:1911.03723.

[163] A. Zhang, Z. C. Lipton, M. Li, and A. J. Smolar. Fully convolutional networks, 2021. https://d2l.ai/chapter_computer-vision/fcn.html. [Accessed: 2021-08-09].

[164] H. Seo, M. Badiei Khuzani, V. Vasudevan, C. Huang, H. Ren, R. Xiao, X. Jia, and L. Xing. Machine learning techniques for biomedical image segmentation: An overview of technical aspects and introduction to state-of-art applications. *Medical Physics*, 47(5): e148–e167, 2020. doi:10.1002/mp.13649. arXiv:1911.02521.

[165] A. G. Kendall. *Geometry and uncertainty in deep learning for computer vision*. PhD thesis, University of Cambridge, 2017.

[166] H. Zhou, Q. Xu, Z. Nie, and N. Li. A study on using image-based machine learning methods to develop surrogate models of stamp forming simulations. *Journal of Manufacturing Science and Engineering*, 144(2), 08 2021. doi:10.1115/1.4051604. 021012.

[167] H. Noh, S. Hong, and B. Han. Learning deconvolution network for semantic segmentation. In *2015 IEEE International Conference on Computer Vision (ICCV)*, pages 1520–1528, 2015. doi:10.1109/ICCV.2015.178.

[168] K. Simonyan and A. Zisserman. Very deep convolutional networks for large-scale image recognition. In *3rd International Conference on Learning Representations, ICLR 2015 - Conference Track Proceedings*, 2015.

[169] V. Badrinarayanan, A. Kendall, and R. Cipolla. SegNet: a deep convolutional encoder-decoder architecture for image segmentation. *IEEE Transactions on Pattern Analysis and Machine Intelligence*, 39(12):2481–2495, 2017. doi:10.1109/TPAMI.2016.2644615. arXiv:1511.00561.

[170] O. Ronneberger, P. Fischer, and T. Brox. U-net: Convolutional networks for biomedical image segmentation. In N. Navab, J. Hornegger, W. M. Wells, and A. F. Frangi, editors, *Medical Image Computing and Computer-Assisted Intervention – MICCAI 2015*, pages 234–241, Cham, 2015. Springer International Publishing.

[171] R. Zhang, P. Isola, A. A. Efros, E. Shechtman, and O. Wang. The unreasonable effectiveness of deep features as a perceptual metric. In *Proceedings of the IEEE Computer Society Conference on Computer Vision and Pattern Recognition*, pages 586–595, Salt Lake City, 2018. doi:10.1109/CVPR.2018.00068.

[172] D. Jha, P. H. Smedsrud, M. A. Riegler, D. Johansen, T. D. Lange, P. Halvorsen, and H. D. Johansen. Resunet++: an advanced architecture for medical image segmentation. In *2019 IEEE International Symposium on Multimedia (ISM)*, pages 225–230, 2019. doi:10.1109/ISM46123.2019.00049.

[173] F. I. Diakogiannis, F. Waldner, P. Caccetta, and C. Wu. ResUNet-a: a deep learning framework for semantic segmentation of remotely sensed data. *ISPRS Journal of Photogrammetry and Remote Sensing*, 162:94–114, 2020. doi:10.1016/j.isprsjprs.2020.01.013. arXiv:1904.00592.

[174] K. He, X. Zhang, S. Ren, and J. Sun. Deep residual learning for image recognition. In *2016 IEEE Conference on Computer Vision and Pattern Recognition (CVPR)*, pages 770–778, 2016. doi:10.1109/CVPR.2016.90.

[175] C. Sacco, A. Baz Radwan, A. Anderson, R. Harik, and E. Gregory. Machine learning in composites manufacturing: a case study of automated fiber placement inspection. *Composite Structures*, 250:112514, 2020. doi:10.1016/j.compstruct.2020.112514.

[176] C. Sacco, A. Baz Radwan, T. Beatty, and R. Harik. Machine learning based AFP inspection: a tool for characterization and integration. In *International SAMPE Technical Conference*, Charlotte, 2019. doi:10.33599/nasampe/s.19.1594.

[177] S. Banga, H. Gehani, S. Bhilare, S. Patel, and L. Kara. 3D topology optimization using convolutional neural networks. *arXiv preprint*, 2018. arXiv:1808.07440.

[178] G. X. Gu, C. T. Chen, and M. J. Buehler. De novo composite design based on machine learning algorithm. *Extreme Mechanics Letters*, 18:19–28, 2018. doi:10.1016/j.eml.2017.10.001.

[179] C. Zimmerling, D. Dörr, F. Henning, and L. Kärger. A meta-model based approach for rapid formability estimation of continuous fibre reinforced components. *AIP Conference Proceedings*, 1960(1):020042, 2018. doi:10.1063/1.5034843.

[180] J. Pfrommer, C. Zimmerling, J. Liu, L. Kärger, F. Henning, and J. Beyerer. Optimisation of manufacturing process parameters using deep neural networks as surrogate models. *Procedia CIRP*, 72:426–431, 2018. doi:10.1016/j.procir.2018.03.046.

[181] C. Zimmerling, C. Poppe, and L. Kärger. Estimating optimum process parameters in textile draping of variable part geometries - a reinforcement learning approach. *Procedia Manufacturing*, 47:847–854, 2020. doi:10.1016/j.promfg.2020.04.263.

[182] J. Krebs, D. Bhattacharyya, and K. Friedrich. Production and evaluation of secondary composite aircraft components - a comprehensive case study. *Composites Part A: Applied Science and Manufacturing*, 28(5):481–489, 1997. doi:10.1016/S1359-835X(96)00148-0.

[183] D. Cowden. CadQuery, 2020. https://github.com/CadQuery/cadquery. [Accessed: 2021-08-03].

[184] M. Petelet, B. Iooss, O. Asserin, and A. Loredo. Latin hypercube sampling with inequality constraints. *AStA Advances in Statistical Analysis*, 94(4):325–339, 2010. doi:10.1007/s10182-010-0144-z. arXiv:0909.0329.

[185] K. Simonyan, A. Vedaldi, and A. Zisserman. Deep inside convolutional networks: visualising image classification models and saliency maps. In *2nd International Conference on Learning Representations, ICLR 2014 - Workshop Track Proceedings*, Banff, 2014.

[186] S. Ioffe and C. Szegedy. Batch normalization: accelerating deep network training by reducing internal covariate shift. *Proceedings of Machine Learning Research*, 37, 2015. doi:10.1080/17512786.2015.1058180.

[187] K. Ding, K. Ma, S. Wang, and E. P. Simoncelli. Image quality assessment: unifying structure and texture similarity. *IEEE Transactions on Pattern Analysis and Machine Intelligence*, pages 1–14, 2020. doi:10.1109/TPAMI.2020.3045810. arXiv:2004.07728.

[188] Z. Wang, A. C. Bovik, H. R. Sheikh, and E. P. Simoncelli. Image quality assessment: from error visibility to structural similarity. *IEEE Transactions on Image Processing*, 13 (4):600–612, 2004. doi:10.1109/TIP.2003.819861.

[189] Z. Wang, E. Simoncelli, and A. Bovik. Multiscale structural similarity for image quality assessment. In *The 37th Asilomar Conference on Signals, Systems and Computers*, volume 2, pages 1398–1402, 2003. doi:10.1109/ACSSC.2003.1292216.

[190] S. Kastryulin, D. Zakirov, and D. Prokopenko. PyTorch image quality: metrics and measure for image quality assessment, 2019. https://github.com/photosynthesis-team/piq. [Accessed: 2021-09-16].

[191] H. Zhao, O. Gallo, I. Frosio, and J. Kautz. Loss functions for neural networks for image processing. *arXiv preprint*, 2015. arXiv:1511.08861.

[192] F. Cao, K. Yao, and J. Liang. Deconvolutional neural network for image super-resolution. *Neural Networks*, 132:394–404, 2020. doi:10.1016/j.neunet.2020.09.017.

[193] N. S. Keskar, J. Nocedal, P. T. P. Tang, D. Mudigere, and M. Smelyanskiy. On large-batch training for deep learning: generalization gap and sharp minima. In *5th International Conference on Learning Representations, ICLR 2017 - Conference Track Proceedings*, Toulon, 2017.

[194] D. Masters and C. Luschi. Revisiting small batch training for deep neural networks. *arXiv preprint*, 2018. arXiv:1804.07612.

[195] D. P. Kingma and J. L. Ba. Adam: A method for stochastic optimization. In *3rd International Conference on Learning Representations, ICLR 2015 - Conference Track Proceedings*, 2015.

[196] S. L. Smith, P. J. Kindermans, C. Ying, and Q. V. Le. Don't decay the learning rate, increase the batch size. *arXiv preprint*, 2017. arXiv:1711.00489.

[197] I. Loshchilov and F. Hutter. Decoupled weight decay regularization. *arXiv preprint*, 2017. arXiv:1711.05101.

[198] P. Hao, D. Liu, K. Zhang, Y. Yuan, B. Wang, G. Li, and X. Zhang. Intelligent layout design of curvilinearly stiffened panels via deep learning-based method. *Materials and Design*, 197:109180, 2021. doi:10.1016/j.matdes.2020.109180.

[199] A. R. Masegosa, R. Cabañas, H. Langseth, T. D. Nielsen, and A. Salmerón. Probabilistic Models with Deep Neural Networks. *Entropy (Basel)*, 23(1), 2021. doi:10.3390/e23010117.

[200] J. Yosinski, J. Clune, Y. Bengio, and H. Lipson. How transferable are features in deep neural networks? *Advances in Neural Information Processing Systems*, 4(January): 3320–3328, 2014. arXiv:1411.1792.

[201] F. J. Schirmaier, K. A. Weidenmann, L. Kärger, and F. Henning. Characterisation of the draping behaviour of unidirectional non-crimp fabrics (UD-NCF). *Composites Part A: Applied Science and Manufacturing*, 80:28–38, 2016. doi:10.1016/j.compositesa.2015.10.004.

[202] F. J. Schirmaier, D. Dörr, F. Henning, and L. Kärger. A macroscopic approach to simulate the forming behaviour of stitched unidirectional non-crimp fabrics (UD-NCF). *Composites Part A: Applied Science and Manufacturing*, 102:322–335, 2017. doi:10.1016/j.compositesa.2017.08.009.

[203] N. Budwal, K. Kasper, J. Goering, and C. Ward. Flexible low-cost tooling solutions for a one-shot resin infusion of a 3D woven and multi-textile preform. *Procedia Manufacturing*, 51:856–863, 2020. doi:10.1016/j.promfg.2020.10.120.

[204] S. J. Pan and Q. Yang. A survey on transfer learning. *IEEE Transactions on Knowledge and Data Engineering*, 22(10):1345–1359, 2010. doi:10.1109/TKDE.2009.191.

[205] Fewer simulations, more results, 2021. https://www.monolithai.com/industry/reduce-simulations. [Accessed: 2021-08-26].

[206] J. Tawney. *Draping of composite structures*. MEng report, Department of Engineering, University of Cambridge, 2014.

[207] S. Arnold. *Draping of composite structures*. MEng report, Department of Engineering, University of Cambridge, 2015.

[208] W. L. A. Oram. *Draping of composite structures*. MEng report, Department of Engineering, University of Cambridge, 2016.

[209] M. Christ, A. Miene, and U. Moerschel. Characterization of the drapability of reinforcement fabrics by means of an automated tester. In *SPE Automotive and Composites Divisions - 12th Annual Automotive Composites Conference and Exhibition 2012*, pages 633–645, Troy, 2012. ISBN 9781622768875.

[210] Ready-to-connect drylin® linear units, 2021. https://www.igus.co.uk/info/linear-guides-actuator. [Accessed: 2021-09-16].

[211] R. Lipsett. Why lead screws are the best fit for many linear motion applications - and how to rightly apply them. Technical report, Thomson Industries, Inc., San Jose, CA, 2016. https://www.thomsonlinear.com/downloads/articles/Why_Lead_Screws_Best_Fit_Linear_Motion_Applications_taen.pdf. [Accessed: 2021-09-16].

[212] drylin® stepper motor NEMA23, 2021. https://www.igus.co.uk/product/1249?artNr=MOT-AN-S-060-020-056-M-C-AAAC. [Accessed: 2021-09-16].

[213] Mini low profile load cell universal/tension or compression, 2020. https://www.transducertechniques.com/mlp-load-cell.aspx. [Accessed: 2021-09-16].

[214] Single axis USB controller plus driver, 2021. https://www.arcus-technology.com/products/single-axis-motion-controller/1-axis-usb-controller-plus-driver/. [Accessed: 2021-09-16].

[215] 45mm RTY-2/C Quick-Change Rotary Cutter, 2021. https://olfa.com/collections/craft/products/olfa-45mm-rty-2-c-quick-change-rotary-cutter-aqua. [Accessed: 2021-09-16].

[216] Graphit 33, 2021. http://www.kontaktchemie.com/koc/KOCproductdetail.csp?division=&product=GRAPHIT33&ilang=en&plang=en. [Accessed: 2021-09-16].

[217] Flaw detector developer 3, 2019. http://www.ambersil.com/wwwcrc/tds/TAI3FDD.PDF. [Accessed: 2021-09-08].

[218] Hi-strength 90 spray adhesive, 2021. https://www.3m.co.uk/3M/en_GB/p/d/v000143947/. [Accessed: 2021-08-28].

[219] F. T. Peirce. The 'handle' of cloth as a measurable quantity. *Journal of the Textile Institute Transactions*, 21(9):T377–T416, 1930. doi:10.1080/19447023008661529.

[220] T. Kurita and P. Boulanger. Computation of surface curvature from range images using geometrically intrinsic weights. In *IAPR Workshop on Machine Vision Applications*, pages 389–392, 1992.

[221] D. T. Chang. Bayesian hyperparameter optimization with BoTorch, GPyTorch and Ax. *arXiv preprint*, 2019. arXiv:1912.05686.

[222] Y. Bengio. Practical recommendations for gradient-based training of deep architectures. In G. Montavon, G. B. Orr, and K.-R. Müller, editors, *Neural Networks: Tricks of the Trade: Second Edition*, pages 437–478. Springer, Berlin, Heidelberg, 2012. doi:10.1007/978-3-642-35289-8_26.

[223] J. V. Viisainen, A. Hosseini, and M. P. F. Sutcliffe. Experimental investigation, using 3D digital image correlation, into the effect of component geometry on the wrinkling behaviour and the wrinkling mechanisms of a biaxial NCF during preforming. *Composites Part A: Applied Science and Manufacturing*, 142:106248, 2021. doi:10.1016/j.compositesa.2020.106248.

[224] J. V. Viisainen and M. P. F. Sutcliffe. Characterising the variability in wrinkling during the preforming. *Composites Part A: Applied Science and Manufacturing*, 149:106536, 2021. doi:10.1016/j.compositesa.2021.106536.

[225] J. V. Viisainen, F. Yu, A. Codolini, S. Chen, L. Harper, and M. P. F. Sutcliffe. Rapid prediction of wrinkles in a biaxial NCF after preforming over a given tool geometry using a deep learning surrogate model. *Composites Science and Technology*, 2022. [In preparation].

[226] J. V. Viisainen and M. P. F. Sutcliffe. Towards finding the cure for wrinkling: a study of fabric deformation. In *Department of Engineering Division C Graduate Student Conference 2019*, Cambridge, 2019.

[227] J. V. Viisainen, J. Zhou, and M. P. F. Sutcliffe. Characterisation of the wrinkling behaviour of a biaxial non-crimp fabic during forming. In *22nd International Conference on Composite Materials*, Melbourne, 2019.

[228] J. V. Viisainen, F. Yu, A. Codolini, S. Chen, L. Harper, and M. P. F. Sutcliffe. A deep learning surrogate model for rapid prediction of geometry-induced wrinkles in fabric preforming. In *International Conference on Manufacturing of Advanced Composites 2021*, Virtual, 2021.

[229] J. V. Viisainen, J. Zhou, and M. P. F. Sutcliffe. Experimental determination of a forming limit diagram for non-crimp fabrics through 3D digital image correlation. In *Department of Engineering Division C Graduate Student Conference 2018*, Cambridge, 2018.

[230] J. V. Viisainen, J. Zhou, and M. P. F. Sutcliffe. Wrinkle formation characterisation during the forming of non-crimp fabrics. In *International Conference on Manufacturing of Advanced Composites 2018*, Nottingham, 2018.

[231] A. G. H. Chow. *Draping of composite structures*. MEng report, Department of Engineering, University of Cambridge, 2019.

Appendix A

Experimental forming rig development

This appendix is supplementary to Chapters 3-4. It outlines how the experimental forming rig utilised was developed, explaining the improvements and design choices that were made in upgrading the inherited forming rig (Section A.1). These include the choice of a DIC system arrangement (Section A.2), the selection of a new actuator system (Section A.3) and the design of a new control system (Section A.4).

A.1   Upgraded forming rig

A.1.1   Inherited rig

The experimental forming rig used in this thesis was developed based on a forming rig inherited from the work of Arnold et al. [25]. This inherited rig was developed over a number of years by successive MEng students at the University of Cambridge Department of Engineering [206–208]. It was originally inspired by a rig proposed by [209] for the draping of fabrics. A schematic of the inherited setup is shown in Figure A.1. It consists of a hemispherical punch of 75 mm in radius, connected to a photographic enlarger head and powered by a stepper motor, allowing it to move down to deform a circular fabric sample of diameter 380 mm. The sample is held in place by a clamping ring of inner diameter 287 mm and dead weights hung from a weight ring placed on top of the clamping rig. The deformation of the fabric is captured by a single DSLR camera that is fixed below the rig, allowing the surface wrinkle amplitudes to be calculated at discrete forming intervals through a 'shape-from-focus' approach [25]. The movement of the punch is controlled by a control algorithm developed in LabVIEW and the punch force on the fabric is recorded via a load cell. While this forming setup has been to be

capable to wrinkle severity characterisation, it was found to be limited in a number of ways that motivated the need for it to be upgraded, as will be described below.
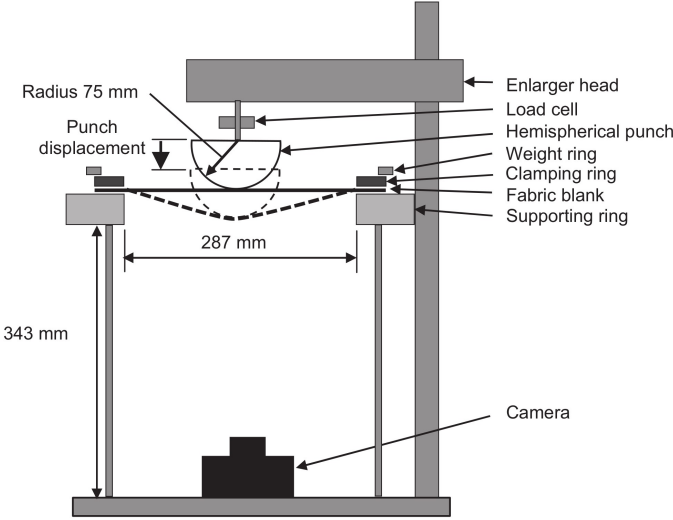

Fig. A.1 The inherited experimental forming setup developed by Arnold et al. [25].
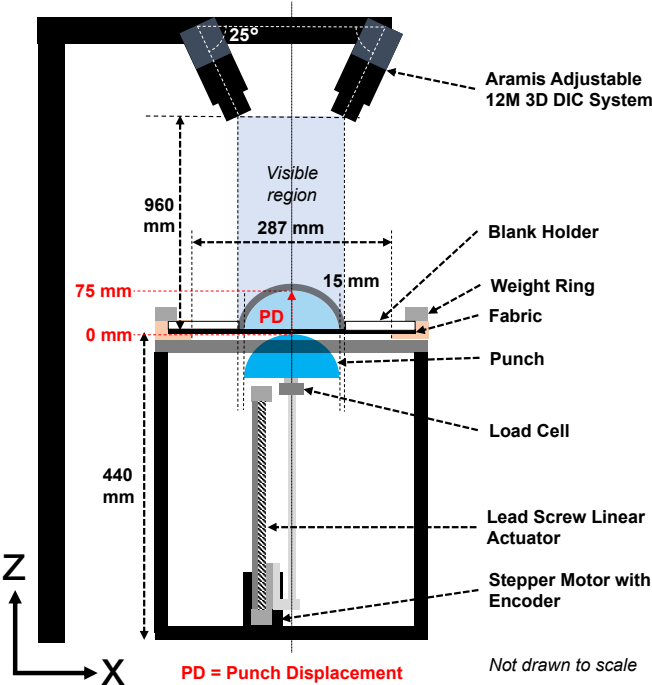
A.1.2 Improvements made to inherited rig

Fig. A.2 The upgraded forming setup used in this thesis.

The upgraded forming rig that was used in this thesis is shown in Figure A.2 and its key features have been previously described in Chapter 3. Relative to the inherited rig, the original frame, supporting rig and weight ring are preserved but numerous changes are otherwise made to improve the operation and functionality of the rig. The following are the key improvements or changes that have been made:

- **3D digital image correlation (DIC) system**: the 3D-DIC system replaces the singular digital camera in the original setup and enables the continuous measurement of wrinkle amplitudes and fabric surface strains, meaning that the development of wrinkling can be related to the development of strains in the fabric. Thus further understanding into the underlying wrinkle mechanisms can be made.

- **Orientation of the forming direction**: The forming direction in the upgraded forming rig is reversed such that the punch geometry moves upwards instead of downwards. The compatibility of different rig orientations with the 3D-DIC system were evaluated in Section A.2 and it was found that this arrangement was the only feasible one.

- **Improved actuator system**: a new linear actuator system assembly, consisting of a linear actuator, a more powerful stepper motor with encoder and a new motor driver/controller, is added to replace the photographic enlarger head and stepper motor in the original setup. This linear actuator system ensures the smooth and consistent motion of the punch geometry throughout the forming process, which was not possible with the enlarger head and undersized motor in the original rig. More details regarding the design of the new actuator system are detailed in Section A.3.

- **Closed loop motor control system**: to accommodate the new actuator system, a new control system had to be designed to operate the forming rig and ensure consistent movement of the forming punch during each test. The addition of the encoder allows the motor speed and position to be closely monitored and controlled during operation meaning that the precision of the punch movement can be ensured, which was not previously possible. Details regarding the motor control system and the associated graphical user interface (GUI) are shown in Section A.4.

- **Top blank holder**: in the inherited setup, there is a large gap between the blank holder and the punch geometry meaning that the fabric does not conform to the surface of the geometry during forming, contrary to an industrial forming process. In the upgraded rig, the distance from the geometry to the inner perimeter of the blank holder is reduced from 68.5 mm to 15 mm. For the hemisphere, this is achieved by introducing a wider top

blank holder with a smaller forming diameter (d_f) of 180 mm (reduced from 287 mm - see Figure A.3a). While the 180 mm blank holder is used in most of the hemispherical forming tests in this thesis, the wrinkling variability results between the two blank holders are compared in Chapter 4.

- **Additional punch geometries**: three additional punch geometries (triangular prism, tetrahedron and double dome - see Figure 3.1c) were manufactured to allow for the effect of tool geometry on wrinkling behaviour to investigated. Like the hemispherical tool, these punch geometries were manufactured out of modelling board. For each geometry, an associated top blank holder was manufactured from 10 mm thick Perspex that maintains a constant distance of 15 mm distance between the inner perimeter of the blank holder and the outline of the tool geometry (Figure A.3b).
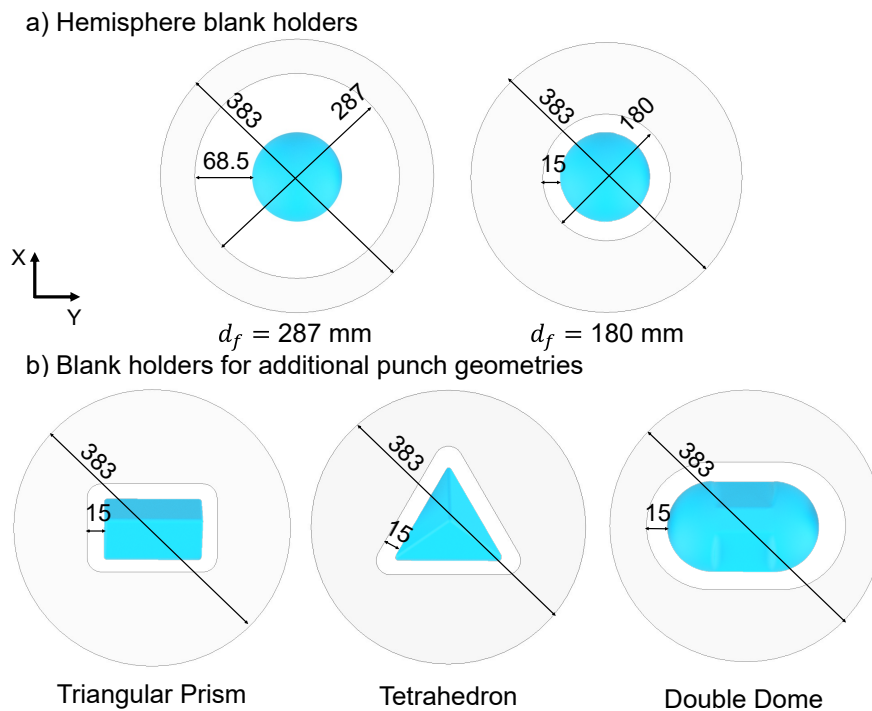
Fig. A.3 a) The two blank holders used with hemisphere punch geometry, with inherited blank holder (left) having a forming diameter (d_f) of 287 mm and the new blank holder (right) having a d_f of 180 mm. b) The blank holders designed for the additional three punch geometries investigated. The distance between the outline each of geometry and the inner blank holder perimeter is constant at 15 mm. All dimensions shown are in mm and the blank holders are all made out of 10 mm Perspex.

A.2 DIC system arrangement

Table A.1 The four different orientations of the DIC system relative to the forming rig that were considered, with the respective advantages and disadvantages of each option shown. Note that the schematics show the case of hemispherical forming with a forming diameter of 287 mm (the inherited forming scenario).

Option	Description	Schematic	Advantages (+) and disadvantages (-)	Feasibility
1	DIC system below		+ Inherited forming configuration - Camera lenses exposed to dirt - Required camera distance not possible	✗
2	DIC system on side		+ Required camera distance possible - Cannot easily apply blank holder force - Process not industrially representative - Difficulties in placing rig horizontal	✗
3	DIC system on side with mirror		+ Required camera distance possible + Inherited forming configuration - Mirror makes system calibration impossible - Image distortion possible	✗
4	DIC system above		+ Required camera distance possible - Limits maximum rig height - Forming direction reversed (from inherited)	✓

Four different orientations of the DIC system relative to the forming rig frame were investigated in order to identify the most feasible arrangement, with the results summarised in in Table A.1. It shows that the only feasible arrangement, is option 4 with the DIC system above the rig and the forming occurring from below. However, this configuration also presented a geometric limitation on the maximum height of the upgraded forming rig. This is because to be able to track the deformation of the fabric sample, the two DIC cameras need to be 960 mm away from the fabric surface and they can only be raised to a maximum of 1400 mm above the ground, due to the tripod. Therefore, the maximum height of the rig was limited to $1400 - 960 = 440$ mm and this informed the choice of the actuator system (Section A.3).
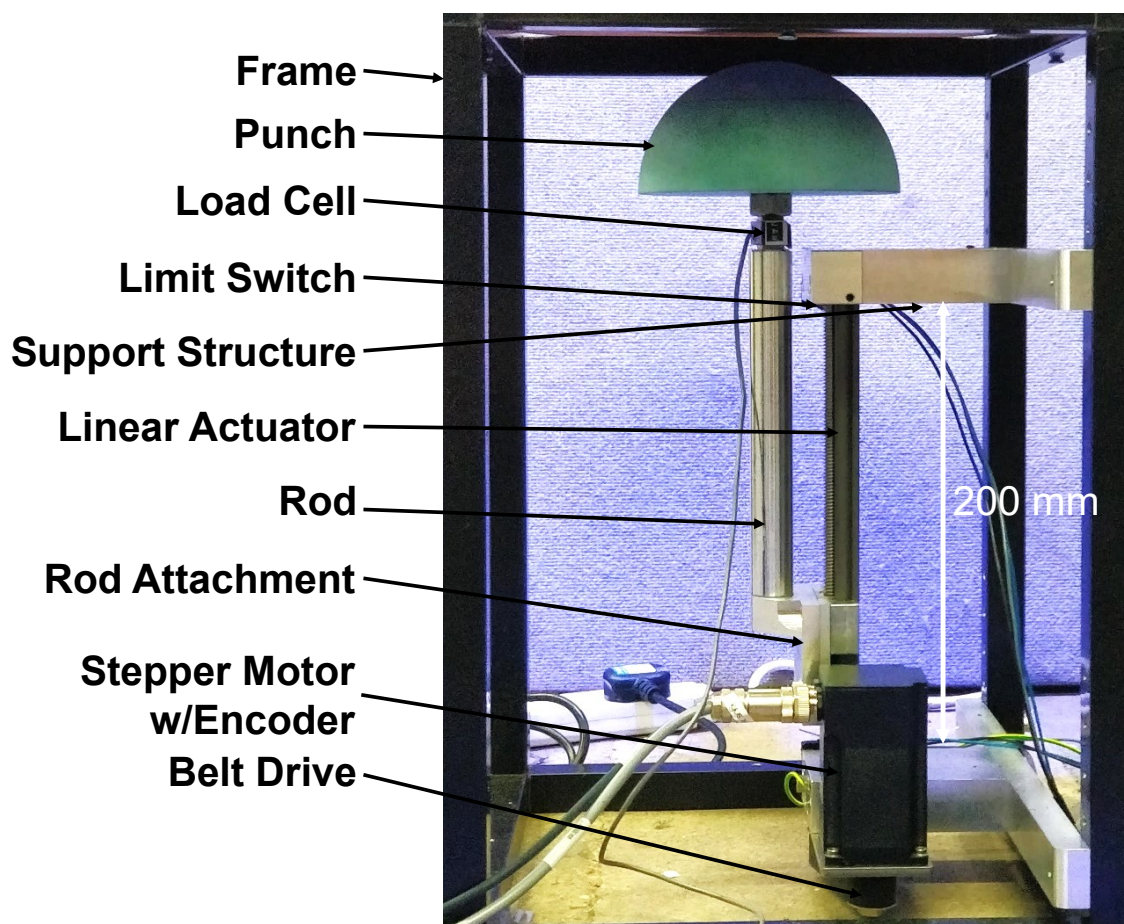
A.3   Actuator system

Fig. A.4 Labelled assembly of the actuator system fitted onto the forming rig, shown from the side view.

Inherited actuation system

The actuation system on the original rig (Figure A.1) was deemed inadequate because it could not provide a consistent movement of the punch that would allow for continuous deformation tracking. This was due to the rack and pinion actuation system within the original enlarger head which was manufactured to an inadequate tolerance, meaning there were significant variations in punch speed during forming. Furthermore, the stepper motor was undersized and thus began to struggle at higher loads resulting in inconsistent punch movements. In addition, the system had no feedback loop to ensure that the punch had moved the desired distance, which could lead to inaccuracies.

Upgraded actuation system

The upgraded actuator system is shown in Figure A.4, consisting of a linear actuator, a stepper motor with encoder and a custom built supporting steel structure that connects the system to the rig frame and the punch geometry. The linear actuator selected is the igus® drylin® SLW-1040 linear module with a trapezoidal 10 mm × 2 mm lead screw and a stroke of 200 mm [210]. This actuator is chosen because it fits within the dimensional constraints of the rig (Section A.2) and is able to raise and lower the punch consistently. The trapezoidal lead screw in the linear actuator also provides high positional accuracy, and because it is self-locking it also prevents the punch from moving back on itself under gravity [211]. The actuator is powered by a NEMA23 stepper motor with an encoder [212]. The stepper motor was selected to be more powerful than in the original forming rig (NEMA19) to ensure that there would be no issues with overloading. The encoder was chosen so that the actuator position could accurately be measured and a closed-loop control could be implemented.

To ensure a better fit within the dimensions of the rig, the stepper motor is connected to the linear actuator via a belt drive so that it could be fitted in parallel to it and not in series, thus reducing the total length of the system (see Figure A.4), as required by the DIC system arrangement (Section A.2). In order to attach the linear actuator within the existing forming rig frame, an adjustable supporting steel structure was manufactured. To attach the punch to the actuator, a steel attachment with a cylindrical rod was made that connects to the carriage of the linear actuator. The punch geometry and the load cell [213] are attached to the steel rod. The punch is fitted so that it is as close to the vertical axis of the actuator in order to minimise any adverse moments that could affect its movement. Two limit switches were fitted at the top and bottom of the actuator stroke, to provide limits for the punch movement. They also provide a

reference position from which to calculate the absolute punch displacement within the control system.

A.4   Closed loop motor control system

Motor driver/controller

A combined driver and controller system, the Arcus ACE-SDE [214], was selected to control the actuator system. This system is wired to the stepper motor and encoder, and controlled through a purpose-made LabVIEW control algorithm.

Control algorithm and GUI

The control algorithm for the forming process was designed and implemented in LabVIEW and replaces the inherited control algorithm used for the original forming rig. The algorithm provides a simple graphical user interface (GUI) (Figure A.5) to control the punch movement and provide a repeatable test sequence that will ensure that the punch moves in the same predictable way during each repeated test. The critical features of the control algorithm and GUI are:

- Encoder data used to feedback to the controller and create closed loop control.

- Automated movement of the punch to the test 'start' position at which the punch lies immediately below the fabric.

- Easily adjustable punch displacement and velocity variables.

- One button operation to start test and one button to reset punch to start position.

- Pop-up display to indicate the end of the test.

- Ability to record accurate load-displacement data for each test.
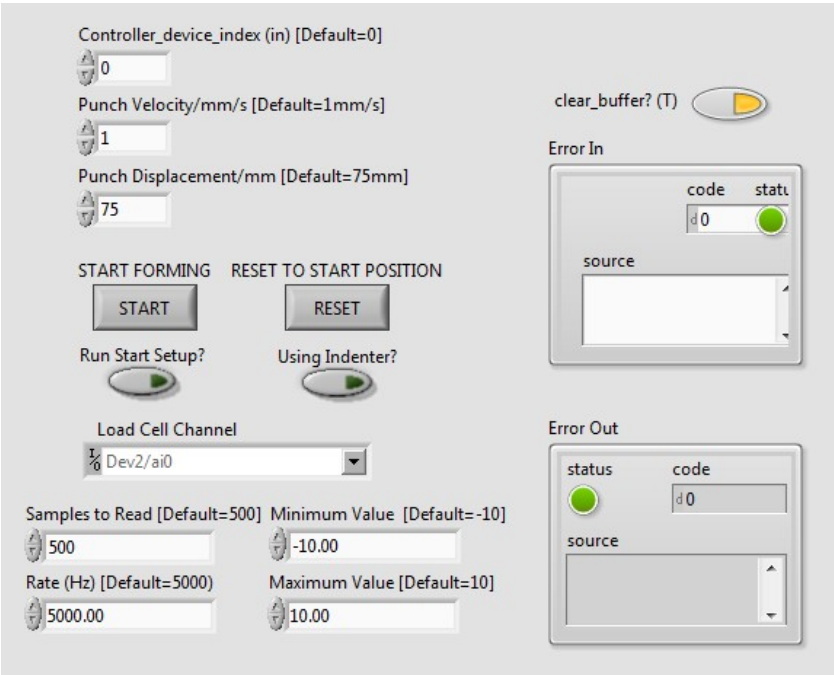
Fig. A.5 The graphical user interface (GUI) of the control algorithm, developed in LabVIEW, that is used to control the experimental forming rig.

Appendix B

Procedure for experimental forming tests

This appendix provides supplementary information relevant to Chapters 3-4 as it outlines the detailed experimental procedure for the forming tests. This experimental procedure is divided into four distinct parts: sample preparation (Section B.1), 3D-DIC preparation (Section B.2), rig preparation (Section B.3) and test procedure (Section B.4). The outlined procedure was developed specifically for the purposes of this thesis and is designed for the rig shown in Figure 3.2. More details regarding the development of the rig are shown in Appendix A while additional details for the speckle pattern application process are described in Appendix C. Beyond the forming rig and the 3D-DIC system (GOM 'ARAMIS 12M' - Table 3.2), and their associated software and equipment, the procedure makes use of the following specialised equipment:

- GOM 'CP20/350' calibration panel

- Circular template of diameter 380 mm

- Rotary cutter [215]

- Spray can gun, modified with a threaded screw (Figure C.2)

- Graphite powder spray [216]

- White flaw detector spray [217]

- Adhesive spray [218]

B.1   Sample preparation

1. Layout a roll of NCF fabric onto an even cutting surface. Place cardboard underneath the fabric to aid in the cutting process.

2. Place a circular template of diameter 380 mm onto the fabric such that the stitch aligns with the straight line drawn across the centre of the template. This ensures that each cut sample is consistent in terms of the stitch pattern.

3. Distribute four flat dead weights of 1 kg each onto the template in order to hold it in place during the cutting procedure.

4. Using a rotary cutter, carefully cut around the template to get a circular fabric sample. Multiple passes of the cutter around the sample are required.

5. Weigh the sample mass using a scale accurate to ± 0.01 g.

6. Select the particular punch geometry to be used for the forming test and take the top blank holder associated with that punch.

7. Place the blank holder onto centre of the sample such that it is aligned in a way that it matches the desired orientation of the sample relative to the punch/blank holder during the forming test.

8. Carefully draw a path around the inner perimeter of the blank holder using a paint marker. The inside of this perimeter is to be sprayed with a speckle pattern and represents the area that will be tracked during the forming test using the 3D-DIC.

9. On the outside of the circle, mark the sample with a number using the same paint marker for identification purposes.

10. Hang up the NCF such that its surface is perpendicular to the ground, using tape to hold it in place.

11. Define a spraying line that is parallel with the surface of the sample 500 mm away in the perpendicular direction, measured using a ruler that is secured to the floor.

12. Prepare the spray can gun attachment such that the distance between the two fixed nuts on the protruding screw is 19.00 mm. Verify this using a Vernier caliper.

13. Using the spray can gun attached to the graphite spray can, evenly spray the surface of the sample with one coat of graphite spray as the base layer for the speckle pattern. The spraying should be done from behind the spraying line with the spray can nozzle perpendicular to the sample. Throughout the process, have the spray can gun trigger pressed as far as it can go to ensure a constant flow. Start the spraying away from the sample and then move horizontally across the sample at a constant speed. Then move down the sample and repeat going in the opposite direction, until you have covered the area within the marked perimeter with one layer of graphite.

14. Remove the sample, lay it flat on the ground or on a table and let it rest for at least five minutes before proceeding with the next step.

15. Using the flaw detector spray (nozzle diameter of at least 0.6 mm required), very lightly press (a quarter of a full press) on the spray can such that the white powder spray spits out and leaves speckles of approximately 3 mm in diameter. Spray at a 45° angle from a distance of 200 mm away and continually sweep can from left to right, and vice versa to get the best results.

16. Continue spraying until there speckle pattern is evenly distributed and there are no empty spots within the marked perimeter. Note that it can take a few seconds for the speckles to appear.

17. Re-weigh the sample using a scale to determine the amount of mass deposited on the surface by the speckle pattern.

18. Check for the effect of the speckle pattern on the fabric's bending stiffness by placing a treated and an untreated sample halfway over the edge of a table and check that they deform by a similar angle. Align both samples such that stitching runs perpendicular to the edge of the table. If there is a vast difference in the bending angle (greater than $\pm 5°$), scrap the treated sample and repeat from step 1.

19. Repeat all steps to produce the required number of samples.

B.2   3D-DIC preparation

1. Power on the GOM 3D-DIC system cameras, lights and attached PC. Allow at least five minutes for them to warm up.

2. Set up the GOM cameras with 50 mm Titanar lenses and no lens extensions.

3. Rotate the cameras such that the lenses point parallel to the ground.

4. Following the instructions provided by GOM for a measuring volume of 350 mm $\times$ 260 mm and using the scale on the camera rig, set the slider distance to 396 mm for both cameras, measured from the inner edge of the cameras to centre of the camera rig.

5. Using gloves, set up the calibration panel (dimensions 350$\times$280 mm) on a tripod in front of the cameras such that the calibration panel is 960 mm away from the cameras (measured from the square at centre of cameras to the front surface of the calibration panel).

6. Secure the wheels on the GOM camera rig so that it cannot longer be moved relative to ground.

7. Open a new project in the ARAMIS Professional 2016 software and in the 'Set Up' view accurately adjust the position of the cameras such that the crosshairs of both cameras point at the centre of the calibration panel and the laser dot. Ensure that the slider distance does not increase beyond 396 mm. If necessary, move the camera rig slightly closer to the calibration to accommodate.

8. Open the camera apertures fully and adjust the focus using the focus ring on each camera until the text on the calibration panel is fully in focus.

9. Position the two lights such that they are above each respective camera and pointed towards the centre of the calibration panel.

10. Set the polarisation filters on the lights and cameras, following the instructions provided.

11. Adjust the aperture on one camera to 8 mm (providing a depth of field of 150 mm) and then adjust the other camera's aperture until they both display the same image intensity.

12. From the ARAMIS software, start the calibration process.

13. Following the on-screen instructions, sequentially rotate the calibration panel and take images until all the calibration steps have been completed.

14. Check that the calibration was successful and record the calibration accuracy.

15. Rotate the cameras to pointing towards the ground and raise them as high as possible on the camera rig (such that cameras are approximately 1.4 m above the ground).

16. From this point onwards, do not adjust the position of the cameras or lights relative to each other.

B.3   Rig preparation

1. Place experimental rig on the floor below the GOM cameras such that the two grooves on the supporting ring are aligned in parallel with the top/bottom edges of the GOM camera views. Use a ruler on the GOM computer screen to ensure that the grooves, as seen from both cameras, are all aligned along a horizontal line across the screen. This enables the alignment of the initial stitch direction ('0' direction) of the NCF material along the global X direction.

2. Fix the experimental rig in place using tape or similar.

3. Attach the desired punch geometry to the screw thread above the load cell and, if it is not a hemisphere, ensure that it is correctly orientated relative to the grooves on the supporting ring.

4. Check that the laser dot points at the centre of the tool geometry. Ensure, using a ruler, that the distances from laser dot to the inner perimeter of the blank holder are as expected. Adjust carefully if necessary.

5. Using gloves, place a prepared NCF sample into the rig for reference. Adjust the height of the cameras until the crosshairs on both cameras align with the laser dot.

6. Connect the additional electrical equipment (motor, controller, power supply, load cell, amplifier and laptop) to the forming rig.

7. Power on the dual power supply such and adjust such that one supply outputs 12V to the controller and the other 24V.

8. Power on the laptop used to control the forming process, and load the associated rig control file ('NCF_Forming_Rig_Control_System.vi') in LabVIEW 2014.

9. Select the name of the attached punch geometry from the drop-down menu in the graphical user interface (GUI).

10. Specify the desired punch displacement (75 mm by default) and punch velocity (1 mm s^{-1} by default) in the GUI.

11. Using gloves, remove the NCF sample from the rig.

12. Press 'Run' in LabVIEW at which point, the punch moves and resets to its initial test position.

B.4 Test procedure

1. Remove the top blank holder and weight ring from the rig.

2. Using gloves, place the NCF sample(s) onto the supporting ring, ensuring that the correct layup orientation is achieved and that the stitch direction of the top-most sample is aligned with the horizontal edge of the two GOM camera views and and an imaginary line drawn through the two grooves on either side of the supporting ring. Ensure that there is minimal slack in the fabric.

3. Place the top blank holder and the weight ring back onto the rig.

4. Attach hanging dead weights (of 2 kg each) onto the weight ring (by default a total of 8 kg). Attach the weights equally on the four hooks of the weight ring such that the weight on opposing hooks is the same.

5. Adjust the height of cameras such that the crosshairs at centre of each camera image line up with the laser dot on the surface of the fabric.

6. Take a reference image in the ARAMIS software.

7. In the software, define a 'Surface Component' and draw a polygon around the edges of the visible sample. Set facet size to 26 pixels and facet distance to 20 pixels.

8. Check the pattern accuracy of speckle pattern using the software. If low accuracy, remove the top sample and spray more white speckles (Section B.1) in order to produce a better speckle pattern.

9. In the software, click on 'Start Measuring Sequence': set the image capture rate to 1 Hz, the maximum number of images to 80 and specify 'lightgate' as the preferred method to start recording. Click 'OK'.

10. In LabVIEW, press 'Start" in the GUI, leading to a pop-up window to define the file in which the punch load and displacement data will be recorded. Name the document accordingly with the file type '.csv'.

11. Simultaneously press OK on the pop-up in LabVIEW and the button on the lightgate switch in order to start the forming process and the DIC image capture at the same time.

12. Wait for the test to complete at which point a pop-up will show up in the Labview GUI. Click OK.

13. Press 'Reset' in the LabVIEW GUI to return the punch to its default position.

14. Spray the deformed sampled generously with an adhesive spray to secure the deformed sample in place. To avoid the adhesive getting onto the rest of the rig, use a piece of paper with a cutout in the shape of the top blank holder.

15. Carefully remove the weights, the weight ring and the top blank holder.

16. Using gloves, take care to remove the NCF sample from the supporting ring without affecting its deformed shape.

17. Wait until the images have all been processed and then save the .aramis file.

18. Using the ARAMIS software, export the X, Y, Z coordinates and number of each facet point on the fabric surface as a .csv file for all the recorded stages (images) of the forming process.

19. Repeat all steps for the other prepared samples.

20. Post-process the .csv files in MATLAB in order to determine the wrinkle amplitudes, fibre strains and shear angles (Chapter 3).

Appendix C

Speckle pattern application

The following is supplementary detail related to Chapters 3-4 explaining how the speckle pattern method for preparing fabric samples for the experimental forming tests was developed.

A non-traditional speckle pattern application method was developed in order to minimise any unintended effects of the speckle pattern on the fabric deformation and wrinkling behaviour. A speckle pattern is needed in order to make DIC tracking possible. However, as noted by Harrison et al. [50], spray paint, which is typically used for DIC, cannot be used on fabrics because it drastically increases the bending stiffness of the fabric, resulting in unrealistic fabric deformations during forming. A number of alternatives to spray paint were qualitatively tested in Section C.1. Based on this, it was decided to apply the graphite powder as a base layer [50] and the flaw developer on top of this to create the white speckles.
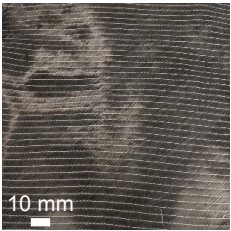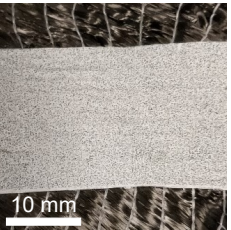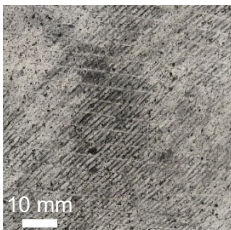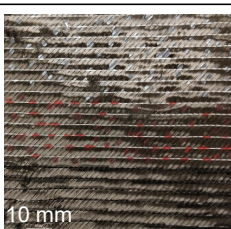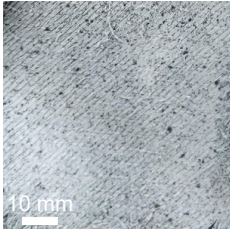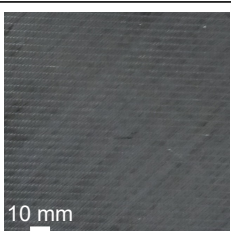
The application of the graphite is carefully controlled (Section C.2) and optimised because it was found that applying excess graphite could still significantly affect the fabric's bending stiffness. To achieve more repeatable and even spray across multiple samples, the spray pressure, orientation and amount of graphite are carefully controlled. Furthermore, the effect of the graphite on the fabric is minimised by optimising the spraying distance (Section C.3).

The speckles are evenly applied using the flaw developer spray (Section C.2). This low-density, dry powder sits on top of the fabric surface, without affecting its deformation. For each sample, only the area of the sample that is visible to the DIC cameras (within the inner perimeter of the blank holder) is sprayed.

The complete steps for applying the speckle pattern are outlined as part of the complete experimental procedure in Appendix B with more details regarding the speckle pattern material selection (Section C.1), controlled application (Section C.2) and spray distance optimisation (Section C.3) described below.

C.1 Speckle material selection

Table C.1 The six different speckle pattern material options that were considered, with their respective advantages and disadvantages shown.

Option	Description	Image (applied on fabric)	Advantages (+) and disadvantages (-)	Feasibility
1	Acrylic paint		- Colour not visible - Seeps into fabric - Deformation affected - Time dependent	✗
2	Transfer paper		+ Visible pattern - Paper bonds tows together - Deformation affected - Application requires heating	✗
3	Plastic primer		+ Visible pattern - Faded colours - Requires large amounts - Time dependent - Deformation affected	✗
4	Paint marker		+ Deformation unaffected - Faded colour - Labour intensive - Speckles too large - Cannot remove reflectiveness	✗
5	Flaw detector spray		+ Spray stays on surface + Time independent + Deformation unaffected + Clear colour/pattern - Easy to brush off	✓
6	Graphite spray		+ Eliminates reflectiveness + Time independent + Does not come off - Deformation (minimally) affected - No contrast with black carbon	✓

An investigation was carried out to determine the most suitable material to apply a speckle pattern on a carbon fibre biaxial NCF without affecting its deformation properties, with the results summarised in Table C.1. Each possible material was sprayed or applied onto a sample of NCF and then its pattern clarity and effect on the fabric were evaluated. The results showed that out of the six options considered, there were only two feasible material choices for the speckle pattern: the white flaw detector spray (option 5) and the black graphite spray (option 6). To take advantage of the strengths of each, it was decided to use both of them in combination for spraying the forming samples. To remove the reflectiveness of the carbon fibre [50], the graphite was used a black base layer with the flaw detector spray used to spray on white speckles. The particular flaw detector spray used is the 'Ambersil Flaw Detector Developer 3' [217] and the graphite spray chosen is the 'Kontakt Chemie Graphit 33' [216].

C.2 Controlled application of speckle pattern

As shown in Figure C.1a, the speckle pattern is applied in two distinct steps, with first the graphite powder spray applied as a black base layer and subsequently, the flaw developer spray applied to create the white speckles. The methods for applying each of these sprays are distinctly different with particularly the application of the graphite spray being tightly controlled in order to minimise its impact on the fabric's deformation during forming.

Graphite spray application

For applying the graphite spray (Figure C.1b), the fabric sample is hung up vertically on metal railings and a spraying line is made along the ground at a distance of 500 mm away from the surface of the fabric. The sample needs to be vertical so that the graphite can be sprayed with the spray can vertical, ensuring the most consistent and repeatable spray flow. The spraying of the graphite is done using the modified spray can gun in Figure C.2 that ensures the pressure to be controlled and kept constant for all samples. For the spraying, the operator presses down the gun trigger to its limit (set by x_{spr}) and moves the gun horizontally across the sample at a controlled speed. x_{spr} is fixed at 19.00 mm for all samples. Once a horizontal line has been sprayed, the gun is lowered slightly and the process is repeated until the area within the marked-out perimeter is fully covered in a single layer of graphite. The spraying distance is chosen to be 500 mm because this was found to be optimal spraying distance at which the amount of graphite is such that the reflectiveness of the carbon fibre is removed but the graphite has a negligible impact of the fabric's bending stiffness (Section C.3)
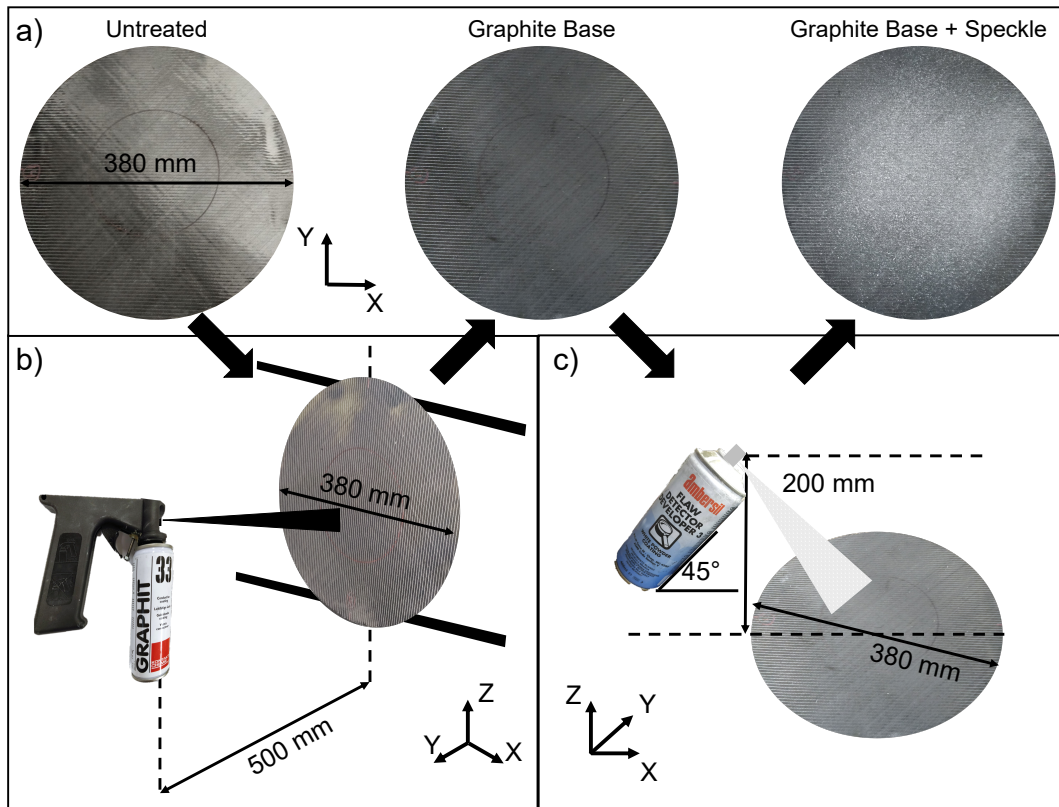
Fig. C.1 An outline of speckle pattern application process: a) the NCF sample before (untreated - left), during (treated with a graphite base layer - middle) and at the end of the process (treated with both graphite and the white speckle pattern), b) a schematic of the graphite application process where the sample is hung up vertically and the graphite is sprayed using a spray can gun from a distance of 500 mm, c) a schematic of the speckle application process where the flaw developer spray is applied with the sample flat on the ground and the spray can at 45° to it. The spray can is pressed lightly in order to create the speckles.

Flaw developer spray application

As depicted in Figure C.1c, the flaw developer spray is applied with the fabric on a flat surface and the spray can pointed down at a 45° angle, while the nozzle is pressed very lightly such that the spray periodically 'spurts out' with speckles. To ensure that speckles are produced it is required that the nozzle of the spray can is at least 0.6 mm wide. The spraying is done with the spray can approximately 200 mm above the sample. During spraying, the spray can is moved back and forth across the fabric surface until the area within the marked-out perimeter is covered in a speckle pattern of regular density.

Fig. C.2 An outline of the modified spray can gun: a) side view of gun attached to the graphite spray can, b) close-up side view of the spray can gun showing the exposed bolt distance (x_{spr}) which controls the maximum trigger movement and thus the spray flow rate, and c) close-up front view of the spray can gun showing how the bolt limits the trigger movement.

C.3 Optimisation of graphite spraying distance

An optimisation study was carried out to ensure that a minimal amount of graphite is applied that still achieves a suitable speckle pattern without significantly affecting the fabric deformation. This optimisation was conducted by measuring the bending stiffness of rectangular (325 mm × 37.5 mm) NCF samples before and after spraying with graphite. The samples are cut with the fibre tows of one layer aligned with the longer sample edge and five samples are sprayed at distances of 200 mm, 300 mm, 400 mm, 500 mm and 600 mm respectively. The bending stiffness of the fabric is measured using the standardised cantilever test, originally developed by Peirce [219]. The experimental rig developed for this test, based on the ASTM standard D1388 [64], is shown in Figure C.3.

With an incline (ϕ) of 41.5° designed into the rig, the linear bending stiffness per unit width along the fibre tow direction (B_{fi}) can be calculated from the overhang length of the fabric ($l_{over}[m]$ - shown in Figure C.3) as follows [219]:

$$B_{fi}[Nm] = Wg\left(\frac{l_{over}}{2}\right)^3 \tag{C.1}$$

where W is the 'areal weight' $= 0.44$ kg m^{-2} and g is the acceleration due to gravity $= 9.81$ m s^{-2}.
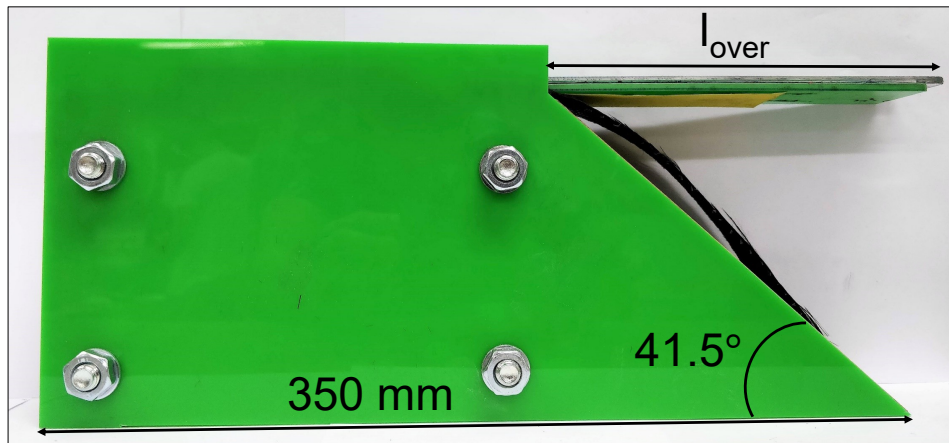
Fig. C.3 The experimental rig used for the cantilever test that measures the bending stiffness of a fabric, designed according to ASTM standard D1388 [64]. This rig was inherited and not developed as part of this thesis.

The results of this investigation are shown in Figure C.4, showing that the minimum graphite spraying distance, at which the bending stiffness of sample treated with graphite is equivalent to the untreated sample's bending stiffness is 500 mm. This spraying distance is thus used for the spraying of the forming samples (Figure C.1b and Appendix B).
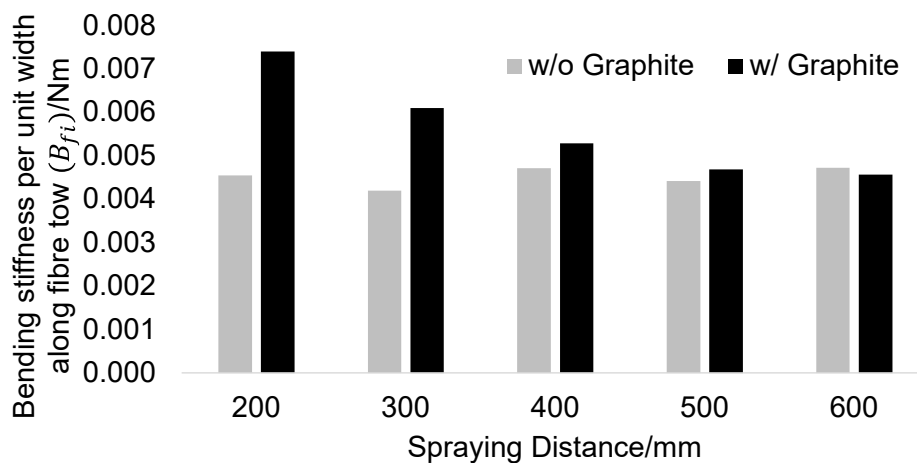
Fig. C.4 The effect of graphite spraying distance on bending stiffness of rectangular samples of a biaxial non-crimp fabric, with the bending stiffness of each sample measured before and after the spraying of the graphite.

Appendix D

Benchmark wrinkle generator and decoupling validation

The following is supplementary material to Chapter 4. It describes the generator used to generate the fictitious benchmark wrinkle surfaces (Section D.1), the details relating to the generated reference wrinkle pattern (Section D.2), and how the wrinkling variability calculation method is validated in being able to produce decoupled results in terms of wrinkle amplitude and wrinkle location (Section D.3).

D.1 Wrinkle generator

In order to evaluate the proposed wrinkling variability method, a parametric wrinkle generator is developed in MATLAB that utilises a number of sinusoidal waves orientated (and increasing in amplitude) radially on a circular sample. The generated wrinkles are loosely based on the wrinkle patterns seen when a circular sample of biaxial NCF is formed over a hemisphere with a blank holder of forming diameter (d_f) of 180 mm and when considering only the visible fabric within the inner perimeter of the blank holder (Chapter 3). The variables that control the appearance of the wrinkle pattern are the total number of wrinkles (n_w), the number of wrinkle groupings (n_g - where each grouping is separated by a non-wrinkle region), the number of wrinkles in each grouping (n_{wg}), the peak amplitude of the wrinkles (a_{max}) and the offset angle (θ_o - the counterclockwise rotation of the wrinkle surface relative to the X direction - see Figure D.1).

Using polar coordinates, the wrinkle amplitude in the z direction ($a_w(r, \theta)$) at each angle ($\theta = [0, 360]°$) and radius ($r = [0, 90]$ mm) is calculated as follows:

$$a_w(r, \theta) = \begin{cases} a_{max} \sin(\omega(\theta - \theta_o)) f(r) & \text{if } (n-2)\theta_s - \theta_\Delta \leq \theta - \theta_o \leq n\theta_s + \theta_\Delta \\ 0 & \text{otherwise} \end{cases} \tag{D.1}$$

where the wrinkle frequency $(\omega) = \frac{n_w}{2}$, the start angle $(\theta_s) = \frac{\pi}{n_g}$ and the wrinkle group width angle $(\theta_\Delta) = \frac{n_w - n_g n_{wg}}{n_g}$, the radial wrinkle distribution $(f(r))$:

$$f(r) = \begin{cases} 0 & \text{if } 0 \leq r < 30 \\ \frac{r}{30} - 1 & \text{if } 30 \leq r < 60 \\ 1 & \text{if } 60 \leq r \leq 90 \end{cases} \tag{D.2}$$

and the start angle factor (n):

$$n = \begin{cases} n+2 & \text{if } \theta - \theta_o \geq n\theta_s + \theta_\Delta \\ n & \text{otherwise} \end{cases} \tag{D.3}$$

where θ is increased from $0°$ to $360°$ in increments of $1°$ and n initially $= -1$. $f(r)$ ensures the wrinkles do not occur near the centre of the fabric and are the largest towards the outer boundary of the visible fabric, as was observed during the experimental tests (Chapter 3).

Similarly to the experimental wrinkling data, each surface is fit to a square grid of 300×300 mm using *gridfit* [145] from which the surface is made into a grayscale image of 301 px $\times$ 301 px that can then be processed according based on the variability calculation method described in Chapter 4 (see Figure 4.3).

D.2   Reference benchmark wrinkle surface

Using the wrinkle generator, a reference generated wrinkle surface (Figure D.1a) is created that consists of four equal-sized, separated sinusoidal wrinkles ($n_w = 4$, $n_g = 4$, $n_{wg} = 1$) of maximum amplitude ($a_{max,ref}$) 1 mm and a maximum width of 11.25 mm that are equally positioned around the circumference of the surface such that the right wrinkle is at $0°$ from the X direction ($\theta_{o,ref} = 0°$) . This surface is used as the reference to which all other generated surfaces in the decoupling study (Section D.3) and the benchmark study presented in Chapter 4 (Figure 4.4).

D.3 Validation of decoupling

The calculated wrinkle amplitude difference and wrinkle location difference are validated to be decoupled, as shown in Figure D.1. The analysis to validate this decoupling was done by generating three sample sets of 11 wrinkle surfaces each (Figure D.1b), which are all compared relative to the reference to calculate the respective values of Δa_w and Δl_w: the first set i) ('Coupled Amplitude and Location') consists of imposing both increasing amplitude (a_{max}) and offset angle (θ_o), the second set ii) ('Decoupled Location') is made up of surfaces of increasing offset angle and the third set iii) ('Decoupled Amplitude') consists of surfaces of increasing wrinkle amplitude. For each generated surface, the specified maximum amplitude relative to reference ($\Delta a_{sp,max}$) is calculated as follows:

$$\Delta a_{sp,max} = a_{max} - a_{max,ref} \tag{D.4}$$

where a_{max} is the maximum amplitude of the particular generated sample. The value of a_{max} is varied between $1-6$ mm for sample sets i) and iii) resulting in the range of $\Delta a_{sp,max}$ being $[0,5]$ mm. Furthermore, the specified offset angle relative to the reference ($\Delta\theta_{sp}$) is calculated as follows:

$$\Delta\theta_{sp} = \theta_o - \theta_{o,ref} \tag{D.5}$$

where θ_o is the offset angle of the particular generated sample. The value of θ_o is varied for sample sets i) and ii) between $0-25°$ resulting in the range of $\Delta\theta_{sp}$ being $[0,25]°$.

If the proposed variability calculated method is fully decoupled in terms of amplitude and location, the results for Δa_w and Δl_w from the first set i) should be equal to the results of Δl_w from the second set and Δa_w from the third set. This is proven to be the case in Figure D.1c, which shows how both the calculated Δa_w and Δl_w increase linearly with the imposed differences in amplitude and location relative to the reference, and the coupled case is near identical to the decoupled cases. Furthermore, Figure D.1c shows that Δa_w and Δl_w are both highly sensitive to imposed changes between two samples with an imposed $\Delta a_{sp,max}$ of 5 mm corresponding to a Δa_w of 2.5 mm and an imposed $\Delta\theta_{sp}$ of 25° causing a Δl_w of 25 mm, highlighting that the proposed method is suitable to identify even minute differences between wrinkle surfaces.
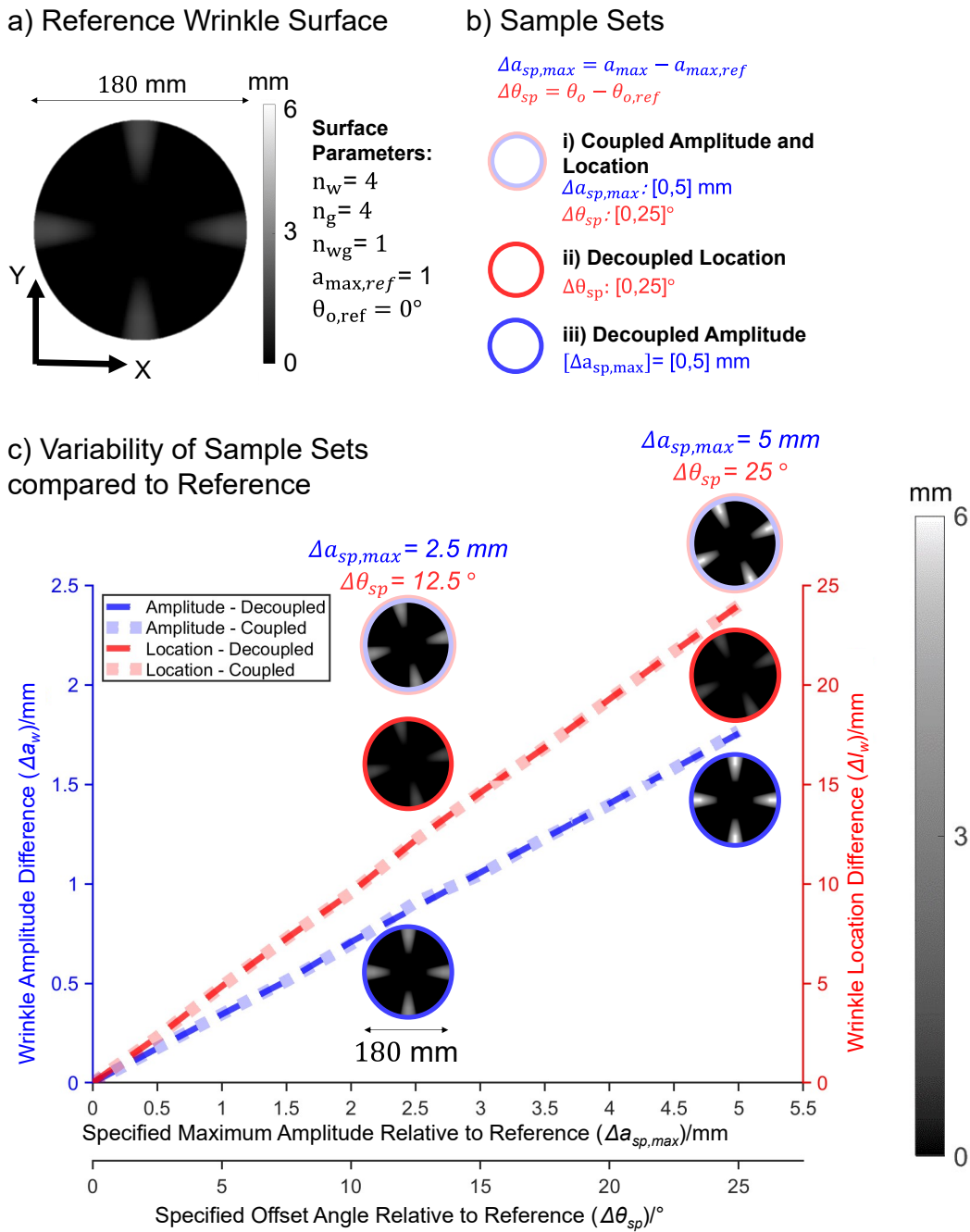
Fig. D.1 Validation of the decoupling in the calculation of wrinkle amplitude difference and wrinkle location difference for the variability characterisation method, based on a set of three generated wrinkle surface sample sets: a) an outline of the reference wrinkle surface against which all the other surfaces are compared, b) summary of the three sample sets (11 wrinkle surfaces generated for each) for which the wrinkling variability is calculated relative to the reference surface: i) coupled amplitude and location (linearly increasing specified maximum amplitude relative to the reference ($\Delta a_{sp,max}$) and specified offset angle relative to the reference ($\Delta \theta_{sp}$) ii) decoupled location (linearly increasing $\Delta \theta_{sp}$ only) iii) decoupled amplitude (linearly increasing $\Delta a_{sp,max}$ only), c) the calculated wrinkle amplitude difference and wrinkle location difference for increasing $\Delta a_{sp,max}$ and $\Delta \theta_{sp}$ showing that the decoupled cases (sample sets ii) and iii)) are identical to the results from the coupled case (sample set i).

Appendix E

Geometrical metrics

This appendix relates to Chapter 5 and describes the definitions of the geometrical metrics that are used to analyse the 10,000 generated tool geometries. The 14 geometrical metrics that are defined in Table E.1 are used to filter the geometries based on specific requirements, characterise them for subsequent correlation with wrinkling severity, as well as to enable the filleting and meshing of them in preparation for input into finite element forming simulations. These geometry definitions are supported by Figure E.1, which displays graphically how these metrics relate to the generated tool geometries, using one exemplar tool geometry from the initial geometry set. Each of the metrics and the way they are calculated are described below.

Table E.1 Details relating to the 14 geometrical metrics used in Chapter 5 for filtering, characterising and filleting the generated geometries.

Number	Type	Symbol/unit	Name	Equation/definition	Usage
1	Spatial	ΔX/mm	Box length	$\Delta X = X_{max} - X_{min}$	Filtering
2	Spatial	ΔY/mm	Box width	$\Delta Y = Y_{max} - Y_{min}$	Filtering
3	Spatial	ΔZ/mm	Box height	$\Delta Z = Z_{max} - Z_{min}$	Filtering
4	Spatial	r_V	Volume ratio	$r_V = \frac{V}{\Delta X \Delta Y \Delta Z}$	Characterisation
5	Spatial	r_A	Area ratio	$r_A = \frac{A_t}{A_b}$	Filleting and characterisation
6	Spatial	$|d_o|$	Offset distance	$|d_o| = \sqrt{\Delta x^2 + \Delta y^2}$	Characterisation
7	Angular	$\theta_{d,min}$	Min draft angle	$\theta_{d,min} = min(\theta_d)$	Filtering and filleting
8	Angular	$\overline{\theta_{int}}$	Mean interior angle	$\overline{\theta_{int}} = mean(\theta_{int})$	Characterisation
9	Angular	$\theta_{int,min}$	Min interior angle	$\theta_{int,min} = min(\theta_{int})$	Filleting
10	Angular	$\overline{\theta_{tt}}$	Mean true twist angle	$\overline{\theta_{tt}} = mean(\theta_{tt})$	Characterisation
11	Angular	$\overline{\theta_{do}}$	Mean overall draft angle	$\overline{\theta_{do}} = mean(\theta_{do})$	Characterisation
12	Surface	$N_{z,min}$	Min normal Z	$N_{z,min} = min(N_z)$	Filtering
13	Surface	H_r	Representative mean curvature	$H_r = mode(H)$	Characterisation
14	Surface	K_r	Representative mean curvature	$K_r = mode(K)$	Characterisation

a) Isometric View

Surface Normal
$$\vec{N} = \begin{pmatrix} N_x \\ N_y \\ \mathbf{N_z} \end{pmatrix}$$

Curvatures
H, K

Coordinates
$X = (x, y, z)$

Volume V

Area A_t

$(X_{min}, Y_{max}, Z_{max})$

ΔZ

$(X_{max}, Y_{min}, Z_{min})$

$(X_{min}, Y_{max}, Z_{min})$

Area A_b

ΔY

ΔX

$(X_{max}, Y_{max}, Z_{min})$

b) Top View

True Twist Angle

θ_{tt}

Interior Angle

θ_{int}

$|d_o|$

Offset distance

c) Side View

Top Polygon

Middle Polygon

θ_d *Draft Angle*

θ_{do}

Bottom Polygon

Overall Draft Angle
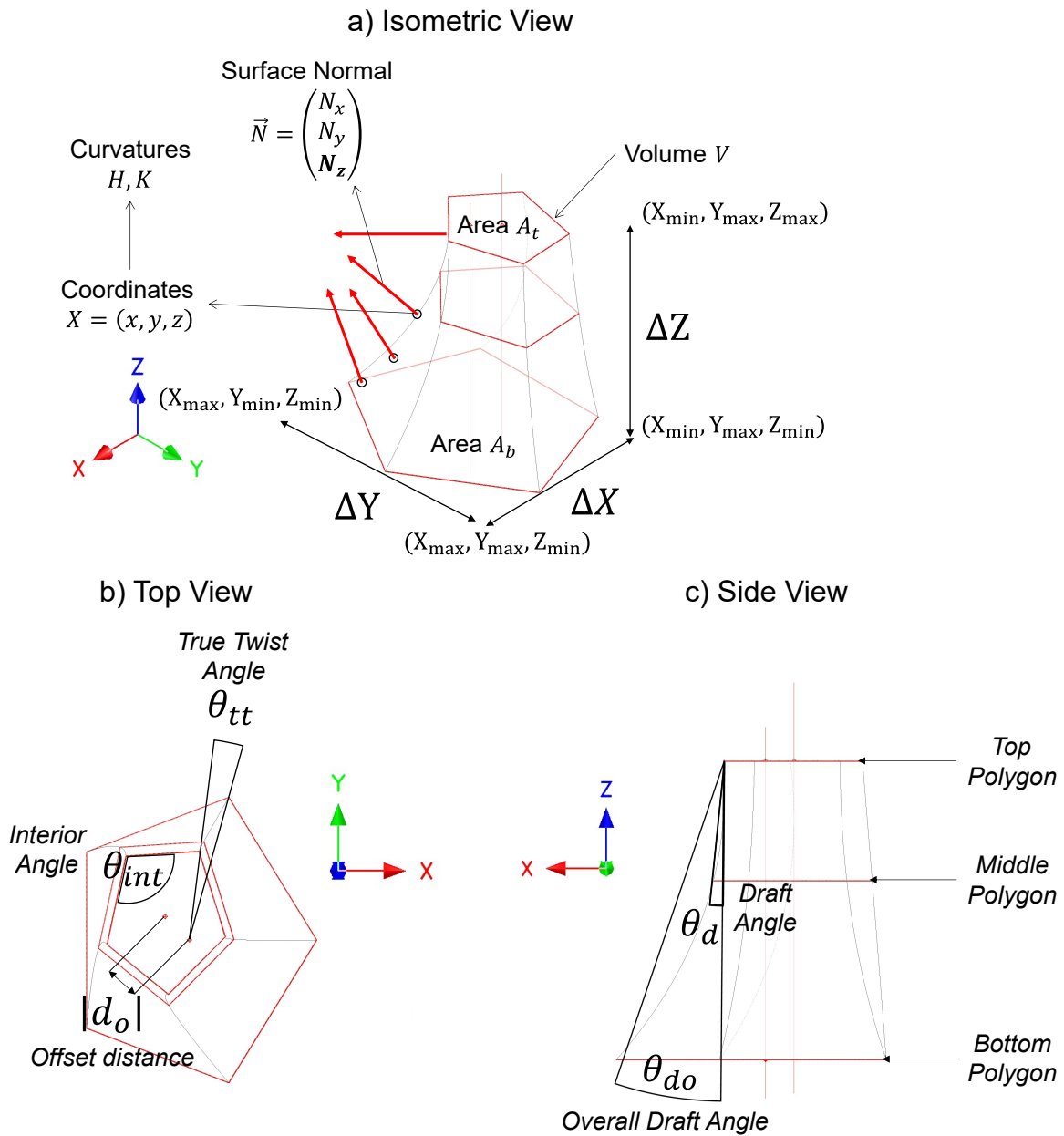
Fig. E.1 The 14 metrics from Table E.1 defined graphically relative to one of the generated tool geometries, which is shown from three different views: a) isometric view, b) top view and c) side view.) Note that the defined angles are calculated for all the corresponding vertices of the polygons in order to obtain the final metric values, as per Table E.1. The three different polygons are derived from the way the geometries are generated in Figure 5.4.

E.1   Spatial metrics

The spatial metrics (numbered 1-6 in Table E.1) include the 'box length' (ΔX), the 'box width' (ΔY), the 'box height' (ΔZ), the 'volume ratio' (r_V), the 'area ratio' (r_A) and the 'offset distance' ($|d_o|$). The maximum dimensions along each axis (ΔX, ΔY and ΔZ) are obtained by calculating the dimensions of the bounding box of the geometry and thus their product corresponds to the volume of the bounding box. Based on this and the true volume of the geometry (V - see Figure E.1a), the volume ratio can be calculated as follows:

$$r_V = \frac{V}{V_b} = \frac{V}{\Delta X \Delta Y \Delta Z} \tag{E.1}$$

The area ratio (r_A) corresponds to the ratio of the area of the top polygon (A_t) to that of the bottom polygon (A_b), which are both shown in Figure E.1a:

$$r_A = \frac{A_t}{A_b} \tag{E.2}$$

Finally, the offset distance ($|d_o|$) is determined from the input shift parameters Δx and Δy, corresponding to the total offset distance of the middle polygon relative to the centre of the bottom polygon:

$$|d_o| = \sqrt{(\Delta x)^2 + (\Delta y)^2} \tag{E.3}$$

E.2   Angular metrics

The angular metrics, numbered 7-11 in Table E.1, are all determined similarly by calculating the angles between the respective polygon vertices, as defined in Figure E.1. Once the (x, y, z) coordinates of the vertices $(1, 2, 3)$ related to each of angular metric have been obtained, the corresponding angle (θ_i) at vertex 2 can be calculated as follows:

$$\theta_i = \arccos \frac{\begin{pmatrix} x_1 - x_2 \\ y_1 - y_2 \\ z_1 - z_2 \end{pmatrix} \cdot \begin{pmatrix} x_3 - x_2 \\ y_3 - y_2 \\ z_3 - z_2 \end{pmatrix}}{\left| \begin{pmatrix} x_1 - x_2 \\ y_1 - y_2 \\ z_1 - z_2 \end{pmatrix} \right| \left| \begin{pmatrix} x_3 - x_2 \\ y_3 - y_2 \\ z_3 - z_2 \end{pmatrix} \right|} \tag{E.4}$$

and is then repeated at all n vertices of the geometry polygon. Once the angles for all vertices of the polygons have been obtained, either the mean is calculated to obtain $\overline{\theta}$ or the minimum value is taken to get θ_{min}.

The 'min draft angle' ($\theta_{d,min}$) is defined as the minimum angle between the top polygon vertices and the corresponding middle polygon vertices from the side-view (Figure E.1c), while the 'mean overall draft angle' ($\overline{\theta_{do}}$) is the mean draft between the top and bottom polygons instead (ignoring any relative twist between them). The 'mean interior angle' ($\overline{\theta_{int}}$) and the 'min interior angle' ($\theta_{int,min}$) correspond to the mean and minimum interior angles of the top polygon, respectively (Figure E.1b). As a result of the averaging, $\overline{\theta_{int}}$ is directly correlated with the number of polygon sides n by $\overline{\theta_{int}} = (n-2) \times \frac{180}{n}$.

The 'mean true twist angle' ($\overline{\theta_{tt}}$), defined as the relative twist between the nearest vertices of the middle and bottom polygons, requires the calculation of the 'mean relative rotation angle' ($\overline{\theta_{rot}}$) and the 'mean twist angle' ($\overline{\theta_t}$). The mean relative rotation angle ($\overline{\theta_{rot}}$) is the mean rotation, from the top-view, of the middle polygon vertices relative to the bottom polygon vertices, measured about the centre of the bottom polygon. The rotation is measured for all vertices of the polygons and then the mean value is taken to obtain $\overline{\theta_{rot}}$. This mean angle is measured based on correlating the polygon vertices that would be nearest with no rotation and thus it is an incomplete measure of the tool geometry twist, as the rotation changes the relative alignment of vertices of the middle and bottom polygon. The true twist angle needs to be measured based on the nearest vertices after the rotation has been completed and accounting for the fact that the maximum possible twist is a function of the mean interior angle ($\overline{\theta_{int}}$). As a result, the mean twist angle ($\overline{\theta_t}$) is initially calculated from $\overline{\theta_{int}}$ and $\overline{\theta_{rot}}$ as follows, noting that any rotation that is a multiple of $180 - \overline{\theta_{int}}$ does not contribute to twisting:

$$\overline{\theta_t} = \overline{\theta_{rot}} \% (180 - \overline{\theta_{int}}) \tag{E.5}$$

where % corresponds to the remainder operator and $180 - \overline{\theta_{int}}$ corresponds to the relative rotation at which the vertices overlap and thus no twist occurs. From this the mean true twist angle ($\overline{\theta_{tt}}$) shown in (Figure E.1b) is calculated accounting for the fact that the maximum true twist is halfway between two polygon vertices before decreasing linearly:

$$\overline{\theta_{tt}} = \begin{cases} \overline{\theta_t} & \text{if } 0 \leq \overline{\theta_t} < \frac{180 - \overline{\theta_{int}}}{2} \\ (180 - \overline{\theta_{int}}) - \overline{\theta_t} & \text{if } \frac{180 - \overline{\theta_{int}}}{2} \leq \overline{\theta_t} < 180 - \overline{\theta_{int}} \end{cases} \tag{E.6}$$

E.3 Surface metrics

The surface metrics (12-14 in Table E.1) are obtained by considering the local variations in the topology of each geometry. A evenly spaced set of coordinates $X(x,y,z)$ are obtained from the tool surface and the surface normal vectors $(\vec{N}(N_x, N_y, N_z))$ at each coordinate are calculated. The minimum of value of the z component of the surface normals (N_z) corresponds to the 'min normal Z' $(N_{z,min})$.

These coordinates and surface normals are obtained by analysing each segmented face of the tool geometry (as seen for example in the geometries of Figure 5.4b). However, as the geometry generator (Figure 5.4a) approximates curvature along the $X - Y$ direction by increasing the number of polygon vertices (n) to a large value $(lim_{n \to \infty})$, it is not possible to accurately calculate local curvatures from the segmented faces of each geometry as these are not representative of the true curvature of the shape formed by the combination of these segmented faces. As a result, the curvatures are obtained instead by fitting a surface through the coordinate points of each geometry such that the true local curvatures become apparent. The tool geometry coordinates are interpolated to a 2D grid $Z(x,y)$ of g mm grid length and then differentiated twice in order to calculate the local mean (H) and Gauss (K) curvatures at each grid point [220]:

$$H = \frac{(Z_x^2 + 1)Z_{yy} - 2Z_xZ_yZ_{xy} + (Z_y^2 + 1)Z_{xx}}{(2(Z_x^2 + Z_y^2 + 1)^{1.5}} \tag{E.7}$$

$$K = \frac{Z_{xx}Z_{yy} - (Z_{xy}^2)}{1 + (Z_x^2) + (Z_y^2)^2} \tag{E.8}$$

where Z_x is the first partial derivative with respect to x, Z_y is the first partial derivative with respect to y, Z_{xx} is the second partial derivative with respect to x, Z_{yy} is the second partial derivative with respect to y and Z_{xy} is the second partial derivative with respect to x and then y. Once the local curvatures are obtained, the 'representative mean curvature' (H_r) and 'representative Gauss curvature' (K_r) are calculated by taking the mode of all locally calculated curvature values:

$$H_r = mode(H) \tag{E.9}$$

$$K_r = mode(K) \tag{E.10}$$

The mode is used instead of the mean in order to ignore the influence of any outliers. As the resultant curvature values were found to be dependent on the grid size (g), g was selected based on evaluating the curvatures for a hemisphere of radius of 50 mm. For this geometry, the

values of K and H are known and constant across the whole surface ($H = -0.02$ mm^{-1} and $K = 0.0004$ mm^{-2}) and thus it allows the optimal grid size to be selected.
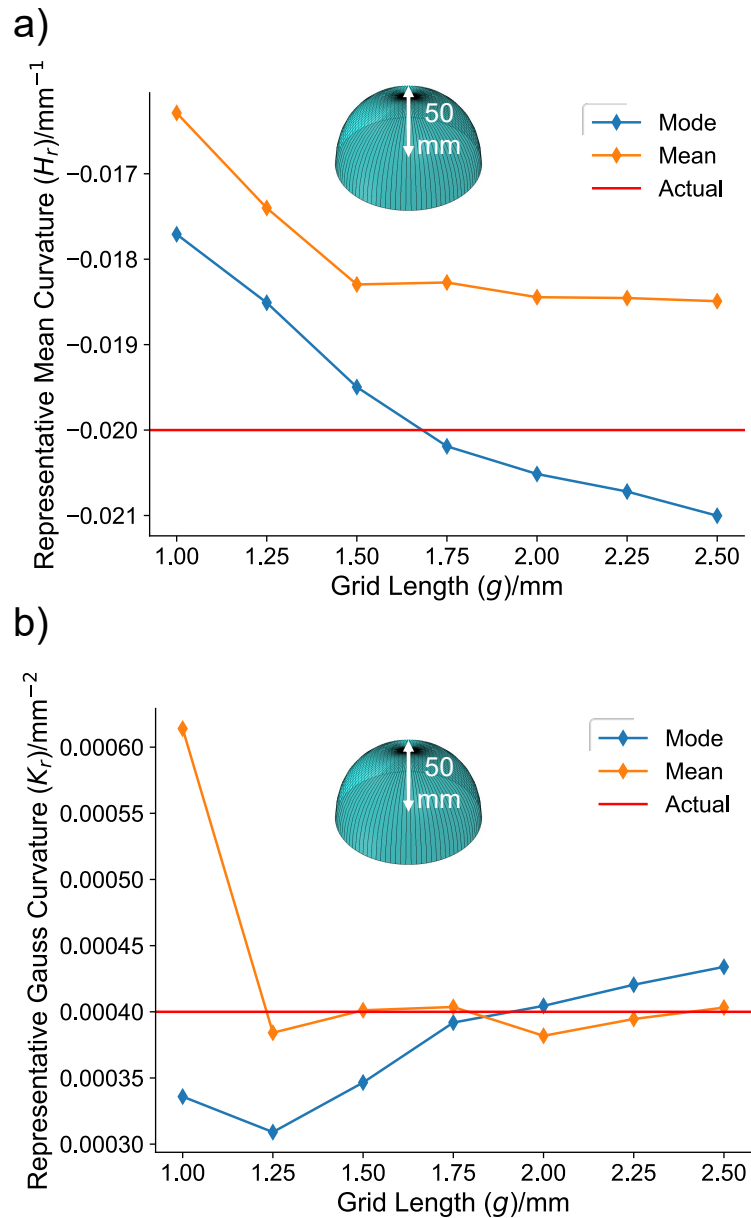

Fig. E.2 Optimisation of the grid length (g) used in surface fitting the tool geometry coordinates for calculating the representative curvatures: a) representative mean curvature for a hemisphere of radius 50 mm, calculated based on the mode and mean of the distribution of local curvature values, plotted against (g), defining the spacing of the grid onto which the coordinates of the hemisphere are fitted, and b) representative Gauss curvature for a hemisphere of radius 50 mm, calculated based on the mode and mean of the distribution of local curvature values, plotted against g.

Figure E.2 shows the representative mean curvature (H_r - in a) and representative Gauss curvature (K_r - in b), calculated using both the mean and mode of the curvature distributions, for a range of values of grid length (g). It shows that the optimal value of g is between 1.75 - 2 mm as this corresponds to when the respective values of H_r and K_r are closest to the expected values. The value of $g = 2$ mm is chosen in this study for consistency and simplicity. Additionally, particularly for H_r in Figure E.2a, it is shown that the mode is a more accurate measure of representative curvature than the mean, as it is not affected by outliers caused by the surface fitting process. The effect of these outliers was found to be significant for many of the generated geometries, thus necessitating the use of the mode. For simplicity, the representative curvature values are referred to as the 'Mean Curvature' and 'Gauss Curvature' in Chapter 5 but the subscript '$_r$' is kept in their respective symbols in order to indicate that these refer to the representative mode values from the overall curvature distributions.

Appendix F

Optimisation of deep learning model

The following is supplementary data for Chapter 5, showing how the hyperparameters of the deep learning surrogate model were selected (Section F.1). Additionally, the apparent model accuracy limit is shown through a comparison of the 10 best performing models (Section F.2).

F.1 Hyperparameter optimisation

The approach taken for the hyperparameter optimisation is to perform a set of parameter sweeps across a range of plausible values for each hyperparameter, then training the model using each one and finally identifying which one results in the largest value of 'image accuracy' ($MS - SSIM$) on the test set. While more complex optimisation methods exist (e.g. Bayesian optimisation [221]), this approach was found to be sufficient for the purposes of this model.

To reduce the computational cost of each training run, the total size of the dataset used is reduced to 448 instead of 1802 (representing approximately 1/4 of all data), with 90% of these geometries used for training and 10% reserved for the test set. As a result, the 'image accuracy' values achieved in the optimisation models are not as high as those recorded for the final trained model (Figure 5.12) but the results of the optimisation are equally applicable.

Each model within the optimisation is trained until the loss on the test set no longer improves based on the early stopping algorithm, using a 'patience' of 6 (the training stops if the loss does not reduce over six consecutive epochs) or if 160 epochs are reached. Then the maximum values of 'image accuracy' for both the training and the test sets are recorded and plotted against the results from the rest of the parameter sweep. In the case of the loss function, the parameter sweep consists of different loss functions not different parameter values but the same principle applies.
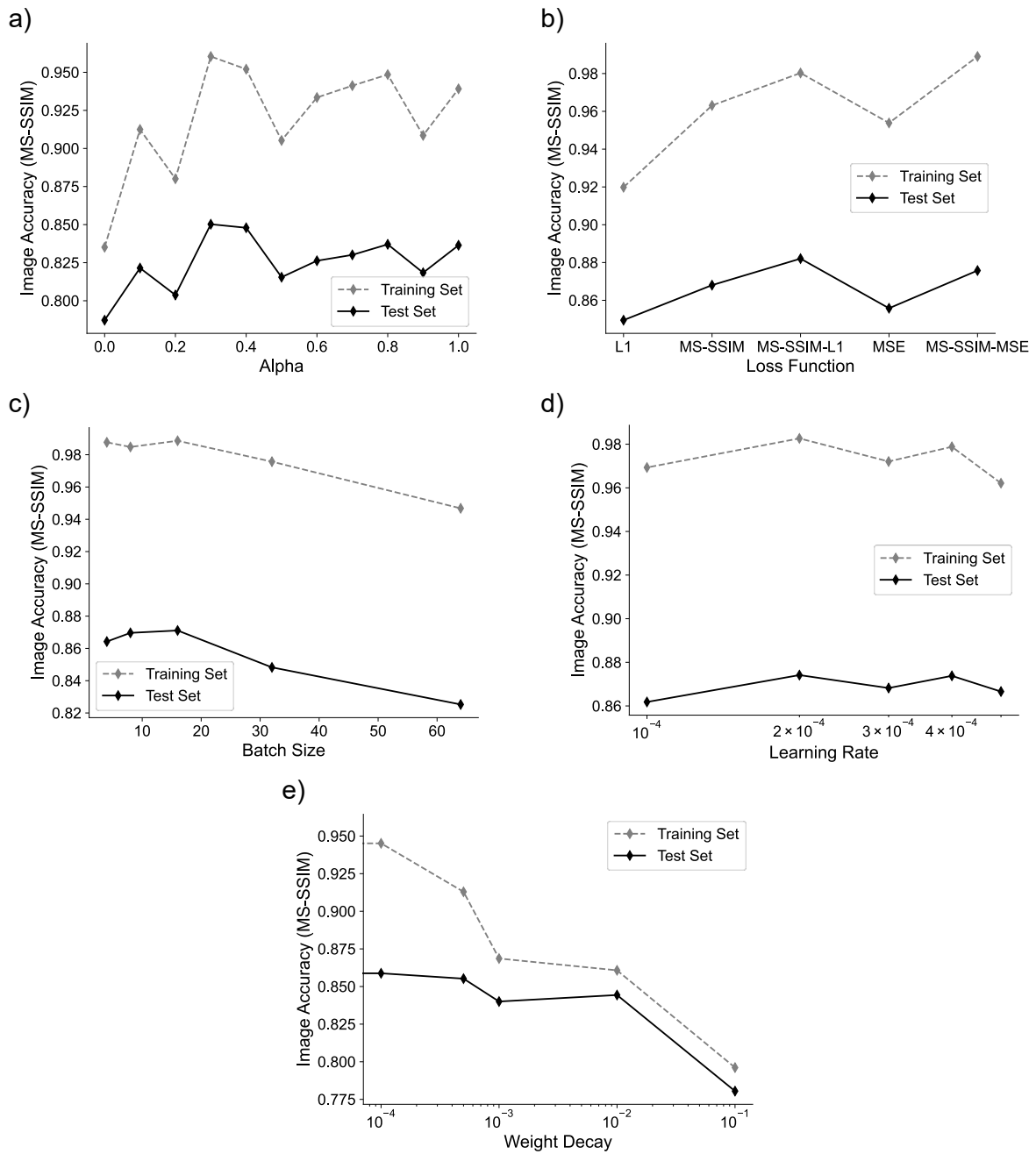
Fig. F.1 The optimisation of various key hyperparameters related to the training of the deep learning surrogate model: a) loss function, b) the value of α for the $L_{MS-SSIM-L1}$ loss function, c) batch size (b) d) learning rate (lr), and e) weight decay (w_d). They are all optimised with respect to the maximum 'image accuracy' on the test set.

Loss function

Three different loss functions ($L_{MS-SSIM}$, L_{L1}, L_{MSE}) and two 'hybrid' loss functions ($L_{MS-SSIM-L1}$ and $L_{MS-SSIM-MSE}$) were compared against each other to identify which results in the highest 'image accuracy' on the test set. $L_{MS-SSIM-MSE}$ is defined in a similar way as $L_{MS-SSIM-L1}$ (Equation 5.13) but using the mean squared error loss (L_{MSE}) instead of the mean absolute error loss (L_{L1}):

$$L_{MS-SSIM-MSE} = \alpha L_{MS-SSIM} + (1-\alpha)L_{MSE} \qquad \text{(F.1)}$$

with an $\alpha = 0.09$ used for $L_{MS-SSIM-MSE}$ and $\alpha = 0.4$ for $L_{MS-SSIM-L1}$ (see below). The optimisation results in Figure F.1a show that the best performing loss function is $L_{MS-SSIM-L1}$ and this motivates its use in Chapter 5.

Loss function balance

The value of α determines the balance between $L_{MS-SSIM}$ (Equation 5.14) and L_{L1} (Equation 5.11) for the $L_{MS-SSIM-L1}$ loss function, with $\alpha = 1$ corresponding to $L_{MS-SSIM-L1}$=$L_{MS-SSIM}$ and $\alpha = 0$ corresponding to $L_{MS-SSIM-L1}$=L_{L1}. The optimal value of $\alpha = 0.4$ for $L_{MS-SSIM-L1}$ is determined from Figure F.1b where the effect of α is investigated over the parameter range $\alpha = [0, 0.1, 0.2...1]$, with the best performing values being $\alpha = 0.3$ and $\alpha = 0.4$. The value of $\alpha = 0.4$ is used in Chapter 5 and for the comparison of loss functions in Figure F.1a.

Batch size

The batch size (b), corresponding to the number of images that are fed to the model during each training iteration, is optimised in Figure F.1c over the parameter range: $b = [4, 8, 16, 32, 64]$. Typically, the lower the value of b the higher the accuracy at the cost of longer training times due to less parallelisation during training. However, in practice, the accuracy also tends to drop for very small values of b, which is what is found in Figure F.1c, where the optimal value is found to be $b = 16$, and this is what is used in Chapter 5.

Learning rate

The learning rate (lr) determines the rate at which the training progresses and is likely the most important hyperparameter to optimise for any gradient-based neural network [222]. The optimal lr was initially explored, as is conventional, over a logarithmic parameter range: $lr = [10^{-5}, 10^{-4}, 10^{-3}, 10^{-2}, 10^{-1}]$ and based on this it was found that $lr = 10^{-4}$ results in the

highest 'image accuracy' on the test. For a more detailed study, lr is investigated over the range $[1,2,3,4,5] \times 10^{-4}$ in Figure F.1d and the optimal value is found to be $2 \times 10-4$. Compared to the initial value of $lr = 10^{-4}$, using the larger $lr = 2 \times 10-4$ is also preferable as it brings down the computational cost associated with training.

Weight decay

The optimisation of the weight decay (w_d) parameter, that is applied to the loss function within the optimiser in order to potentially improve model generalisability, is shown in Figure F.1e for the range $w_d = [0, 5 \times 10^{-4}, 10^{-4}, 10^{-3}, 10^{-2}, 10^{-1}]$. The results show that the optimal value of w_d is 0, suggesting that any amount of weight decay has a negative effect on the accuracy of this model.

F.2 Model accuracy limit

Over the course of the model development and optimisation process, hundreds of models were trained with different configurations in order to identify the best performing surrogate model and through this process, it became apparent that there appears to be a limit to the maximum achievable model accuracy using this dataset. Figure F.2 shows a comparison of the 10 best performing models that were all trained on the whole 1802 image dataset but were each run with slightly different sets of hyperparameters. It shows that the maximum accuracy achieved was just above 0.9, with all the other models achieving similar levels of accuracy. These accuracy results are representative optimal cases of all models that were trained during this investigation. Given that none of the models are able to reach close to the perfect accuracy of 1, it suggests that there is an underlying accuracy limit that cannot be overcome through parameter modification. It is suggested that this limit is due to certain discrepancies in the underlying dataset of tool geometry and wrinkle surface images, as discussed in Chapter 5.
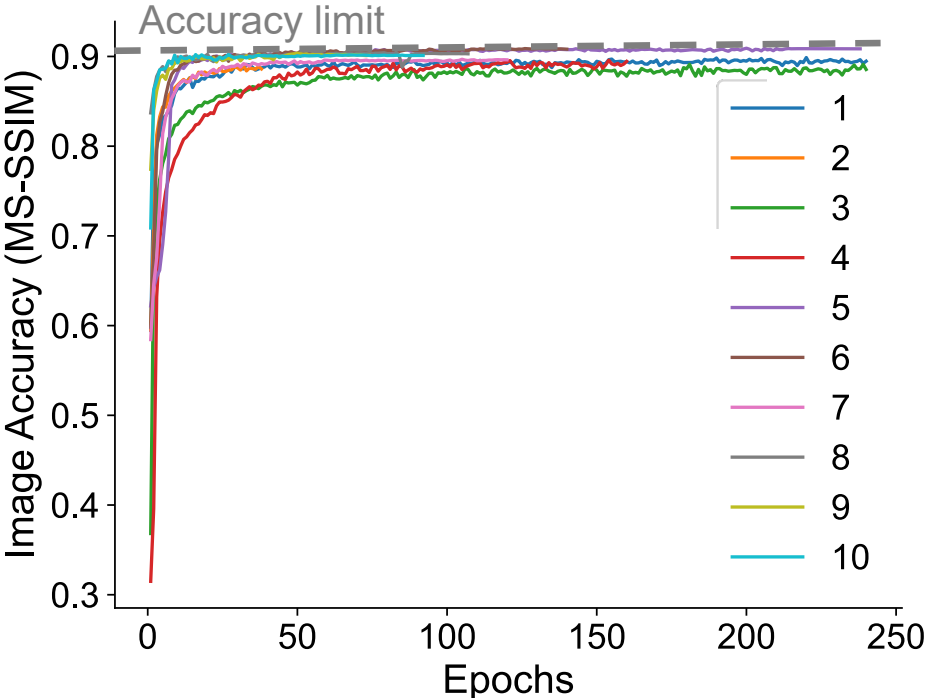
Fig. F.2 A comparison of the 10 best performing models that were trained during the optimisation process, showing the progression in the 'image accuracy' on the test set with increasing numbers of training epochs. The maximum accuracy achieved is 0.909 with all models achieving an accuracy similar to this.

Appendix G

Research outcomes

G.1 Journal publications

- F. Yu, S. Chen, J. V. Viisainen, M. P. F. Sutcliffe, L. T. Harper, and N. A. Warrior. A macroscale finite element approach for simulating the bending behaviour of biaxial fabrics. *Composites Science and Technology*, 191, 2020. doi:10.1016/j.compscitech.2020.108078

    – Not a part of this thesis but cited throughout

- J. V. Viisainen, A. Hosseini, and M. P. F. Sutcliffe. Experimental investigation, using 3D digital image correlation, into the effect of component geometry on the wrinkling behaviour and the wrinkling mechanisms of a biaxial NCF during preforming. *Composites Part A: Applied Science and Manufacturing*, 142:106248, 2021. doi:10.1016/j.compositesa.2020.106248

    – Publication of Chapter 3

- J. V. Viisainen and M. P. F. Sutcliffe. Characterising the variability in wrinkling during the preforming. *Composites Part A: Applied Science and Manufacturing*, 149:106536, 2021. doi:10.1016/j.compositesa.2021.106536

    – Publication of Chapter 4

- J. V. Viisainen, F. Yu, A. Codolini, S. Chen, L. Harper, and M. P. F. Sutcliffe. Rapid prediction of wrinkles in a biaxial NCF after preforming over a given tool geometry using a deep learning surrogate model. *Composites Science and Technology*, 2022. [In preparation]

    – Publication of Chapter 5

G.2   Conference presentations and posters

Presentations:

- J. V. Viisainen and M. P. F. Sutcliffe. Towards finding the cure for wrinkling: a study of fabric deformation. In *Department of Engineering Division C Graduate Student Conference 2019*, Cambridge, 2019

- J. V. Viisainen, J. Zhou, and M. P. F. Sutcliffe. Characterisation of the wrinkling behaviour of a biaxial non-crimp fabic during forming. In *22nd International Conference on Composite Materials*, Melbourne, 2019

- J. V. Viisainen, F. Yu, A. Codolini, S. Chen, L. Harper, and M. P. F. Sutcliffe. A deep learning surrogate model for rapid prediction of geometry-induced wrinkles in fabric preforming. In *International Conference on Manufacturing of Advanced Composites 2021*, Virtual, 2021

Posters:

- J. V. Viisainen, J. Zhou, and M. P. F. Sutcliffe. Experimental determination of a forming limit diagram for non-crimp fabrics through 3D digital image correlation. In *Department of Engineering Division C Graduate Student Conference 2018*, Cambridge, 2018

- J. V. Viisainen, J. Zhou, and M. P. F. Sutcliffe. Wrinkle formation characterisation during the forming of non-crimp fabrics. In *International Conference on Manufacturing of Advanced Composites 2018*, Nottingham, 2018

G.3   Co-supervision of MEng students

- A. G. H. Chow. *Draping of composite structures*. MEng report, Department of Engineering, University of Cambridge, 2019